A NOVEL CRYOGENIC FABRY-PÉROT INTERFEROMETER FOR FAR-INFRARED ASTRONOMY

IAN VEENENDAAL
Bachelor of Science, University of Lethbridge, 2013
Master of Science, University of Lethbridge, 2016

A Thesis
Submitted to the School of Graduate Studies
of the University of Lethbridge
in Partial Fulfillment of the
Requirements for the Degree

DOCTOR OF PHILOSOPHY

Department of Physics and Astronomy
University of Lethbridge
LETHBRIDGE, ALBERTA, CANADA

A NOVEL CRYOGENIC FABRY-PÉROT INTERFEROMETER FOR FAR-INFRARED ASTRONOMY

IAN VEENENDAAL

Date of Defence: August 6, 2019

Dr. David Naylor Thesis Supervisor	Professor	Ph.D.
Dr. Locke Spencer Thesis Examination Committee Member	Associate Professor	Ph.D.
Dr. Ken Vos Thesis Examination Committee Member	Associate Professor	Ph.D.
Dr. Behnam Seyed-Mahmoud Internal External Examiner	Associate Professor	Ph.D.
Dr. Nasser Moazzen-Ahmadi External Examiner	Professor	Ph.D.
Dr. Chad Povey Chair, Thesis Examination Committee	Instructor	Ph.D.

Dedication

To my wife and adventuring companion, Alexis. Thank you for your constant encouragement during the adventure that was the writing of this thesis.

Abstract

The continued improvement in the sensitivity of far-infrared detectors has caused scientists to reconsider the design of cryogenically cooled instruments which can fully exploit their potential. The SAFARI instrument on the SPICA observatory is one such instrument which will employ a medium resolution grating-based spectrometer, with an optional high-resolution module. While a Martin-Puplett Fourier transform spectrometer was ultimately selected for the high-resolution module, an initial design was a Fabry-Pérot interferometer This thesis presents the design and performance of a cryogenic, angle-scanned Fabry-Pérot interferometer for future far-infrared astronomical spectrometers. In addition, multiple custom subcomponents were required in order to characterize the interferometer, including a tunable terahertz line source, a cryogenic diffraction grating monochromator, and a cryogenic, laser-based position metrology system. Novel features of the design were discussed, and the spectral response of the instrument was modelled. Spectral line profiles were verified using specialized calibration line sources.

Acknowledgments

First and foremost, I would like to thank my supervisor, Professor David Naylor, for taking me on as a research assistant during the second year of my undergraduate degree (even after I missed the application deadline), and continuing to support and encourage me through the completion of my undergraduate degree, Master's degree, and now, my Ph.D.

I would also like to thank the members of the Astronomical Instrumentation Group, both past and present, who played crucial roles in the completion of this thesis. To Brad Gom, thank you for imparting to me your vast knowledge of cryogenic and optical systems, and for demonstrating a patient and meticulous attitude, which has proven to be crucially important for the successful completion of the work presented in this thesis. Also, a huge thank you to Sudhakar Gunuganti for always being able to provide a helping hand around the lab when it was needed, for providing critical feedback on many of my ideas, and for operating and performing maintenance on the TFC whenever I was unable to do so. Without your help, this thesis would not have shown the marvellous results that it does. To Trevor Fulton, thank you for tireless efforts in writing multiple simulators with which to compare my results. Discussions with you on the techniques used to model the interference effects proved to be invaluable.

To the technical services team at the University of Lethbridge, especially Geoff Minors, Rebecca Sirota, and Kalle Kiiskinen. Without the assistance you all gave in fabricating the optical elements, cryogenic mechanisms, readout electronics, and cryostat cycling and temperature readout circuitry, I would not have had a thesis to

write.

To the team at SRON who developed the silicon etalon which was characterized in this thesis, including Willem Jellema, Martin Eggens, Carolein Feenstra, Marcel Ridder, Willem Jan Vreeling, and I am sure many others. While we originally anticipated that your task in developing the etalon may prove extremely difficult, you have all demonstrated the value of forward planning and resourcefulness, and have pulled through to deliver the exact device we wished for on paper. I could not have asked for a better collaboration.

To the many co-op students who worked with me on this project, thank you for your ideas, your hard work and dedication towards the tasks I assigned to you. Pawel Kapusta, Charing Chen, Steve Zimmerman, and Tony Huber: without your efforts, I would have long since given in to despair over the amount of work required to complete this project. Thank you all for applying your unique skill sets to this project.

To my fellow graduate students, thank you for all your assistance, both directly and indirectly. Thank you, Adam Christiansen, for your endless programming tips, and for your incredible work on the three-phase metrology system. The end result worked better than any of us would have expected, and that is in no small part thanks to the perfectionism you show in all things. To Geoffrey Sitwell, Chris Benson, Vince Weiler, you have all made my job more interesting, and I will miss working alongside each of you.

I would like to thank my thesis committee, Professor Locke Spencer and Professor Ken Vos, for providing helpful feedback through every step of the way. The thesis has been much improved from your comments and suggestions.

I have received support from many different organizations through the duration of this project, without whose funding I would never have embarked on this research path. I would like to give special thanks to the Natural Sciences and Engineering Research Council of Canada Canadian Graduate Scholarship (NSERC-CGS), Alberta

Innovates Tech Futures (AITF), and the Flights and Fieldwork for the Advancement of Science and Technology (FAST) funding initiative through the Canadian Space Agency.

To my parents, Adrian and Ellis, and family, thank you for keeping me motivated for the last ten years of my post-secondary education. To my parents especially, I will never forget the values you have worked so hard to instill in me.

Lastly, to Alexis, the most important person in my life, thank you for proof-reading the thesis in its entirety. Thank you also for being a more loving and supportive wife than I could have asked for. The end of this thesis marks the beginning of a new chapter in our lives, and I am thankful and relieved that I have you to share it with. You provide me with just the right amount of level-headedness and ensure our lives never get too stressful or too boring. I can't thank you enough for the confidence and open-mindedness you give to me.

Contents

Contents viii

List of Tables xii

List of Figures xiv

List of Abbreviations xxi

1 Far-Infrared Astronomy 1
- 1.1 Far-Infrared Wavelengths . . . 2
- 1.2 Far-Infrared Astronomy . . . 4
  - 1.2.1 The interstellar medium . . . 6
  - 1.2.2 Star Forming Regions . . . 7
  - 1.2.3 Protoplanetary Disks . . . 9
  - 1.2.4 Cycling of Matter . . . 10
  - 1.2.5 Role of Water . . . 10
  - 1.2.6 Galaxy Formation and Evolution . . . 11
  - 1.2.7 Onset of heavy elements . . . 11
  - 1.2.8 Star Formation Rates in High-Z Galaxies . . . 12
  - 1.2.9 Supermassive Black Hole Growth . . . 13
- 1.3 Observing Challenges . . . 13
  - 1.3.1 Atmospheric Extinction . . . 13
  - 1.3.2 Detector Technology . . . 14
- 1.4 Cryogenics in space . . . 15
- 1.5 Conclusion . . . 18

2 SPICA-SAFARI 19
- 2.1 The Space Infrared Telescope for Cosmology and Astrophysics (SPICA) 19
  - 2.1.1 Instruments on Space Infrared Telescope for Cosmology and Astrophysics (SPICA) . . . 20
- 2.2 Science Goals . . . 22
  - 2.2.1 Galaxy Evolution . . . 23
  - 2.2.2 Rise of Metals and Dust . . . 25
  - 2.2.3 Early Stars and Galaxies . . . 26
  - 2.2.4 Magnetic Fields . . . 27
  - 2.2.5 Protoplanetary Disks . . . 27
  - 2.2.6 Ices and Minerals . . . 28
- 2.3 Mission Requirements . . . 29

2.4 Instrument Design . . . 30
2.4.1 Detector Noise . . . 31
2.4.2 Dispersive Element . . . 31
2.4.3 High Resolution Interferometer . . . 33
2.5 Conclusion . . . 36

3 Fabry-Pérot Interferometry **38**
3.1 Ideal Fabry-Pérot . . . 38
3.1.1 Free Spectral Range . . . 42
3.1.2 Line Width . . . 43
3.1.3 Finesse . . . 44
3.1.4 Resolving Power . . . 44
3.2 Practical Fabry-Pérot . . . 45
3.2.1 THz Reflectors . . . 46
3.2.2 Practical Finesse . . . 51
3.2.3 Beam *Walk-off* . . . 53
3.2.4 FPI Design . . . 55
3.3 FPI Operation . . . 56
3.4 Angle Scanning Simulations . . . 58
3.4.1 Reflectivity Simulations . . . 60
3.4.2 *Walk-off* Simulations . . . 62
3.5 Experimental Design . . . 64
3.6 Thesis Overview . . . 67

4 Calibration Sources **69**
4.1 Introduction . . . 69
4.2 THz Photomixer . . . 71
4.2.1 Principle of Operation . . . 71
4.2.2 Original Photomixer . . . 76
4.2.3 Photomixer Upgrades . . . 78
4.2.4 Photomixer Automation . . . 79
4.3 HCl/DCl Gas Cell . . . 82
4.3.1 Rotational Transitions . . . 82
4.3.2 HCl Isotopologues . . . 83
4.4 Atmospheric Water Vapour . . . 85
4.5 Conclusions . . . 86

5 Diffraction Grating **87**
5.1 Motivation . . . 87
5.2 Grating Theory . . . 88
5.2.1 The Grating Equation . . . 88
5.2.2 Grating Monochromators . . . 92
5.2.3 Dispersion . . . 93
5.2.4 Resolving Power . . . 94
5.2.5 Free Spectral Range . . . 95

5.2.6 Blaze Angle . . . 95
5.3 Optical System Design . . . 96
5.3.1 Etendue . . . 96
5.3.2 Anamorphic Magnification . . . 97
5.3.3 Stray Light . . . 98
5.4 Grating Design . . . 99
5.4.1 Optical Design . . . 99
5.4.2 Grating Parameters . . . 101
5.4.3 Slit Sizes . . . 102
5.4.4 Grating Actuation . . . 104
5.4.5 Radiation Shielding . . . 107
5.4.6 Cryogenic Considerations . . . 107
5.4.7 Adhesiveless Bearings . . . 108
5.5 Grating Control . . . 109
5.6 Grating Operation . . . 110
5.6.1 Operating Modes . . . 110
5.7 Validation and Testing . . . 111
5.7.1 Stepper Repeatability . . . 111
5.7.2 Wavelength Calibration . . . 112
5.7.3 Resolving Power . . . 114
5.7.4 Efficiency . . . 117
5.7.5 Polarization . . . 118
5.8 Conclusions . . . 119

6 Instrument Design 120
6.1 Optical Layout . . . 120
6.1.1 Requirements Analysis . . . 121
6.1.2 Source Design . . . 122
6.1.3 FP Optical Design . . . 123
6.1.4 Grating Design . . . 125
6.1.5 Detector Design . . . 125
6.1.6 System Integration . . . 127
6.2 Pendulum Design . . . 128
6.2.1 Pendulum . . . 130
6.2.2 Rotary Voice Coil . . . 131
6.2.3 Flexures . . . 132
6.2.4 Metrology . . . 133
6.3 Etalon Development . . . 137
6.4 Test Facility Cryostat . . . 141
6.5 Control Software . . . 142
6.6 Conclusion . . . 143

7 Instrument Operation, Data Processing and Calibration 144
7.1 Thermal Characteristics . . . 146
7.2 Instrument Control . . . 150
7.3 Scanning Strategies . . . 152
7.3.1 Scan Initialization . . . 154
7.3.2 lock-in amplifier (LIA) Detection . . . 155
7.3.3 continuous scan (CS) Mode . . . 155
7.3.4 step and integrate (SI) Mode . . . 156
7.3.5 System Calibration Scans . . . 156
7.4 Data Processing . . . 157
7.4.1 Fringe Count to Angle Conversion . . . 158
7.4.2 Timing Corrections . . . 159
7.4.3 Calibration Products . . . 160
7.4.4 Data Products . . . 160
7.5 First Light . . . 160
7.6 End-to-End Verification . . . 162
7.7 Wavelength Calibration . . . 162
7.7.1 Grating Wavelength Calibration . . . 162
7.7.2 Fabry-Perot Wavelength Calibration . . . 163
7.8 Line Profile . . . 167
7.8.1 Grating Line Profile . . . 167
7.8.2 Fabry-Perot Line Profile . . . 168
7.9 Resolving Power . . . 173
7.10 Conclusions . . . 176

8 Future Work 177
8.1 Sources . . . 178
8.2 Grating . . . 179
8.3 Detector . . . 180
8.4 Fabry-Pérot Interferometer . . . 180
8.4.1 Lessons Learned . . . 180
8.4.2 Suggested Improvements . . . 182
8.5 Conclusion . . . 184

A SPICA Instruments 201

B Photodiode IV Characteristics 205

C FPI/Grating Operating Modes 207
C.1 Operating Modes . . . 207
C.2 Data Processing . . . 207

D Three Phase Metrology 214

List of Tables

1.1 Transitions of carbon in ionized, atomic and molecular states (CO) and the equivalent thermal energy required to excite these transitions. Adapted from [13]. 8
1.2 Overview of far-infrared (FIR) space observatories. 17

2.1 Redshifted line centers for common fine structure lines of highly ionized species which trace AGN activity. Some of the mid-infrared (MIR) lines are out of the SpicA FAR-infrared Instrument (SAFARI) range for nearby galaxies, but are shifted into the SAFARI band for $z > 0.4$ [25]. 25
2.2 A simple comparison of the Fabry-Pérot interferometer (FPI) and Martin-Puplett interferometer (MPI) in terms of their suitability for a cryogenic, high-resolution spectrometer. 35

4.1 HCl line centers for molecular rotations which fall near the SAFARI VLW band, and the resolving power R required to separate the two lines. 85
4.2 DCl line centers for molecular rotations which fall near the SAFARI VLW band, and the resolving power R required to separate the two lines. 85

5.1 Grating specifications. ϕ is the angle between the incident and diffracted beam, which remains constant over the entire range in the Czerny-Turner configuration. The exit focal length requires an f/6 optic on the output. 104
5.2 Phytron stepper motor specifications 105

6.1 FPI/grating instrument requirements 121
6.2 Thermal filters 125
6.3 Rotary voice coil actuator (RVCA) estimated specifications. The angle sensitivity and maximum current were determined using the flexure specifications from Table 6.4. 132
6.4 Estimated flexure specifications found by scaling the manufacturer specifications to the appropriate material. 133
6.5 Etalon specifications 141

7.1 Thermometer locations on the FPI/Grating. Thermometer serial numbers are also given. 147
7.2 Comparison of the calibrated grating parameters from the standalone grating calibration and the grating-only scanning mode. The parameters A, B, and C are coefficients in a second order polynomial fit $\lambda = A\theta^2 + B\theta + C$ 164

7.3 Variable parameters in the wavelength calibration of the FPI. 165
7.4 Parameters from the wavelength calibration of the etalon. 167

List of Figures

1.1 The transmission of earth's atmosphere over the infrared to millimetre wavelength ranges. This diagram shows a high atmospheric opacity between 10 µm and 1 mm, which encompasses the FIR waveband. The colors represent the atmospheric conditions at the sites of different ground (Atacama Large Millimetre Array (ALMA) [5]), air (Stratospheric Observatory for Infrared Astronomy (SOFIA) [6]), and high-altitude balloon based instruments [7]. 3

1.2 Rest frame FIR and submillimeter spectrum of ARP 220, a merging starburst galaxy. The spectrum was obtained using the Herschel Spectral and Photometric Imaging Receiver (SPIRE) instrument. The continuum emission arises from thermal emission of warm dust, and the emission and absorption lines arise from a range of molecules including CO, H_2O, and HCN. This image was reproduced from [11]. 5

1.3 Cross-sectional representation of a protoplanetary disc. Image taken from [18]. 10

1.4 Thermal emission estimates for the <6 K SPICA telescope are shown in relation to the thermal emission of Herschel and the developing James Webb Space Telescope (JWST), as well as common galactic regions. The 10^{-6} reduction in intensity of thermal emission for SPICA as compared to Herschel puts the thermal emission of SPICA below the background emission levels along the plane of the Solar System and the Milky Way [38]. 16

2.1 A rendering of the SPICA telescope. 20

2.2 The sensitivity of SPICA with respect to other observatories operating in this waveband [38]. 21

2.3 Star Formation Rate densities in the FUV (blue points) and in the FIR (red points) [53, 54]. Note that the bulk of the energy produced by stars and accreting black holes emerges in the infrared; in the IR many more objects than in the UV can be used to establish this relation. The black hole accretion history from X-ray is shown in green shading) and from the IR in blue shading, scaled up by a factor of 3300, compared to star formation rate history. Reproduced from [25]. 24

2.4 The spectrum of a typical nearby active galaxy which has been artificially redshifted up to $z = 4$ with lines labelled which correspond to important tracers of AGN activity and star formation. Redshifts of $z = 1$, 2, 3, and 4 are shown as well as the change in flux on the telescope. Also overlaid are the expected 5σ detection limits of SAFARI in low resolution (LR) mode and Spica Mid-Infrared Instrument (SMI) in low and medium resolution modes (LR and MR) for 1 and 10 hour integration times. Figure from [25]. 26
2.5 (a) Herschel/SPIRE image of the Taurus B211/B213 filament in the Taurus molecular cloud. (b) IRAM/NIKA image of the central part of the Herschel field on the left, showing at least three prominent dense cores. Image from [55]. 28
2.6 A model spectrum for a protoplanetary disc. This figure shows the wealth of information available at FIR wavelengths. It also shows the importance of high-resolution spectra for determining gas species and properties. The image was taken from [38]. 29
2.7 A 3D model of one of the SAFARI grating modules [38]. The scale bar is an approximation. 32
2.8 The original design for Martin and Puplett's interferometer [58]. . . . 34
2.9 The optical beam layout for the MPI high resolution instrument. With a linear displacement of the center double rooftop mirror, the corresponding change in optical path will be 8× larger [38]. 36

3.1 Multiple beam interference by a parallel plate by division of amplitude [66]; see text for details. 39
3.2 The transmission of a monochromatic source through an etalon as a function of the phase difference on successive reflections. Each profile is generated using the corresponding reflectance R of the etalon surfaces. 43
3.3 Visual representations of the definitions of free spectral range (FSR) and full width at half maximum (FWHM). Also shown are two monochromatic sources which are separated by a FWHM and the resulting transmission profile showing that the separate peaks can be identified. . . 45
3.4 Examples of metal mesh filter geometries and their frequency-dependent transmission. 47
3.5 E- and H-fields at the boundaries of a dielectric slab. 49
3.6 Simple visual representation of the beam walking off the etalon aperture with successive reflections. 54
3.7 Schematic of the mechanism which tilts the collimated beam angle with respect to the etalon. 58
3.8 Variation in the transmission function of an etalon with transmitted angle. 59
3.9 Angular throw for different initial offset angles across the waveband. . 60
3.10 Transmission profiles for three monochromatic sources, showing both the transverse electric (TE) and transverse magnetic (TM) transmission modes. The effects of *walk-off* are not included in these models. 61

3.11 Simulations of the complex reflectivity and transmissivity coefficients for select wavelengths and incident angles. These figures show the coefficients for an air-to-silicon interface. 63
3.12 Simulations of the complex reflectivity and transmissivity coefficients for select wavelengths and incident angles. These figures show the coefficients for a silicon-to-air interface. 63
3.13 Simulation of the transmission profile for the etalon, including the angle and wavelength dependence of a dielectric mirror on both etalon surfaces as well as the effect of a finite etalon with a changing overlap area. This plot only considers the TE linear polarization state. 64
3.14 A simple diagram depicting the number of reflections a ray entering the etalon experiences depending on the incident location. 65
3.15 Simulated multiple beam interference across etalon surface for an incident angle of 12°. This figures shows the number of passes through the etalon for each segment across the etalon aperture before exiting. . . 65
3.16 Linear schematic of the FPI system 66

4.1 Schematic of a typical fiber optic photomixer. By tuning the frequencies of the lasers, THz radiation is produced at the difference frequency. A spectrum analyzer allows for real-time measurement of the frequencies and powers of the lasers. 72
4.2 The structure of a p-i-n photodiode. When incident radiation is absorbed, electron-hole pairs are produced in the depletion region, which are swept to the electrodes by an applied bias [92]. 74
4.3 The dependence of laser frequency on temperature for the original laser diodes (LD1 and LD2). Red and blue lines on the plot show a driving current of 20 mA and 90 mA respectively [81]. 77
4.4 The variation of THz output power with frequency for a LT-GaAs photomixer. In the high frequency limit, the THz power drops at 12 dB/octave [81]. 78
4.5 The variation in input laser frequency with temperature. 80
4.6 The variation in input laser frequency with power. 81
4.7 Theoretical wavelength positions of line transitions for HCl and DCl at equal pressures. The transition numbers are labelled in Table 4.1 and Table 4.2. 84
4.8 Model of atmospheric transmission between 25 cm^{-1} to 50 cm^{-1}. The model was completed in Blue Sky Spectroscopy transmission and radiance atmospheric model (BTRAM) version 3.9.2 [97]. The various overlaid plots indicate an increasing relative humidity ranging from 5 % to 50 % in steps of 5 %. The path length is 0.5 m, the temperature is 295 K, and the pressure is 1 atm. 86

5.1 A linear array of coherent oscillators showing the condition for constructive interference [93]. 89

5.2 The interference pattern of a grating or multi-slit aperture. As the number of slits increases, the principal maxima narrow. Each curve in the figure is normalized to 1. 91
5.3 The Czerny-Turner monochromator configuration [99]. 92
5.4 Visualisation of the relationship between angle definitions for the monochromator compared to the fundamental grating equation [61]. 93
5.5 Optical layout and raytrace of the grating system (private communication with David Arrazola, CAB INTA). 99
5.6 Side view of the grating, focussing optics, and stepper motor driven gear train. 101
5.7 The effect of increasing the slit size from 1 mm to 2 mm on the resolving power. 103
5.8 Worm and wheel gear train for tilting the grating, consisting of a cryogenic stepper motor, flexible coupling, and worm and wheel gears. . . 106
5.9 CAD renderings of the grating assembly. 107
5.10 Section view of the 600 µm free play between the c-block and sidewall connecting fasteners. 108
5.11 Bearing mounting arrangements in the grating assembly. 109
5.12 The magnetic reed switch which was used to home the grating. A permanent magnet was attached to the side of the grating and the switch was bolted to the frame. The grating triggered the switch at $\theta = 45.20(4)^\circ$ where θ is the grating angle defined in Section 5.2.2. . . 110
5.13 Test setup for step repeatability measurements. 113
5.14 The wavelength of peak grating response variation with grating angle θ. The peak was determined by a Gaussian fit to detector readings from a variable monochromatic source (i.e. the photomixer). The "fit" and "theory" curves are explained in the text. 115
5.15 An example of a Gaussian fit to the measured signal at different photomixer wavelengths for one grating position. 116
5.16 The grating resolving power as compared to theory for a 2 mm entrance slit. The theoretical resolving power is lower than that in Figure 5.7 because an f/3 collimating optic was used, which magnified the entrance slit image. 117
5.17 Grating efficiency compared to mirror. 118

6.1 System level block diagram for FP/Grating Instrument. The horizontal path indicates the path that light takes from the source to detector. . 122
6.2 Optical components of the room temperature calibration sources. . . 123
6.3 Sketch of the optical layout for the FP. The schematic shows two positions of the pendulum, highlighting the change in beam angle with respect to the etalon. Since the pendulum pivots about the apex defined by the rooftop mirror, the output beam location does not change. 124
6.4 Sketch of the optical layout for the diffraction grating and detector. . 126
6.5 Sketch of the bolometer detector, feed horn, and filter [83]. 127

6.6 3D model of the grating and FPI on the 4 K plate. The detector is shown, but the He10 fridge is not included for image clarity. Also missing is the exit slit and radiation shields surrounding the grating module and detector. 128
6.7 The required incident angle and pendulum angle to cover a full order for an etalon with $d = 8$ mm, and $\theta_0 = 15°$. Note that these values show the single-ended angular ranges, and the total angular ranges are greater by a factor of 2. 129
6.8 The FPI pendulum. 131
6.9 Schematic diagram of the three-phase interferometer. Red arrows indicate fiber connections. The unit, including the laser, operates under vacuum at room temperature. A custom, armoured dual core fiber carries the probe and reference beams to the 4 K workspace. The lengths of the two fibers differ by less than 0.5%. 135
6.10 Dual core fiber metrology system. distributed feedback (DFB) laser (lower left), photonics module (immediately above laser), armored, dual core fiber connected to fiber collimators which launch beams to retroreflectors mounted on the pendulum arms. 136
6.11 Residual error from pendulum scanning of 9.1 nm in optical path which is equivalent to a displacement uncertainty of 2.3 nm. 137
6.12 Comparison of the transmission function of an ideal FPI (red) versus an angle-scanned FPI (black). The left plot shows an airgap etalon with an offset of 3°, and the right plot shows a silicon etalon ($\mu = 3.4$) with an offset angle of 15°. 138
6.13 139
6.14 The etalon substrate is mounted in a custom-made aluminum frame for cryogenic use. The etalon is suspended within the frame using SPIRA flexible gaskets [119] so that differential thermal contraction between the mount and etalon does not damage the optics. 140
6.15 The Test Facility Cryostat (TFC) uses two Cryomech PT415 coolers to cool a 70 L volume to 4 K. The rectangular design allows for a selection of viewports, and the CFRP support plates and flexible thermal straps provide vibration isolation from the PTCs. 142

7.1 The spectral response functions for the grating, FPI, and photomixer. By tilting the grating, rotating the pendulum, or changing the laser temperatures respectively, the spectral response functions could be shifted to higher or lower wavelengths. The measured signal at the detector at any given time was the product of all spectral response functions. 145
7.2 Thermometer locations on the FPI/grating (yellow arrows) and the location of a heat strap to facilitate cooling of the pendulum (red arrow). 148
7.3 Difference in temperature between the etalon disc and the etalon holder during a cooling cycle. Uncertainties are driven by uncertainties in the calibration curves for the thermometers ∼0.1 % 149

7.4 Temperatures of components of the instrument during a cooling cycle to 4 K. Temperature spikes between 20 hours to 27 hours are due to tests of individual components of the He-10 cooler. Temperature spikes once the device reaches 4 K are caused by keeping the stepper motor active for extended periods of time. 150
7.5 Zoomed in version of previous figure. The sharp temperature increases are due to prolonged operation of the stepper motor. The vertical lines indicate instances where the the stepper motor was activated or deactivated, which are identified by the rise or decrease in temperature of the stepper motor respectively. 151
7.6 Cooling time for the pendulum with and without the added heat straps. 151
7.7 An organizational flowchart of all active components of the FPI/grating instrument. Solid lines indicate a transfer of information via electrical, optical, or mechanical signals. Dotted lines indicate connections which will be implemented in the future. Bold blue dashed lines separate different environments. 153
7.8 First light result obtained on Nov. 28, 2018. The red points show raw data overplotted from several scans; the blue curve shows the preliminary transmission model. 161
7.9 Example of a Gaussian fit to the grating profile. 163
7.10 The wavelength of peak grating response variation with grating angle θ. The "theory" curve shows the result of a least squares fit to determine the combined parameter $d\cos\theta$ (given in the text). The "fit" curve shows the results of a second order polynomial fit. 164
7.11 Results of the calibration scheme which minimized the variance in the offset angles. A second order polynomial fit is overlaid, which was used to find the refractive index which minimized the variance. 167
7.12 Resolving element of the grating as defined by the FWHM of the Gaussian fit to the linespread function. The results are compared to the modelled value which is determined by the optical spot size on the grating exit slit. Discrepancy between data and theory is likely the result of temperature or bias current fluctuations in the photomixer lasers, as discussed in Chapter 5. 168
7.13 Comparisons between photomixer calibration data and modelled transmission profiles for both the multilayer model and the *walk-off* model. In the top figure, the photomixer output was 284.26(1) µm and in the bottom figure it was 301.21(1) µm. 171
7.14 Comparisons between calibration data and modelled transmission profiles for both the multilayer model and the *walk-off* model. In the top figure, the photomixer output was 307.03(1) µm and in the bottom figure it was 314.25(1) µm. 172
7.15 Resolving power of the grating measured in "Grating Only" mode. . . 174
7.16 Resolving power of the FPI measured in "Continuous Scan" mode. Vertical bars show the design wavelength range of the etalon. 175

8.1 A schematic of the FPI optics with plans for a flip mirror which can either be set so that the beam passes through the etalon (solid lines), or so that the beam bypasses the etalon and pendulum (dashed lines). 182
8.2 Back view of the pendulum assembly. The retroreflector target was moved from the back of the pendulum arm to beneath the RVCAs. The permanent magnets and fin for added damping are shown in the right of the picture. In later tests, the copper fin damping proved too strong at 4 K, so it was replaced with an aluminum fin. 184

A.1 SAFARI Fact Sheet 202
A.2 SMI Fact Sheet 203
A.3 POL (B-BOP) Fact Sheet 204

B.1 Typical VI characteristics of a photodiode. Each curve represents a different incident power. 206

C.1 Flow chart of FPI operation during Continuous Pendulum Scanning mode. 208
C.2 Flow chart of FPI operation during Step-and-Integrate mode. 209
C.3 Flow chart of FPI operation during a calibration scan with the photomixer using the instrument in CS mode. 210
C.4 Flow chart of FPI operation during a calibration scan with the photomixer using the instrument in SI mode. 211
C.5 Flowchart of data processing steps for a normal operation scan. . . . 212
C.6 Flowchart of data processing steps for a calibration scan. 213

List of Abbreviations

AGN active galactic nucleus

AIG Astronomical Instrumentation Group

ALMA Atacama Large Millimetre Array

AR anti-reflection

AWG American wire gauge

B-BOP B-fields with BOlometers and Polarizers

BTRAM Blue Sky Spectroscopy transmission and radiance atmospheric model

CMB cosmic microwave background

CMM coordinate measurement machine

COTS commercial off-the-shelf

CS continuous scan

CW continuous wave

DAQ data acquisition

DFB distributed feedback

DRIE deep reactive-ion etching

ELT Extremely Large Telescope

EM electromagnetic

ESA European Space Agency

FIR far-infrared

FPA focal plane array

FPI Fabry-Pérot interferometer

FSR free spectral range

FTS Fourier transform spectrometer

FWHM full width at half maximum

GMC giant molecular cloud

HIFI Heterodyne Instrument for the Far Infrared

HRFZ high resisitivity, float zone

ILS instrumental line shape

IRAS Infrared Astronomical Satellite

ISM interstellar medium

ISO Infrared Space Observatory

JAXA Japan Aerospace Exploration Agency

JCMT James Clerk Maxwell Telescope

JWST James Webb Space Telescope

LIA lock-in amplifier

MIR mid-infrared

MPI Martin-Puplett interferometer

NASA National Aeronautics and Space Administration

NEP noise equivalent power

NIR near-infrared

OAP off-axis parabola

OPD optical path difference

PAH polyaromatic hydrocarbons

PID proportional integral derivative

QCL quantum cascade laser

RMS root mean square

RVCA rotary voice coil actuator

SAFARI SpicA FAR-infrared Instrument

SED spectral energy distribution

SFR star formation rate

SI step and integrate

SMBH supermassive black hole

SMI Spica Mid-Infrared Instrument

SNR signal-to-noise ratio

SOFIA Stratospheric Observatory for Infrared Astronomy

SPICA Space Infrared Telescope for Cosmology and Astrophysics

SPIRE Spectral and Photometric Imaging Receiver

SRON Netherlands Institute for Space Research

TE transverse electric

TFC Test Facility Cryostat

THz terahertz

TM transverse magnetic

UV ultra-violet

VCO voltage controlled oscillator

Chapter 1

Far-Infrared Astronomy

> In the beginning the Universe was created. This has made a lot of people very angry and been widely regarded as a bad move.
>
> *The Restaurant at the End of the Universe*
> Douglas Adams

The breadth of our Universe is immense. In fact, the scale of the Universe is so large, that distances between its constituents are expressed in terms of light-years – where a light-year is equivalent to 9.46×10^{12} km. At these distances, we are unable to study these objects with the same scrutiny that we do on Earth. However, there are certain ways in which we can measure the properties of these astronomical objects. Light and the recently detected gravitational waves [1] are emitted and able to be detected from these objects. Using these measurements, we can discern a great deal about the object's composition, temperature, density, velocity, and magnetic influence. Apart from rare detections of very fast moving high-energy particles emitted from nearby galaxies [2], light and gravitational waves are the only known methods of gathering information from beyond our Solar System.

Regarding light – which consists of electromagnetic waves which propagate through space – for much of human history, the study of the cosmos was limited to the very narrow band of wavelengths discernible by the human eye. However, the electromagnetic spectrum extends in essence from infinitesimally small to infinitely large wavelengths. The continuing development of optical elements and detectors which are able to measure different parts of this spectrum have allowed us to obtain infor-

mation which is otherwise inaccessible using only visible wavelengths. In particular, observations of interstellar matter within our own Galaxy and others, particularly at far-infrared wavelengths, provide incredible insights into the origins of stars, planets, galaxies, and the Universe itself.

1.1 Far-Infrared Wavelengths

The FIR waveband ranges from wavelengths of 30 µm to 300 µm [3]. Some disciplines also refer to this as the terahertz (THz) band, loosely defined as being 1 THz to 10 THz, depending on the dominant unit convention in the field. Since FIR astronomy lies at the intersection of both radio and infrared astronomy, there are multiple unit conventions which carry over from both fields: the wavelength (measured in microns, µm), the wavenumber (measured in inverse centimetres, cm^{-1}), and frequency (measured in hertz, Hz). The main reason for the lack of consistency in the unit of measurement for the FIR lies in the fact that FIR measurements inherit both the techniques and challenges of both radio and infrared instruments, often requiring some hybrid of technology from both disciplines.

The FIR waveband remains a relatively unexplored region. Far from being due to a lack of interest in the field, the lack of technology in FIR detection is largely due to the absorption of FIR radiation by atmospheric water vapour (Figure 1.1), suppressing the drive to develop terrestrial technologies which use this band [4]. Consequently, the astronomical community has been the driver for the advancement of FIR detector technology. Furthermore, the capabilities of FIR astronomical observatories have been limited by the low atmospheric propagation, requiring specialized facilities located at high-altitude sites with little atmospheric water vapour, or air-, balloon-, or space-based observing platforms. These requirements incur a steep increase in development and maintenance costs for such facilities.

Additionally, many sources whose peak emission lies in the FIR are difficult to

detect, owing to the low energy of individual photons emitted as compared to those at optical wavelengths. This is due to the inverse proportionality between wavelength and photon energy, E,

$$E = h\nu = hc/\lambda \qquad \text{[eV]} \quad (1.1)$$

where h is Planck's constant, c is the speed of light in a vacuum, λ is the photon wavelength, and ν is the photon frequency. FIR photons have an energy $<4 \times 10^{-2}$ eV.

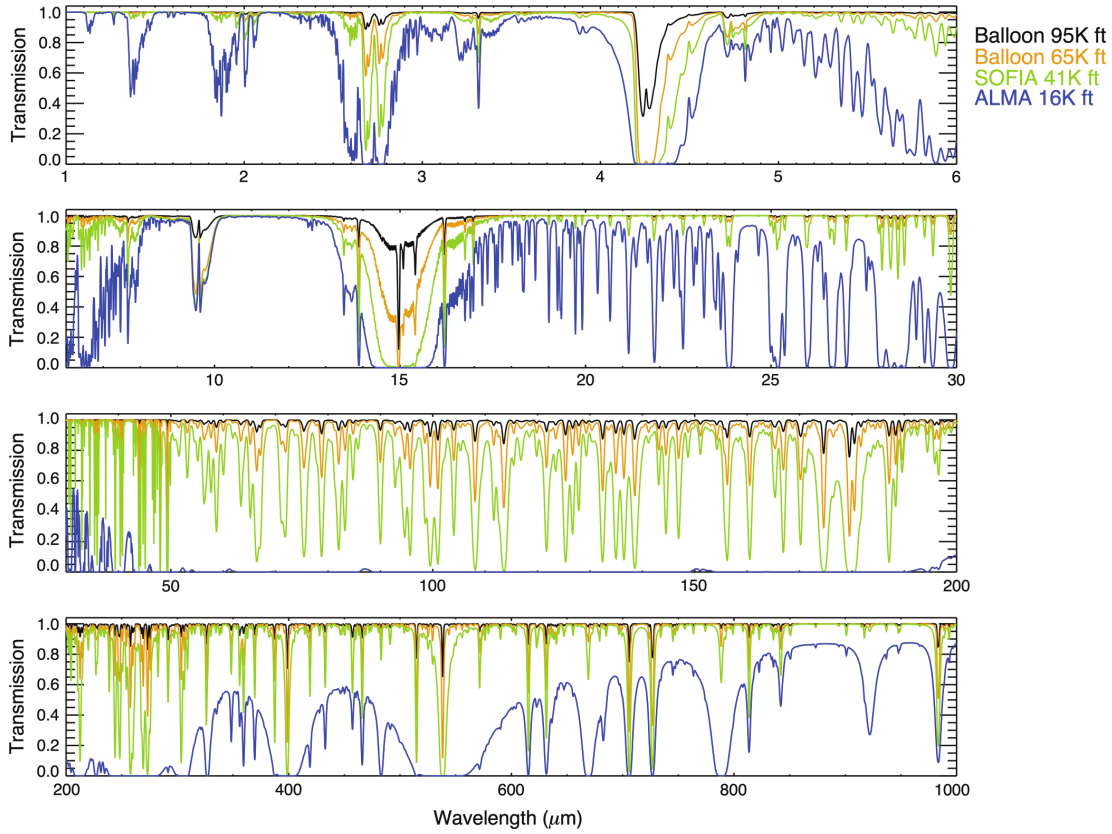

Figure 1.1: The transmission of earth's atmosphere over the infrared to millimetre wavelength ranges. This diagram shows a high atmospheric opacity between 10 µm and 1 mm, which encompasses the FIR waveband. The colors represent the atmospheric conditions at the sites of different ground (ALMA [5]), air (SOFIA [6]), and high-altitude balloon based instruments [7].

Despite the challenges with observing at FIR wavelengths, there are other fields which make use of this band. Applications are limited in radar and telecommunications to short range systems. However, the spectroscopic identification of lightweight molecules makes FIR spectrometers useful for remote sensing. Additionally, tissue

samples have peak absorption coefficients in the FIR waveband. Cancerous tissue has been found to have a higher absorption coefficent as compared with healthy tissue samples, owing in part to different concentrations of water within the samples [8]. Therefore, the detection of cancer through FIR imaging is seen as another potential application for FIR technologies.

1.2 Far-Infrared Astronomy

The significance of FIR astronomy lies in the fact that the Universe emits nearly half of its radiation at these wavelengths [9]. Cold dust and gas clouds which are prevalent throughout the Universe readily absorb short wavelength light (visible, UV, X-ray) emitted by high energy areas, such as star formation regions and active galactic nuclei (AGNs), and re-emit the light at longer wavelengths. Additionally, the Universe is expanding so that emitted radiation is shifted to longer wavelengths an amount approximately proportional to the distance between the source and observer – an observation which was used to formulate Hubble's Law [10].

Broadly speaking, there are two general forms that FIR emission can take: continuum thermal emission, and line emission. The combination of these forms of emission gives a spectrum of the source which takes the form of a broad distribution overlaid with narrow lines of varying strength (i.e. Figure 1.2).

FIR thermal emission is produced by interstellar dust grains, which absorb short-wavelength radiation (such as visible, UV, and X-ray) readily due to a high optical extinction. Absorption increases the dust temperature, causing it to emit as graybody emission over a broad wavelength range which tends to peak in the FIR. The spectral energy distribution (SED) of thermal emission from dust can provide information on the temperature, distribution, composition, and size of the dust particles. Additionally, the extinction of FIR radiation by further dust particles is small, which allows measurements of FIR radiation deep within regions which are enshrouded by dust,

such as galactic nuclei or protostars.

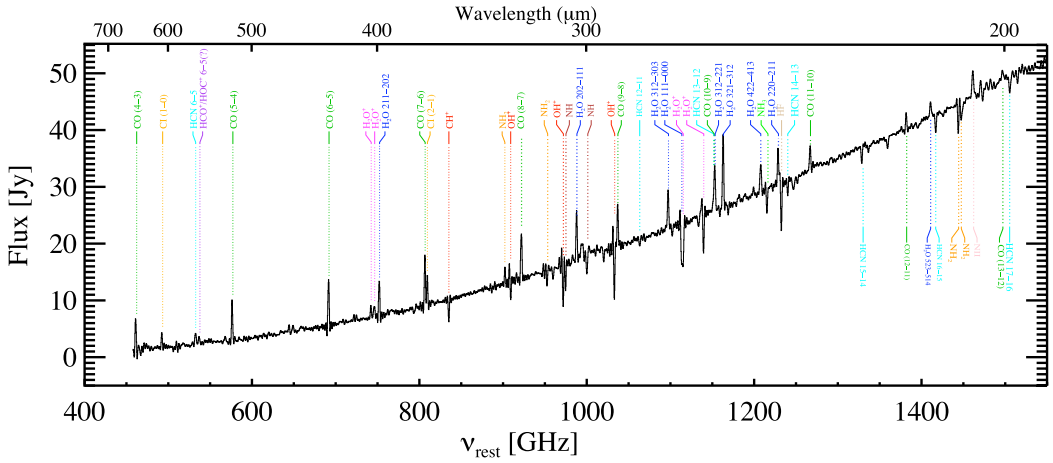

Figure 1.2: Rest frame FIR and submillimeter spectrum of ARP 220, a merging starburst galaxy. The spectrum was obtained using the Herschel SPIRE instrument. The continuum emission arises from thermal emission of warm dust, and the emission and absorption lines arise from a range of molecules including CO, H_2O, and HCN. This image was reproduced from [11].

Line emission, on the other hand, is produced by changes in rotational, vibration, or electronic energy states within molecules, atoms, and ions. Rotational lines of simple molecules, in particular CO, H_2O, OH, HD, and HCN, are prevalent in the FIR region. These molecules may be used to trace the gas temperature, pressure, and velocity conditions of molecular clouds – regions which have low enough temperatures and high enough densities to form molecules. It is these cold and dense regions which are the ideal sites for star formation.

Furthermore, high temperature atoms and ions may also emit FIR line radiation due to fine-structure transitions of the bound electrons. Since molecular dissociation and ionization are products of the absorption of high-energy photons, these fine-structure lines, because they fall in the FIR and therefore are less susceptible to extinction, can be used to trace the conditions within the cloud. Ionic fine structure lines (eg. NeII, SIII, OIII) may be used to probe the ionized medium surrounding hot, young stars or alternatively, measure the cooling processes within warm, ionized clouds. Highly ionized spectral lines (eg. NeV, OIV) probe the conditions of

AGNs [12].

As explained above, FIR radiation is unique in its ability to directly trace areas with vastly differing physical conditions within the nuclei, disks, and halos of our own galaxy as well as distant galaxies. It is by the measurements of all components of a galaxy that we may discern the processes occurring within, thereby modelling the conditions in which it was formed and has evolved. However, in order to discuss these processes, we require more background on the cycle of matter within galaxies.

1.2.1 The interstellar medium

Our Galaxy, the Milky Way, is a Class SBc barred spiral galaxy whose disk measures 10^5 Ly in diameter and is approximately 10^3 Ly thick. Our solar system is located within the Orion-Cygnus Arm, approximately 2.7×10^4 Ly from the galactic center [13]. From our vantage point, the Milky Way is seen as a diffuse band of light across the night sky. Inspecting detailed structure within the diffuse band reveals bright regions produced by the nearly 400 billion stars within the Galaxy interspersed with dark regions between the stars which mark the location of large amounts of dust and gas, the interstellar medium (ISM). These clouds are often referred to as giant molecular clouds (GMCs) and contain a gas to dust ratio by mass of approximately 100 : 1. GMCs may be $10^3\,M_\odot$ to $10^7\,M_\odot$ [13], making them the most massive components of the Galaxy. The dust within GMCs scatters and absorbs visible and ultra-violet (UV) starlight, re-radiating the energy as thermal emission in the FIR, making them the predominant sources of FIR emission. Far away from sources of UV photons, the gas is predominantly H_2 which has only very weak transitions in the FIR. However, trace amounts of other molecules, such as HD or CO, can be used to trace the presence of H_2. The detection, or lack thereof, of other molecules or atomic species provide limits on the temperature and pressure conditions of different regions within GMCs, along with the underlying chemical processes involved in their creation

or dissociation. It is by observation of these different chemical processes that we can determine the underlying life cycle of matter within the ISM which gives insight into the formation process of stars. Furthermore, by detecting these features in distant galaxies as a function of redshift, we can study the evolution of galaxies over cosmic time.

1.2.2 Star Forming Regions

The formation of dense regions within GMCs is a prerequisite for the formation of stars, yet this process is not fully understood. Since optically thick dust in these dense clouds absorbs high energy photons, FIR measurements of dust emission provide a good indication of the location of star forming regions. Theories behind the formation of these star-forming sites can be developed based on observations of ionic, atomic, and molecular species and their temperatures by characterization of their spectral lines which probe the different physical conditions within an emitting region. The high extinction of UV photons by dust necessitates that these observations take place at FIR wavelengths. Molecular clouds are made up primarily of molecular hydrogen and atomic helium, which are not easily measured in the FIR. Fortunately, it is possible to probe the conditions of these clouds using tracer elements. An example is the observation of carbon in many different forms: including ionized CII, atomic CI and molecular CO, and their isotopes. All three of these forms of carbon have readily-observable transitions at FIR wavelengths, and provide insight into the physical conditions within the cloud (Table 1.1).

In general, the conditions for a cloud to collapse and begin the stellar formation process relies on the gravitational forces exceeding the interior thermal pressure of the cloud. The critical mass that must be exceeded is known as the Jean's Mass [14]:

$$M_J = \left(\frac{5kT}{G\mu}\right)^{3/2} \left(\frac{3}{4\pi\rho}\right)^{1/2}. \qquad \text{[kg]} \quad (1.2)$$

Table 1.1: Transitions of carbon in ionized, atomic and molecular states (CO) and the equivalent thermal energy required to excite these transitions. Adapted from [13].

Species	**Line**	**Wavelength** [μm]	**Temperature** [**K**]
CII	$^2P_{3/2} \longrightarrow {}^2P_{1/2}$	157.9	91
CI	$^3P_2 \longrightarrow {}^3P_1$	335.9	63
CI	$^3P_1 \longrightarrow {}^3P_0$	609.5	24
^{12}CO	$J = 13 \rightarrow 12$	200.4	503
^{12}CO	$J = 11 \rightarrow 10$	236.8	365
^{12}CO	$J = 9 \rightarrow 8$	289.3	249
^{12}CO	$J = 7 \rightarrow 6$	371.9	155
^{12}CO	$J = 6 \rightarrow 5$	433.8	116
^{12}CO	$J = 4 \rightarrow 3$	650.8	55
^{12}CO	$J = 3 \rightarrow 2$	867.6	33

where k is the Boltzmann constant, G is the gravitational constant, μ is the mass per particle, ρ is the mass density of the cloud. Note that M_J is proportional to $T^{3/2}$ and $\rho^{-1/2}$, meaning that cold, dense clouds have a lower critical mass, and are more likely to exceed the Jean's mass condition.

Cooling mechanisms that allow clouds to radiate away their internal energy and lower their core temperatures arise from emission of FIR photons that escape the cloud. In particular, transitions between quantized rotational states of molecules produce long wavelength photons which are much more likely to escape the cloud than photons of shorter wavelengths. The observation of these spectral features allows astronomers to determine the abundance, temperature, and kinetics of different gas species and so model the gas conditions within the cloud. The low temperatures associated with cold molecular clouds are optimally studied at FIR wavelengths, since the dust is optically thin, which allows accurate modelling of average dust temperatures and mass [15]. By observing pre-stellar cores in different environments, thereby capturing different stages of stellar evolution, we can gain insight into the underlying process of stellar formation. Since stars are the optical building blocks of galaxies, an

expanding knowledge of star formation in all stages is essential for the understanding of galactic evolution.

1.2.3 Protoplanetary Disks

During the later stages of star formation, conservation of angular momentum causes the increased rotation rate of matter around the core as it contracts. The core is known as the *protostar*, and the disc which forms from the increased rotation rate is called an *accretion disc*. In order to transfer rotational energy away from the disc, the protostar will form jets along the rotational axis which transfers some gas back to the ISM. This facilitates the cooling of the accretion disc which settles into a *protoplanetary disc* as the accretion process fuelling the protostar dies and the protostar becomes a young star. The protoplanetary disc may eventually coalesce into a planetary system. The observation of this process is typically done with high angular resolution telescope interferometers such as the ALMA [5]. This telescope array allows imaging of the protoplanetary disc structure as well as spectral observations of localized regions within the disc to determine their temperature and chemical composition [16].

As with the rest of the ISM, protoplanetary discs are composed of dust and gas. While dust in the diffuse ISM is attributed to small silicate structures, graphite, and polyaromatic hydrocarbonss (PAHs) with $r \leq 0.1\,\mu\text{m}$ [17], in the protoplanetary discs, molecules of gas freeze out onto the dust grain surfaces, producing icy mantles. Additionally, the higher density causes grains to combine together to form larger planetesimals ($r \geq 1\,\text{cm}$). Measurement of the thermal emission from protoplanetary discs, which peaks in the FIR, provides information on the dust composition and temperature. In terms of gas content of discs, the wide range of conditions between the inner and outer parts of the disc result in many different spectral features, such as ionized NeII near the young star, which tend to trace hot surfaces of the disc ionized

by the young star, as well as jets from the central star and CO molecular lines, which trace the cold, low density regions of the outer edges of the disc [17]. Measuring the strength of these lines gives insight into the temperature and mass of gas in discs in contrast to the dust temperature and mass, which provide constraints which can be applied to models which describe their formation and evolution (Figure 1.3).

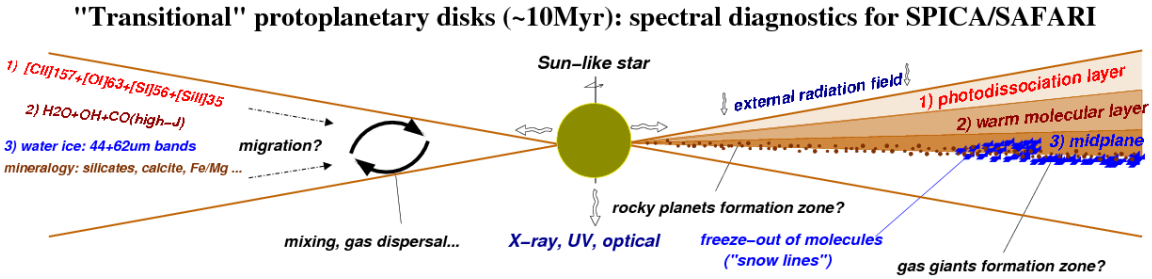

Figure 1.3: Cross-sectional representation of a protoplanetary disc. Image taken from [18].

1.2.4 Cycling of Matter

The formation of young stars and protoplanetary discs marks a key time period in the life cycle of matter within the ISM. Over the lifetime of the star, elements within the core are fused to form heavier elements in a process known as *nucleosynthesis*. The end of a star's life is marked by the shedding of its outer layers into the surrounding ISM. Overlapping shock waves from supernovae produced by high-mass stars intersect and form warm ionized clouds. Cooling processes through line emissions, like those measured in the FIR, allow the clouds to condense, forming atoms and then molecules. High density regions within cold molecular clouds condense into star forming regions and the cycle is repeated. Each iteration of the cycle introduces heavier elements into the ISM in a process known as *galactic enrichment* [15].

1.2.5 Role of Water

The fact that terrestrial water vapour is such a strong absorber of FIR radiation indicates that FIR spectroscopy provides an excellent means of detecting water vapour

within the ISM. Like other simple molecules, water lines act as a tracer for cold, molecular clouds. However, water also plays an essential role in the chemistry of molecular clouds. Since water is the first of the common ISM molecules to condense, water is the predominant component in icy mantles which form around dust grains. Water also forms strong hydrogen bonds, making it difficult for the ice to return to the gas phase once formed [19]. Icy mantles are believed to aid the coagulation of dust, leading to the formation of planetesimals [20]. The strength of water vapour emission lines with respect to water ice spectral features gives information on the gas-to-ice ratio of water and consequently, the extent of icy mantle formation on the dust within the molecular cloud.

1.2.6 Galaxy Formation and Evolution

Measurements of the large scale star formation rates and black hole accretion rates within galaxies gives an insight into the galactic evolution process and how it has progressed throughout cosmic time. In general, the photons which are produced by hot, young stars and active galactic nuclei lie in the optical, UV, and X-ray. Since young stars and the accretion discs of AGNs are generally embedded in dense, dusty regions, a large portion of the high-energy photons are absorbed by galactic dust and are reradiated as thermal emission in the infrared. Models indicate that the re-radiated thermal emission accounts for about half the overall energy emitted by stars and galactic cores [21]. Therefore, infrared observations of galaxies are required to understand their internal processes. Moreover, the expansion rate of the universe redshifts photons from many of these diagnostic measurements into the FIR region.

1.2.7 Onset of heavy elements

Current models of the early stages of the universe explain how the majority of matter is in the form of hydrogen and helium with trace amounts of lithium. Since this allows little cooling in the form of emission lines (mainly weak H_2 emission lines),

the first stars that formed must have been massive ($>$ 100 solar masses [22]). These stars would have lived short lives and produced violent supernovae explosions, capable of preventing star formation nearby. It is believed that the first galaxies would form during the next generation of smaller, cooler stars [23]. However, these first stars, the so called Population III stars, are responsible for the production of the first heavy elements in the universe. Understanding where these stars formed and their masses would be instructive in updating our current cosmological models. It would allow better convergence on the parameters which predict the distribution and total amount of dark matter as well as regular baryonic matter. It would also serve to provide better estimates for the initial conditions when the first galaxies emerged, including gas temperatures, and metallicities. Models also indicate that Population III stars were responsible for production of the first dust particles. This is because those stars with masses greater than 140 solar masses were thought to leave no compact cores behind, ejecting a significant fraction of their core matter as dust [24]. One consequence of this would be that regions of Population III stars would quickly enshroud themselves in dust, which absorbs UV photons and remits in the infrared. Hubble's Law indicates that infrared photons emitted by these far off sources would be redshifted such that they would appear luminous in the FIR.

1.2.8 Star Formation Rates in High-Z Galaxies

It is generally understood that the star formation rate (SFR) in most galaxies has not remained constant over time [25]. Observations show that galaxies with a redshift of 1 to 3 are most luminous in the infrared, indicating a large amount of star formation occurring within dust-obscuring clouds [22, 25]. While fewer data exists for higher redshifts, it appears that SFR falls off at increasing redshifts. However, since much of the observed light comes from secondary processes rather than the primary source (being the stars themselves), there are large uncertainties associated with these

measurements. The main uncertainty is the extent of the extinction of the original UV light.

1.2.9 Supermassive Black Hole Growth

FIR observations also reveal the role that the growth of supermassive black holes (SMBHs) which reside in the center of galaxies, has on star formation within the galaxy. It is widely accepted that the mass of a galaxy's SMBH correlates with the amount of matter located in a galaxy's stars [26, 27]. This suggests that feedback mechanisms from the infall and outflow of matter in an AGN facilitate star formation within the galaxy. Far infrared OH lines are used to trace fast outflows which indicate jets in active galaxies [28]. By measuring these outflows along with fine structure and molecular lines in the FIR, we may learn more about the correlation between an active galaxy and its black hole accretion rate and rate of star formation. By understanding how these processes are linked, we can better understand how galaxies evolve.

1.3 Observing Challenges

As the previous section has shown, the FIR waveband is an important region for spectroscopic studies of the evolution of galaxies, stars, and planets. However, the challenges associated with observing in the FIR have limited the progression of FIR astronomy. In fact, only in the last few decades has the field been able to overcome the obstacles, and begun to make FIR observations. The field has progressed steadily since its inception, and continues to advance at an accelerating rate. This section will give an overview of the challenges which need to be addressed when observing in the FIR.

1.3.1 Atmospheric Extinction

As discussed previously, astronomers observe relatively little of the FIR waveband compared to the rest of the electromagnetic (EM) spectrum, primarily due to the

absorbing nature of H_2O vapour in the atmosphere. Since FIR photons excite water vapour rotational energy levels, water vapour also emits these frequencies, but in random directions. The diffuse emission of the atmosphere is the dominant source of noise for many ground-based FIR observatories. The low transmission of the atmosphere can be overcome by constructing high-altitude observing platforms, such as the James Clerk Maxwell Telescope (JCMT) on Mauna Kea, Hawaii. These platforms are built in high and dry places where the column density of water vapour in the atmosphere is much diminished as compared to sea level. To achieve even lower levels of atmospheric emission, observatories are built at even higher altitudes. SOFIA is a high-altitude aircraft based observing platform which can fly above the troposphere for even more precise measurements [29]. Ultimately, the best FIR observatories are located outside the atmosphere. Space-based observing platforms, such as Infrared Space Observatory (ISO) [30], Spitzer [31], Akari [32], and Herschel [33] have been in place for over three decades and are continuing to provide increasingly superior results in the mid- and far-infrared bands.

1.3.2 Detector Technology

The second challenge when observing in the FIR is that the photon energy is so low that it is difficult to fabricate detectors with sufficient sensitivity. Currently, there are two different detection techniques which may be used, coherent and incoherent. Coherent detection involves measurement of both amplitude and phase of incoming radiation – which is the underlying principle behind heterodyne receivers. While these detectors are becoming more widespread in their use for FIR astronomy, since they provide very high spectral resolution yet over a narrow band, most spectroscopic measurements rely on interferometric instruments coupled to sensitive incoherent detectors, of which there are two principle types. These are classified into photon and thermal detectors. Photon detectors respond to the incident photons by exciting free

charge carriers. The wavelength response is determined by the bandgap energy of the semiconducting detector material ($\sim$10 meV). Unfortunately, the low energy of FIR photons preclude the use of photon detectors. The required band gap is so small that thermal agitation would cause electrons to cross the bandgap, contributing to the detector noise. This means that to develop low noise FIR detectors, new device concepts must be developed. The second type of detector is the thermal detector (e.g. bolometer). Here, radiation is absorbed by the detector and the resulting temperature change is measured by a sensitive thermometer. These detectors have a broader spectral coverage because they are not limited by electronic bandgaps. Since the sensitivity of bolometer detectors is due to the ability to detect a small change in temperature, cryogenic detectors offer the best advantage, because of their superior sensitivity to incident power – expressed as noise equivalent power (NEP) [34]. With the application of cryogenics in detector technology, one can also utilize superconducting materials which have a very sharp resistive transition at cryogenic temperatures, making them extremely sensitive to small temperature changes. Only recently have detector sensitivities of $10^{-19}\,\mathrm{W}/\sqrt{\mathrm{Hz}}$ been achieved [35].

Detectors with such a high sensitivity necessitate instruments which are also cryogenically cooled, typically to liquid helium temperatures, so as not to be a dominant source of thermal emission themselves. The combination of low temperature instrumentation and sensitive detectors, which will be used in future missions such as SPICA [36], yields sufficient sensitivity that detector noise is not limited by the instrument, but by the background zodiacal and galactic cirrus emission [37] (Figure 1.4).

1.4 Cryogenics in space

From the previous discussion, it should be clear that the ultimate sensitivity of observations in the FIR can only be achieved by placing large telescopes in space,

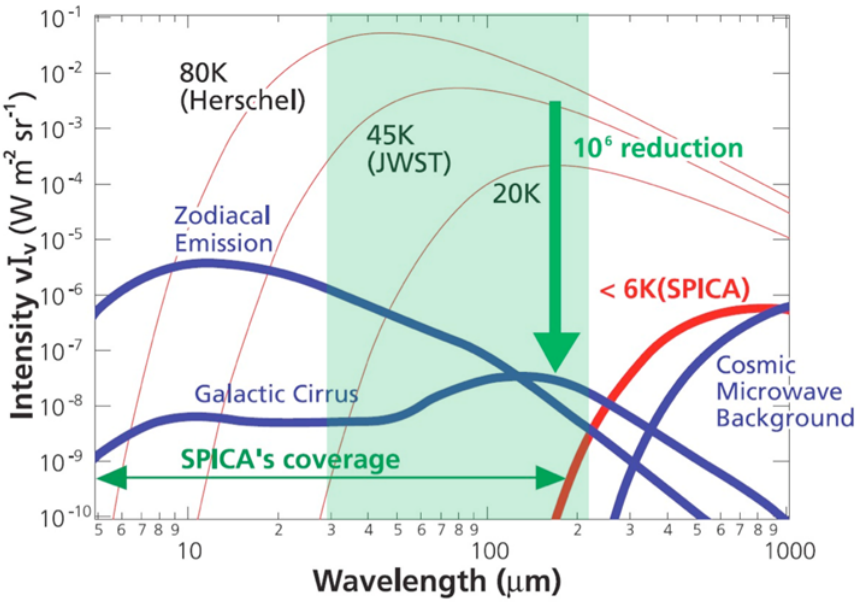

Figure 1.4: Thermal emission estimates for the <6 K SPICA telescope are shown in relation to the thermal emission of Herschel and the developing JWST, as well as common galactic regions. The 10^{-6} reduction in intensity of thermal emission for SPICA as compared to Herschel puts the thermal emission of SPICA below the background emission levels along the plane of the Solar System and the Milky Way [38].

operating at cryogenic temperatures, with extremely sensitive detectors. Drawing upon the success of past FIR space missions such as Infrared Astronomical Satellite (IRAS) [39], ISO [30], Akari [32], Spitzer [31], and Herschel [40], there are now multiple missions under development that will employ active cooling of large aperture telescope optics and instrumentation to <6 K to achieve background radiation levels on the same order of magnitude as the cosmic microwave background (CMB). SPICA is a joint venture led by the European Space Agency (ESA) and the Japan Aerospace Exploration Agency (JAXA) which aims to observe the early universe at mid- and far-infrared wavelengths [38]. Chapter 2 gives an overview of the development of SPICA with a focus on the FIR instrument, SAFARI. The Origins Space Telescope (OST) is a National Aeronautics and Space Administration (NASA) flagship mission aimed to measure mid to far infrared wavelengths [41]. A summary of past and future FIR space observatories is given in Table 1.2.

Table 1.2: Overview of FIR space observatories.

Mission	Agency	Launch Date	Primary Diameter [m]	Waveband [µm]	Primary Temperature [K]	Location	Instruments	Source
IRAS	NIVR NASA SERC	January 26, 1983	0.57	7.5 - 100	<10	low earth orbit (900 km)	LRS, CPC	[39]
ISO	ESA	November 17, 1996	0.60	2.5 - 240	3	elliptical earth orbit (70 600 km max)	ISOCAM, ISOPHOT, LWS, SWS	[30]
Spitzer	NASA	August 25, 2003	0.85	3.6 - 160	5.5	solar orbit	IRAC, IRS, MIPS	[31]
Akari	JAXA	February 21, 2006	0.71	2 - 180	5.8	low earth orbit (700 km)	FIS, IRC	[32]
Herschel	ESA	May 14, 2009	3.5	55 - 671	85	L2	HIFI, PACS, SPIRE	[33]
JWST	NASA	∼ 2021	6.6	0.6 - 29	<50	L2	NIRCam, NIRSpec, TFI, MIRI	[42]
SPICA	ESA/JAXA	∼ 2032	2.5	5 - 230	<6	L2	SMI, SAFARI, B-BOP	[38]
OST	NASA	∼ 2035	5.9	5 - 600	4	L2	FIP, OST, MISC, OSS	[41]

With a sufficiently cold telescope, background limited performance of an FIR instrument may be achieved. As SPICA will demonstrate, a decrease in the intensity of telescope emission of 10^6 as compared to Herschel, as shown in Figure 1.4, will manifest itself as an increase in signal-to-noise ratio (SNR) of 10^3 with sufficiently sensitive detectors.

1.5 Conclusion

In summary, the FIR wavelength range is a unique band in which the properties of widely differing astronomical targets may be studied. This allows the study of the evolution of stars and galaxies by surveying many different sources in different developmental stages. The field of FIR astronomy is rapidly progressing with the advancement of technology in space-based instrumentation and sensitive detectors. One of the proposed future FIR missions is SPICA, which will be described further in Chapter 2. The chapter will give an overview of the project and a description of the onboard FIR spectroscopic instrument, SAFARI. The chapters following will describe the role I took in the development of an interferometer concept that was a candidate for the high resolution spectrometer on the SAFARI instrument.

Chapter 2

SPICA-SAFARI

> Eventually, we reach the utmost limits of our telescopes. There, we measure shadows and search among ghostly errors of measurement for landmarks that are scarcely more substantial.
>
> *The Realm of the Nebulae*
> Edwin Powell Hubble

In this chapter, I will discuss the scientific goals of the SPICA mission (Figure 2.1), with a focus on the SAFARI instrument. The requirements for sensitivity and spectral resolution of SAFARI based on the scientific objectives will be reviewed. SAFARI will contain a high-resolution module for measuring narrow emission lines. Working designs for the high-resolution module included an FPI and an MPI. This chapter will discuss the working concept for each instrument design, and will illustrate why the MPI was ultimately selected, but will give the assurance that the angle-scanned FPI is still a worthwhile instrument concept to explore further.

2.1 The Space Infrared Telescope for Cosmology and Astrophysics (SPICA)

SPICA is an ESA-JAXA observatory-class mission that will provide imaging and spectroscopic capabilities in the 5 µm to 230 µm wavelength range with a 2.5 m aperture telescope cooled to a temperature of <8 K [38]. SPICA will be combined with the next generation of sensitive detectors to produce an overall instrument sensitivity which is over two orders of magnitude greater than Herschel [33] and Spitzer [31] (Fig-

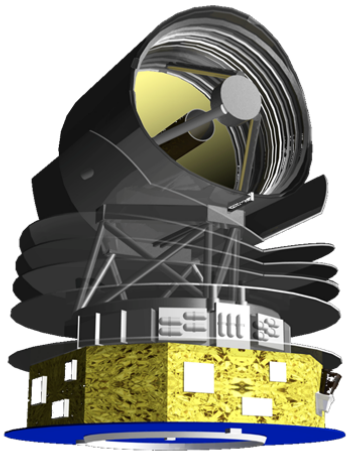

Figure 2.1: A rendering of the SPICA telescope.

ure 2.2). From the inverse square relation between apparent brightness and distance, the increase in sensitivity directly translates to a 10× increase in the measurable distance, and thus a 1000× greater volume of the universe to explore. In fact, the increase in observable distance is even greater when the negative-K correction is considered, which shows that mean intensities fall off at a slower rate than the inverse square relation predicts [43]. As Figure 2.2 also shows, SPICA will cover a wavelength range which complements the capabilities of ALMA, JWST, and the Extremely Large Telescopes (ELTs), providing a much needed increase in sensitivity in the "FIR gap [44]".

2.1.1 Instruments on SPICA

The current SPICA payload contains three scientific instruments: SAFARI, an FIR grating spectrometer with a polarizing Fourier transform spectrometer (FTS) for high-resolution; SMI, an MIR spectrometer/imager; and B-fields with BOlometers and Polarizers (B-BOP), an imaging polarimeter. All instruments will be cooled by a complement of passive cooling radiators and mechanical cryocoolers. In the current design, the instruments will achieve a temperature of <5 K while the detectors are cooled below this, to a temperature of 2 K for the SMI instrument and as low as

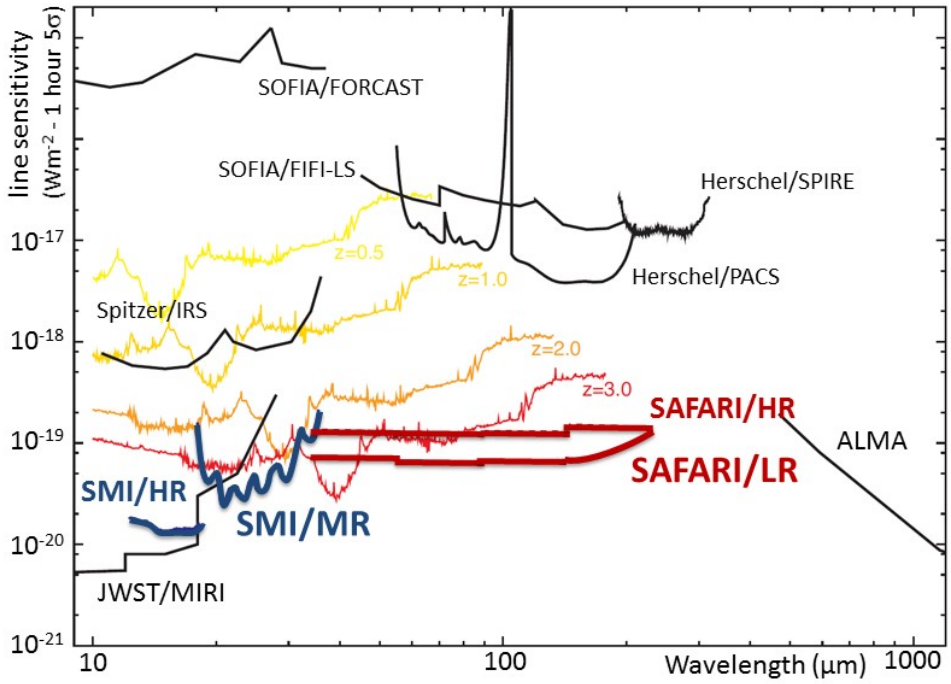

Figure 2.2: The sensitivity of SPICA with respect to other observatories operating in this waveband [38].

50 mK for SAFARI and B-BOP [45]. Maintaining such a low temperature enclosed in a low background thermal emission environment allows these instruments to use the most sensitive detectors developed to date. What follows is a brief description of each instrument, while the fact sheet for each instrument can be found in Appendix A. For more information, the reader is referred to [38].

The SAFARI spectrometer covers the range 34 µm to 230 µm with two spectral operating modes. A low resolution grating spectrometer gives a moderate resolution of $R = 300$, and a Martin-Puplett FTS in tandem with the grating provides an optional high resolution mode with $R = 1500 - 11000$.

The SMI instrument covers the wavelength range 12 µm to 36 µm in four separate channels. The low-resolution spectroscopy function SMI/LR, $R = 50 - 120$, for

the 17 µm to 36 µm range, the broad-band ($R = 5$) imaging function SMI/CAM at the central wavelength of 34 µm, the mid-resolution spectroscopy function SMI/MR, $R = 1300 - 2300$, for 18 µm to 36 µm, and the high-resolution spectroscopy function SMI/HR, $R \sim 28000$, in the 12 µm to 18 µm range.

B-BOP is an imaging polarimeter which requires a large dynamic range, requiring high sensitivity detectors which can withstand high flux levels. The wavelength bands for the photometer are 100 µm, 200 µm, and 350 µm. The detectors will be polarization sensitive, in order to map the filamentary structures within the Galaxy.

2.2 Science Goals

SPICA will allow astronomers to study the physical processes that govern the formation and evolution of galaxies across cosmic time, as well as understand formation and evolution of planetary systems and the conditions required for the emergence of systems similar to our Solar System. In Chapter 1, the importance of FIR radiation for measuring the properties of the early universe and discerning details regarding the evolution of galaxies and planetary systems was discussed. In particular, FIR observations allow astronomers to observe both low and high energy processes, through thermal emission from dust and ices, or molecular rotational lines and fine-structure lines. FIR observations allow astronomers to observe even those regions which are heavily obscured by dust, which extinguishes higher energy photons.

SPICA seeks to answer a range of fundamental outstanding questions in astronomy, namely:

- What are the roles of star formation, accretion onto and feedback from central black holes and supernova explosions in shaping galaxy evolution over cosmic time?

- How are metals and dust produced and destroyed in galaxies? How does the

matter cycle within galaxies and between galactic discs, halos and the intergalactic medium?

- How did primordial gas clouds collapse into the first galaxies and black holes?
- What is the role of magnetic fields at the onset of star formation in the Milky Way?
- When and how does gas evolve from primordial discs into emerging planetary systems?
- How do ices and minerals evolve in the planet formation era, as seed for Solar Systems, acting as the seeds for planet formation?

Further details on each of these questions are addressed in a series of publications by the SPICA consortium [46, 25, 38, 28, 47, 22, 12, 48]. Brief descriptions of each question and the role SPICA will take to address them are discussed in the remainder of this section.

2.2.1 Galaxy Evolution

The capabilities of current instruments are such that astronomers are able to uncover statistically significant samples of spectra of only the very brightest high-z galaxies and only the nearby protoplanetary discs [49]. The deepest cosmological surveys with Herschel ([9, 50, 51, 52]) mapped out the SFR density to $z \sim 3$ for the first time, but detected only small numbers of the most luminous ($L \geq 10^{12}\ L_{\odot}$) star-forming galaxies at $z > 3$. Conclusions from these surveys suggest that the peak of star formation and AGN activity occurred around $z = 1 - 3$ (Figure 2.3) [25]. Further sampling of a larger range of sources is required to discern if these findings are representative of the majority of the galaxy population. In order to study the peak of galaxy formation and look at the first primordial gas clouds, a greater sensitivity is required. The spectrometer must be sufficiently sensitive to measure the line strengths

for tracers of AGN and star formation activity and measure redshift in low luminosity objects of $z = 1 - 2$ for most lines and higher redshifts for brighter lines. Redshifted MIR lines which trace AGN activity fall into the SAFARI band for redshifts $z > 0.4$, particularly the [OIV] 25.9 µm, [NeV] 24.3 µm and [SIII] 33.5 µm fine structure lines (Table 2.1). Instruments with capability to measure the above lines will also be able to measure the fine structure lines which trace high rates of star formation, namely [OI] 63 µm, [SiII] 35 µm, and [OIII] 88 µm.

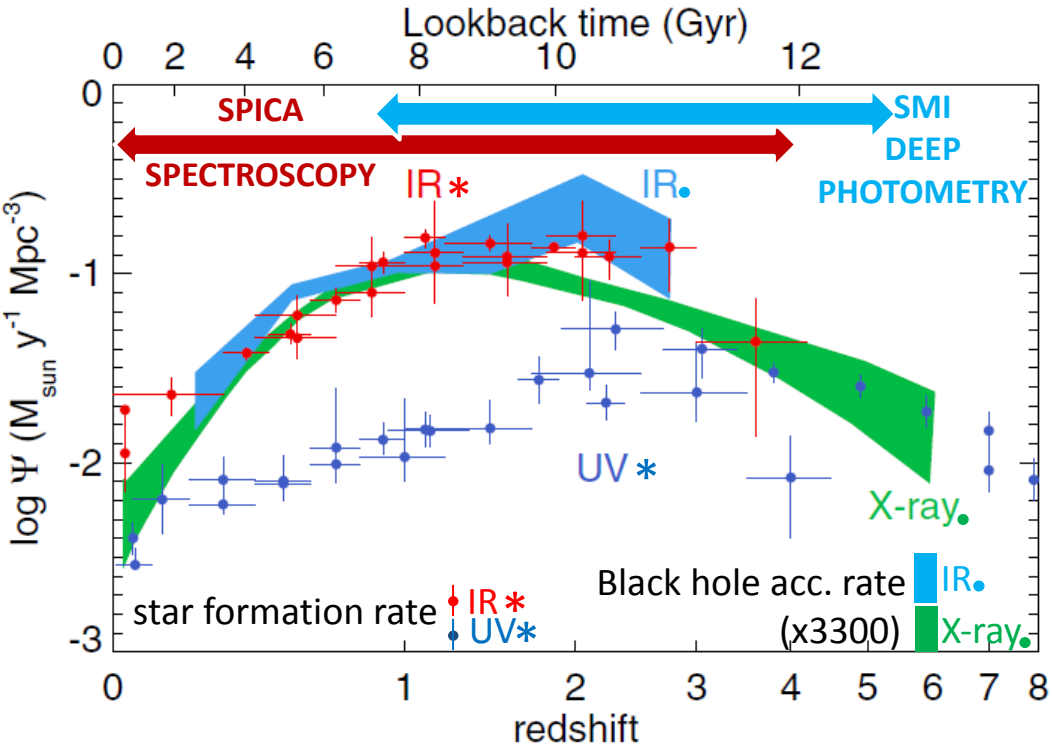

Figure 2.3: Star Formation Rate densities in the FUV (blue points) and in the FIR (red points) [53, 54]. Note that the bulk of the energy produced by stars and accreting black holes emerges in the infrared; in the IR many more objects than in the UV can be used to establish this relation. The black hole accretion history from X-ray is shown in green shading) and from the IR in blue shading, scaled up by a factor of 3300, compared to star formation rate history. Reproduced from [25].

Star formation regions may be measured with low-ionization lines such as NeII, NeIII, and SIII while the accretion rates within AGNs may be measured with high-ionization lines such as OIV and NeV. Previous missions such as Spitzer and Herschel

Table 2.1: Redshifted line centers for common fine structure lines of highly ionized species which trace AGN activity. Some of the MIR lines are out of the SAFARI range for nearby galaxies, but are shifted into the SAFARI band for $z > 0.4$ [25].

Line	λ_0	λ **at** $\mathbf{z = 0.4}$
OIV	25.9 µm	36.3 µm
NeV	24.3 µm	34.0 µm
SIII	33.5 µm	46.9 µm

were only able to detect these lines for the very brightest AGNs and star forming galaxies at $z > 0.5$. However, as demonstrated in Figure 2.4, these lines will be observable for the majority of the galaxy population up to $z = 4$.

2.2.2 Rise of Metals and Dust

To an astronomer, a metal is defined as an element which is heavier than helium. These elements play an important role in the cooling processes within the ISM, leading to the collapse of molecular clouds, and ultimately, the formation of stars and planets. Within galaxies, metals accumulate through stellar feedback, where the elements are produced in the cores of stars and distributed back into the ISM, enriching the gas therein. Heavy elements are also the main components of the dust grains, meaning the evolution of these components are closely linked. Even though metals have a small contribution to the mass of a galaxy (<1 %), they play a major role in the chemical processes that take place in the ISM. This is evident by the role of metals as tracers of galactic processes such as star formation and black hole accretion. Since metals and dust are the main products of the cycle of matter within galaxies, measurements of their abundances give insight into the history of a galaxy's evolution. Moreover, the formation and destruction of dust grains from metals across differing environments and across cosmic time is not well understood. Since the majority of galactic processes occur in dust-embedded regions, the metallicity of galaxies cannot be accurately estimated from UV, visible, or near-infrared (NIR) observations due to

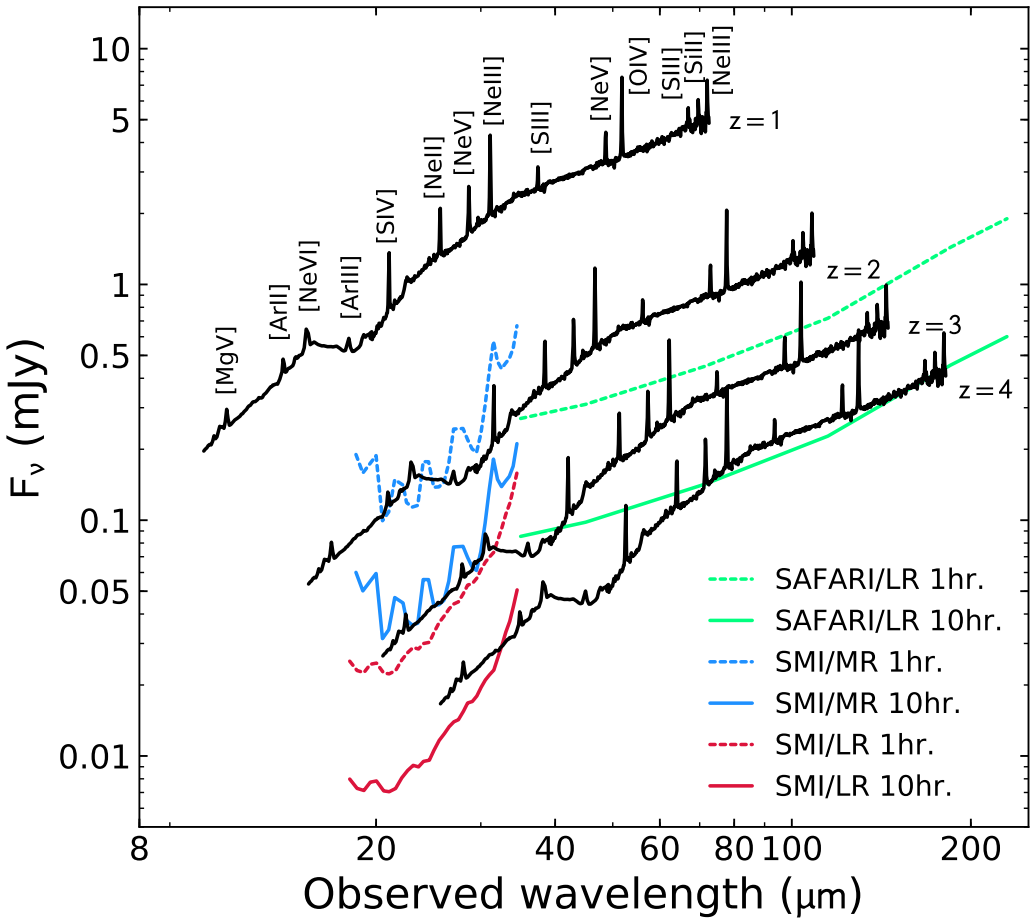

Figure 2.4: The spectrum of a typical nearby active galaxy which has been artificially redshifted up to $z = 4$ with lines labelled which correspond to important tracers of AGN activity and star formation. Redshifts of $z = 1$, 2, 3, and 4 are shown as well as the change in flux on the telescope. Also overlaid are the expected 5σ detection limits of SAFARI in low resolution (LR) mode and SMI in low and medium resolution modes (LR and MR) for 1 and 10 hour integration times. Figure from [25].

the effects of opacity, but must be inferred from tracer lines in the FIR, where the dust is optically thin.

2.2.3 Early Stars and Galaxies

The earliest stars and galaxies would have formed in metal-poor environments where gas cooling was limited. As such these first stars would have had to be extremely massive ($>100\,M_\odot$ [22]). Models of the formation of these so called Population III stars predict that the resultant supernovae would have produced large amounts of

dust. Measurement of the production of the first dust grains is an important topic, which could reveal the chemical processes which lead to the formation of the first galaxies. Models predict that the dominant source of dust emission would arise from SiO_2 lines, which will be redshifted into the proposed SPICA band.

2.2.4 Magnetic Fields

Past surveys of GMCs have shown that filamentary structures, which are present throughout the ISM, play a major role in star formation. Results from Herschel show that some filaments contain matter at a higher density than the surrounding medium, and are therefore ideal sites for stellar formation (Figure 2.5). Additionally, wide-field dust polarization measurements with the Planck telescope show a widespread structure of magnetic fields in the ISM which are aligned with the filamentary structures. It is likely that these magnetic fields are responsible for the compression of interstellar matter, leading to the production of filamentary structures of molecular gas. The densest of these filaments are able to trigger the collapse of molecular clouds into prestellar cores, leading to the production of stars and planets. The polarimeter onboard SPICA will be able to map these filamentary structures throughout the local ISM, and determine the extent of their role in the star formation of the Milky Way and other galaxies.

2.2.5 Protoplanetary Disks

The wavelength range of SPICA provides unique access to a large series of gas cooling lines from disks such as HD, H_2, CO and water, to the FIR water ice features, and to a series of key dust features tracing the composition of protoplanetary discs (Figure 2.6). SPICA will have the sensitivity to survey a large sample of protoplanetary discs, and will measure the diagnostic HD and OI lines to measure the evolution of the disc mass from the inception of the disc to its aggregation into planets. The onset (epoch) of planet formation and the conditions and chemistry required for this

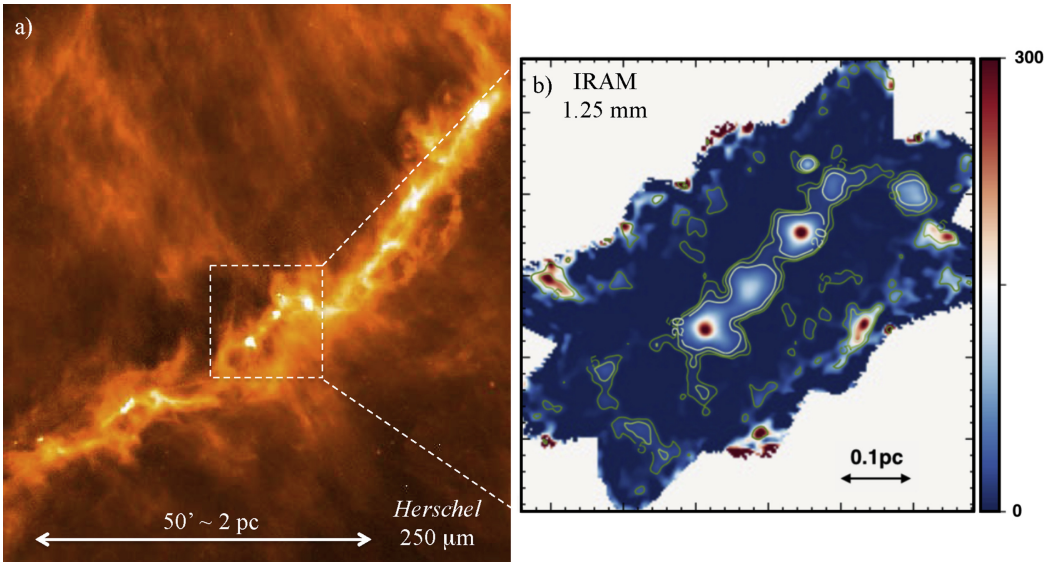

Figure 2.5: (a) Herschel/SPIRE image of the Taurus B211/B213 filament in the Taurus molecular cloud. (b) IRAM/NIKA image of the central part of the Herschel field on the left, showing at least three prominent dense cores. Image from [55].

process to begin will be measured. With high spectral resolution, SPICA will be able to quantify stellar feedback processes which occur from the disc and its host star, including the dispersal of gas and dust by jets and stellar winds. Comparisons with the high spatial resolution provided by large array telescopes such as ALMA will be able to link the chemical processes with the disc structure. High resolution spectroscopy will also be able to distinguish isotope ratios of trace gasses, providing unique information which may differentiate between various protoplanetary disc models.

2.2.6 Ices and Minerals

SAFARI will also be capable of measuring a wide range of water spectroscopic features. This will allow astronomers to measure the transition of water vapour from its gaseous form in the ISM to the icy phase within protoplanetary disks. The current understanding of the role of water ice is that it enhances the solid material in the cold, outer part of the disk beyond the snow line, which promotes the formation of gas-giant planet cores. Certain candidate water lines are able to measure the presence of the snow line – where water molecules can condense to form solid ice grains – which

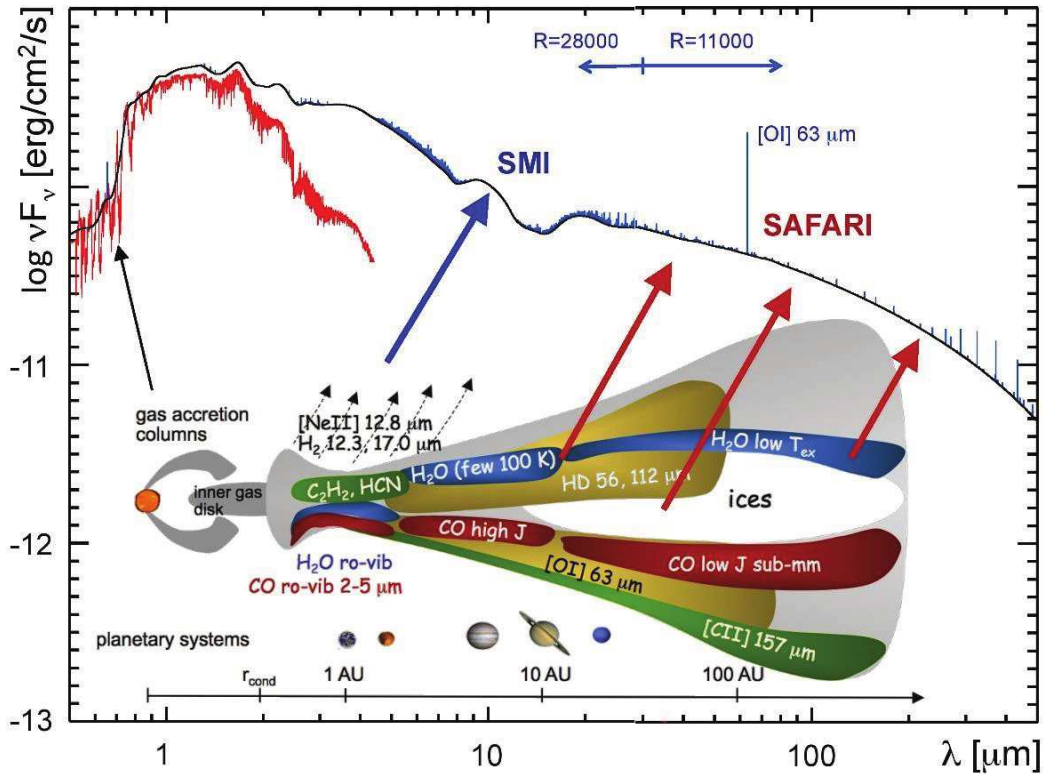

Figure 2.6: A model spectrum for a protoplanetary disc. This figure shows the wealth of information available at FIR wavelengths. It also shows the importance of high-resolution spectra for determining gas species and properties. The image was taken from [38].

separates gas giants from rocky planets. By determining the abundance of water in both gas and ice form, as well as the position of the snow line, astronomers can better predict the initial conditions required for the formation of Earth-like planets [56].

2.3 Mission Requirements

The SAFARI instrument on the SPICA telescope will be designed to address the science themes in Section 2.2, with its broad wavelength coverage and variable spectral resolving power. To this end, the main operating condition of the instrument will be moderate resolution ($R \sim 300$) instantaneous scans of the wavelength range from 34 μm to 230 μm. Here the SAFARI detectors will be optimized for the highest sensitivity, allowing for rapid acquisitions of high-redshifted galaxies and measurements of

the abundance of key elements responsible for cooling of GMCs, as well as the broad PAH and dust features to survey the production and destruction of dust within these galaxies.

SAFARI will be able to detect gas lines with sensitivities of $\sim 5 \times 10^{-20}\,\mathrm{W\,m^{-2}}$ (5σ, 1 hr) with the current detector NEP of $2 \times 10^{-19}\,\mathrm{W}/\sqrt{\mathrm{Hz}}$ [38]. This represents an increase of two orders of magnitude over Herschel/SPIRE [57], which will allow detection of important spectral lines for a broader selection of targets, encompassing both the less-luminous targets, as well as the more distant ones. With the unprecedented sensitivities that SPICA will provide, astronomers will have a wider and more in depth collection of observed sources from which to test and update their models for the formation and evolution of planetary systems and on a larger scale galactic evolution.

SAFARI will also have a high resolution mode, to separate and identify narrow spectral lines. These will survey the rate of in-fall and outflow of matter within AGNs, as well as other kinetic processes which may shift or broaden the lines. High resolution measurements will also be able to uncover fine-structure lines of rarer isotopes which helps realize the localized radiation field and metallicity within high-z galaxies.

2.4 Instrument Design

The payload of SPICA will consist of a high-resolution spectrometer SAFARI in combination with a new generation of ultra-sensitive detectors (Dark NEP $\sim 10^{-19}$ $\mathrm{W}/\sqrt{\mathrm{Hz}}$) [35]. In addition, the cold telescope will, for the first time, allow astronomers to achieve cosmic background limited sensitivity over this wavelength range. In the event that the sensitivity of the TES detectors increases due to ongoing development it will directly lead to an increase in instrument performance. Since a diffraction grating spectrometer provides only comparatively low-resolution spectroscopy, a complementary high-resolution component is required to resolve narrower

astronomical spectral features. Two high resolution modules were considered initially: a polarizing MPI [58], and an FPI [59], which are discussed further below.

2.4.1 Detector Noise

A detector's sensitivity may be characterized by its noise performance. Since noise may arise from a number of different sources, the total noise level of a detector is the quadrature sum of the individual components. A common way to express noise is Noise Equivalent Power (NEP), which is defined as the required input power received by the detector to achieve a signal-to-noise ratio of 1 over a 1 Hz bandwidth, and is a means of expressing the minimum detectable signal. Since the detectors are operating in a background limiting condition, the dominant source of noise is photon shot noise produced by a variance in the thermal background emission. The background photon noise may be expressed as the root mean square (RMS) noise power of absorbed radiation [60]:

$$\mathrm{NEP}_p = \left(\bar{P}_p^2\right)^{1/2} = 8A_D\beta\eta\sigma k\left(T_1^5 + T_2^5\right)B \qquad [\mathrm{W}/\sqrt{\mathrm{Hz}}] \quad (2.1)$$

where A_D is the detector surface area, β is the detector fill factor, η is the emissivity (absorptivity) of the area A_D, σ is the Stefan-Boltzmann constant, k is the Boltzmann constant, T_1 is the temperature of the detector, T_2 is the temperature of the thermal background, and B is the receiving bandwidth of the detector. It can be clearly seen that photon shot noise is proportional to detected bandwidth B. To this end, a dispersive spectrometer based upon a diffraction grating is used to reduce the photon noise from the astronomical source to below the detector noise level.

2.4.2 Dispersive Element

The grating modules provide an effective low resolution spectrum instantaneously for each observation. SAFARI will utilize a reflection grating configuration consisting

of the telescope beam focusing onto an input slit. The beam is then propagated through a collimating mirror and incident on the reflective grating at high incidence to disperse the beam. The output is incident on a focusing mirror, which directs light to a linear module of detectors on the focal plane, called the focal plane array (FPA) (Figure 2.7). Because of the different optimum grating configurations for the large wavelength range covered, there are four such grating modules which split up the SAFARI band and operate simultaneously. The input to each module is taken from the main telescope beam through a series of mirrors and dichroics. The high incidence of the grating modules allows a high angular dispersion which allows the optics to be compact. The compactness of the optics is necessitated by the allowed volume and cooling power of the 1.8 K enclosure where the grating modules are located. However, the high incident angle also has the effect that the gratings are only efficient for a single linear polarization state [61], a fact that can be exploited by a polarizing MPI.

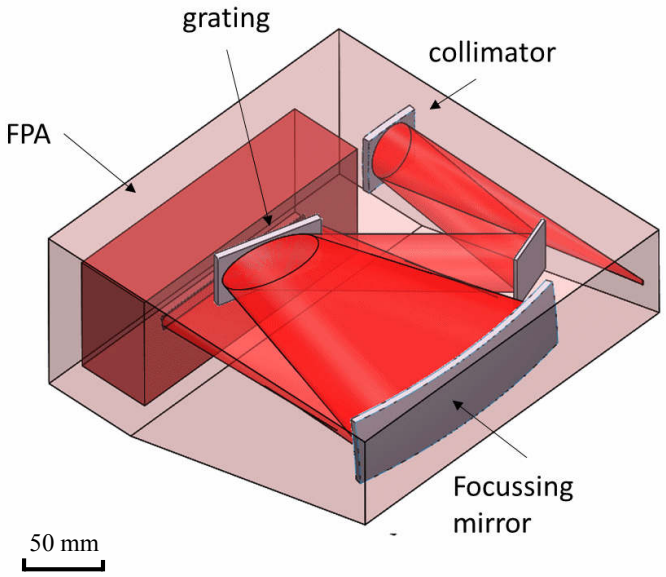

Figure 2.7: A 3D model of one of the SAFARI grating modules [38]. The scale bar is an approximation.

2.4.3 High Resolution Interferometer

For high resolution operation of SAFARI, a scanning interferometer is added into the beam before the grating and detector modules. The two designs considered were an MPI [58], or a Fabry-Pérot Interferometer (FPI) [59]. A Martin-Puplett interferometer is similar in design and construction to the classical Michelson interferometer [62]. However, the conventional beamsplitters are replaced with wire grid polarizers. Additionally, the plane mirrors in the interferometer arms are replaced with rooftop mirrors (Figure 2.8). The polarizers are designed to reflect one linear polarization and transmit the orthogonal polarization. The rooftop mirrors serve to rotate the polarization of light by 90° on reflection. On re-encountering the polarizer, the reflected light transmits where it was first reflected and reflected when it was first transmitted. Since each path will be orthogonally polarized, a final polarizer is required at 45° to both linearly polarized states, so that interference can occur. Additionally, a Martin-Puplett interferometer confers the normal advantages of an FTS, namely it has high throughput, is broadband, capable of multiplexing many signals, and has a well determined instrumental line shape (ILS) [63]. However, with such sensitive detectors which are photon shot noise limited, the multiplex capabilities of the instrument actually confers a disadvantage on the performance, which necessitates the post-dispersion provided by the grating.

The operation of an FPI constitutes the majority of the thesis and will be described fully in Chapter 3. However, it should be stated here that the chief advantage of using an FPI is that the multiple beam interference produced by the device enables the most compact instrument design when confined to using incoherent detection methods. While the FTS has no intrinsic limit on its resolution, it relies on long path lengths, requiring a heavy degree of folding the optical path. This is inefficient both in terms of mass and volume, which undermines the potential of this instrument for a space-based observing platform. However, the drawback of the FPI is that the

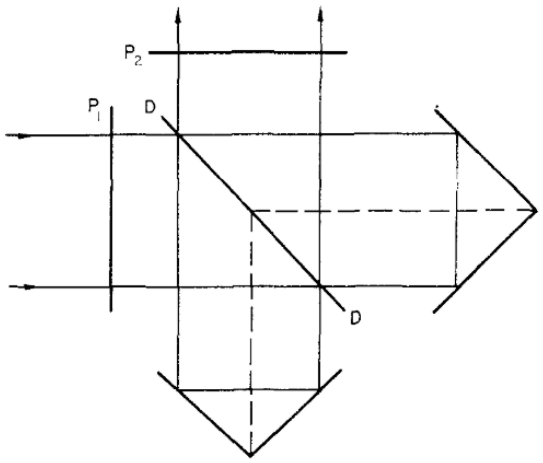

Figure 2.8: The original design for Martin and Puplett's interferometer [58].

spectral range of the instrument before overlap with the next interference order – defined as the FSR – is small, especially as compared to the broad spectral coverage of an FTS. While this issue may be mitigated by dispersing the resulting interference pattern with a grating, the FPI etalon must be uniquely matched to the grating. Since there are four grating bands/modules in SAFARI, this requires four unique etalons, each with its own actuators and metrology. By comparison, a single MPI may be used to cover the entire SAFARI band, making the FTS a more viable option for the wideband coverage desired for SAFARI.

Additionally, in a space-based cryogenic platform such as SPICA, the cooling capabilities are severely limited. Limitations on the dissipated power from active components are in place, which prevent the simultaneous operation of too many components. Since four FPIs as high-resolution elements would require four separate mechanical actuation systems, whereas the single MPI required only one, the observation times would have increased by a factor of four. Historically, each FPI also requires three actuators to maintain the parallelism of the reflecting plates which comprise the device. Ultimately, a shorter time to collect spectral scans allows for longer integration time to detect weaker targets, which makes the MPI a more viable option.

A table which outlines the trade-offs between the FPI and MPI instrument con-

cepts is given in Table 2.2. Due to the broadband capabilities of the FTS and the shorter time scales required to scan the wide spectral range, SAFARI will implement a Martin Puplett interferometer before the diffraction gratings to achieve a high-resolution mode. The incoming signal will be modulated by the MPI before being distributed to the grating, and post-dispersed to the detector arrays. Each detector will measure the convolution of an interferogram produced by the MPI with a filter function corresponding to the grating and detector with its feedhorn. A complete spectrum is obtained by Fourier transformation of the individual detector readouts and combining the result. Since the grating modules are themselves most efficient to a single polarization state, the grating preferred polarization may be matched to the output of the MPI. In this way, SAFARI itself may be able to measure the degree of polarization of its observing targets by performing observations at orthogonal telescope orientations.

Table 2.2: A simple comparison of the FPI and MPI in terms of their suitability for a cryogenic, high-resolution spectrometer.

Property	**FPI**	**MPI**
Compact	Yes	No
Broadband	No	Yes
Observation Time (Full Band)	Long	Short
Polarizing	No	Yes
Heat Dissipation	High	Low
ILS	Complex	Simple

The SAFARI design currently requires a maximum optical displacement of 25 cm which will be achieved by a mechanical displacement of around 3 cm and a folding of the beam by a factor of 8 (Figure 2.9). This yields a spectral resolution which ranges from 1500 at 230 µm to 11000 at 34 µm [38].

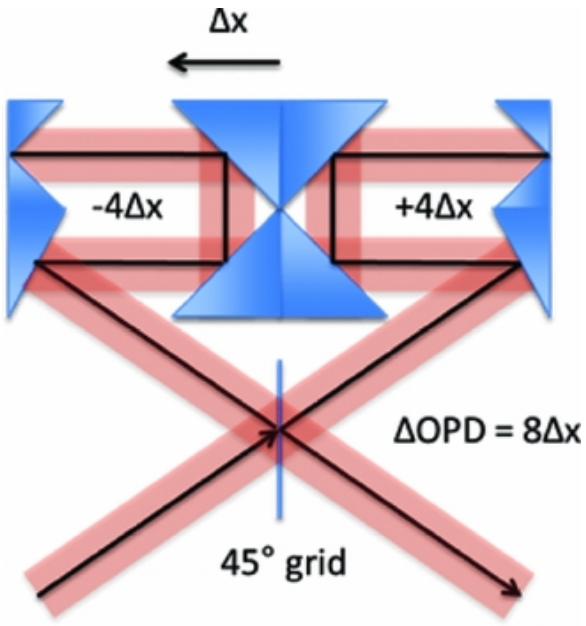

Figure 2.9: The optical beam layout for the MPI high resolution instrument. With a linear displacement of the center double rooftop mirror, the corresponding change in optical path will be 8× larger [38].

2.5 Conclusion

The SAFARI instrument on SPICA aims to provide unprecedented sensitivity for the 34 µm to 230 µm wavelength range. Instantaneous $R \sim 300$ spectra will be acquired with a four-band dispersive grating spectrometer, which will allow SAFARI to measure a large volume of high-redshifted galaxies to determine AGN activity and star formation rate across cosmic time. An optional high resolution module, which will consist of a Martin-Puplett interferometer, will allow spectral resolution of $R \sim 1500 - 11000$ to separate narrow spectral lines, and determine gas velocities to measure kinematics of protoplanetary discs. A Fabry-Pérot Interferometer was originally considered as a potential high-resolution module, but has since been discounted due to the uniqueness of the FPIs required so that one must be matched to each grating, as well as the high-heat dissipation for simultaneous operation of the FPIs. The unique matching to grating bands is an inevitable consequence of the system design, but if the number of actuators required for each FPI were to be decreased,

the competitiveness of the FPI in a SAFARI-like system could be reinstated.

In this thesis, I present the design and discuss the performance of an FPI I have developed as an alternate approach for a space-based, cryogenic, high resolution FIR spectrometer. The FPI I designed confers the advantages of requiring one actuator instead of three, is compact, and dissipates minimal heat, making it a competitive choice for further FIR instrumentation. The following chapters are dedicated to the theory, modelling, design, fabrication, and performance testing of this FPI design.

Chapter 3

Fabry-Pérot Interferometry

> ... at several times we have thought that optics was a finished science, where the last word had been said, or almost. Each time the discovery of new facts, the overthrow or extension of accepted theories, reminded us that science is never finished.
>
> Maurice Paul Auguste Charles Fabry

The invention of the FPI was timely, providing a new methodology for high resolution spectroscopy when the wavelength accuracies of Rowland's grating spectrometer and the two-beam Michelson interferometer were reaching their practical limitations, based on manufacturing limitations of the day [59]. The theoretical analysis of multiple beam interference had been described seventy years earlier by an English astronomer, George Airy [64], but it wasn't until 1896 that two French physicists: Alfred Pérot and Charles Fabry, designed and built an interfering device which offered unprecedented wavelength resolution [65]. Consisting of a pair of parallel reflective plates, the device is simple and elegant in its construction and operational theory as well as useful over a wide range of wavelengths from the radio to the ultraviolet.

3.1 Ideal Fabry-Pérot

The ideal FPI consists of two parallel plates with reflective coatings, commonly called an *etalon*. The surfaces may be curved, to create a spherical reflecting cavity, but in the vast majority of instruments the plates are plane and parallel. There-

fore, these investigations will be limited to this form of etalon. An incident ray on the first surface will be partially reflected, transmitted, or absorbed. Rays that are transmitted through the first reflector travel through the intervening region, reaching the second surface, and are again partially transmitted, reflected, or absorbed. The reflected beams continue to resonate in decreasing amplitude so that a theoretically infinite number of reflected and transmitted rays are produced, as shown in Figure 3.1. Combining the electric fields for either the reflected or transmitted waves produces an interference pattern. It is the measured intensity of the interference pattern which forms the basis for the operational qualities of this instrument

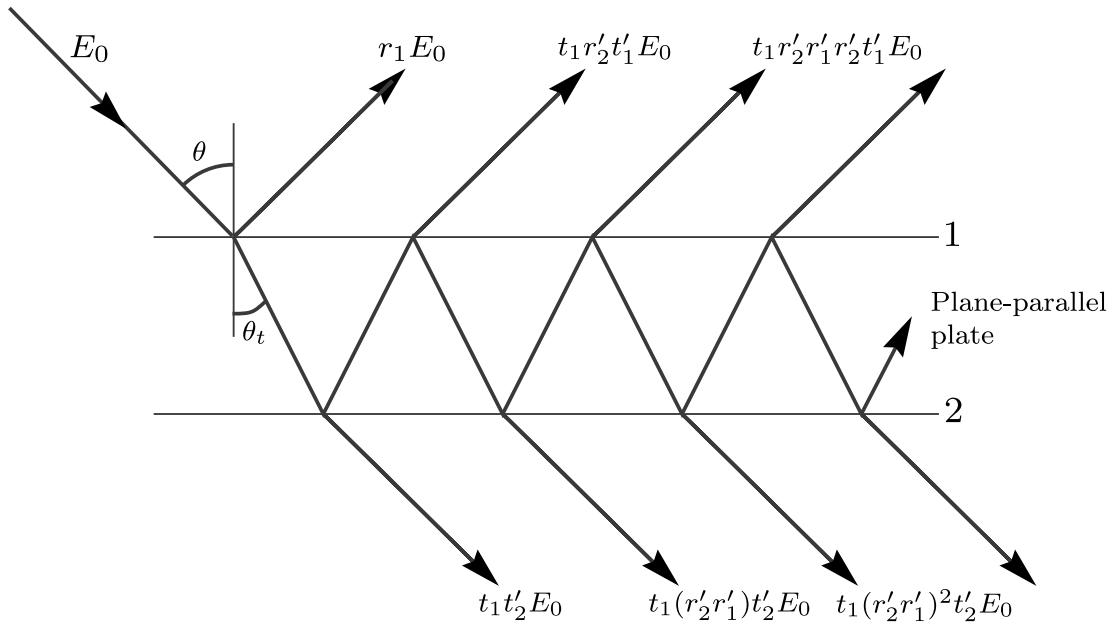

Figure 3.1: Multiple beam interference by a parallel plate by division of amplitude [66]; see text for details.

The reflected and transmitted interference patterns are complementary so that only one must be used to utilize the full capabilities of the FPI. In fact, in the absence of absorption from the reflecting surfaces and surrounding media, the combination of the total reflection and transmission reproduces the incident E-field. This demonstrates the conservation of energy and reversibility of the device. For this analysis, only the transmitted interference pattern will be investigated.

Considering a plane wave of monochromatic light incident on the first surface of the etalon, successive transmitted beams experience a phase difference which is equal to [66],

$$\delta = \frac{4\pi}{\lambda}\mu d\cos\theta_t, \qquad \text{[rad]} \quad (3.1)$$

where λ is the incident wavelength, μ is the refractive index of the etalon substrate, d is the thickness of the etalon, and θ_t is the angle of the transmitted beam within the etalon. Note that this phase delay does not account for phase changes on reflection, which are accounted for by the complex reflection coefficients described later in this chapter. The transmitted beam angle is related to the incident beam angle θ_i by Snell's law of refraction [66]:

$$\mu_0 \sin\theta_i = \mu \sin\theta_t \quad (3.2)$$

where μ_0 is the refractive index of the surrounding medium, assumed to be a vacuum in this derivation.

With the travelling wave encountering a surface, the change in the **E**-field can be identified in terms of reflection and transmission coefficients, r, r', t and t', where the prime coefficients denote a wave travelling from the etalon substrate to outside, and the non-prime coefficients are a wave travelling from outside into the etalon. Note that the vector notation may be dropped, since parallel rays are used, as long as the relevant phase shifts are taken into account. If the amplitude of the incident beam is $E_0(r,t)$, the amplitude of the first transmitted beam is $t_1 t_2' E_0(r,t)$, where the 1 and 2 subscripts denote the first and second surface of the etalon for a right travelling wave passing through. Note that there is also a phase delay introduced between the incident and transmitted beams, but since it is common to all transmitted beams, it may be ignored. The next wave to transmit through the etalon encounters two more internal reflections, so that the amplitude is $t_1 r_2' r_1' t_2' E_0(r,t)e^{i\delta}$. Further transmitted beams each encounter another set of internal reflections such that the n-th transmitted

beam is $t_1 \left(r_2' r_1'\right)^{n-1} t_2' E_0(r,t) e^{i(n-1)\delta}$. Combined with the phase delay introduced by each round trip through the etalon, the sum of the transmitted electric fields becomes:

$$E_T(r,t) = \sum_{n=1}^{\infty} t_1 \left(r_2' r_1'\right)^{n-1} t_2' E_0(r,t) e^{i(n-1)\delta}. \qquad [\mathrm{V\,m^{-1}}] \quad (3.3)$$

The series sum converges to the expression,

$$E_T(r,t) = t_1 t_2' E_0(r,t) \Big(1 - r_2' r_1' e^{i\delta}\Big)^{-1}. \qquad [\mathrm{V\,m^{-1}}] \quad (3.4)$$

The flux density (intensity) of the beam is defined by the Poynting vector magnitude [67], which is proportional to the product of the electric field with its complex conjugate.

$$I_T \propto E_T E_T^* \qquad [\mathrm{W\,m^{-2}}] \quad (3.5)$$

By assuming reflection and transmission coefficients are identical for both plates, the fractional power reflectance R and transmittance T may be determined by:

$$t_n = t_n' \quad (3.6)$$

$$t_1 t_2 = T \quad (3.7)$$

$$r_n = -r_n' \quad (3.8)$$

$$r_1^2 = r_2^2 = R. \quad (3.9)$$

A convenient expression for the intensity of the transmission profile becomes:

$$\begin{aligned} I_T &= I_0 T^2 \Big(1 + R^2 - 2R\cos\delta\Big)^{-1} \\ &= I_0 T^2 \Big((1-R)^2 + 4R\sin^2(\delta/2)\Big)^{-1} \end{aligned} \qquad [\mathrm{W\,m^{-2}}] \quad (3.10)$$

By normalizing the intensity of the incident beam, this becomes the Airy Function [64],

$$I_T = \left(\frac{T^2}{(1-R)^2}\right)\frac{1}{1+F\sin^2\delta/2} \qquad [\mathrm{W\,m^{-2}}] \quad (3.11)$$

where F is the coefficient of finesse, defined as:

$$F = \frac{4R}{(1-R)^2} \quad (3.12)$$

As can be seen in the above expressions and from Figure 3.2, the point of peak intensity is the point of full constructive interference for all transmitted beams, when the phase delay is an integer multiple of 2π. The integer is usually denoted as m which is the interference order of the etalon at the appropriate wavelength. When the phase difference is not precisely $2m\pi$, the transmitted intensity falls off. In the case of an ideal FPI the sharpness of the resulting interference peak depends on the reflectivity of the parallel plates.

3.1.1 Free Spectral Range

The separation between wavelengths of peak transmission is called the FSR. The extent of the FSR is governed by the change in wavelength which results in a difference in phase delay of 2π. Considering two monochromatic beams of light with wavelengths λ_0 and $\lambda_0 + \Delta\lambda$, the difference in phase delay between the two beams is:

$$\Delta\delta = 2\pi(2\mu d\cos\theta)\Delta\lambda/\lambda_0^2. \qquad [\mathrm{rad}] \quad (3.13)$$

Setting $\Delta\delta$ to 2π results in the overlap of the m^{th} order of wavelength λ_0 with the $(m-1)^{\mathrm{th}}$ order of $\lambda_0 + \Delta\lambda$. Using $\Delta\lambda$ as the required wavelength difference, $\Delta\lambda = \mathrm{FSR}$, and:

$$\mathrm{FSR} = \frac{\lambda_0^2}{2\mu d\cos\theta}, \qquad [\mu\mathrm{m}] \quad (3.14)$$

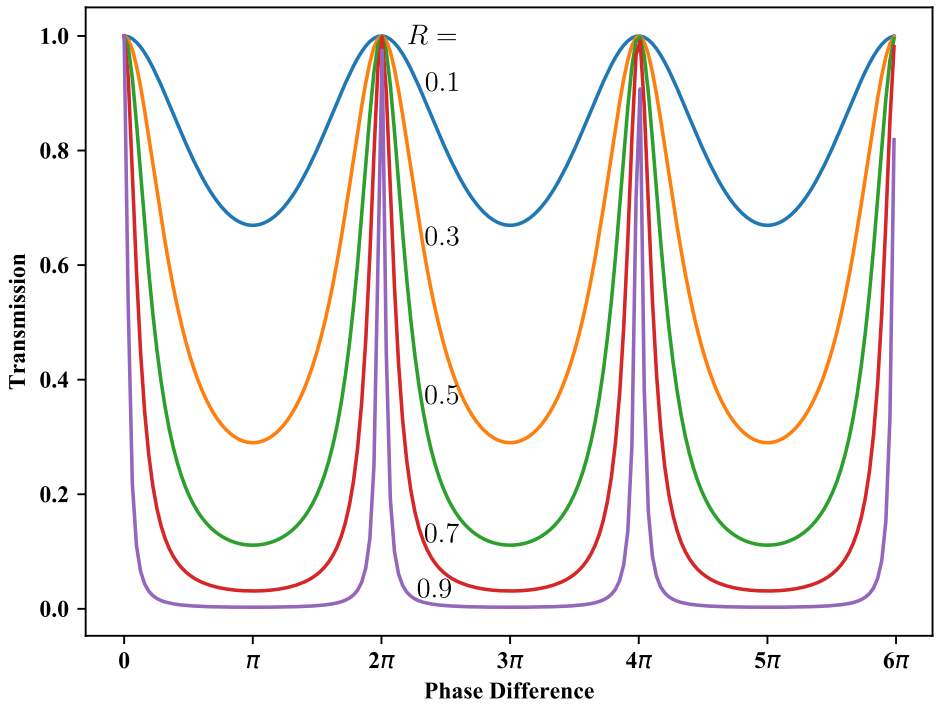

Figure 3.2: The transmission of a monochromatic source through an etalon as a function of the phase difference on successive reflections. Each profile is generated using the corresponding reflectance R of the etalon surfaces.

which can be further simplified to:

$$\text{FSR} = \frac{\lambda_0}{m}. \qquad [\mu\text{m}] \quad (3.15)$$

3.1.2 Line Width

The sharpness of the transmission peaks increases with increasing reflectivity of the parallel plates. A convenient way to express the sharpness is to report it as the ratio of the free spectral range to the FWHM of the fringe, a property known as the *finesse*. From Equation (3.11), the points of half intensity are found when:

$$F \sin^2(\delta/2) = 1. \quad (3.16)$$

For a sufficiently large F, the required phase delay to reach half the max intensity is $\delta_{1/2} = 2/\sqrt{F}$. Since fringes are symmetrical about the peak, a phase delay of $2\delta_{1/2}$

identifies the FWHM of the peak in units of phase delay.

3.1.3 Finesse

Having recovered the width of the interference peak in units of phase delay, there is a convenient way to express the ratio of the phase delay between successive peaks and the width of an individual peak. Since the FSR in terms of phase delay is always 2π, the ratio of the two can be expressed as:

$$N_r = \frac{2\pi}{2\delta_{1/2}} = \frac{\pi\sqrt{R}}{1-R}. \tag{3.17}$$

The term N_r is called the reflectivity finesse (or just the finesse) of the ideal FPI.

There are other forms of finesse including parallelism finesse, surface defect finesse, and beam divergence finesse which result in a decrease in the overall finesse from the ideal value above. This will be discussed in Section 3.2.2.

3.1.4 Resolving Power

Since the fringes which correspond to monochromatic radiation are broadened by the instrument response, as the phase difference $\Delta\delta$ between two monochromatic sources decreases, eventually the fringes will overlap and become inseparable. The most common system for identifying the minimum separation so that the fringes are separable is the Rayleigh criterion [68]. However, the Rayleigh criterion is primarily used for unresolved interference lines which have subsidiary maximum, and is a somewhat artificial means of determining minimum separation [59]. A more convenient method of determining separability is the use the criterion that two lines may be resolved if the phase separation between peaks is no smaller than the FWHM of a single peak:

$$\Delta\delta_{\min} = 2\delta_{1/2} = 4/\sqrt{F} = 2\pi/N_r. \qquad \text{[rad]} \tag{3.18}$$

The resolving power is expressed as the ratio of a certain wavelength to the mini-

mum resolvable wavelength separation:

$$\mathcal{R} = \lambda_0/\Delta\lambda = 2\pi m/\Delta\delta_{\min} = mN_r. \tag{3.19}$$

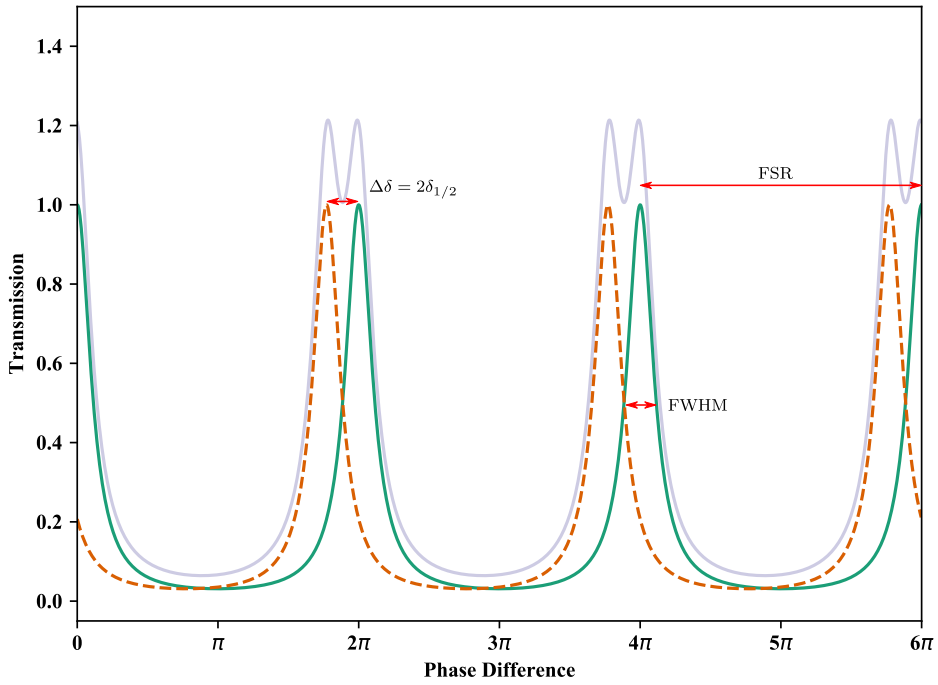

Figure 3.3: Visual representations of the definitions of FSR and FWHM. Also shown are two monochromatic sources which are separated by a FWHM and the resulting transmission profile showing that the separate peaks can be identified.

3.2 Practical Fabry-Pérot

While the preceding section covers a theoretical analysis of the etalon, there are practical limitations to the development of such a device. In this section, the availability of high-reflectivity surfaces for the THz waveband, as well as the effects of manufacturing errors and optical tolerances on the resolving power of the etalon, will be discussed. Also the effects of a non-incident beam on the etalon are examined, which will become important for the experimental design presented at the end of this chapter.

3.2.1 THz Reflectors

The etalon relies on a high-reflectivity of the plates to achieve high resolving power. Section 3.1.3 describes the dependence of the line width on the reflectivity finesse. In the THz domain, finding materials which have high reflectivity as well as low absorption for transmitted beams is a considerable challenge. Since reflectors made from solid metal deposits on a dielectric are either too thin to reflect effectively, or too thick to have low absorption, other materials are required. The wavelengths are on the order of micromachining capabilities so it is possible to develop metamaterials which have desirable properties over the required wavelength range. Historically, THz reflectors have been developed from thin metallic mesh structures deposited on thin Mylar sheets [69]. However, etching and micromachining techniques also allow for the use of dielectric stacked coatings which mimic high reflectivity for narrow wavelength bands by utilizing constructive interference on multiple reflections (the principle on which the etalon itself functions).

Metallic Mesh Filters

The relatively long wavelengths in the FIR range allow for quasi-optical metamaterials to be used, to create effective reflectivity and transmissivity from the interaction of an incident EM wave with a free space transmission line. The use of free space transmission lines dates back to the 1880s with Heinrich Hertz, who demonstrated polarization of EM radiation using parallel metallic wires. The use of wire grids as frequency selecting elements was first demonstrated in 1967 by Ulrich [70]. He created metallic grids with regularly spaced square openings, as well as arrays of metallic squares on a thin dielectric substrate to create inductive or capacitive meshes respectively, which act as high pass or low pass optical filters. Through superimposing the two filter types, a third type can be made which acts as an optical band-pass filter. The three filter types are shown in Figure 3.4 along with frequency-dependent

transmission functions.

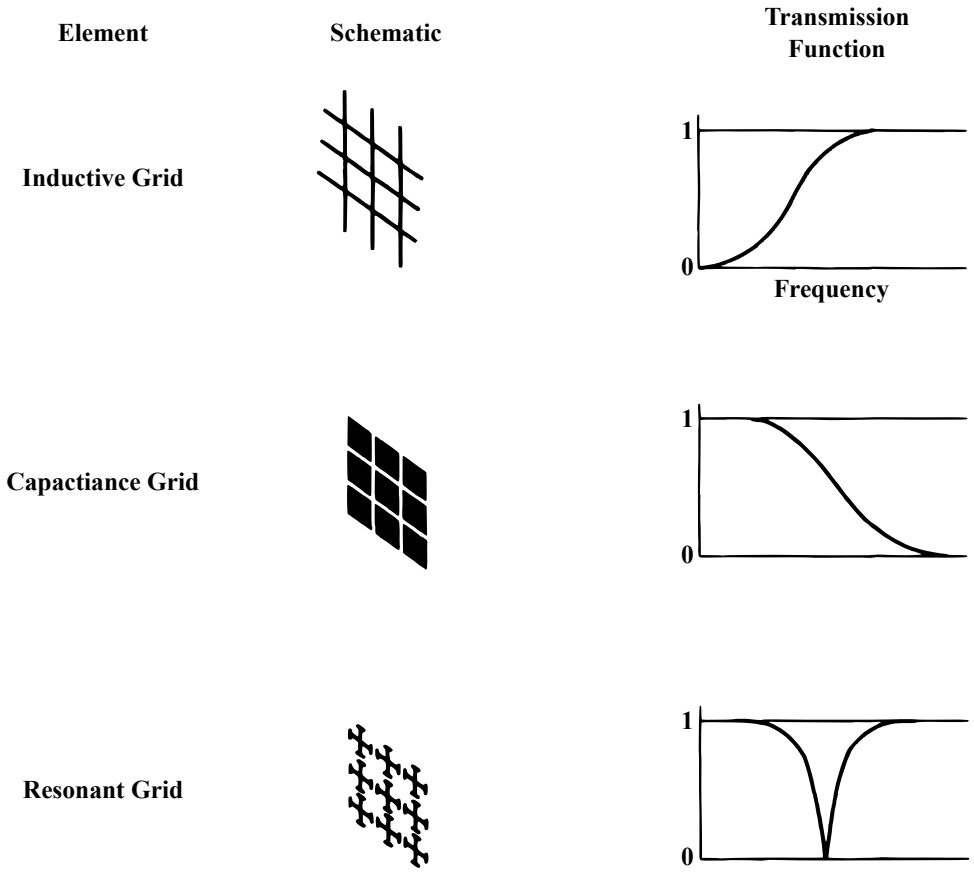

Figure 3.4: Examples of metal mesh filter geometries and their frequency-dependent transmission.

The geometry of free standing metal meshes which provide a high reflectivity at the desired wavelengths can be derived from [71], although the design of metal mesh filters is not the focus of this thesis. Optimized filters can be used to create an FPI, typically by creating an airgap of adjustable width between two filters [72]. However, in practice metal meshes can be applied directly to the surface of a substrate used as the etalon. Incorporating a dielectric etalon creates additional Fresnel reflections at the etalon interfaces, introducing significant deviations from the free standing filter properties, and significantly complicating the reflectivity models. One method of avoiding the added complications with a dielectric etalon is to leave a small airgap between the filter and the dielectric, creating a resonant cavity. In this way, the

optical properties of the filter are identical to those in free space, and the resonant cavity width may be set to enhance/reduce the transmission as desired.

Dielectric Stack Reflectivity

As the name suggests, a dielectric stack reflector is comprised of a series of layered dielectric substrates. Fresnel's equations show that at every boundary between materials with different refractive indices, a fraction of the total incident EM wave is reflected back. With multiple layers of dielectric substrates, it becomes convenient to define the total E-fields in each substrate as the sum of all possible waves from multiple reflections. Following the derivation in [67], continuity across the boundaries defines the boundary conditions which form solutions to the equations that define the total transmission and reflection.

For the diagram in Figure 3.5, the tangential components of the electric field and the normal components of the magnetic field are continuous at the boundaries [67]. The **H** field is related to the **E** field by the unit propagation vector $\hat{\mathbf{k}}$ by:

$$\mathbf{H} = \sqrt{\frac{\epsilon_0}{\mu_0}} n \hat{\mathbf{k}} \times \mathbf{E}, \qquad [\mathrm{A\,m^{-1}}] \quad (3.20)$$

where ϵ_0 and μ_0 are the vacuum permittivity and permeability respectively, and refractive index is n in this derivation so as not to confuse it with permeability. Dropping the vector notation, but ensuring the sign of H is properly represented, at the first boundary Figure 3.5.

$$E_1 = E_{i1} + E_{r1} = E_{t1} + E'_{r2} \qquad [\mathrm{V\,m^{-1}}] \quad (3.21)$$

$$H_1 = \sqrt{\frac{\epsilon_0}{\mu_0}} (E_{i1} - E_{r1}) n_0 \cos\theta_{i1} \qquad [\mathrm{A\,m^{-1}}] \quad (3.22)$$

$$H_1 = \sqrt{\frac{\epsilon_0}{\mu_0}} (E_{t1} - E'_{r2}) n_1 \cos\theta_{t1}. \qquad [\mathrm{A\,m^{-1}}] \quad (3.23)$$

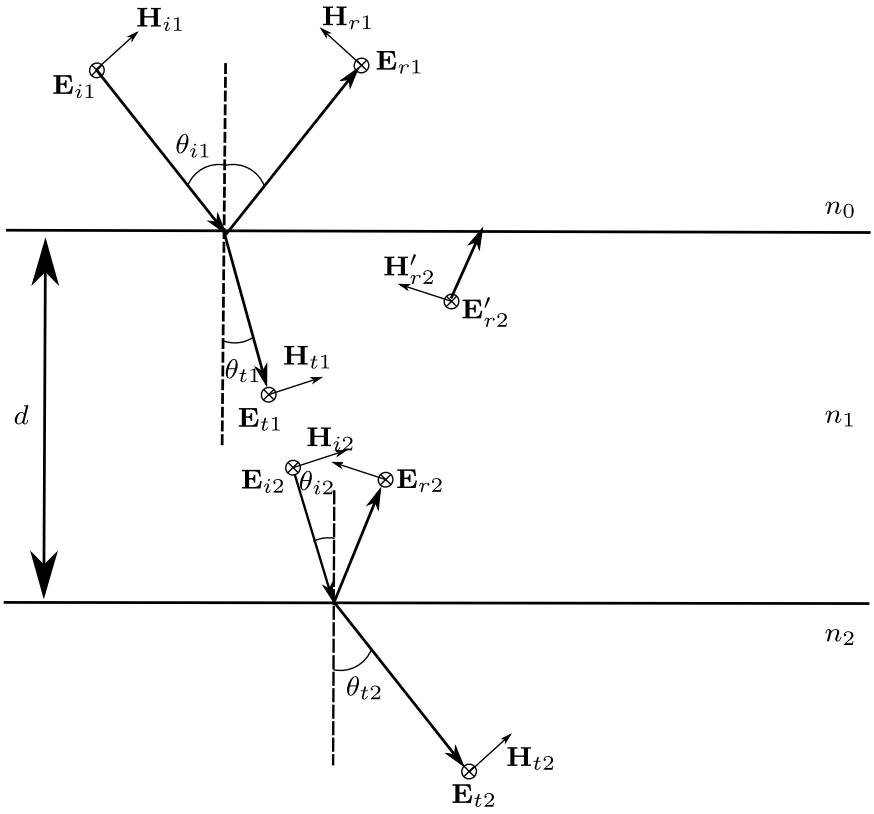

Figure 3.5: E- and H-fields at the boundaries of a dielectric slab.

Likewise, at the second boundary, the continuity conditions are:

$$E_2 = E_{i2} + E_{r2} = E_{t2} \qquad [\mathrm{V\,m^{-1}}] \quad (3.24)$$

$$H_2 = \sqrt{\frac{\epsilon_0}{\mu_0}}(E_{i2} - E_{r2}) n_1 \cos\theta_{i2} \qquad [\mathrm{A\,m^{-1}}] \quad (3.25)$$

$$H_2 = \sqrt{\frac{\epsilon_0}{\mu_0}} E_{t2} n_2 \cos\theta_{t2}. \qquad [\mathrm{A\,m^{-1}}] \quad (3.26)$$

Some equalities that simplify the expressions between the two boundaries are:

$$\theta_{t1} = \theta_{i2} \quad (3.27)$$

$$E_{i2} = E_{t1} e^{-i\delta} \qquad [\mathrm{V\,m^{-1}}] \quad (3.28)$$

$$E_{r2} = E'_{r2} e^{+i\delta}, \qquad [\mathrm{V\,m^{-1}}] \quad (3.29)$$

where

$$\delta = 2\pi n_1 d \cos\theta_{t1}/\lambda. \qquad \text{[rad]} \quad (3.30)$$

Substituting into the equalities at the boundary, a linear set of equations can be found which relate the **E** and **H** fields between boundary 1 and boundary 2, which can be expressed in matrix form as:

$$\begin{bmatrix} E_1 \\ H_1 \end{bmatrix} = \begin{bmatrix} \cos\delta & (i\sin\delta)/Y_1 \\ Y_1 i \sin\delta & \cos\delta \end{bmatrix} \begin{bmatrix} E_2 \\ H_2 \end{bmatrix} \tag{3.31}$$

where Y_1 is the admittance of the substrate the beam is entering, and is defined as:

$$Y_1 \equiv \sqrt{\frac{\epsilon_0}{\mu_0}} n_1 \cos\theta_{i2}. \qquad \text{[S]} \quad (3.32)$$

The matrix in 3.31 is the *characteristic matrix* M_1 of the dielectric substrate n_1. For a stack of differing dielectrics, the resultant characteristic matrix of the entire system is the matrix product of all characteristic matrices for each component of the stack. For a stack of s dielectrics, the output **E** and **H** fields can be expressed as:

$$\begin{bmatrix} E_1 \\ H_1 \end{bmatrix} = M_1 M_2 ... M_{s-1} \begin{bmatrix} E_s \\ H_s \end{bmatrix}, \tag{3.33}$$

and the resultant characteristic matrix of the entire stack is:

$$M = M_1 M_2 ... M_{s-1}. \tag{3.34}$$

The transmission and reflection coefficients can be derived for a general characteristic matrix by:

$$r = E_{r1}/E_{i1} \quad \text{and} \quad t = E_{ts}/E_{i1}. \tag{3.35}$$

The reflectivity and transmissivity coefficients are:

$$r = \frac{Y_0 m_{11} + Y_0 Y_s m_{12} - m_{21} - Y_s m_{22}}{Y_0 m_{11} + Y_0 Y_s m_{12} + m_{21} + Y_s m_{22}} \tag{3.36}$$

and

$$t = \frac{2Y_0}{Y_0 m_{11} + Y_0 Y_s m_{12} + m_{21} + Y_s m_{22}}. \tag{3.37}$$

In the above equations, Y_s is the admittance of the last substrate (Y_2 in the single dielectric slab case), and m_{ij} refer to the elements of the characteristic matrix in Equation (3.31). These reflectivity and transmissivity coefficients may be input into Equation (3.4) to create the transmission function for the etalon.

3.2.2 Practical Finesse

In practice, the finesse which defines the resolving power of the FPI is not only a function of the reflectivity, but also of the surface roughness, parallelism, and surface bowing of the reflectors – which are commonly defined together as the defect finesse – as well as the solid angle of the input beam, referred to as the aperture finesse. The defect and reflectivity finesse are a result of the manufacturing of the etalon, and the aperture finesse is due to illumination of the etalon. Each of these effects may be treated independently, with the final effective finesse, N_e the inverse quadrature sum of all contributions [73]:

$$N_e^{-2} = N_r^{-2} + N_d^{-2} + N_a^{-2}, \tag{3.38}$$

where N_r is the reflectivity finesse, N_d is the defect finesse, and N_a is the aperture – or beam divergence – finesse.

The total defect finesse is the inverse quadrature sum of each of the three forms of defects mentioned above:

$$N_d^{-2} = N_s^{-2} + N_p^{-2} + N_b^{-2} \tag{3.39}$$

Irregularities in the surfaces of the mirrors will cause irregularities in the path lengths for different regions of the etalon. With a Gaussian rms gap variation Δs, it can be shown that [74]:

$$N_s =\approx \frac{\lambda}{4.7\mu\Delta s}. \tag{3.40}$$

If one mirror is tipped with respect to the other at an angle θ, then the cavity resonates at different wavelengths at different locations. To model this effect, assume the resonant wavelength is λ_0 on one end of the etalon and λ_1 on the other. The maximum resolving power of the etalon is then,

$$\mathcal{R}_{\max} = \frac{\lambda_0 + \lambda_1}{2(\lambda_0 - \lambda_1)} = mN_p. \tag{3.41}$$

For a deviation from parallelism, θ_p, the gap difference between either end is $D_c \sin\theta_p$ where D_c is the clear diameter of the etalon, and

$$\begin{aligned}(\lambda_0 - \lambda_1) &= 2\mu d/m - 2\mu(d + D_c\sin\theta_p)/m \\ &= -2\mu D_c \sin\theta_p/m.\end{aligned} \quad [\mu\text{m}] \tag{3.42}$$

Combining the above expressions and letting $(\lambda_0 + \lambda_1)/2 = \lambda$:

$$N_p = \frac{\lambda}{2\mu D_c \sin\theta_p}. \tag{3.43}$$

The effect of spherical bow in one of the etalon reflectors with respect to the other on the finesse is similar to the parallelism effects. In this case, some areas of the etalon resonate at different wavelengths than other areas. If the maximum difference in separation of the plates due to bowing is Δs, then the effective finesse can be shown to be [74],

$$N_b = \frac{\lambda}{2\mu\Delta s}. \tag{3.44}$$

Aperture finesse N_a represents the case where radiation in a finite solid angle is in-

cident on the etalon. Each transmitted angle has a slightly different cavity length, and therefore different resonant wavelength. For a solid angle defined by beam divergence of θ_d, the aperture finesse can be defined as [74],

$$N_A = \frac{2\pi}{m\Omega} \tag{3.45}$$

where Ω is the solid angle of the cone of rays passing through the FPI. The optimum case is when the rays entering the etalon are collimated, but in practice this is rarely the case. However, with a high refractive index medium between the reflectors, the solid angle of the rays is reduced and the effect of aperture finesse on limiting the overall finesse of the etalon is reduced.

3.2.3 Beam *Walk-off*

From the equation for transmitted intensity of the FPI (Equation (3.11)) and that for the phase difference (Equation (3.1)), the effect of changing the angle of incidence has a similar effect as changing the etalon spacing, if one simply combines the two terms $d\cos\theta_t$. However, changing the angle of incidence not only serves to change the phase difference between interfering beams, but also changes the number of interfering beams within the etalon. This effect, which tends to reduce the number of interfering beams and therefore broaden the line profile, is known as beam *walk-off*.

Walk-off occurs when the angle of incidence is not 0° so that each successively transmitted (or reflected) beam shifts laterally across the aperture (Figure 3.6). The number of reflected beams within the etalon is then limited due to the finite aperture diameter. If the angle of incidence is sufficiently high, the reduced number of reflected beams renders the approximation implicit in deriving the transmitted intensity equation no longer valid. In this case, it is necessary to use an alternate derivation for the transmitted intensity [75].

If the effect of reduced beam overlap is ignored, *walk-off* can be described as the

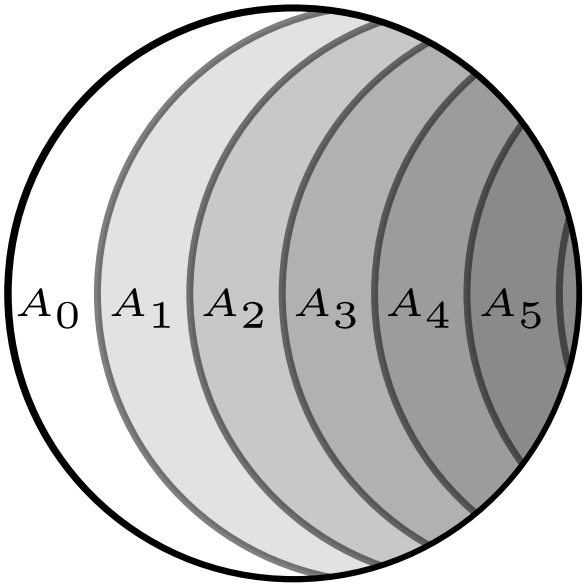

Figure 3.6: Simple visual representation of the beam walking off the etalon aperture with successive reflections.

sum of only a finite number of terms in the otherwise infinite series. If n is the number of round trips, the series sum for transmitted intensity with n terms may be expressed as,

$$I_T = \frac{I_0(1-R^{2n})^2}{1+\left[4R^2/(1-R^2)^2\sin^2(\delta/2)\right]}\left\{1+\left[4R^{2n}/\left(1-R^{2n}\right)^2\right]\sin^2(n\delta/2)\right\}. \qquad [\mathrm{W\,m^{-2}}] \quad (3.46)$$

The fractional part of the above equation shows the overall drop in peak transmitted intensity from *walk-off*, and the part of the equation in braces describes the broadening of the intensity profile with decreasing n. The number of round trips may easily be determined by finding the lateral shift in the beam for each pass through the etalon. This is given by the expression [72]:

$$W = 2d\tan\theta_t \qquad [\mathrm{m}] \quad (3.47)$$

where θ_t is the internal angle of the beam with respect to the etalon normal and d is the etalon thickness. Note that in the case of a finite aperture, the transmitted

cross-sectional area of each beam drops as the area overlap between the beam and the aperture becomes smaller as the beam walks off. With an aperture stop diameter D_c, then only the overlapping area with each beam within the aperture contributes to the interference. Relative *walk-off* can be defined as,

$$w = W/D_c, \tag{3.48}$$

and the total number of round trips before the beam completely leaves the aperture is $n = 1/w$. After j round trips, the overlapping area fraction with the original aperture is,

$$f(j) = \frac{2}{\pi}\left[\sin^{-1}\sqrt{1-(jw)^2} - jw\sqrt{1-(jw)^2}\right]. \tag{3.49}$$

The amplitudes of each interfering beam is weighted by a factor of $\sqrt{f(j)}$. The transmission series then becomes [72]:

$$T_{\mathrm{FPI}}(\theta_t, \lambda) = T^2\left|\sum_{j=0}^{n} R^n e^{in\delta}\sqrt{f(n)}\right|^2. \tag{3.50}$$

3.2.4 FPI Design

I initially designed two Fabry-Pérot etalons in collaboration with Cardiff University and the Netherlands Institute for Space Research (SRON) for use in the instrument described in this thesis. The first approach was a hybrid etalon of reflective metal meshes and a low-loss, high refractive index silicon substrate, with an airgap between the mesh and substrate. This device was built by Prof. Peter Ade in Cardiff University, and was expected to be the more reliable of the two constructed etalons, based on space-flight heritage in ISO SWS/LWS.

The other approach used a fully silicon etalon, where the substrate remained a high refractive index slab of silicon, and the reflectors were comprised of thin silicon wafers with an airgap between the wafer and substrate to create a high reflectance for

the desired wavelengths. The fully silicon etalon was built by SRON, based on deep reactive-ion etching and an experimental silicon bonding technique.

While in theory both approaches were shown to yield a viable etalon, reliably controlling the air gap between the metal mesh reflectors and the silicon substrate proved challenging at low temperatures, due to differential thermal contraction between the etalon components. At the same time, there were rapid successes in the development of the fully silicon etalon. Approximately one year into the design of the etalon, the decision was made to adopt the fully silicon etalon solution.

3.3 FPI Operation

From the above analysis, when observing a broadband source, the etalon effectively transmits a set of wavelengths, which are integer multiples of each other, limiting its usability as a standalone spectroscopic device.

In order to use the etalon as an interferometer, some method of scanning the etalon transmission over a variable set of wavelengths must be incorporated. In other words, the cavity resonances must be changed to allow different wavelength sets through, and the resonant wavelengths must be separable (i.e. order-sorted) by other filters or spectroscopic devices, such as a diffraction grating [76], or an etalon with a lower order of interference placed in series [72]. If the etalon resonances can be scanned through a full FSR, and the transmitted orders are separated, a continuous spectrum can be obtained.

There are many different experimental arrangements which allow the cavity resonances to be changed. However for all methods, the reflective plates must maintain parallelism throughout the measurement. The primary methods may be condensed into three basic arrangements. In the first, a fixed etalon is presented with a diverging beam, and an array of detectors is fixed at the output such that each detector will see a slightly different optical thickness of the etalon based on the change in transmitted

beam angle. The second method is similar, but requires mechanical scanning of an aperture over the fringe plane and subsequent imaging onto a single detector. When used in these forms, the instrument is known as an Imaging Fabry-Pérot [77].

The third method involves isolation of the central order onto a single detector, and varying the cavity size of the etalon. Generally, the etalon is presented with a parallel beam, and re-imaging optics focus the central order onto a detector at the image plane. When used in this form, the instrument is known as a Scanning Fabry-Pérot [77].

The scanning method involves a variation in the refractive index μ or the physical gap d. Variation in μ can be accomplished by exploiting the temperature-dependence of μ in the etalon substrate, or by varying the density if the substrate is a gas. However, it is difficult to allow a consistent variation across the entire etalon using these methods, and a departure of parallelism between the plates degrades the effective finesse of the instrument. Variation in d requires accurate mechanical displacement of one of the reflective plates with respect to the other while simultaneously maintaining parallelism. While this method typically requires three actuators and sensors to maintain parallelism, it is historically the preferred method of scanning the FPI [78], since the resonant wavelengths vary linearly with respect to the plate separation.

Finally, there is another method of scanning the etalon which is investigated in this thesis. The etalon may be presented with a parallel beam, and the etalon orientation may be tilted with respect to the beam axis, varying θ_t in Equation (3.1). In tilting the parallel beam orientation with respect to the etalon, the effective cavity size can be changed, in a method that is a hybrid of the scanning and imaging approaches to Fabry-Pérot interferometry. In this case, the parallel rays may be reimaged onto a single detector, and the resonant wavelengths are dependent on the transmitted beam angle within the etalon. In doing so, the resonant wavelengths vary as $\cos\theta_t$.

The principal advantage of the approach presented in this thesis is that it leads to a simple scanning mechanism based on a single rotary drive and flex-pivot bearing.

Instead of requiring three drives to act in unison to scan the etalon gap and maintain parallelism across the required range, a single drive changes the incident beam angle on a fixed gap etalon. Historically, this method of scanning has been avoided because of *walk-off* effects which change the fundamental transmission properties of the FPI for high angles of incidence by a difference in the number of effective interfering beams. As such, this technique is limited to a small variation in the angle of incidence. However, we have shown for the first time that this method can achieve spectral resolving powers on the order of 10^4 for THz frequencies, which make them suitable for a SAFARI-like instrument. A schematic of the scanning mechanism design is show in Figure 3.7. The output as a function of incident angle is shown in the following section.

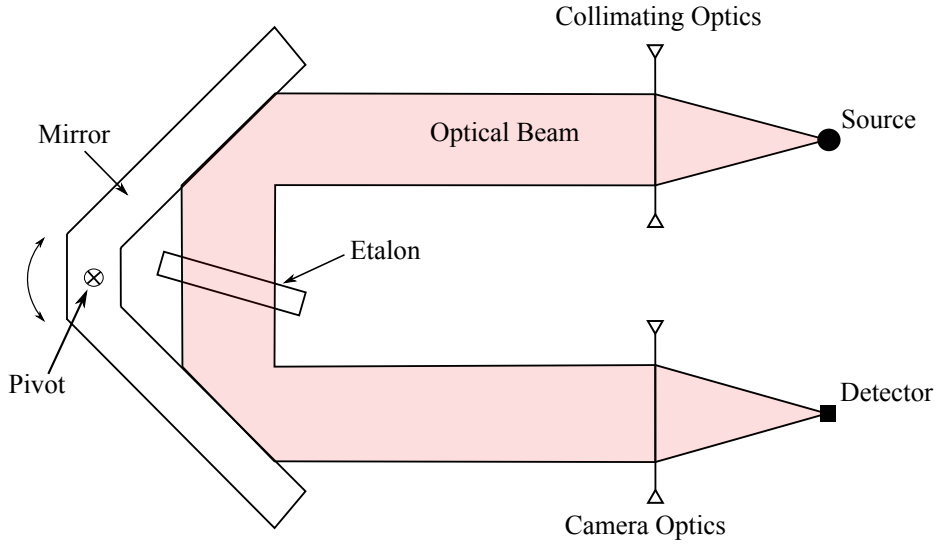

Figure 3.7: Schematic of the mechanism which tilts the collimated beam angle with respect to the etalon.

3.4 Angle Scanning Simulations

Since tuning the resonant wavelength by scanning the angle of incidence results in a non-linear transmission curve, it becomes necessary to model the effects of a changing incident angle to include the effects of *walk-off* and angle-dependent reflectivity on the line profile. Figure 3.8 shows the transmission profile as a function of transmitted

angle through an etalon, ignoring aperture and varying angle-dependent reflectivity effects. It can be seen that the spacing between orders decreases as angle increases.

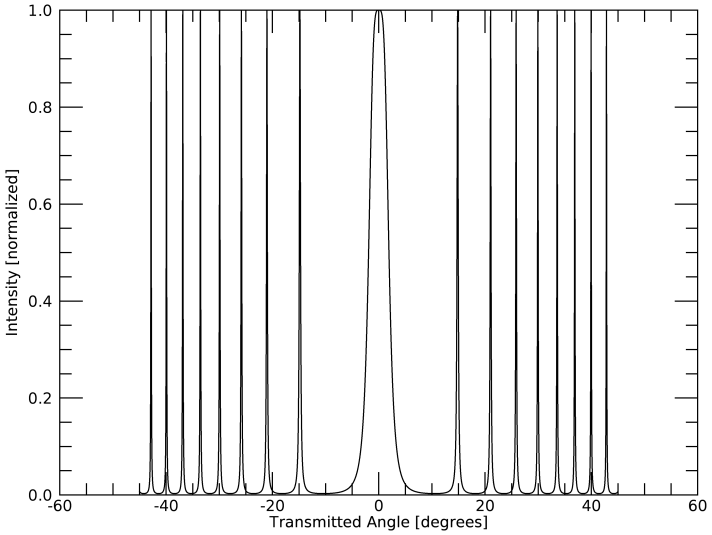

Figure 3.8: Variation in the transmission function of an etalon with transmitted angle.

The variation in order spacing introduces an important consideration, which is the required angular range (angular throw) for a given initial angular offset. Angular throw is the angle that the device must sweep in order to cover the full free spectral range. Figure 3.9 shows the effect that changing the initial offset angle has on the required angular throw, which was determined using the expression:

$$\Delta\theta = \sin^{-1}\left[\frac{\mu\lambda}{4d\sin\theta_0}\right], \qquad \text{[rad]} \quad (3.51)$$

where θ_0 is the initial offset angle, and $\Delta\theta$ is the single-sided angular range required. Limitations on the allowed angular range of the etalon determined the initial offset required. In Chapter 6, the selected flexure bearings gave an allowed angular range of $\pm 7.5°$. Although the eventual pendulum design effectively doubled this angular range, the offset angle constraint was left at $\pm 7.5°$ in order to increase the lifetime of the bearings, allow for a different etalon rotating design, and extend the range to

longer wavelengths if required. The selected initial offset angle was 15°.

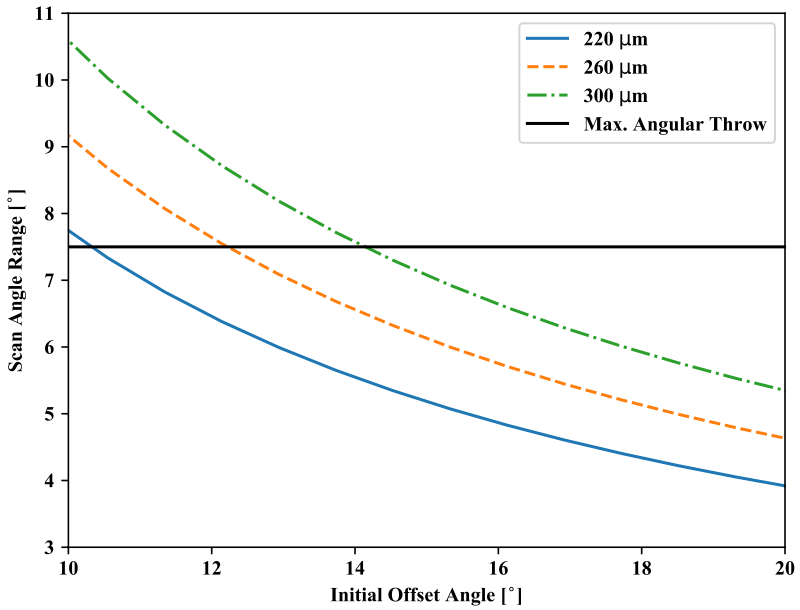

Figure 3.9: Angular throw for different initial offset angles across the waveband.

3.4.1 Reflectivity Simulations

Based on the derivations in Section 3.2.1, the theoretical optical properties of a dielectric etalon were simulated. Simulations were completed first for the complete etalon structure, which consisted of a H/L/H/H/L/H refractive index stack, where H represents a layer of high refractive index substrate and L represents an airgap. However, these simulations assumed an etalon of infinite diameter, so that *walk-off* did not contribute to the total transmission and reflection. In order to simulate a dielectric etalon with *walk-off*, simulations of the reflectivity of both etalon faces were performed independently, which could be included in the geometric etalon simulations including *walk-off*. These simulations were based largely on the work of Carolien Feenstra, an intern who assisted in the development of the silicon etalon at SRON.

For simulations of the complete etalon, not including *walk-off*, the etalon was modelled as a symmetric five layer dielectric stack within a vacuum. The outer layer

of each face consisted of a high-resistivity silicon membrane. The next layer inwards on each side was an airgap (vacuum in the simulations). Finally, the center was a high-resistivity silicon slab. The silicon slab was designed to be near 8 mm in thickness, and the refractive index was initially modelled using its room temperature value of 3.42. The thickness of the membrane and airgap were parameters in Feenstra's models to achieve the required spectral resolving power in the design wavelength range, which resulted in an optimum membrane thickness of 52 µm and an airgap of 60 µm. The simulated transmission profiles for selected wavelengths with the design range and for incident angles varying from 0° to 25° are shown in Figure 3.10. Both TE and TM modes were simulated.

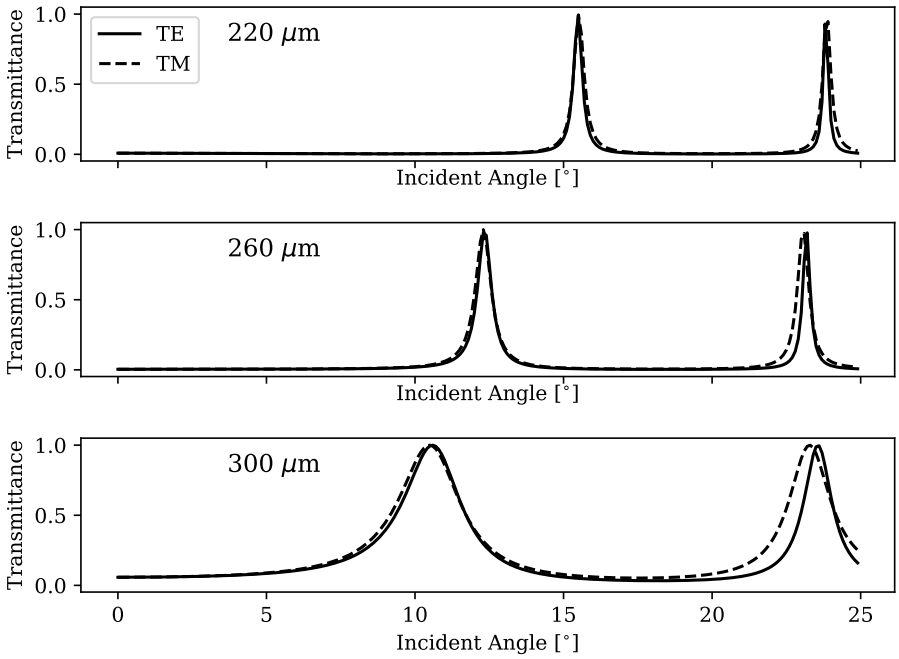

Figure 3.10: Transmission profiles for three monochromatic sources, showing both the TE and TM transmission modes. The effects of *walk-off* are not included in these models.

Simulations of the membrane-airgap dielectric mirror reflectivity were completed for the same conditions and geometry, which produced reflection and transmission coefficients that could be applied to the classical FPI expressions. The dielectric

mirror models were completed for two cases: one in which the incident medium was a vacuum and the output medium was silicon, which represented the front surface of the etalon; and one in which the incident medium was silicon and the output medium was a vacuum, representing the back surface of the etalon. Note that the resulting coefficients were complex, representing shifts in phase which occurred at these boundaries. The vacuum-to-silicon case is shown in Figure 3.11, and the silicon-to-vacuum case is shown in Figure 3.12.

3.4.2 *Walk-off* Simulations

Without taking the overlapping area of the incrementing interfering beams into account, Figure 3.13 shows the effect on the shape of the transmission line profile as the number of effective interfering beams decreases with increasing angle, following determination of n round trips in Section 3.2.3. The figure shows the progression of modelling methods, beginning with a reflectivity which was constant for all angles, adding in the angle-dependent reflectivity and transmissivity coefficients, and finally, including the fractional area overlap.

The effects of varying beam overlap during *walk-off* are illustrated in the following figures. The illustrations in Figure 3.14 show how, for a given angle of incidence θ_i, the number of interfering beams changes as a function of the initial position of incident beam on the etalon. Those beams initially incident on the lower portions of the etalon undergo more reflections than those initially incident on the upper portions of the etalon. The resultant transmitted intensity is the sum of all of these contributions weighted by the area of the chord of each set of incident beams.

The chord approach mentioned above is an approximation which breaks down at the edges of a circular aperture, but remains useful in explaining the concept of *walk-off*. In our simulations, the chord method for calculating *walk-off* has been replaced by a grid method. Here, the aperture is divided into a square grid and the *walk-off*

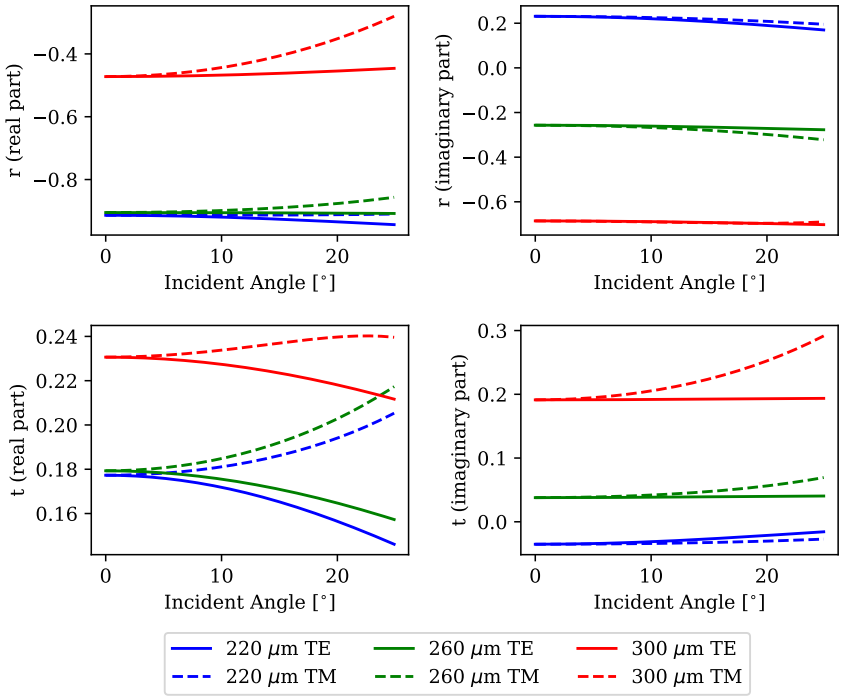

Figure 3.11: Simulations of the complex reflectivity and transmissivity coefficients for select wavelengths and incident angles. These figures show the coefficients for an air-to-silicon interface.

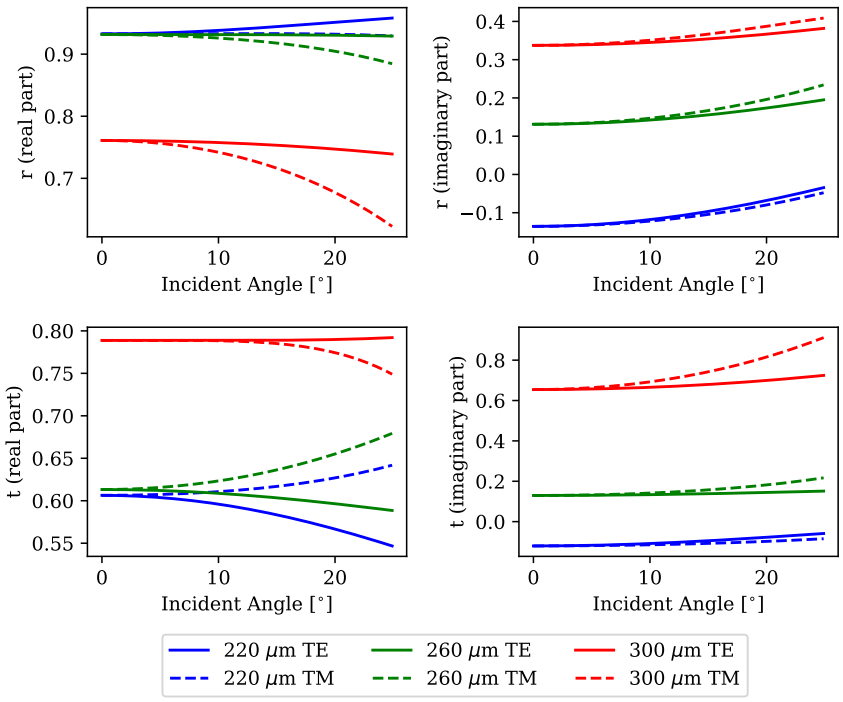

Figure 3.12: Simulations of the complex reflectivity and transmissivity coefficients for select wavelengths and incident angles. These figures show the coefficients for a silicon-to-air interface.

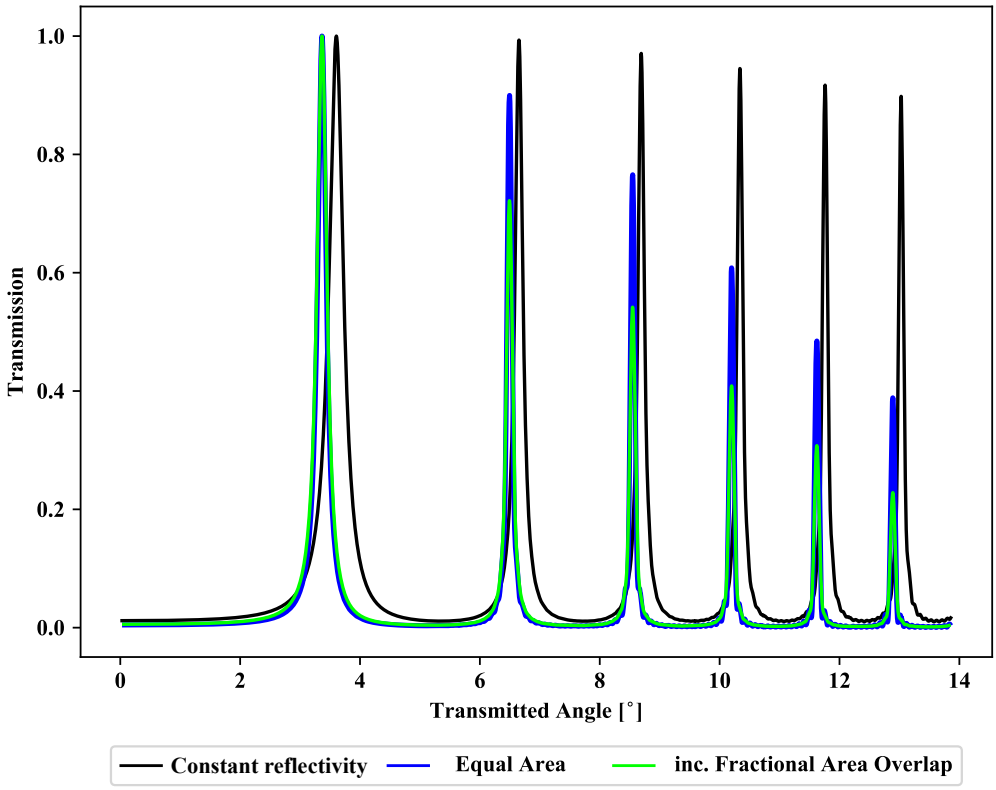

Figure 3.13: Simulation of the transmission profile for the etalon, including the angle and wavelength dependence of a dielectric mirror on both etalon surfaces as well as the effect of a finite etalon with a changing overlap area. This plot only considers the TE linear polarization state.

is calculated for each segment. Since the *walk-off* is directly related to the number of interfering beams, all that is required is to calculate the number of interfering beams for a ray incident on a particular square of the grid. The overall transmitted intensity is then found by the sum of all of the contributing grids. The plots in Figure 3.15 show how the length of the interference path and the number of interfering beams change across the etalon aperture for an angular tilt of 12° and a wavelength of 280 µm.

3.5 Experimental Design

As part of the work presented in this thesis, I have designed, fabricated, and tested an instrument based on the angle-scanned FPI concept which was outlined in this chapter. The design wavelength was chosen to be near the SAFARI VLW band

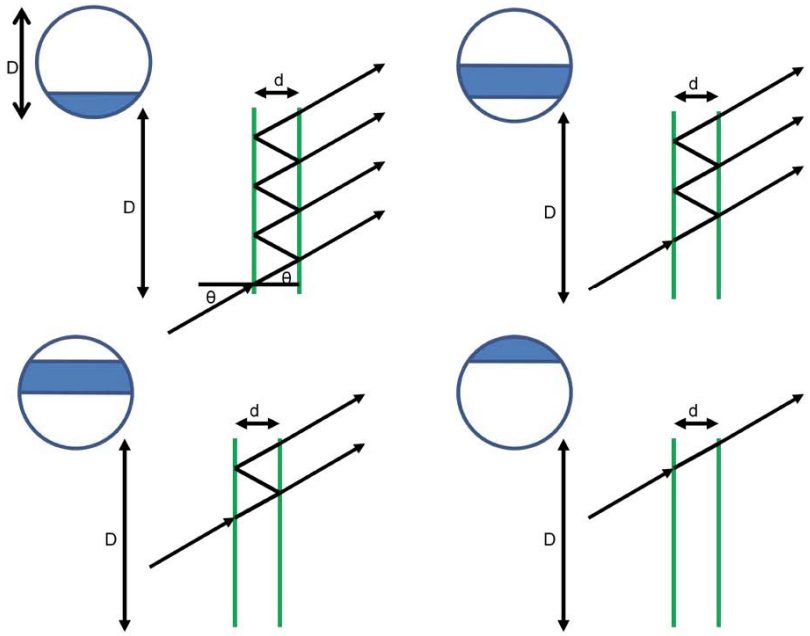

Figure 3.14: A simple diagram depicting the number of reflections a ray entering the etalon experiences depending on the incident location.

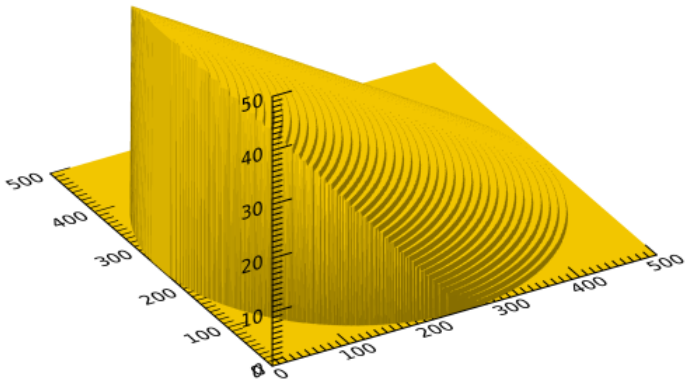

Figure 3.15: Simulated multiple beam interference across etalon surface for an incident angle of 12°. This figures shows the number of passes through the etalon for each segment across the etalon aperture before exiting.

in order to demonstrate the feasibility for the use of an angle-scanned FPI for THz astronomical spectroscopy. In the following chapters, I discuss the additional optics to separate the transmission orders of the FP, review the choice of calibration sources, and describe the novel fabrication technique invented by collaborators at SRON for a silicon substrate etalon with dielectric stacked reflective coatings fabricated through deep reactive-ion etching (DRIE).

The silicon etalon was designed to transmit wavelengths near the SAFARI band in order to demonstrate its feasibility as a potential high-resolution spectrometer for the SAFARI instrument. While a post-dispersed Martin-Puplett interferometer has been adopted for SAFARI, the etalon is still being considered as a potential in-flight calibration source for the instrument, by transmitting a narrow band of frequencies which can be interpreted by the flight instrument [79]. Since the instrument was designed to be only SAFARI-like, the exact wavelength range was determined by the availability of existing calibration sources.

In order to avoid the effect of beam divergence in the FPI etalon, a collimated beam from the source is incident on the etalon so that the transmission may be described with a single incident angle [80]. Beyond the etalon, the transmitted orders are dispersed using a custom diffraction grating spectrometer that I designed and built, which is described further in Chapter 5. The spatial dispersion from the grating requires both an entrance and exit slit in order to contain the angular size of the source as well as limit the spectral bandpass on the detector. A linear representation of the required optical elements of the system is shown in Figure 3.16.

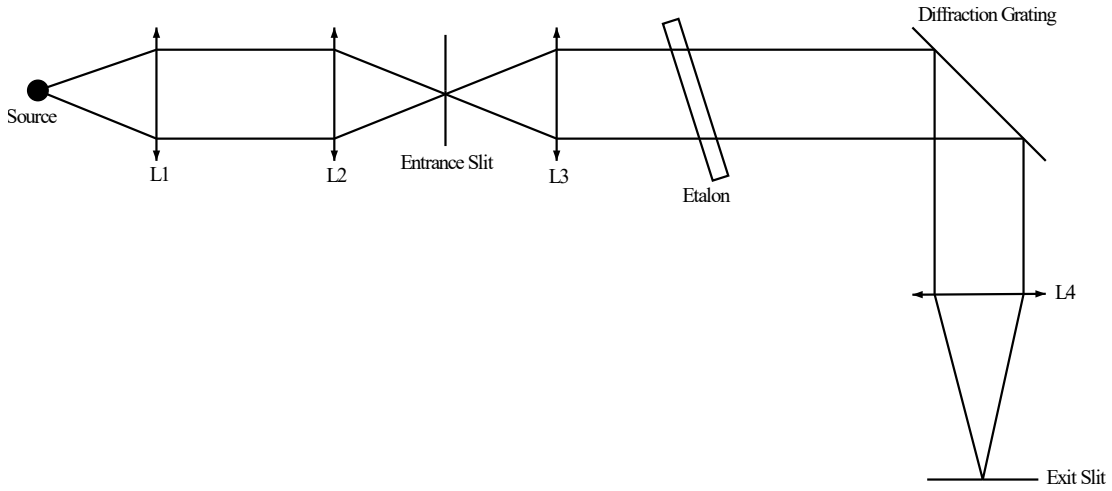

Figure 3.16: Linear schematic of the FPI system

3.6 Thesis Overview

In Chapter 4, I discuss a number of potential sources including a conventional terahertz photomixer – designed and developed by a past member of the Astronomical Instrumentation Group (AIG) research group [81] – with an extended range to higher frequencies, an HCl/DCl gas cell which shows a "double-doublet" of rotational transition lines near the SAFARI band, and the ever-present atmospheric water vapour lines near the SAFARI band. Since manufacturing tolerances become less important with increasing wavelength, longer wavelengths were preferred. The final wavelength range of the testbed FPI was 220 µm to 300 µm.

In order to utilize state-of-the-art detectors, achieve the sensitivity requirements for using these calibration sources, and mimic a space-like environment (i.e. high vacuum, low temperature and vibrational environment similar to Herschel), the optics and detector were cooled to 4 K and 300 mK, respectively. The FPI instrument was designed to fit on the 4 K optical bench in a pre-existing TFC [82]. The detector used was a composite Ge:Ga semiconducting bolometer [83], which required a ^{3}He-^{4}He adsorption cooler with a base temperature of 280 mK [84]. It should be noted that the theory presented in this chapter is compatible with a room temperature device. For low temperature operation, the temperature dependence of the etalon dimensions, refractive index, and reflectivity must be considered.

In Chapter 5, the post-dispersion element – the grating spectrometer – is discussed. This involves a post-dispersive technique which is used to spatially separate FPI orders to avoid spectral confusion. The selected element, was a custom-made reflective grating monochromator, with a bandpass of less than one order of the FPI.

In Chapter 6, the instrument is designed, assembled, and tested. A brief summary of the etalon development process is presented. The temperature dependent results and etalon parameters are modelled in the instrument results given in Chapter 7. Results on the line profile and spectral resolving power of both the grating and the

etalon/grating combination are presented, and are compared to the requirements for a SAFARI-like instrument.

Finally, Chapter 8 addresses the lessons learned in the design and initial measurements of the cryogenic FPI/grating instrument. Areas in which the instrument could be improved are identified, and future plans to implement these changes are detailed.

Chapter 4

Calibration Sources

> Accurate and minute measurement seems to the non-scientific imagination, a less lofty and dignified work than looking for something new. But nearly all the grandest discoveries of science have been but the rewards of accurate measurement and patient long-continued labour in the minute sifting of numerical results.
>
> Baron William Thomson Kelvin

4.1 Introduction

Any spectroscopic system requires stable and well-defined calibration targets in order to measure its performance. Wavelength calibration of the FPI/grating requires a device which produces narrow-line THz emission, in order to measure both the wavelength of peak transmission and the ILS at each instrument setting. However, the generation of THz radiation is challenging. One of the challenges with developing THz spectrometers is the lack of stable, cost-effective line sources at these frequencies. Narrow-band emission cannot be produced in the THz by conventional semiconductor lasers, since no materials with suitable band gaps exist. quantum cascade lasers (QCLs) can generate frequencies above 1 THz but require low operating temperatures (40 K). Molecular lasers are able to use the vibrational states of molecular gases to give rise to THz emission, but are complex and expensive to operate, and only produce output at discrete wavelengths [85]. Voltage controlled oscillators (VCOs) in conjunction with frequency multipliers can reach the 100 GHz domain [86]. However,

it is inefficient and expensive to extend their output further into the THz.

Fortunately, an efficient and cost effective way to generate THz is through a THz photomixer. These devices are able to generate tunable, narrow-band emission using commercially available components. A photomixer mixes two telecom NIR lasers and emits electromagnetic radiation at the difference frequency. The radiation illuminates a biased semiconductor device which varies in conductance with illuminated power. The resultant photocurrent which is produced by the semiconductor is coupled to an antenna which is the source for THz generation. A photomixer has been developed and characterized by a previous graduate student in the AIG [81], which has been modified to operate near the long wavelength limit of SAFARI. The operation principle of the photomixer is described in Section 4.2.

Gas lines measured in absorption or emission can also be used to produce well defined spectra, resulting in spectral features at specific wavelengths and with well characterized line shapes. There are many simple molecules which contain rotational spectral features in the THz band, which is precisely why astronomers use this band to probe molecular clouds. Therefore, a gas cell measured in absorption using one of these molecular gases was a considered calibration target. The chosen component was the diatomic molecule HCl and its natural isotopologues because of a convenient "double-doublet" which falls near the long wavelength end of SAFARI Figure 4.7.

Finally, the atmosphere itself may also be a viable method of spectral calibration for early measurements. The atmosphere contains a variety of molecular gases which produce THz spectral lines, including a series of H_2O lines which fall near the SAFARI band. Therefore, by varying the relative humidity in front of a calibration source, the instrument may be calibrated against the locations of these absorption lines.

Originally, the FPI was designed to coincide with one of the four bands of SAFARI in order to test its feasibility as a SAFARI-like instrument. However, since the architecture of SAFARI was changed to use an MPI, the FPI was no longer constrained

by these bands. Instead, the design of the FPI was set near the SAFARI range and constrained by the availability of calibration line sources.

The calibration sources developed were based on pre-existing devices possessed by the AIG. With some modifications, these techniques could be made viable for the calibration of the SAFARI instrument itself, demonstrating that the lessons learned during the development and testing of these calibration sources will be beneficial beyond the scope of this project.

4.2 THz Photomixer

The first calibration source is a continuous wave (CW) terahertz photomixer [87], based on optical heterodyning between two Fitel NIR DFB lasers [88]. To produce THz radiation, the difference (heterodyne) frequency between the two input lasers is set to be in the THz domain. The lasers are then focused onto a metal-semiconductor-metal interface, causing a variation in the conductivity of the semiconductor material due to the generation of free charge carriers in the semiconductor. With a bias voltage applied to the material, which accelerates charge carriers towards the metal electrodes, a time-dependent photocurrent is produced, which is modulated by the heterodyne frequency of the two lasers. When coupled to an antenna, THz radiation is produced that can be directed using free-space optical components, such as an optical feed-horn or a high resistivity silicon lens. Using this technique, CW THz line sources can be produced with a linewidth on the order of 1 MHz. A schematic showing the configuration of a typical photomixer is shown in Figure 4.1.

4.2.1 Principle of Operation

When two lasers of different frequencies illuminate the photomixer element, the total time-dependent electric field amplitude on the photomixer is the result of the linear sum of the individual electric fields, $E_1(t) + E_2(t)$, where $E_1(t) = E_{01}\cos(2\pi\nu_1 t)$

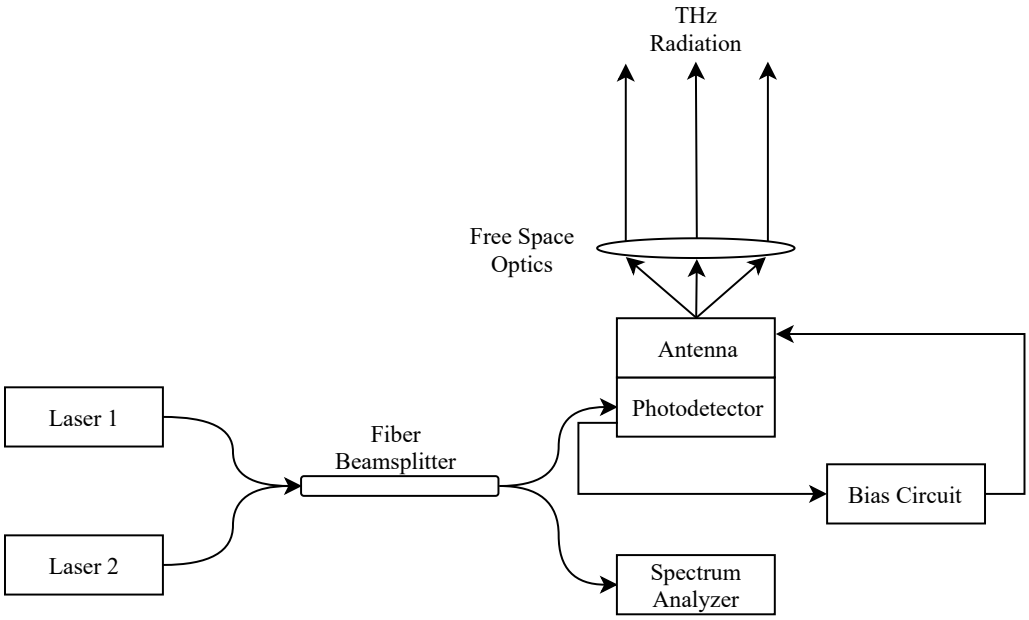

Figure 4.1: Schematic of a typical fiber optic photomixer. By tuning the frequencies of the lasers, THz radiation is produced at the difference frequency. A spectrum analyzer allows for real-time measurement of the frequencies and powers of the lasers.

and $E_2(t) = E_{02}\cos(2\pi\nu_2 t)$. Since the radiant power is related to the electric field by $P \propto |E|^2$, the time-dependent optical power can be expressed as [89],

$$P(\nu, t) = |E_1|^2 + |E_2|^2 + \sqrt{m}E_{01}E_{02}[\cos 2\pi(\nu_2 - \nu_1)t + \cos 2\pi(\nu_2 + \nu_1)t]. \qquad (4.1)$$

Here, $\nu = \nu_2 - \nu_1$, representing the difference frequency between the two lasers, and m is a value between 0 and 1 which represents the degree of overlap between the interfering beams. Perfect overlap is represented by $m = 1$ and no overlap by $m = 0$.

In order for the photomixer to generate THz radiation, the energies $h\nu_1$ and $h\nu_2$ must both be greater than the bandgap of the photoconductive material. Additionally, the difference frequency must correspond to a period which is much longer than the electron-hole recombination time of the photoconductor, and the period resulting from the input frequencies must be much shorter than the recombination time. When these conditions are met, the second term in Equation (4.1) may be ignored, and the effective incident power averaged over shorter time scales than the recombination time

may be expressed as:

$$P(\omega, t) = \langle P_0 \rangle + 2\sqrt{m\langle P_1 P_2 \rangle}\cos\omega t, \tag{4.2}$$

where $P_0 = P_1 + P_2$, $P_i \propto |E_i|^2$, and $\omega = 2\pi(\nu_2 - \nu_1)$.

The photomixing element itself is generally a high efficiency photoconductor or photodiode. The selected material is one with a sufficient bandgap for the individual lasers to generate charge carriers, while also having a low rate of thermally generated charge carriers (or dark current). In general, photodiodes are better suited for high sensitivity and low dark current, and have a faster response which is beneficial for detecting THz frequencies.

The ideal photodiode material for 1550 nm light is the type III-V semiconductor indium gallium arsenide (InGaAs). The typical InGaAs semiconductor composition has a bandgap energy E_g of 0.75 eV, corresponding to an absorption edge at 1660 nm wavelengths [90], which makes this alloy useful for the C-band infrared transmission window, commonly used for fiber optic communication. The C-band includes the wavelength range 1530 nm to 1565 nm [91].

In addition to the material, the detector may also be characterized by its quantum efficiency, sensitivity, and response time. Often times, these parameters are dependent on each other, such that trade-offs must be made to optimize performance of the detector for the specific application. The structure of the photodiode is characteristic of a p-i-n diode, with a p-type semiconductor at one electrode, an n-type material at the other, and an intrinsic layer between them (Figure 4.2). The p- and n-type materials create a built-in potential across the diode, created by an initial exchange of charge carriers between the two doped semiconductor types, which leaves a *depletion region*, and a potential which prevents further motion of charge carriers. The depletion region is an effectively neutral region between the electrodes, giving the photodiode

an intrinsic capacitance C which depends on the width of the depletion region W as:

$$C = \frac{\epsilon A}{W}, \tag{4.3}$$

where ϵ is the permittivity of the material and A is the diode cross-sectional area. The capacitance of the diode affects the speed of response to incident photons, since the time constant τ of the circuit, which is a measure of the transit time of electrons/holes through the p-i-n structure can be expressed as:

$$\tau = RC, \tag{4.4}$$

from which it can be seen that for a given circuit resistance R, the speed of response can be increased by decreasing the capacitance of the detector.

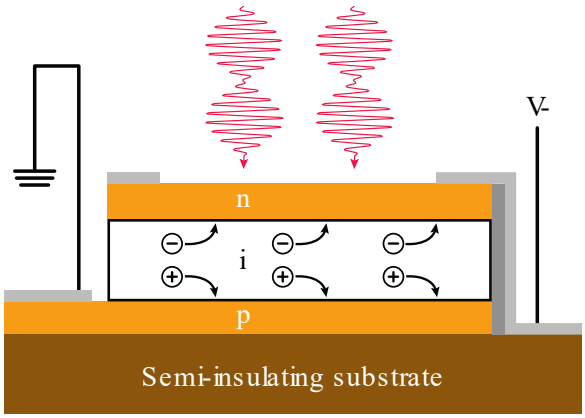

Figure 4.2: The structure of a p-i-n photodiode. When incident radiation is absorbed, electron-hole pairs are produced in the depletion region, which are swept to the electrodes by an applied bias [92].

In addition to a fast response, a high sensitivity is another desirable aspect of a photodetector. A high sensitivity implies that the device is also low noise. In most room temperature photodiode detectors, the dominant noise factor is dark current, which is the flow of charge with no illumination of the device. The three main components of dark current are: diffusion, generation-recombination, and tunnelling. Each

are separate mechanisms which allow current through the diode, though they are not described here, and the reader is referred to [93] for a description of each type.

The sensitivity of a device is also a function of the number of electron-hole pairs created by incident photons. The ratio of the two parameters is a value less than unity (with the exception for *avalanche breakdown* devices), and is labelled the *quantum efficiency*, η, of the detector. In order for a photon to generate an electron-hole pair it must be absorbed by the device, which indicates that η is highly dependent on the absorption coefficient α of the material. In order to minimize reflections, many detectors include an anti-reflective (AR) coating to minimize reflections. With a good anti-reflection (AR) coating, InGaAs photodiodes can achieve quantum efficiencies above 95 % at 1550 nm wavelengths [93].

There are two basic operating conditions in which a photodiode may be used. Photovoltaic mode is when the electrodes of the photodiode are held at zero bias. In this condition, charge carriers generate an additional voltage difference across the depletion region. Since creating this potential difference is essentially a means of storing electrical energy, this is the working principle behind solar cells.

In photoconductive mode, the diode is reverse biased, which widens the depletion region. In this form, charge carriers generated by absorbed photons are swept towards the electrodes, creating a photocurrent. Widening the depletion region has the effect of decreasing the capacitance of the diode, increasing the speed of its response. While a diode operating in reverse bias generates slightly more dark current, in addition to a faster response, the advantage of this operating mode is that the photocurrent is linearly proportional to absorbed photon power. The dark current dependence on bias voltage and the linearity of absorbed power to photocurrent is further detailed in Appendix B.

The photocurrent produced by a diode is directed into an antenna which couples the electric field to free space, producing THz radiation. There are a number of

differing antenna structures (eg. log-spiral, log-periodic, bow-tie, dipole, etc.) [94]. Spiral and periodic antenna have the effect of producing circular polarized light, while bow-tie and dipole antenna produce linear polarized light. In many cases, these antennae are planar structures, such that they may be deposited directly onto the structure containing the mixing element for a compact design.

The photomixer which was utilized was developed by a past graduate student (Dr. Gibion Makiwa) and its features are described in [81]. Some elements of the pre-existing instrument were modified to change the frequency range and to increase the output power, which are further described here. To begin, I review the specifications of the original device as developed by Makiwa.

4.2.2 Original Photomixer

The original photomixer was capable of emitting radiation in the range of 250 GHz to 650 GHz (1200 µm to 462 µm), which unfortunately was too far from the SAFARI long wavelength limit (230 µm) to be able to adequately test the performance of a SAFARI-like FPI. This limitation was due to two factors, namely, the tunable ranges of the two laser diodes, and the frequency response of the photomixer. Figure 4.3 shows the tunable range by the allowable difference frequencies between the two lasers based on their temperature variation. These lasers had a nominal output frequency of 193.00 THz and 193.38 THz respectively at maximum bias current (200 mA) and 25 °C.

Due to the frequency response of the photomixer, the THz power output drops 12 dB/octave in the high frequency limit. The theoretical power output of the original THz photomixer is given in Figure 4.4, showing the THz power output is around 10 pW in the 1 THz (300 µm) range and drops off rapidly following the 12 dB/octave roll-off. The rate of roll-off matches a ν^{-4} dependence of power on frequency, which is consistent with what is expected given that the output power is a function of

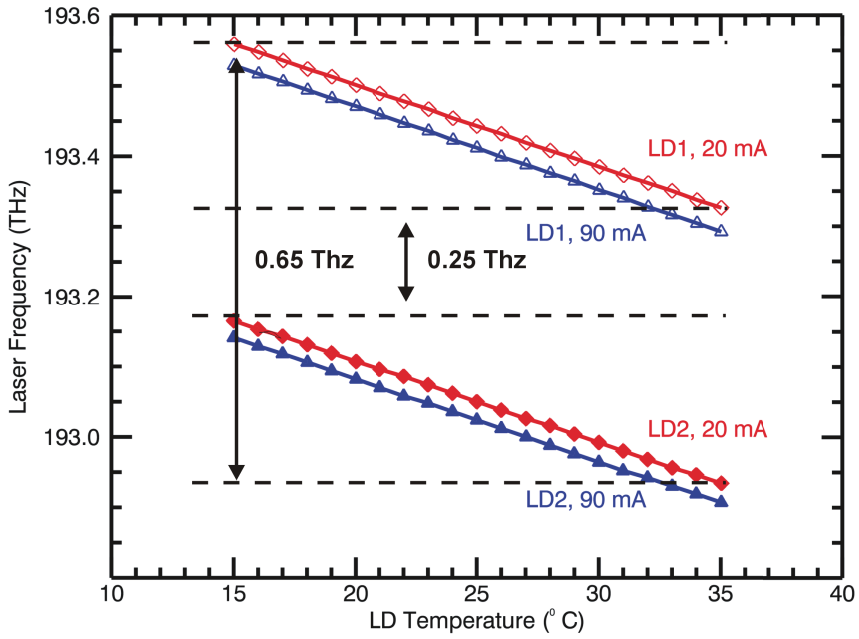

Figure 4.3: The dependence of laser frequency on temperature for the original laser diodes (LD1 and LD2). Red and blue lines on the plot show a driving current of 20 mA and 90 mA respectively [81].

the carrier transit time and RC time constant. Both of these vary as ν^{-2} at high frequencies [89].

The original circuit used to bias the photomixer is based on the Howland Current Pump and can supply bi-directional current [95]. The current limits are 1.0 mA at a maximum voltage of 0.6 V, and −5.0 mA at a minimum voltage of −2.5 V. The limits are monitored by dual limit window comparators which trigger a latched solid state relay in the case of an overstress, shorting the photomixer bias voltage. When in manual operation the current is supplied to the photomixer from the bias box front panel mounted potentiometer which operates on two 6 V/1 A batteries. While the original bias circuit was reliable, the parameters were matched to the requirements of the original photomixing element.

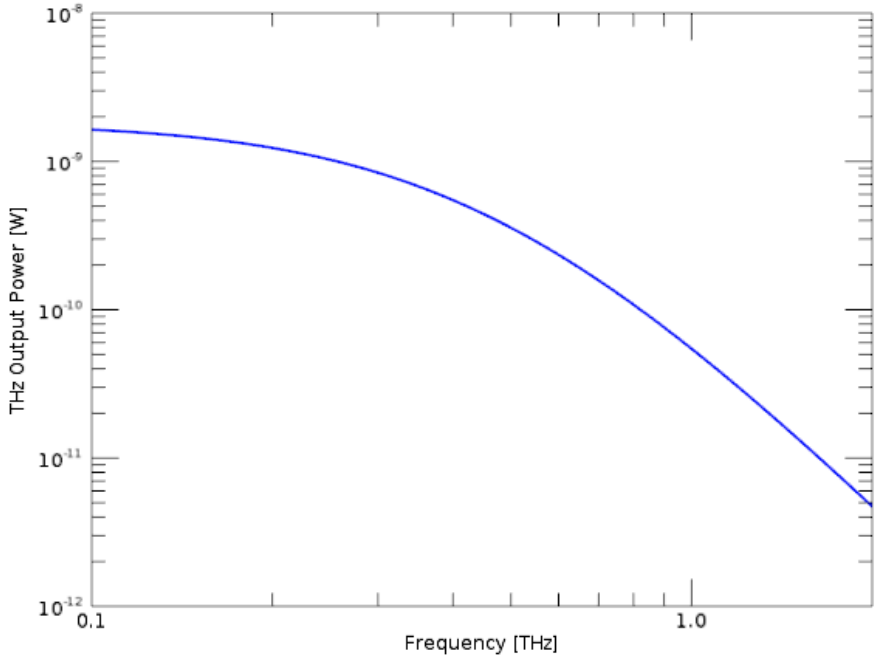

Figure 4.4: The variation of THz output power with frequency for a LT-GaAs photomixer. In the high frequency limit, the THz power drops at 12 dB/octave [81].

4.2.3 Photomixer Upgrades

Since the photomixer design had to be upgraded to change the allowable wavelength range closer to the SAFARI VLW band, I designed an upgraded version of the photomixer, and procured a new laser, photomixing element, and bias circuit.

The original paired lasers gave a minimum output wavelength of 460 µm, far from the desired upper wavelength limit for the FPI, which was 300 µm (1 THz). To extend the range of the photomixer to the desired wavelength band, the first requirement was to obtain a new laser to change the allowable output wavelength range. Based on the previous DFB lasers which exhibit a 0.012 THz/°C frequency shift, the new laser was selected to be used with either of the original lasers to extend the range to 0.9 THz to 1.7 THz. The new laser had a nominal 25 °C frequency of 194.50 THz, which in combination with the 193.00 THz laser produces a range of 1.26 THz to 1.74 THz when temperature is restricted to the range 15 °C to 35 °C for both lasers. Likewise, when combined with the 193.38 THz laser, the output range is 0.88 THz to 1.36 THz

(Figure 4.5)

Since the output power of the photomixer drops 12 dB/octave in the high frequency limit, the estimated output power of the photomixer in the 1 THz to 1.5 THz range would have been <0.1 pW. To shift the range of the photomixer to higher frequencies, a new mixing/emitting element was procured and a new bias circuit was created.

The new photomixer was purchased from TOPTICA Photonics [92], with an InGaAs photodiode for efficient and fast response to 1550 nm photons. The structure of the chip is a bow-tie antenna which also serves as the photodiode electrodes. At the center of the bow-tie the electrode structures are in the form of interdigitated thin structures. This electrode structure facilitates fast response because of the closeness of the electrodes, and high efficiency (absorption) because of the large area of the absorbing region between the electrodes. The bow-tie antenna, ensures that the output is linearly polarized, which allows the polarization state to be matched to the highest efficiency orientation for the diffraction grating. In addition, the bow-tie allows for consistent output power over a wide frequency band.

4.2.4 Photomixer Automation

Since many of the calibration procedures for the FPI involving the photomixer required a scan of the instrument through a set of photomixer settings, the calibration process could take many hours. A system to automate the photomixer frequency selection was necessary.

The output frequency for each DFB laser was first characterized as a function of both temperature and bias current using an EXFO Optical Spectrum Analyzer (WA-1500) to record the output frequency and an ILX 4-Channel Laser Diode Controller (LDC-3900) to set the temperature and bias current for each laser. To determine the output frequency for an arbitrary bias current and temperature, the temperature-dependence was fit with a first order polynomial at each current setting, and the

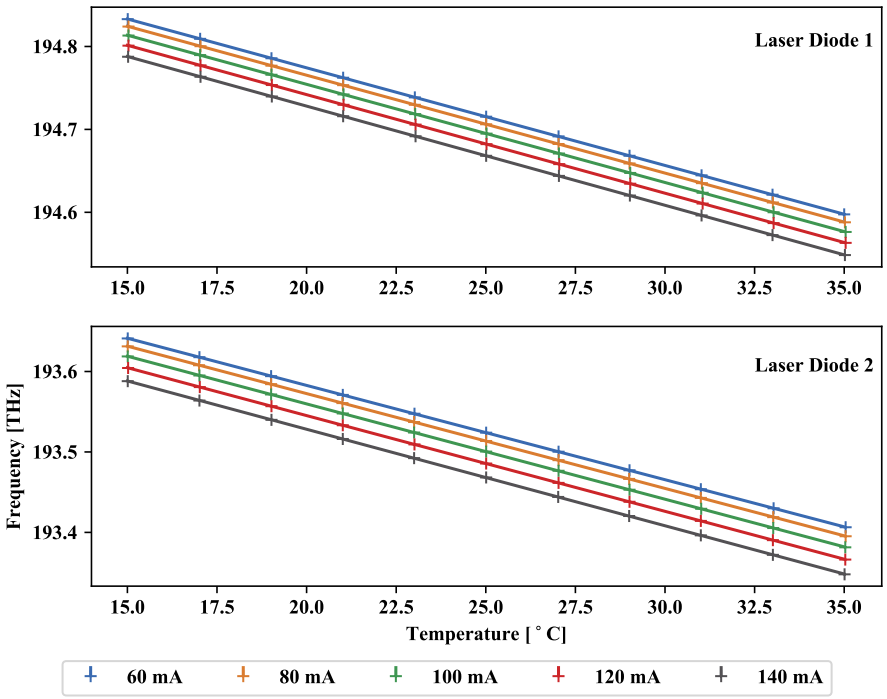

Figure 4.5: The variation in input laser frequency with temperature.

current-dependence was fit with a second order polynomial at each temperature setting. The results are shown in Figure 4.5 and Figure 4.6. The set of curves defined by these fits produced a 2D surface where the laser frequency could be determined for any point on the surface. Using the surface curves to generate a grid of points which defined the surface, 2D cubic interpolation was used to provide an output frequency for any set of temperature and current. The boundaries of this surface were set to be within the operating limits of the lasers, and were defined to be 15 °C to 35 °C in temperature, and 40 mA to 180 mA in laser bias.

When selecting a photomixer frequency, the user is required only to input the desired THz frequency and an automated procedure selects the temperatures and currents for each laser. Since there are infinitely many combinations of laser frequencies to output the desired difference frequency, the algorithm contains preferred settings that are kept as defaults. First, since only the low frequency end of the photomixer was used, the default setting was to hold the 193.38 THz laser (LD2)

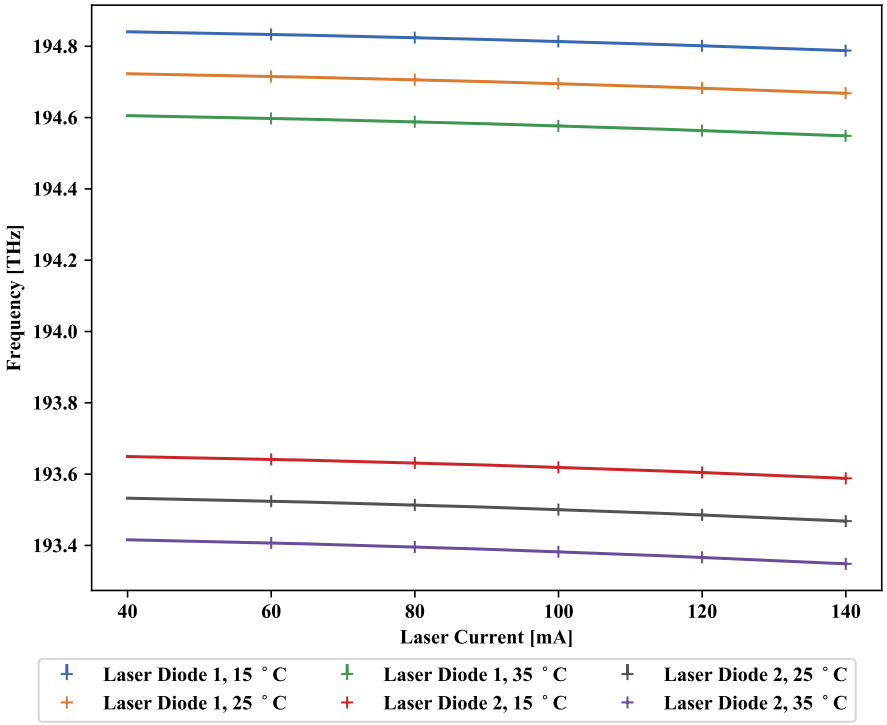

Figure 4.6: The variation in input laser frequency with power.

at 15 °C. Additionally, if no current inputs were specified, the automation was designed to maintain the laser bias currents at 77 mA for the 193.38 THz laser (LD2) and 100 mA for the 194.50 THz laser (LD1). These settings generated approximately the same output power for each laser over the temperature range, which maximized fringe visibility of the resulting interferogram, maximizing the output power of the photomixer. If further fine-tuning of the laser frequencies was required to generate the desired output, the bias current of the 193.38 THz laser (LD2) was varied by up to 1 mA.

The photomixer calibration process was completed in Python 3, which allowed the 2D interpolation Python object structure to be serialized and implemented directly into the photomixer frequency selection software for the complete instrument (also written in Python 3) during instrument calibration.

4.3 HCl/DCl Gas Cell

The second proposed calibration source is based upon the rotational transitions of the diatomic molecule HCl and its isotopologues in a short path length ($\sim$1 cm) gas cell containing a 1 : 2 parts mixture of the diatomic molecules HCl and DCl.

4.3.1 Rotational Transitions

The HCl molecule has rotational transitions which produces spectral lines in the THz region. The rotational energy levels may be described by the quantum mechanical linear rigid rotor model [93]. The term rigid indicates that vibration of the molecular bond is not considered, as the bond is assumed to be both inflexible and massless. The moment of inertia of the rigid rotating system rotating about its center of mass is:

$$I = \sum_i m_i r_i^2 \qquad [\mathrm{kg\,m^2}] \quad (4.5)$$

where m_i is the mass of an individual atom, and r_i is the distance of that atom from the center of mass of the system. For a two-body system, this reduces to:

$$I = \mu R^2 \qquad [\mathrm{kg\,m^2}] \quad (4.6)$$

where R is the separation between atoms and μ is the reduced mass of the system, defined as:

$$\mu = \frac{m_1 m_2}{m_1 + m_2}, \qquad [\mathrm{kg}] \quad (4.7)$$

where m_1 and m_2 are the masses of the H and Cl atoms respectively. Solutions to the Schrodinger wave equation with zero potential are satisfied by spherical harmonics, and the allowed energy states satisfy [96]:

$$E_r = \frac{\hbar^2}{2\mu R^2} J(J+1). \qquad [\mathrm{J}] \quad (4.8)$$

The rotational angular momentum quantum number J takes integer values $J = 0, 1, 2, ...$ In the rigid rotating case, R is a constant R_0, and the moment of inertia for zero vibration can be expressed as $I_0 = \mu R_0^2$. The energy levels are written as:

$$E_r = B_0 J(J+1), \quad \text{[J]} \quad (4.9)$$

where:

$$B_0 = \frac{\hbar^2}{2I_0} \quad \text{[J]} \quad (4.10)$$

and is known as the rotational constant of the system.

For diatomic molecules in Σ-symmetry electronic states, the dipole-allowed transitions obey the selection rule:

$$\Delta J = \pm 1. \quad (4.11)$$

The energy of the rotational transition $J = J' \rightarrow J''$ is:

$$\Delta E = B_0[J'(J'+1) - J''(J''+1)] \quad \text{[J]} \quad (4.12)$$

and since the selection rule gives $J' = J'' + 1$,

$$\Delta E = 2B_0 J'. \quad \text{[J]} \quad (4.13)$$

4.3.2 HCl Isotopologues

In the case of substitution of either H or ^{35}Cl atoms with another isotope, such as D or ^{37}Cl, the changes to the rotational energy levels are due to the effects on the reduced mass of the molecule. Replacing H with D effectively doubles the reduced mass, which doubles the moment of inertia and correspondingly halves the rotational constant B_0 which halves the energy level separation. Hence, we would expect to see the $J = J' \rightarrow J' - 1$ transition of HCl fall near to the $J = 2J' \rightarrow 2J' - 1$ transition of

DCl. Alternatively, replacing ^{35}Cl with ^{37}Cl changes the reduced mass by ∼0.15 % for HCl and 0.3 % for DCl, which leads to a minor change in the energy level separation. Consequently, the spectral lines for these isotopologues fall close together.

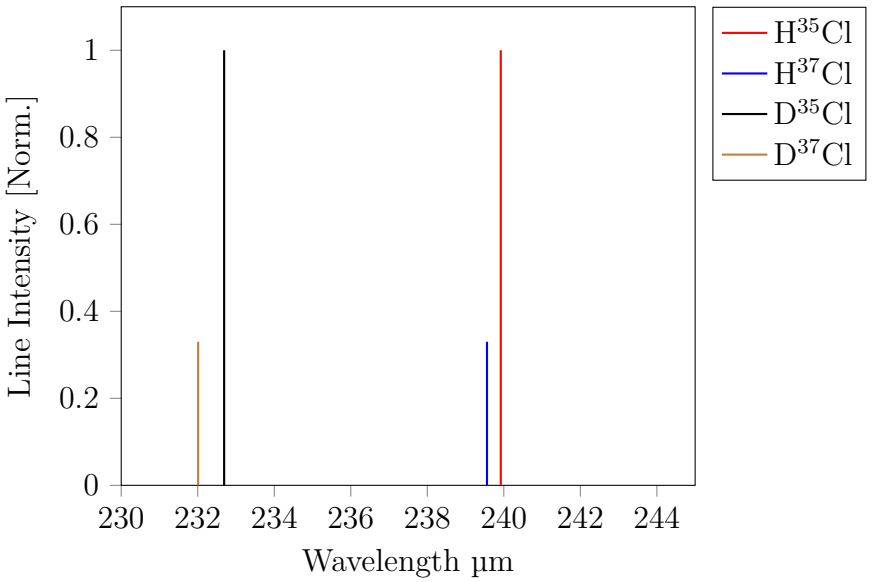

Figure 4.7: Theoretical wavelength positions of line transitions for HCl and DCl at equal pressures. The transition numbers are labelled in Table 4.1 and Table 4.2.

The wavelengths of the $J = 2 - 1$ transition of H^{35}Cl and the $J = 4 - 3$ transition of D^{35}Cl lie close to one another at 239.92 µm and 232.69 µm respectively (Figure 4.7). While these transitions fall just beyond the longest wavelength band of the proposed SAFARI instrument, they provide a simple means of validating the wavelength and intensity calibration of the FPI. Moreover, the separation of the isotopic lines of H^{35}Cl and H^{37}Cl requires a resolving power of $R \sim 700$ (Table 4.1), and the D^{35}Cl and D^{37}Cl lines can be separated with a resolving power of $R \sim 350$ (Table 4.2). A SAFARI-like instrument can barely resolve the DCl doublet with the grating alone, while the HCl doublet can only be resolved by the FPI, bringing an added level of realism to interpreting the spectra. The potential of using this calibration source extended the lower design limit on the wavelength band of the FPI to 220 µm.

Table 4.1: HCl line centers for molecular rotations which fall near the SAFARI VLW band, and the resolving power R required to separate the two lines.

Transition	**$H^{35}Cl$** [µm]	**$H^{37}Cl$** [µm]	**R**
$J = 2 \rightarrow 1$	239.92	239.56	666
$J = 3 \rightarrow 2$	160.02	159.78	666

Table 4.2: DCl line centers for molecular rotations which fall near the SAFARI VLW band, and the resolving power R required to separate the two lines.

Transition	**$D^{35}Cl$** [µm]	**$D^{37}Cl$** [µm]	**R**
$J = 4 \rightarrow 3$	232.69	232.01	341
$J = 5 \rightarrow 4$	186.24	185.69	342
$J = 6 \rightarrow 5$	155.28	154.83	342

4.4 Atmospheric Water Vapour

The final calibration target was proposed not as a rigorous determination of the frequency response of the instrument, but more as an interesting by-product of the large wavelength range of the proposed FPI. The range of the FPI and grating passes through a number of atmospheric windows. The edges of these windows are defined by the location of atmospheric water absorption lines. Since H_2O is a more complex molecule than HCl, the rotational (and vibrational) energy levels are more challenging to predict from first principles, but have been well studied and their transitions tabulated because of their importance to atmospheric studies and remote sensing. Therefore, by varying the relative humidity in front of a calibration source, the instrument may be calibrated against the locations of these lines, since relative humidity is proportional to the density of water vapour. Figure 4.8 shows the atmospheric transmission as a function of wavenumber (cm^{-1}) at 295 K and 1 atm for variations in relative humidity ranging from 5 % to 50 %. The water vapour absorption lines near 33 cm^{-1}, 36.5 cm^{-1}, and 37.2 cm^{-1} are of particular interest since they are seen during instrument calibration using the photomixer.

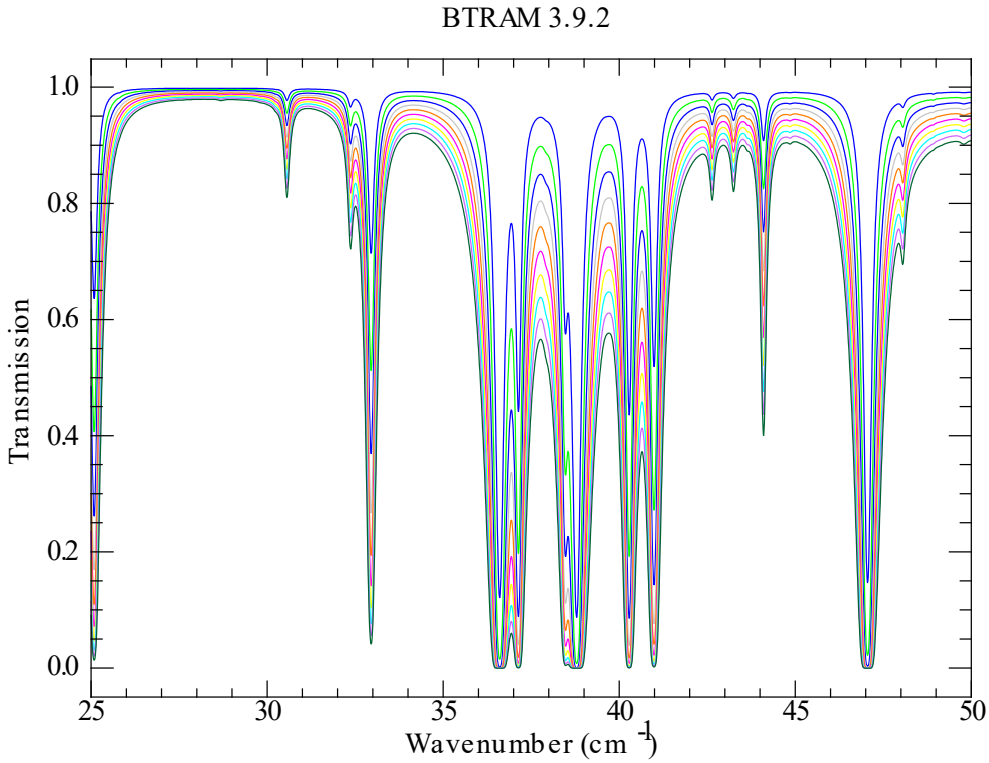

Figure 4.8: Model of atmospheric transmission between 25 cm^{-1} to 50 cm^{-1}. The model was completed in BTRAM version 3.9.2 [97]. The various overlaid plots indicate an increasing relative humidity ranging from 5 % to 50 % in steps of 5 %. The path length is 0.5 m, the temperature is 295 K, and the pressure is 1 atm.

4.5 Conclusions

In this chapter, I have discussed three independent methods for spectral calibration of the FPI. Given its narrow line width and tunability, the photomixer presents the most powerful method of determining the end-to-end spectral response function of the system. Since the FPI was no longer constrained to use the same wavelength range as the SAFARI grating bands, the optimized range was selected to include the photomixer at its longest wavelength settings, where it produced the highest output power, as well as HCl/DCl absorption lines near 230 µm. Therefore, it was decided the FPI operating band would be optimized from 220 µm to 300 µm with added functionality to extend to longer wavelengths if the design constraints allowed.

Chapter 5

Diffraction Grating

> It will reward enough for me if, by the publication of the present experiment, I have directed the attention of investigators to this subject, which still promises much for physical optics and appears to open a new field.
>
> *The Wave Theory, Light and Spectra.*
> Joseph von Fraunhofer

5.1 Motivation

The resonance criteria of the FPI is met by multiple interference orders simultaneously, as discussed in Chapter 3. To avoid confusion of spectral information, a method of separating overlapping orders is required. The component which achieves this separation of orders is typically labelled the "order sorting" element. Order sorting elements are typically a dispersive element such as a grating or prism [98], or lower order FP etalons placed in series with the original etalon [72]. When using a dispersive optic, there are two common methods of observing multiple FPI orders: either by using a fixed grating and dispersing the complete spectrum over a linear array of detector pixels, or by rotating the grating, thereby scanning the output across a single detector. In either case, the grating must limit the observed waveband for a single pixel or grating position to less than one free spectral range of the FPI (Chapter 3). In the instrument described in this thesis, a detector array was not available, so I developed a reflective grating monochromator which could be tuned by adjusting the

angle of the grating using a cryogenic stepper motor and a worm-wheel gear train, to allow the FPI to measure broadband sources.

5.2 Grating Theory

To begin, the theory behind the dispersive nature of a diffraction grating is discussed.

5.2.1 The Grating Equation

A diffraction grating may be described using a condition of multiple beam interference, where the grating can be modelled as a linear array of equispaced coherent point sources or slits illuminated by a plane wave. Each slit can be considered to radiate secondary wavelets, following Huygen's Principle [67]. The **E**-field at any point beyond the grating can be determined by the sum of the **E**-fields produced by each wavelet at that point. The following derivation follows those found in [67, 93]. The simplest case is where the wavefront of the illuminating plane wave is parallel to the slits, or equivalently, the coherent point sources are all in phase. Defining a slit separation d determines the optical path difference (OPD) between successive diffracted beams for a given output angle as $\mu d \sin\beta$ (Figure 5.1), where μ is the refractive index of the medium around the grating, and β is the diffracted angle measured with respect to the grating normal. Assuming the grating is operating under vacuum, and is not immersed in a dielectric, the refractive index term μ is unity. The corresponding phase delay between successive wavelets is

$$\delta = \frac{2\pi d \sin\beta}{\lambda}. \qquad \text{[rad]} \quad (5.1)$$

Extending the successive slit phase delays for a number of slits j, the phase delay introduced from the j-th slit is:

$$\delta_j = \frac{2\pi\mu(j-1)d\sin\beta}{\lambda}. \qquad [\text{rad}] \quad (5.2)$$

Assuming that the amplitude of the EM wave emitted from each slit is the same, E_0, the field from the j-th slit at a position $\mathbf{r}$ from the grating is:

$$\mathbf{E}_j(\beta) = \mathbf{E}_0(\mathbf{r})e^{i(\mathbf{k}\cdot\mathbf{r}-\omega t)}e^{i(j-1)\delta}. \qquad [\text{N C}^{-1}] \quad (5.3)$$

where $\mathbf{k}$ is the propagation vector. In the case where the $\mathbf{E}$-field is observed far from the grating (i.e. $\mathbf{r}$ is large), the individual $\mathbf{E}$-fields are approximately parallel, and the the vector notation can be dropped. Additionally, each oscillator produces spherical wavelets which propagate in the direction of $\mathbf{r}$, so the propagation vector reduces to the propagation amplitude $k = 2\pi/\lambda$, and the dot product reduces to a scalar product.

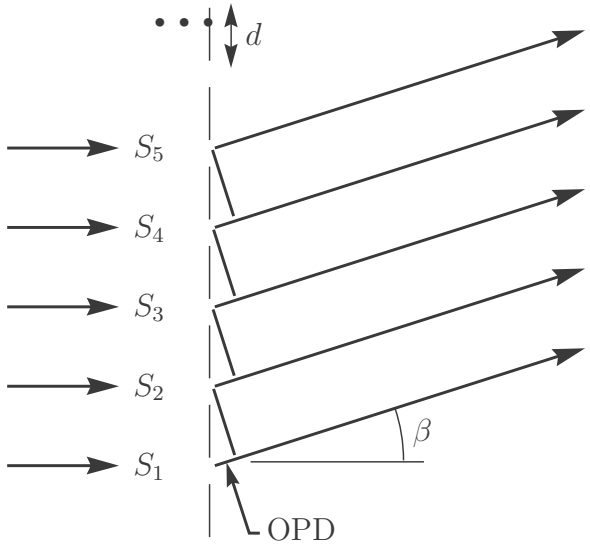

Figure 5.1: A linear array of coherent oscillators showing the condition for constructive interference [93].

Combining the E-fields of all slits, the total field amplitude is,

$$E(\beta) = E_0(r)e^{i(kr-\omega t)}\sum_{j=1}^{N}(e^{i\delta})^{j-1}. \qquad [\mathrm{N\,C^{-1}}] \quad (5.4)$$

The terms within the summation can be reduced to:

$$\frac{e^{i\delta N}-1}{e^{i\delta}-1}, \qquad (5.5)$$

which can be rearranged to the form,

$$e^{i(N-1)\delta/2}\left(\frac{\sin N\delta/2}{\sin \delta/2}\right). \qquad (5.6)$$

From the relation that the E-fields are related to the flux density, I by $I \propto EE^{\star}$ for a complex E, the above expression may be expressed in terms of flux density which simplifies to,

$$I(\beta) = I_0\left[\frac{\sin^2(N\delta/2)}{\sin^2(\delta/2)}\right]. \qquad [\mathrm{W\,m^{-2}}] \quad (5.7)$$

The numerator in the above equation describes a rapidly varying waveform which is modulated by the slowly varying wave in the denominator. For large N this produces sharp principal maxima which are separated by many smaller subsidiary maxima (Figure 5.2). The principal maxima points occur when the diffracted E-fields interfere constructively, that is at angles where the phase delay between successive wavelets is:

$$\delta = 2\pi m. \qquad [\mathrm{rad}] \quad (5.8)$$

The condition in which this is met is expressed as,

$$m\lambda = d\sin\beta, \qquad [\mu\mathrm{m}] \quad (5.9)$$

which is called the *grating equation* for a normal incidence wave.

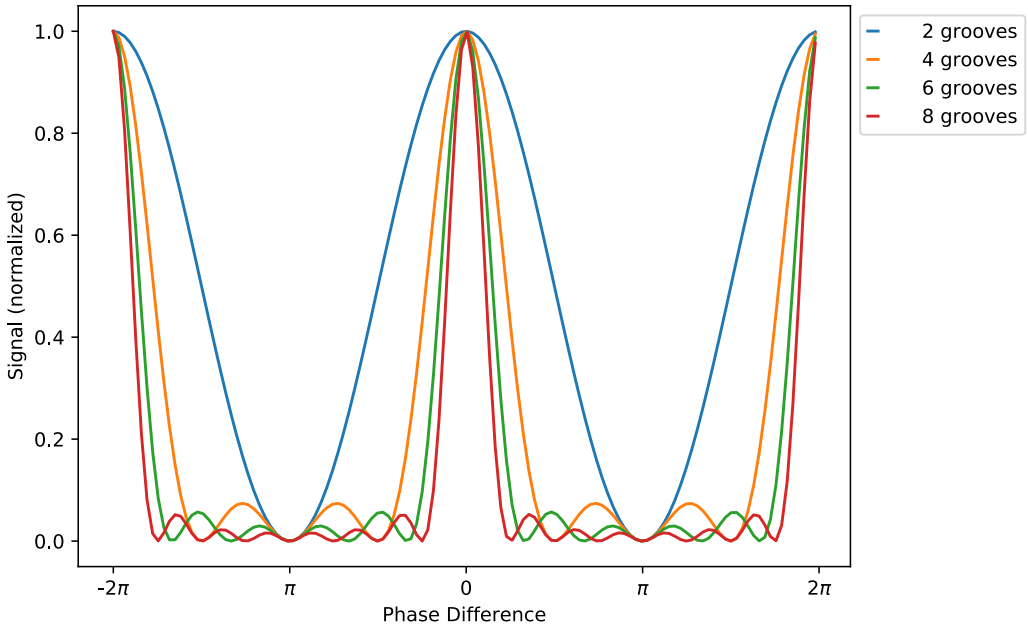

Figure 5.2: The interference pattern of a grating or multi-slit aperture. As the number of slits increases, the principal maxima narrow. Each curve in the figure is normalized to 1.

If the incident plane wave approaches at an angle, it may be modelled as a phase delay between subsequent slits or point sources, and the condition for maximum intensity is expressed as the *fundamental grating equation*,

$$d(\sin(\alpha) + \sin(\beta)) = m\lambda \qquad [\mu m] \quad (5.10)$$

where α is the incident angle, β is the diffracted angle, λ is the incident wavelength, and m is the diffraction order. The corresponding phase delay between successive grating grooves is

$$\delta = 2\pi d(\sin\alpha + \sin\beta)/\lambda. \qquad [\text{rad}] \quad (5.11)$$

In this expression of the grating equation, for a beam approaching from the left of the grating normal, a left hand angle is a positive angle and a right hand angle is negative (Figure 5.4). For a complete view of the change in phase that results from an oblique

angle of incidence, the reader is referred to [67].

5.2.2 Grating Monochromators

A monochromator is a device which is designed to mechanically select a narrow waveband from a broadband input. A common form of monochromator is the Czerny-Turner configuration which uses a tilting grating with fixed input and output slits. Light which is diverging from the entrance slit is collimated by a curved mirror (the collimator, M_1) and diffracted light from the grating is focused on the exit slit using a second curved mirror (the camera, M_2) (Figure 5.3). In the monochromator configuration, the angle between the incident and diffracted rays (the deviation angle, 2ϕ, in Figure 5.4) is held constant, where $2\phi = \alpha - \beta$.

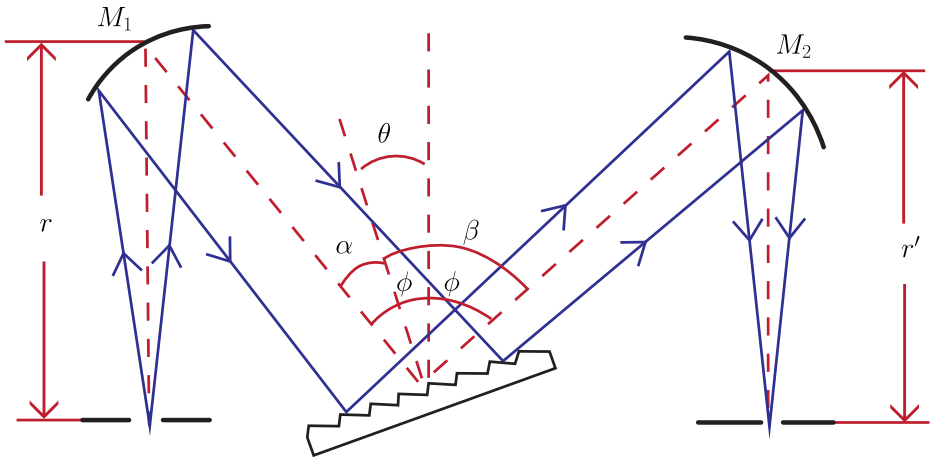

Figure 5.3: The Czerny-Turner monochromator configuration [99].

For a monochromator, a convenient way to express the grating equation is,

$$m\lambda = 2d\sin(\theta)\cos(\phi), \qquad [\mu\text{m}] \quad (5.12)$$

where θ is the angle between the grating normal and the line that bisects the deviation

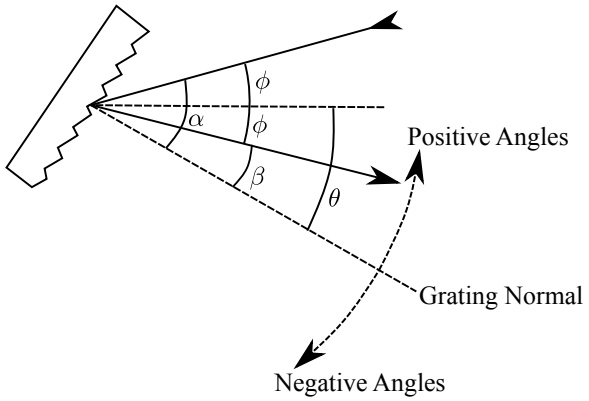

Figure 5.4: Visualisation of the relationship between angle definitions for the monochromator compared to the fundamental grating equation [61].

angle. The angle definitions are related by:

$$\alpha = \theta - \phi, \text{and} \qquad [\text{rad}] \quad (5.13)$$

$$\beta = \theta + \phi. \qquad [\text{rad}] \quad (5.14)$$

5.2.3 Dispersion

Angular dispersion measures the wavelength separation as a function of observing angle. It is defined as the derivative of diffracting angle with respect to the resonant wavelength,

$$\mathcal{D} = \frac{d\beta}{d\lambda} \qquad [\text{rad}\,\mu\text{m}^{-1}] \quad (5.15)$$

$$= \frac{m}{d\cos\beta}. \qquad [\text{rad}\,\mu\text{m}^{-1}] \quad (5.16)$$

While the angular dispersion relates the change in wavelength as a function of grating tilt, the camera optic images this to a linear wavelength distribution on the exit slit. The linear dispersion of the system is the product of the angular dispersion and the exit focal length of the system, r',

$$r'\mathcal{D} = \frac{mr'}{d\cos\beta} \qquad [\text{mm}\,\mu\text{m}^{-1}] \quad (5.17)$$

5.2.4 Resolving Power

In a monochromator, the dispersed beam is focussed onto an exit slit of width w'. The size of the slit and the extent of the linear dispersion determines the spectral bandpass,

$$B = \frac{w'}{r'\mathcal{D}}. \qquad [\mu m] \quad (5.18)$$

Note that this simple expression of the monochromator bandpass is only relevant in the geometric ray tracing regime. The value w' is more accurately described as the convolution of the image of the entrance slit with the exit slit. If the image of the entrance slit is near the diffraction limited spot size of a point source, diffraction must also be included in the determination of the entrance slit image size. The implications of diffraction through the entrance slit are discussed in more detail in Section 5.7.3.

Furthermore, the grating has an intrinsic limit on the resolving power regardless of slit sizes or diffraction, which is dependent on the number of illuminated grating grooves. The width of the peak which defines a principal maxima is dependent on the location of the first subsidiary minima on either side of the peak. The subsidiary minima are defined where

$$\frac{\sin^2(N\delta/2)}{\sin^2(\delta/2)} = 0, \quad (5.19)$$

which is where

$$\delta = \pm\frac{2n\pi}{N} \qquad [rad] \quad (5.20)$$

where $n = \pm1, \pm2, ...$ excluding where n is an integer multiple of N. For the first subsidiary minima, $n = \pm1$ and,

$$\Delta\delta = \frac{2\pi}{N}. \qquad [rad] \quad (5.21)$$

Combining the derivative of Equation (5.11) with respect to the diffracted angle β

and the angular dispersion in Equation (5.16),

$$\frac{d\delta}{d\lambda} = \frac{2\pi m}{\lambda}. \qquad [\text{rad}\,\mu\text{m}^{-1}] \quad (5.22)$$

By equating the differentials to small deviations, the intrinsic resolving power of the grating can be determined,

$$\begin{aligned} \mathcal{R} &= \frac{\lambda}{\Delta\lambda} \\ &= \frac{2\pi m}{\Delta\delta} \\ &= mN. \end{aligned} \quad (5.23)$$

In both the diffraction limited, slit limited, or grating limited cases, the bandpass defines the difference in wavelength $\Delta\lambda$ between the half maximum intensity points of either side of the intensity maximum, FWHM. This width determines the spectral resolving power,

$$\mathcal{R} = \frac{\lambda}{B} = \frac{\lambda}{\Delta\lambda}. \quad (5.24)$$

5.2.5 Free Spectral Range

Since the solutions to the grating equations give integer multiples of wavelengths, the conditions for constructive interference are met by multiple interference orders simultaneously. To avoid the overlap of spectra, the range of wavelengths illuminating the grating should be less than the FSR, analogous to the free spectral range of an FPI defined in Chapter 3. FSR for the grating is defined as,

$$m(\lambda_0 + \Delta\lambda_{\text{FSR}}) = (m+1)\lambda_0 \qquad [\mu\text{m}] \quad (5.25)$$

$$\Delta\lambda_{\text{FSR}} = \frac{\lambda_0}{m}. \qquad [\mu\text{m}] \quad (5.26)$$

5.2.6 Blaze Angle

The grooves on diffraction gratings are often engineered to have a specific shape in order to improve their efficiency in the desired order and waveband. This is known

as *blazing* the grating. In a conventional grating, much of the energy is lost to the specular reflection from the 0-th order. However, if the grooves are angled so that specular reflection occurs nearer the desired order, less power is wasted in unwanted orders.

For maximum efficiency at the center wavelength, the blaze angle is determined by,

$$\theta_B = \arcsin\left(\frac{m\lambda_0}{2d\cos\phi}\right), \qquad \text{[rad]} \quad (5.27)$$

where λ_0 is the center wavelength, and the other variables are defined previously. It can be seen that the blaze angle θ_B is equal to the grating angle θ for the optimized wavelength λ_0.

5.3 Optical System Design

The Czerny-Turner monochromator configuration is fundamentally an optical instrument and is subject to all rules that apply to a system of optical elements. These rules must be taken into account in order to design an efficient system. The foremost of these considerations are the overall collection and propagation of energy in the system as well as magnification and distortion by the active elements.

5.3.1 Etendue

The geometric etendue of an optical system is a measure of its optical throughput, and is a function of the area, S, of the source and the accepted solid angle, Ω. This property may be evaluated sequentially for each component in an optical system.

$$G = \int\int \mu^2 dS\cos\theta d\Omega \qquad \text{[sr m}^2\text{]} \quad (5.28)$$

where μ is the refractive index, θ is the angle of the ray to the aperture normal, dS is an infinitesimal area of the aperture, and $d\Omega$ is an infinitesimal solid angle. The solid

angle differential can be represented in spherical coordinates as,

$$d\Omega = \sin\theta d\theta d\phi \qquad [\text{sr}] \quad (5.29)$$

For a cone of light normal to the aperture of area S in a vacuum, the etendue becomes,

$$G = \pi S \sin^2\theta \qquad [\text{sr m}^2] \quad (5.30)$$

where θ is the half angle of the cone. The numerical aperture of an optical element is

$$\text{NA} = \mu \sin\theta \quad (5.31)$$

and the numerical aperture is related to the f-number by,

$$(\text{f}/\#) \approx \frac{1}{2(\text{NA})}. \quad (5.32)$$

A convenient way to express the etendue of an optical element is,

$$G = \frac{\pi S}{(2(\text{f}/\#))^2}. \qquad [\text{sr m}^2] \quad (5.33)$$

Since etendue is a singular property of the entire system, the value is determined by the least optimized element of the system, and the optimized optical system will match etendues for all its components. In our case, the optics were constrained by the cryostat dimensions, as discussed in Section 5.4.1, which determined the optimum dimensions of the entrance slit with respect to the exit slit.

5.3.2 Anamorphic Magnification

Another factor that must be addressed in designing a grating spectrometer is that the magnification of the entrance slit depends on the grating angle, causing the grating

to produce different magnifications along perpendicular radii. For an entrance slit of height h and width w, with the length perpendicular to the dispersion plane, the magnifications of h and w are different. Magnification of h is:

$$\mathrm{X}_h = \frac{h'}{h} = \left(\frac{f_{\mathrm{cam}}}{f_{\mathrm{col}}}\right) \tag{5.34}$$

Where f_{cam} is the focal length of the camera (exit optics), f_{col} is the focal length of the collimator (input optics), and h' is the height of the image of the entrance slit.

The magnification of the width has an additional factor which emerges from the unequal incident and diffracted angles with respect to the grating normal. Implicitly differentiating the grating equation:

$$\cos\alpha \; d\alpha + \cos\beta \; d\beta = 0. \tag{5.35}$$

The anamorphic magnification is the derivative of the diffracted angle with respect to the incident angle. The magnification of the entrance slit width can then be expressed as:

$$\begin{aligned} \mathrm{X}_w &= \frac{w'}{w} \\ &= \left(-\frac{d\beta}{d\alpha}\right)\left(\frac{f_{\mathrm{cam}}}{f_{\mathrm{col}}}\right) \\ &= \frac{\cos\alpha}{\cos\beta}\left(\frac{f_{\mathrm{cam}}}{f_{\mathrm{col}}}\right) \end{aligned} \tag{5.36}$$

where w' is the width of the image of the entrance slit.

5.3.3 Stray Light

Since the grating operates on the principle of scattering incident light, the issue of stray light and background radiation on the signal to noise ratio of the instrument is ever present.

Stray light may be a result of:

1) Incorrect illumination of the spectrometer, introducing unwanted reflections from the grating support structure.

2) Re-entrant spectra caused by unwanted diffracted wavelength finding a reflected path back to the grating or detector.

3) Grating ghosts created from irregularities in the grating profile.

5.4 Grating Design

In this section, we describe the design process that went into fabricating a custom grating solution, given our unique conditions and constraints.

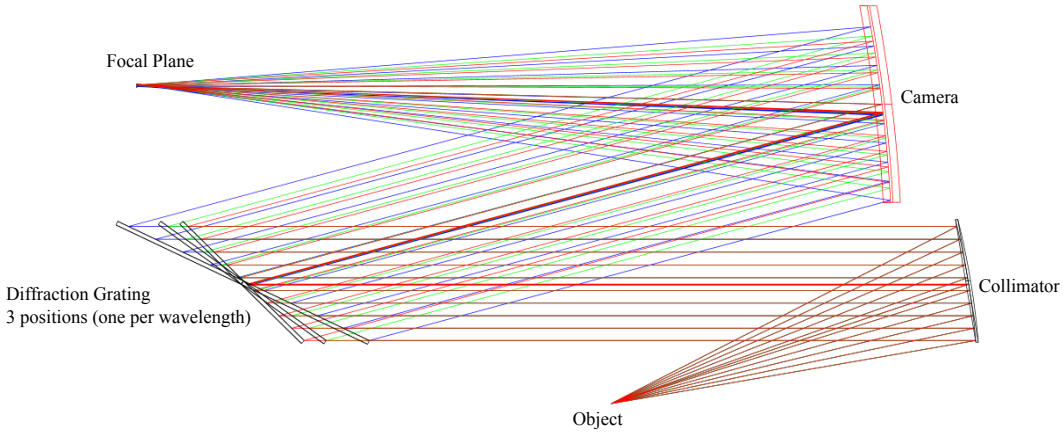

Figure 5.5: Optical layout and raytrace of the grating system (private communication with David Arrazola, CAB INTA).

5.4.1 Optical Design

Due to constraints on the position of the sensitive composite bolometer detector within the TFC, due to the location of the 300 mK cold head, the maximum focal length of the camera optic was predetermined. Since linear dispersion – and therefore resolving power – increases proportionally with exit focal length (Equation (5.17)), the system was designed to use the full length available. Additionally, the height of the detector was predetermined by the 300 mK coldhead location, and out of the plane

of the entrance windows inside the TFC. Therefore, additional optics were required to raise the beam out of the horizontal plane going through the center of the cryostat windows. To minimize the number of optical components and provide a compact system, the vertical displacement of the beam was incorporated into the dispersion angle of the grating.

To keep the size of the beams and the cost of the optics manageable, the collimated beam size was limited to 40 mm diameter, allowing commercial off-the-shelf (COTS) optics to be used.

Figure 5.6 shows the module for dispersion, which consists of a custom-designed grating that is coupled to a gear train, and powered by a cryogenic stepper motor. Directly across from the grating is a 15° off-axis parabola (OAP) mirror, and a plane 45° fold mirror below the OAP, which together with the grating define the deviation angle, $2\phi = 15°$. Collimated light from the Fabry-Pérot reflects from the 45° fold mirror and travels towards the grating. The grating angle can be controlled with a 200-steps-per-revolution bipolar cryogenic stepper motor to sort between the FPI interference orders [100]. The preselected deviation angle of 15° determines the wavelength band which reflects from the upper 15° OAP mirror and focus onto the exit slit placed directly before the detector. Figure 5.6 shows a sample beam of light with the above described path of travel. Note that all of this will occur with the assembly cooled down to 4 K. All out of band light misses the OAP and is scattered and absorbed by a carborundum-infused Epotech epoxy coating on the interior of radiation shields which surrounds the assembly. In addition, a 4 K 50 cm^{-1} low pass optical filter is placed directly before the 45° fold mirror, and a 0.3 K 50 cm^{-1} low pass filter is placed on the optical feedhorn which couples radiation into the detector. A detailed layout of the optical filters and their locations is shown in the Chapter 6.

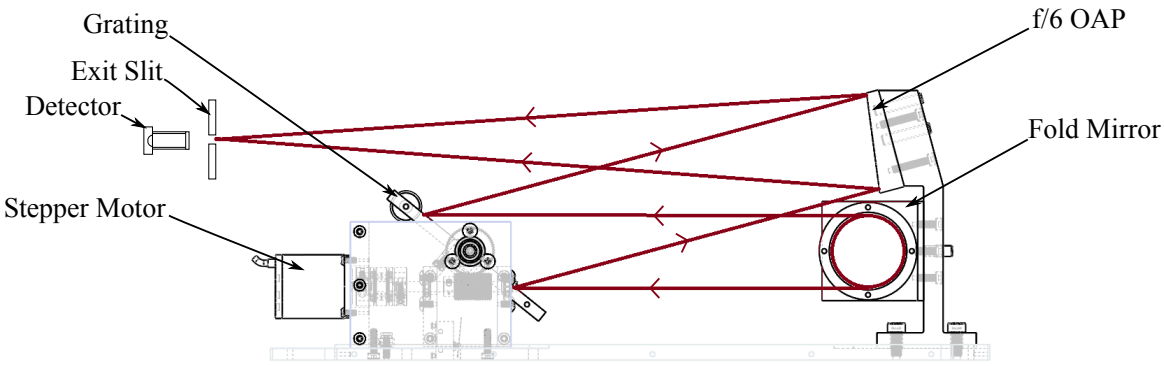

Figure 5.6: Side view of the grating, focussing optics, and stepper motor driven gear train.

5.4.2 Grating Parameters

The desired waveband of the complete spectrometer is 220 µm to 300 µm, requiring the grating to be optimized for the center wavelength, $\lambda_c = 260\,\mu\text{m}$, and having a free spectral range of at least 80 µm. This limited the operational order of the grating to be $|m| \leq 3$.

Additionally, the spectral bandpass of the grating monochromator was required to be less than one free spectral range from the Fabry-Pérot etalon, in order to avoid the confusion of FPI orders. A target resolving power of 300 was selected, to provide a bandpass of less than 1 µm at all points. Using the grating limited condition of $R = mN$, the constraint became,

$$R \approx 300 = \frac{mD}{d\cos\alpha}. \tag{5.37}$$

Since the beam must not overspill the grating, the lower limits on the physical size of the grating were determined, $W \geq D$, and $H \geq D/\cos\alpha_{\text{max}}$. The size of the grating was limited such that it could freely rotate when positioned at a height of 56 mm above the 4 K optical bench, coinciding with the height of the optical viewports in the vacuum chamber allowing for the optical elements before the grating to be built in the same plane. Combining the restricted diameter of the beam to $D = 40\,\text{mm}$,

and limiting the grating height to 100 mm, the maximum incident angle of the grating was constrained,

$$\alpha_{\max} = \arccos\left(\frac{D}{H}\right) = 66^\circ \tag{5.38}$$

Since the deviation angle was already set at $\phi = 7.5^\circ$, the maximum grating angle was also set $\theta = 58.5^\circ$.

The grating equation now determined the minimum value of the ratio d/m, and the minimum grating angle using that ratio. The ratio d/m was designed to be as near to its minimum value as possible, in order to maximize the spectral resolution. The first order ($m = 1$) was selected so that the grating could be be tilted beyond the maximum angles set in Equation (5.38) so that longer wavelengths, where the photomixer provided more power (Figure 4.4), could be measured. Equation (5.10) was used to determine the minimum groove spacing, $d = 157\,\mu\text{m}$, while the actual groove spacing was set to 180 µm to avoid illuminating the grating edges to reduce stray light and allow for small beam divergence. The final grating design parameters are presented in Table 5.1, and B-Con Engineering [101] fabricated an aluminum grating with these specifications.

5.4.3 Slit Sizes

In an optimal grating, the resolving power determined by the slit spacing is matched to that of the grating to preserve resolving power requirements while providing the highest throughput. To reach the target resolving power of $\mathcal{R} \sim 300$ over the entire waveband with the constrained size of the grating, the optimum slit width was found to be ∼1 mm. The height of the exit slit was set to match the diameter of the detector feedhorn at 10 mm. However, diffractive losses at the entrance slit interface with a 50.8 mm f/6 collimating mirror indicated a 75 % loss in signal from overfill of the optic. Therefore, the sizes of the exit slit and entrances slit image were expanded to 2 mm to capture 50 % of the incident radiation, while still reaching a

resolving power of 300 above 260 µm where the THz photomixer power output was highest (Figure 5.7). For efficient magnification of the entrance slit when the grating was used alone by an input f/3 mirror, the optimum entrance slit was set to 5 mm in height with a 1 mm width. This constraint in the initial design meant that the desired resolving element for the short wavelength end of the instrument could not be reached. However, since the available calibration sources showed better performance at longer wavelengths, we opted to verify the FPI by it's performance in the long wavelength regime.

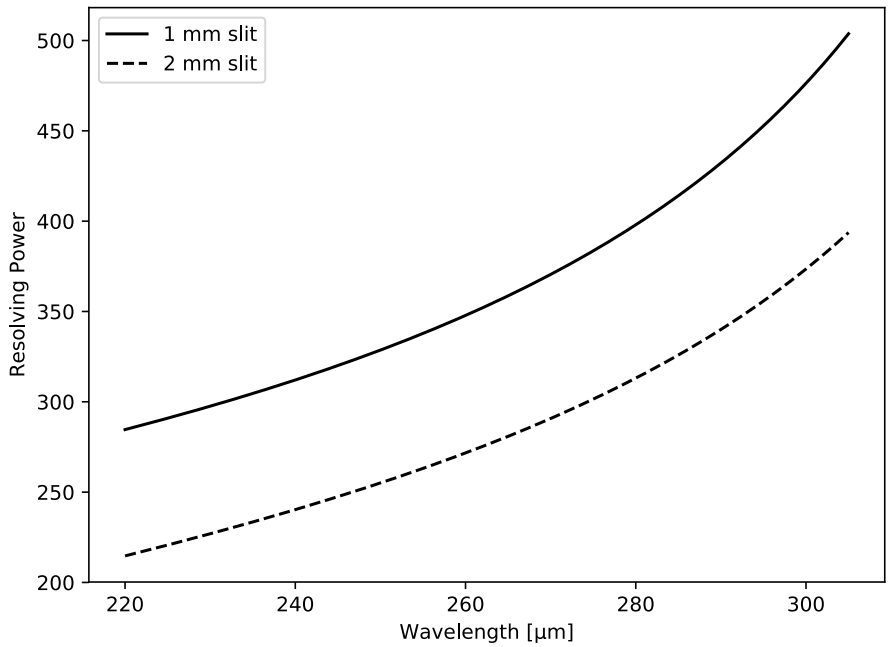

Figure 5.7: The effect of increasing the slit size from 1 mm to 2 mm on the resolving power.

The blaze angle was set so that the maximum efficiency of the grating was tuned to $\lambda_c = 260$ µm and $m = 1$. For maximum efficiency at the center wavelength, the blaze angle was set to:

$$\theta_B = \arcsin\left(\frac{m\lambda_c}{2d\cos\phi}\right) \tag{5.39}$$

For $d = 180$ µm, $\theta_B = 47$ °.

Table 5.1: Grating specifications. ϕ is the angle between the incident and diffracted beam, which remains constant over the entire range in the Czerny-Turner configuration. The exit focal length requires an f/6 optic on the output.

Parameter	**Value**
Height (H)	100 mm
Width (W)	50 mm
Order	1
Spacing	180 µm
2ϕ	15°
Blaze	47°
Focal Length	310 mm
Exit Slit Width	2 mm

In line with the required bandpass and spectral resolution, the required angular step size was determined. The minimum step size occurred at the smallest wavelength, corresponding to $\Delta\theta = 0.2°$. This $\Delta\theta$ limitation set the requirements on the grating drive, in Section 5.4.4.

5.4.4 Grating Actuation

A 60 : 1 worm and wheel gear train was used to actuate the grating. One major drawback to worm and wheel systems is that they have lower efficiencies in comparison to other gear trains. This lower efficiency means that there is more frictional loss, and thus more heat generation within the gears. With this said, worm and wheel systems do allow for very high gear ratios with minimal gears used. Furthermore, in the current design the grating shaft is not able to drive the worm gear, allowing the hold torque on the stepper motor to be minimized while still holding the grating steady. Since a constant holding torque dissipates heat, minimizing this quantity is desirable for a cryogenic system.

As per the grating specifications,the minimum step size was 0.2°. The gear train and stepper motor selected provided a 0.03° angular step size using a 200 steps-per-revolution Phytron cryogenic stepper motor [100], and a 60 : 1 gear ratio on the worm

Table 5.2: Phytron stepper motor specifications

Parameter	**Value**
Part #	VSS 32.200.1.2
Size	32 mm
Steps/ rev	200
# Phases	2
I/Ph	1.2 A
R/Ph	1.25 Ω
L/Ph	1.2 mH
Holding Torque	40 mNm
Detent Torque	3 mNm
Rotor Inertia	0.01 kgcm^2
Axial Load	5 N
Radial Load	15 N
Mass	0.17 kg

and wheel (Table 5.2).

The mechanical advantage of the worm-wheel systems can be determined by finding the relation between the tangential forces on the worm W_{Wt} and the gear W_{Gt} [102]:

$$\frac{W_{Wt}}{W_{Gt}} = \frac{\cos\phi_n \sin\lambda + f\cos\lambda}{f\sin\lambda - \cos\phi_n \cos\lambda} \tag{5.40}$$

where ϕ_n is the normal pressure angle, λ is the lead angle (90° from helix angle), and f is the coefficient of friction.

Since the gear is only free to rotate about the axis of the shaft, the torques are defined as the product of the gear radii and the associated tangential force, i.e. $\tau_W = r_W W_{Wt}$.

Unlike a conventional spur gear train, where the motion of the gears relative to each other is a rolling motion of the meshed teeth, the primary motion in a worm-wheel system is the sliding motion of the teeth across connected gears. Consequently, friction plays an important roll in the overall efficiency of the system. By assuming a coefficient of friction, we can determine the approximate efficiency of the gear system.

The derivation in chapter 13 of [102] results in the expression,

$$\eta = \frac{\cos\phi_n - f\tan\lambda}{\cos\phi_n + f\cot\lambda}, \tag{5.41}$$

Furthermore, as the motor was stepped, because of the free play between the gears, there was a fixed degree of backlash. To accommodate this, a preloaded spring system was required. As only 20° of rotation was needed from the grating, the backlash was managed by preloading the grating to one side through the use of an extension spring. Thus, as the grating was stepped, the system was always biased to one side. Figure 5.8 shows a section view of the worm and wheel system, with the bearings, flex coupling, and motor attached; all components were designed to operate at 4 K.

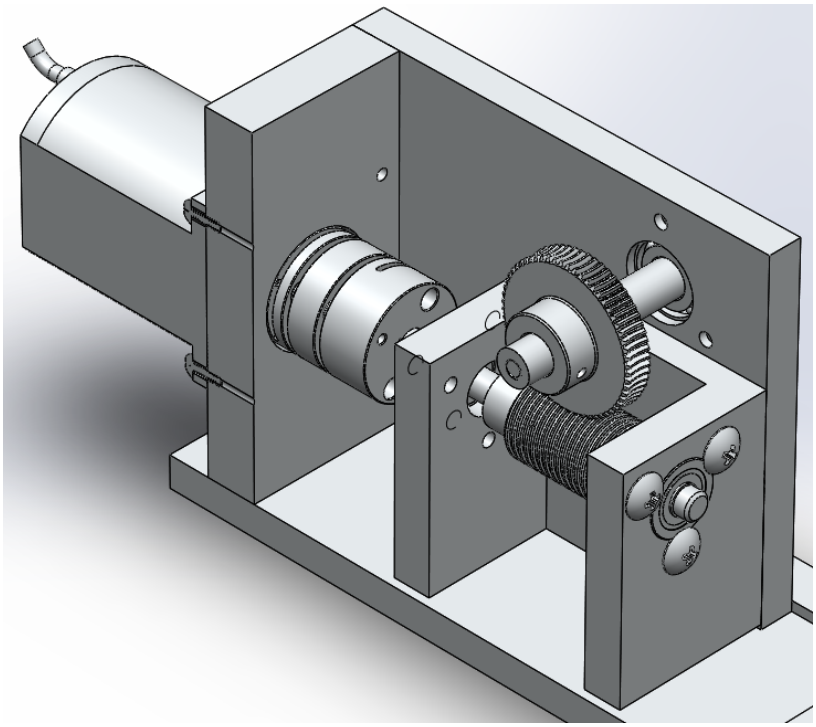

Figure 5.8: Worm and wheel gear train for tilting the grating, consisting of a cryogenic stepper motor, flexible coupling, and worm and wheel gears.

5.4.5 Radiation Shielding

To reduce the effects of radiative heat transfer, shields are used to surround any objects which may radiate heat, such as the stepper motor and the gear train. Additionally, a shield surrounds the entire grating assembly to absorb light which does not pass through the exit slit, in order to avoid re-entrant spectra. The inner surfaces of these shields were painted black and roughened with a mixture of carbon black powder in an Epotek cryogenic epoxy [103] and carborundum pellets to absorb scattered radiation from the grating surface, and minimize spectral reflection. In this way, the diffracted radiation that did not have a direct path to the exit slit was scattered and absorbed. The grating assembly's shields can be seen in Figure 5.9.

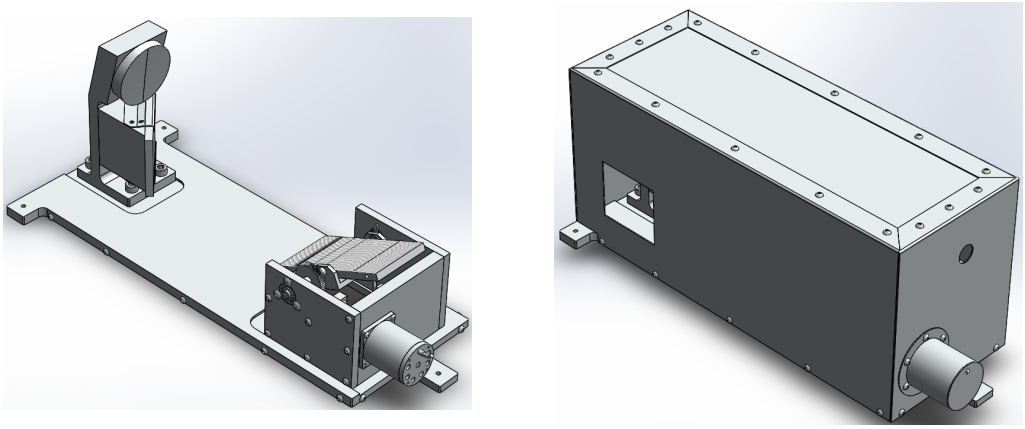

(a) Grating Assembly

(b) Radiation Shielded Grating

Figure 5.9: CAD renderings of the grating assembly.

5.4.6 Cryogenic Considerations

Since the grating assembly is designed to operate at 4 K, consideration was taken to avoid binding of moving parts due to differential thermal contraction. The majority of parts used are made from aluminum, however the bearings and worm gear are stainless steel, and the wheel gear is bronze. Since aluminum contracts more than stainless steel and bronze, the gear meshing was intentionally given a $\sim$100 µm clearance at room temperature so the gears would not bind at low temperatures. Preliminary

calculations found that the gear spacing will change by roughly 11 µm at 4 K. To allow for adjustability of the gear meshing to account for both thermal expansion and machining tolerances in the mounting plates, bearing locations, and drive shaft angle, gaps of 600 µm were put in the through holes which mount the c-block containing the worm to the side wall. Furthermore, a flexible coupling was used to attach the motor and primary drive shaft so that small misalignments could be accommodated. The gap between the two components can be seen in red, in Figure 5.10.

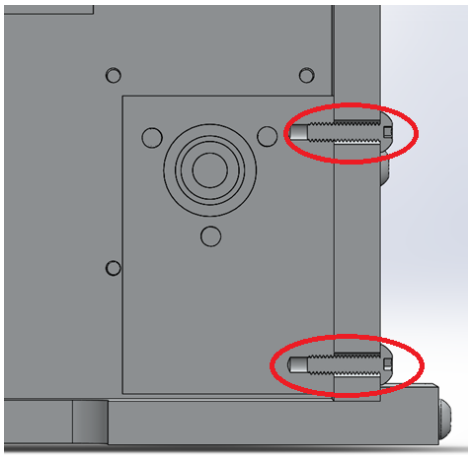

Figure 5.10: Section view of the 600 µm free play between the c-block and sidewall connecting fasteners.

5.4.7 Adhesiveless Bearings

All of the bearings on the grating assembly were mounted in such a way that no adhesive or epoxies were needed. Three large head M3 screws were placed on the outer race of each bearing, as can be seen in Figure 5.11a. The bearings were placed into counterbored holes which were slightly smaller than the thickness of the bearings. Thus, the second side of the bearings outer race was clamped by the counterbored hole. On the primary drive shaft, the center bearing's inner race was floating, which accommodated slight misalignments. On the other hand, the edge bearing's inner race was held by a shoulder on the shaft and a lock ring. The bearings on the grating shaft were press fit, as they were on the very edge of the shaft. Figure 5.11b shows

a closer view of the lock ring and shoulder setup for the primary drive shafts end bearing.

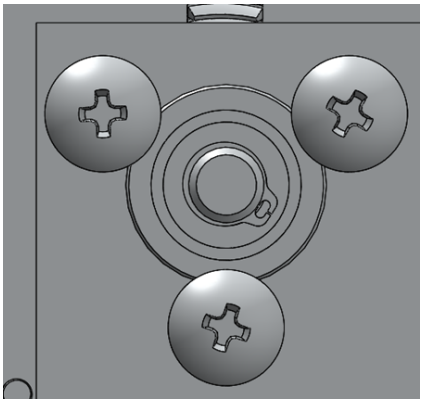

(a) Bearing fasteners.

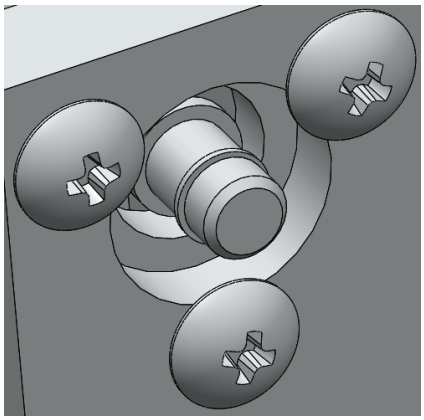

(b) Close-up of the shoulder and lock ring setup.

Figure 5.11: Bearing mounting arrangements in the grating assembly.

5.5 Grating Control

The cryogenic stepper motor was controlled using a Phidgets stepper motor controller (1067 PhidgetStepper Bipolar HC [104]). Since there was no feedback on the stepper motor or the controller, a magnetic reed switch was placed on the grating housing and a permanent magnet placed at the end of the grating (Figure 5.12). In the presence of a magnetic field, the ferromagnetic reeds of the switch would close, allowing current to flow. When the source of the magnetic field was removed, the spring force of the reeds would open the switch. A single digital channel on a Measurement Computing Data Acquisition (MCDAQ) board (USB-1808 Series [105]) was used to read the switch state. This switch acted as an angular reference for the grating. In order to link the data acquisition (DAQ) device recording the switch to the stepper motor controller, a Python 3 script was written utilizing the Phidgets API.

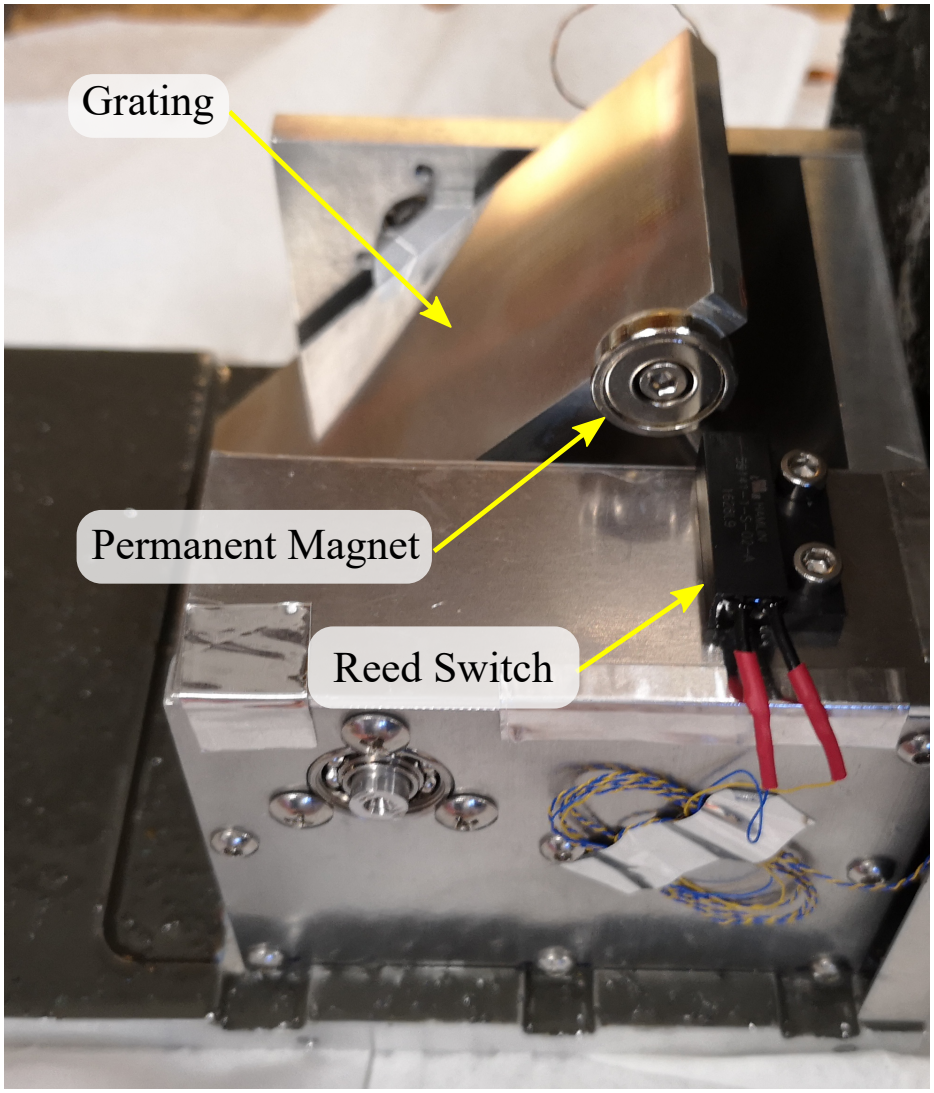

Figure 5.12: The magnetic reed switch which was used to home the grating. A permanent magnet was attached to the side of the grating and the switch was bolted to the frame. The grating triggered the switch at $\theta = 45.20(4)°$ where θ is the grating angle defined in Section 5.2.2.

5.6 Grating Operation

5.6.1 Operating Modes

The grating assembly was designed to function in two optical configurations: as a stand alone monochromator; or in tandem with the FPI as an order sorter. Interchanging between the modes was accomplished by replacing the 45° fold mirror with a 50.8 mm, f/3 OAP facing the opposite direction. In this case, the OAP focus was

on one of the 77 K shield apertures, which was also the new location of the entrance slit. The stand alone operational mode also changed the optical magnification of the spectrometer by changing the f-number of the entrance optic, which changed the optimal slit sizes. However, this operational mode proved extremely useful, as it allowed for verification of the grating before the etalon had been manufactured.

5.7 Validation and Testing

Validation of the grating was accomplished by measuring:

- the repeatability of the grating positioning
- the frequency calibration of the grating with respect to angle
- the resolving power of the grating compared to theory

5.7.1 Stepper Repeatability

The grating position was not monitored during a scan, but relied on the open loop control of the stepper motor to determine the angle. The advantage of using this method was that an angular measurement system for large angles ($> 60°$) and at cryogenic temperatures did not need to be developed. However, the drawback was that if any steps were lost or if the grating stuck during positioning, there would be no feedback and the grating would have to be homed again. Therefore, it was required that the grating positioning was reliable over many scans, with no loss in accumulated step count over the operating range.

The repeatability of the stepper and worm-wheel system was first measured using a flat mirror attached to a dummy mass in place of the grating and measuring the tilt of the grating as a function of step count. The tilt was measured with a PLX Autocollimator [106] which had a $42'$ field of view. For larger ranges, the stepper motor was moved outside the autocollimator range a certain number of steps and the

change in angle after reversing by the same number of steps was measured. Note that this method did not account for steps skipped equally in both travel directions. The grating was then stepped at 60 rpm for various step counts and the start and end angle were measured through the use of the autocollimator. The test setup can be seen in Figure 5.13, below.

The stepping tests showed that for single steps, the motor can achieve $0.031(5)^\circ$ $(1.9(3)')$ of rotation. The predicted step length with our given stepper motor and gear train yields an average step of 0.03° $(1.8')$. Step repeatability was also measured with the grating itself and a stable monochromatic source. The grating was repeatably moved on and off the source a number of times to ensure no steps were skipped. Note that this method also did not account for steps skipped in both directions. It was found that the step repeatability was nearly perfect with rare cases demonstrating a ± 2 step discrepancy over ~ 100 trials. This was deemed suitable for testing of the FPI.

5.7.2 Wavelength Calibration

The bandpass calibration of the monochromator was measured using the tunable photomixer source described in Chapter 4. Since the photomixer power was only appreciable over the long wavelength end of the grating waveband (260 µm to 300 µm), the calibration curve was extrapolated to shorter wavelengths.

It was found that the agreement between predicted grating wavelength and photomixer output wavelength was linear but with a non-unity slope, which implied a discrepancy between the grating as-designed and the grating as-fabricated. The discrepancies could be due to a combination of any of the following parameters from their design values:

- groove spacing d
- deviation angle ϕ

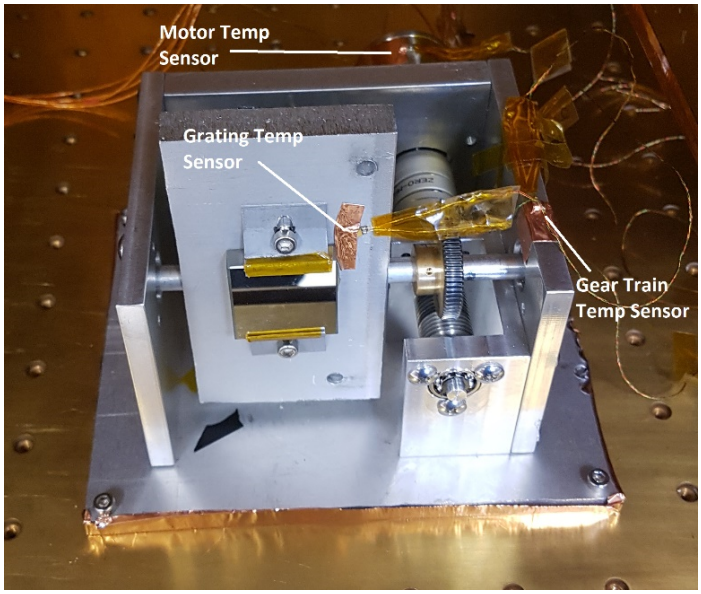

(a) Placement of the temperature measurement diodes.

(b) Autocollimator setup on the test facility cryostat.

Figure 5.13: Test setup for step repeatability measurements.

- rotation per step.

Since the rotation per step is set by the discrete number of teeth on the gears, the rotation per step should not vary for large step counts. With least squares fitting, fits

to the data could converge with an allowed variation of $\pm 2\,\mu m$ for the grating spacing and 0.1° for the deviation angle. However, it was difficult to separate the effects of both of these varied parameters. The theoretical curve in Figure 5.14 shows the best fit to the measured peak wavelength as a function of grating angle using a combined parameter for the groove spacing and deviation angle, $d\cos\phi = 179.61(7)\,\mu m$. The least squares fit also determined the grating angle at which the limit switch was triggered as $\theta_0 = 45.20(4)°$

Another solution was to define a function which gave the wavelength corresponding to the peak response of the grating as a function of the grating angle. For this, a second order polynomial was used, and the fitted results are shown in the "fit" curve in Figure 5.14. The polynomial fit was of the form

$$\lambda = A\theta^2 + B\theta + C, \tag{5.42}$$

where

$$A = -127(5),\ B = 448(9), \text{ and } C = -19(4)$$

5.7.3 Resolving Power

Measurements of the resolving power of the monochromator were also accomplished with the photomixer line source. As the grating was stepped through positions, the line source was scanned across the expected wavelength band. A Gaussian fit was applied to the signals for each grating position, and the fit FWHM was taken to be the wavelength bandwidth (Figure 5.15). The resolving power was defined earlier as the ratio between the peak wavelength and the bandwidth. Slits sizes of 1 mm to 2 mm were used to tune the resolving power. However, slits sizes of 1 mm and less resulted in significant diffractive losses. A slit size of 2 mm produced a sufficiently high resolving power to test the grating performance at $>280\,\mu m$.

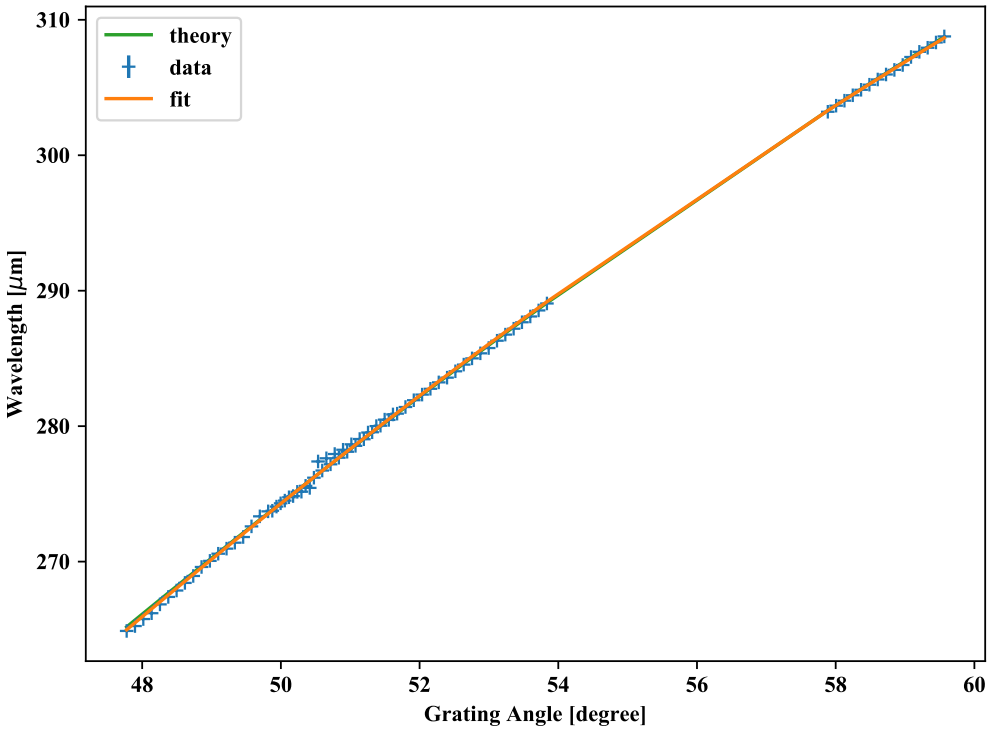

Figure 5.14: The wavelength of peak grating response variation with grating angle θ. The peak was determined by a Gaussian fit to detector readings from a variable monochromatic source (i.e. the photomixer). The "fit" and "theory" curves are explained in the text.

The FWHM for a Gaussian fit to the grating linespread function of the form:

$$f(x) = \frac{1}{\sigma\sqrt{2\pi}} \exp\left[-\frac{(x - x_0)^2}{2\sigma^2}\right] \tag{5.43}$$

is found by scaling the standard deviation σ,

$$\text{FWHM} = 2\sqrt{2\ln 2}\sigma. \tag{5.44}$$

The theoretical resolving power is found by first estimating the bandpass by the physical Gaussian spot size and the exit slit dimensions. The physical spot size from

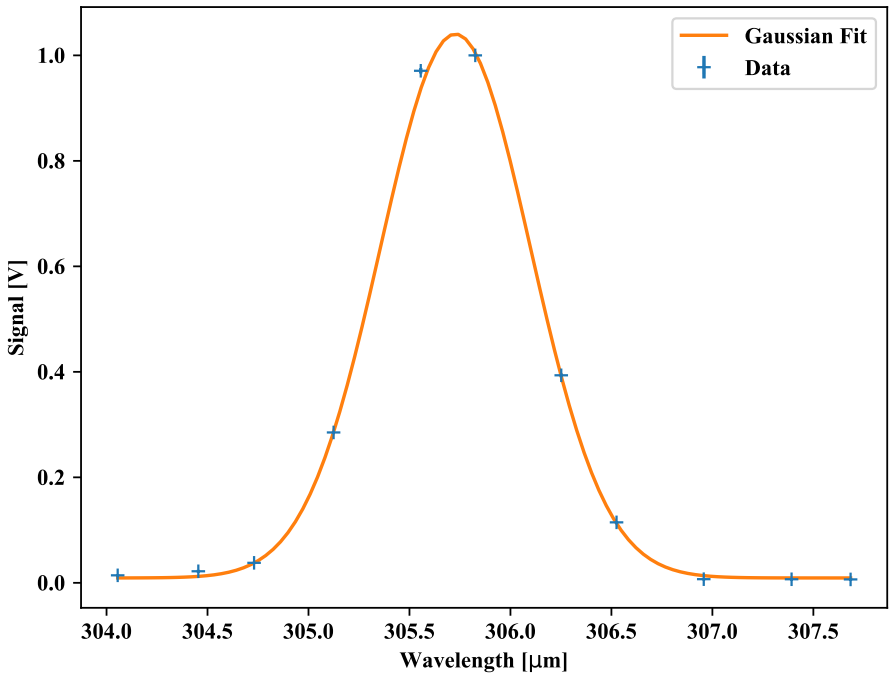

Figure 5.15: An example of a Gaussian fit to the measured signal at different photomixer wavelengths for one grating position.

the exit optics may be approximated by a Gaussian with an RMS width of:

$$\sigma \approx 0.42 \lambda N_{\text{cam}} \tag{5.45}$$

The Gaussian is smoothed by a boxcar function which is the width of the exit slit. The resolving power is then found by using the linear dispersion to determine the smoothed Gaussian width in the spectral domain. The FWHM of this Gaussian is the resolution element. The ratio of the peak center location to the FWHM is the resolving power (Figure 5.16). The data points in this plot show a larger departure from theory than their error bars would indicate. Since the resolving power is dependent on the wavelength stability and power stability of the photomixer, which is not measured simultaneously with the detector signal, the large spread in data points is likely a result of variations in temperature or bias current of the photomixer lasers.

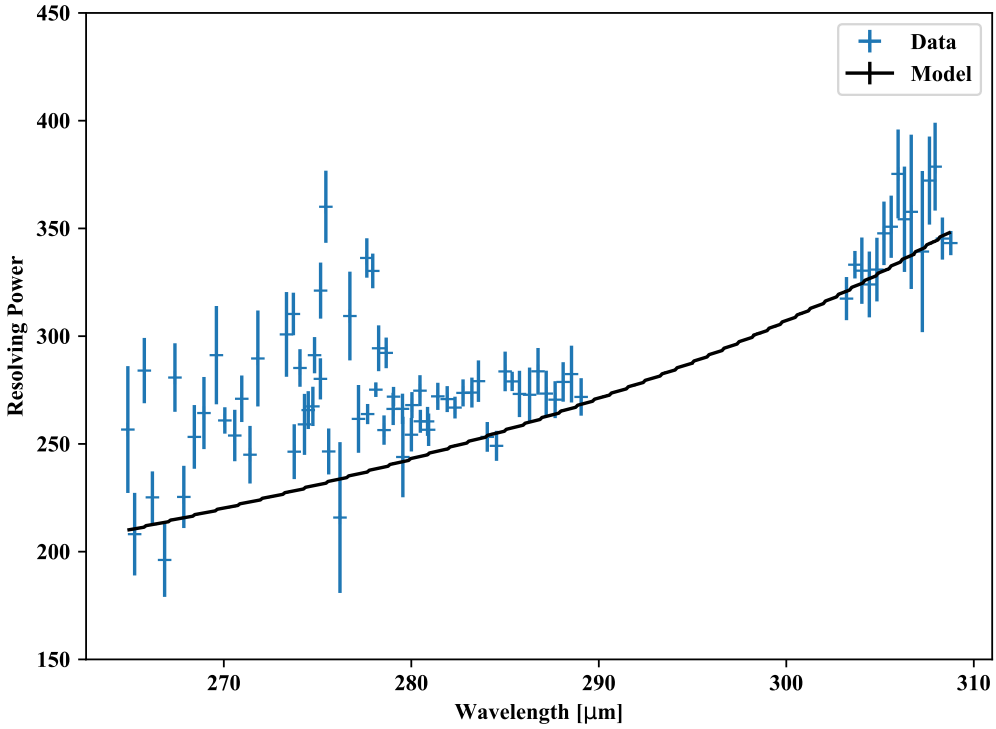

Figure 5.16: The grating resolving power as compared to theory for a 2 mm entrance slit. The theoretical resolving power is lower than that in Figure 5.7 because an f/3 collimating optic was used, which magnified the entrance slit image.

5.7.4 Efficiency

The relative efficiency of the grating was measured for a single wavelength by replacing the grating with a mirror for one test run. By tilting the mirror to scan the image of the entrance slit across the exit slit, we determined the total power of the beam, after any losses in the optics within the optical system. By repeating the scan for the same monochromatic source with the grating, the ratio of the total power incident on the detector, integrated across the grating profile for the grating compared to the mirror was the grating efficiency at that wavelength. In principle this may be repeated for any wavelength. Note that a few assumptions must be made using this method, namely:

- the mirror surface and the surface of the grating share the same reflectivity,

- the beam does not overfill any of the optical components,
- the detector power response is linear.

Figure 5.17 shows the resulting profiles taken by scanning the mirror/grating for the photomixer set to 1 THz as the source. By taking the ratio of the areas underneath each profile, the relative efficiency was found to be 79(1) %.

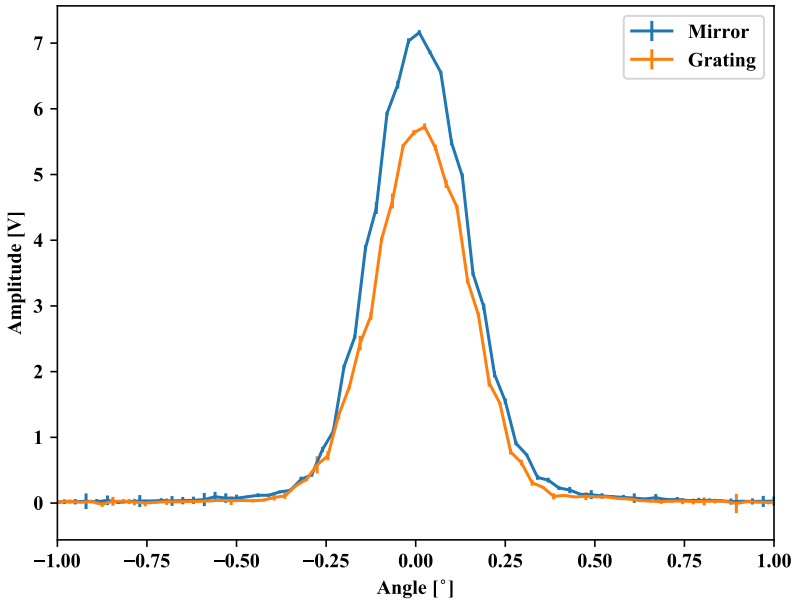

Figure 5.17: Grating efficiency compared to mirror.

5.7.5 Polarization

For gratings with a very high blaze angle (>40°), the efficiency of the device is highly dependent on the linear polarization of the incoming radiation [61]. Linear polarization is described by the combination of two states. P-plane or TE polarized light is oriented such that the E-fields are parallel to the grating grooves. S-plane or TM polarized light is oriented so that the E-fields are perpendicular to the grating grooves. While the determination of efficiency for each polarization state is a complex

process for which specialized software is used, some rules of thumb can be used to select the appropriate polarized source.

In general, a grating with a high blaze angle is more efficient for P-plane polarized light, although this condition holds only when the ratio of wavelength to groove spacing λ/d is greater than 1 [61]. Since λ ranges from 220 µm to 300 µm and d is 180 µm, this condition holds for the full range. Therefore, when a linearly polarized calibration source such as the photomixer was used, the P-plane orientation was used. By comparing the signal strength for the same grating angle and photomixer output wavelength, the ratio of the efficiency for S-plane to P-plane polarization was found to be 0.25(5). This efficiency was confirmed by simulations performed by David Arrazola at CAB-INTA (Centro de Astrobiología – National Institute of Aerospace Technology).

5.8 Conclusions

In this chapter, I have presented the design of a grating spectrometer that was required to enable the evaluation of the FPI. In the design, fabrication, and performance testing of the grating order sorter, I have developed a grating spectrometer for far-infrared wavelengths with $R \sim 300$, and which functions at 4 K. The resolving power matches the requirements for the angle-scanned etalon, and also acts as a standalone system for moderate resolution spectroscopy. Considerations were made to account for thermal expansion misalignments, as well as radiative heating of the surrounding 4 K environment. We also found that with a cryogenic stepper motor and a high mechanical advantage gear train, the grating could be tilted with arcminute precision.

Chapter 6

Instrument Design

> A natural law regulates the advance of science. Where only observation can be made, the growth of knowledge creeps; where laboratory experiments can be carried on, knowledge leaps forward.
>
> Michael Faraday [Attributed, probably incorrectly]

In previous chapters, I have detailed the requirements of the etalon and described the performance of the calibration sources and post-dispersion system to separate FPI orders. In this chapter, I will describe the configuration of the optical system within a 4 K environment, and the integration of the source, post-dispersion system, and detector with the FPI etalon. I will describe in detail the pendulum mirror and associated actuators and position feedback sensors, which tilt the incident beam to achieve angle-scanning of the etalon to scan the resonant wavelengths. The manufacturing technique developed by SRON to fabricate the etalon(s) under test will be described. Finally, an overview of the cryostat cooling mechanisms and control software will be given.

6.1 Optical Layout

The end-to-end verification of the etalon for a variety of calibration sources required efficient optical beam coupling for all components between the source and detector. The optical coupling of the post dispersion system has been described in

Chapter 5. This section describes the coupling from the source to the entrance slit, from the entrance slit through the etalon to the post-dispersion system, and from the exit slit of the post-dispersion system to the detector.

6.1.1 Requirements Analysis

As laid out in Chapter 3, the purpose of building an angle-scanned Fabry-Pérot interferometer (FPI) with a diffraction grating as an order-sorter was to determine its suitability for use as a SAFARI-like instrument (Chapter 2). As such, the requirements of the instrument were set by the resolving power and waveband of the SAFARI instrument. The spectral range of the instrument has been extended to longer wavelengths to allow for less-stringent mechanical/optical tolerances and to allow the use of existent calibration sources. The requirements are detailed in Table 6.1.

Table 6.1: FPI/grating instrument requirements

Parameter	**Value**
Waveband	220 µm to 300 µm
Resolving Power	>3000
Beam Diameter	40 mm
Operational Temperature	<6 K

To show the overall interaction between components of the instrument, a block diagram is given in Figure 6.1. Both the FPI and grating have active components which are controlled by external electronics. In the case of the grating, a cryogenic stepper motor and worm-wheel drive tilt the grating, with a magnetic reed switch providing a unique angular reference point. In the case of the FPI, a pendulum, into which is built a monolithic rooftop mirror, is used to vary the incident angle of the beam on the etalon. The pendulum is driven by two RVCAs and it receives constant position feedback from a custom-built laser interferometer, described in Section 6.2.4.

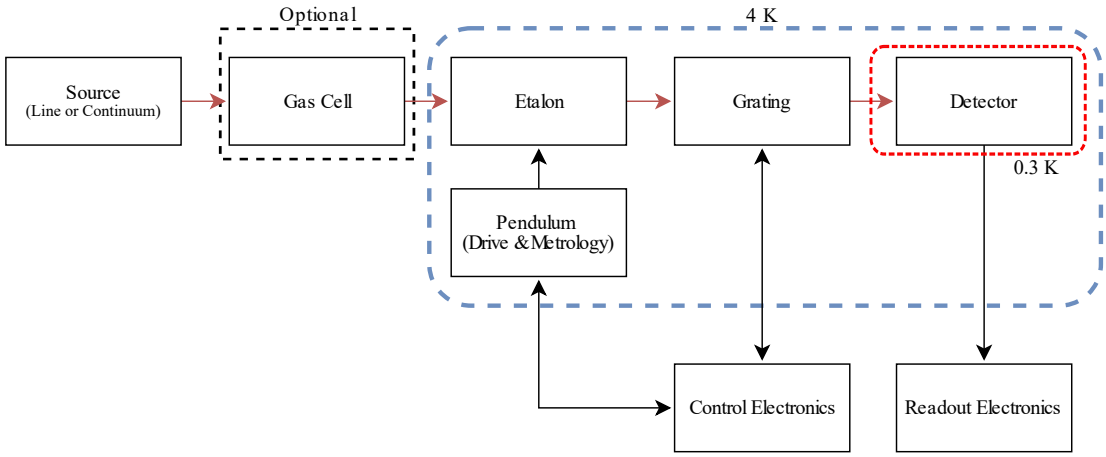

Figure 6.1: System level block diagram for FP/Grating Instrument. The horizontal path indicates the path that light takes from the source to detector.

6.1.2 Source Design

From Chapter 4, several methods for wavelength calibration were considered. The most convenient method is the use of the THz photomixer, as it provides a fully tunable narrow-line source at any point in the wavelength range of the instrument. However, other calibration sources were also considered, such as an HCl/DCl gas cell measured in absorption. In addition, the possibility of using the gas cell in emission was also considered, and this is detailed in Chapter 8. Chapter 4 also introduces the HCl/DCl gas cell concept, in which a pair of absorption line doublets are introduced in the waveband of the instrument. These doublets cannot be resolved by the grating alone, but are easily resolved by the FPI. An inert molecular gas such as N_2 may be introduced into the gas cell to pressure broaden the lines. In order to characterize the gas cell, the HCl/DCl gas cell could be illuminated by the THz photomixer. As discussed in Chapter 4, by tuning the diode lasers in the photomixer, the output THz frequency could be swept through the gas absorption features to profile the lines. The gas cell could then be used to impose narrow absorption lines on a background continuum source, which could then be used to calibrate the spectrometer. To accommodate the gas cell and either the blackbody or photomixer source, I developed an optical system, external to the cryostat, into which the gas cell could be inserted. The mirror

system was also designed to transform the ∼f/4 output of the photomixer to an f/8 output for the FP/grating system. Since an f/8 beam was required at the grating output due to the size constraints of the cryostat and detector system (detailed in Chapter 5), the input f-number was matched to avoid reduction in the resolving power of the grating by unnecessary magnification of the entrance slit.

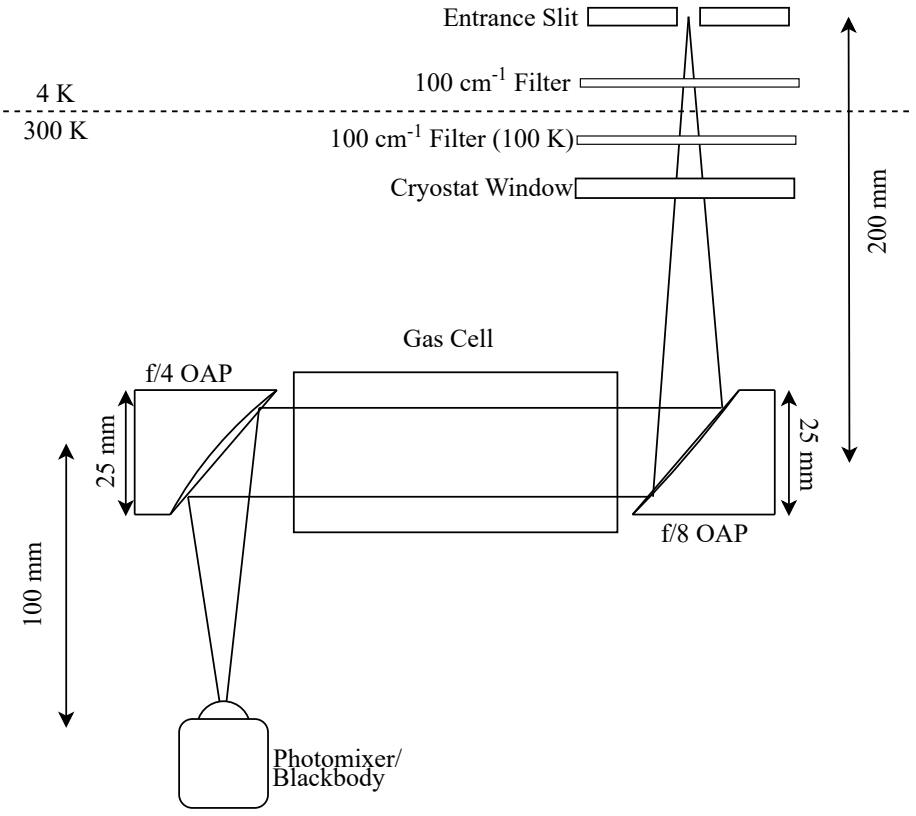

Figure 6.2: Optical components of the room temperature calibration sources.

6.1.3 FP Optical Design

The f/8 beam from the source optics was directed into the cryostat so that the focus was at the spectrometer entrance slit on the 4 K plate. Thermal filters were placed in this converging beam, on the vacuum chamber, and 1st and 2nd stage shields ($100\,\mathrm{cm}^{-1}$ low-pass) as listed in Table 6.2. Beyond the entrance slit, a collimator and plane mirror were used to direct the beam towards the rooftop mirror formed from the

pendulum assembly. The collimating mirror was a 50.8 mm f/6 OAP mirror, so that the mirror size was not the limiting diameter of the beam. With the etalon placed between the pivoting mirrors, the incident angle of the beam on the etalon surface was changed without affecting the beam orientation outside the rooftop. The etalon holder contained absorbing panels which served as the aperture stop for the optical system. Beyond the rooftop, the beam was directed through a fourth filter (50 cm^{-1} low-pass) mounted on the grating radiation shields and into the grating assembly.

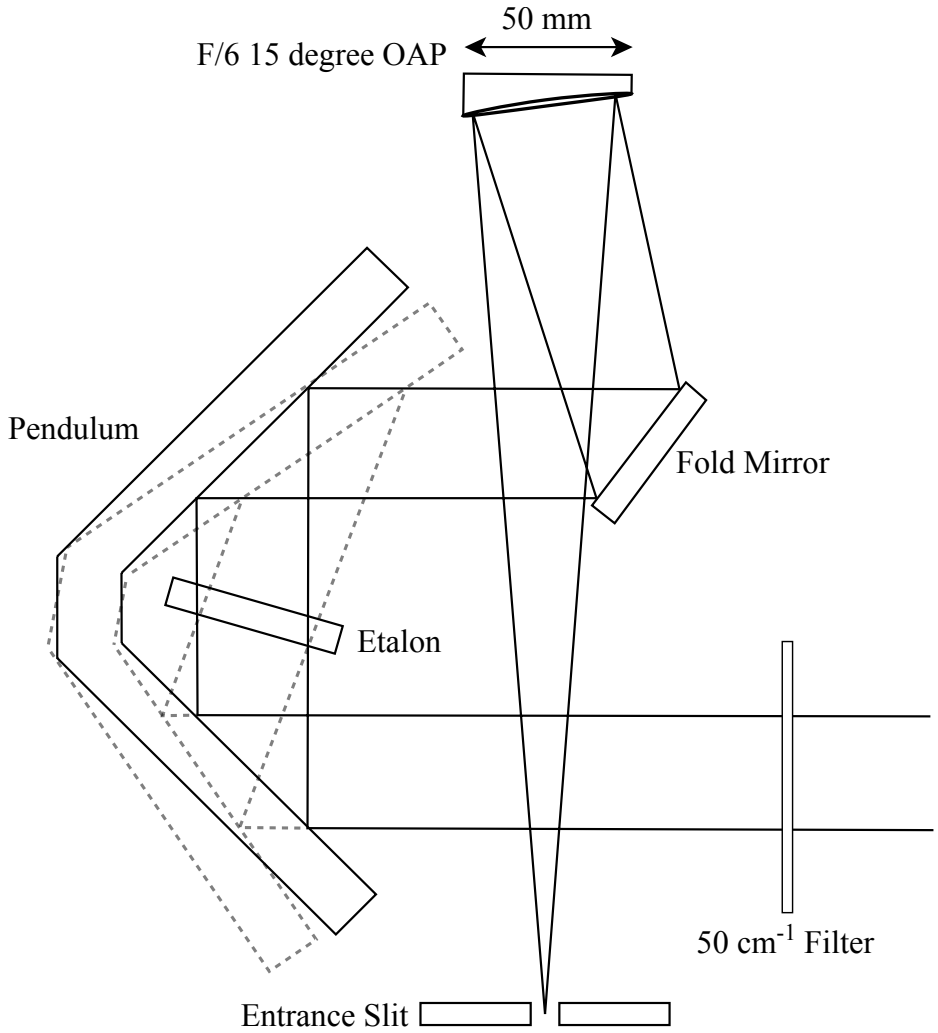

Figure 6.3: Sketch of the optical layout for the FP. The schematic shows two positions of the pendulum, highlighting the change in beam angle with respect to the etalon. Since the pendulum pivots about the apex defined by the rooftop mirror, the output beam location does not change.

Table 6.2: Thermal filters

Location	**Temperature** [K]	**O.D.** [mm]	**C.A.** [mm]	**Cut-off Frequency** [cm^{-1}]
Vacuum Window	300	60	50	100
1st Stage Shields	50	50	40	100
2nd Stage Shields	4	50	40	100
Grating Shields	4	50	40	50

6.1.4 Grating Design

The grating module, shown in Figure 6.4, consists of a flat folding mirror which redirects a collimated beam towards the grating. The rotating grating then tilts the diffracted beam out of the plane defined by the incident optical beam, and the diffracted beam is directed towards a final off-axis parabola which focusses the beam on the exit slit, as shown in Figure 6.4. The detector and feedhorn are situated immediately behind the exit slit to capture all transmitted light. In the ideal case, all the light transmitted through the entrance slit, located before the FPI, is transmitted through the exit slit. However, as shown in Chapter 3, the size of the image of the entrance slit is wavelength dependent.

6.1.5 Detector Design

A Ge:Ga composite bolometer with a nominal NEP of $10^{-16}\,W/\sqrt{Hz}$ at 0.3 K was selected for characterizing the spectral response of the FPI/grating [83]. The detector is cooled to <300 mK with a Chase Research Cryogenics He-10 refrigerator (one ^{4}He stage and two ^{3}He stages) [84], which is contained in the 4 K region of the instrument cryostat, encased within an individual set of radiation shields cooled to 4 K. The He-10 fridge was newly installed in the instrument cryostat, and I completed the detector wiring, and wrote custom software to perform the requisite cooling cycle.

Along with the bolometer element, the detector consists of an integrating cavity and an f/3 feed horn (Figure 6.5). The feed horn serves to concentrate the incident

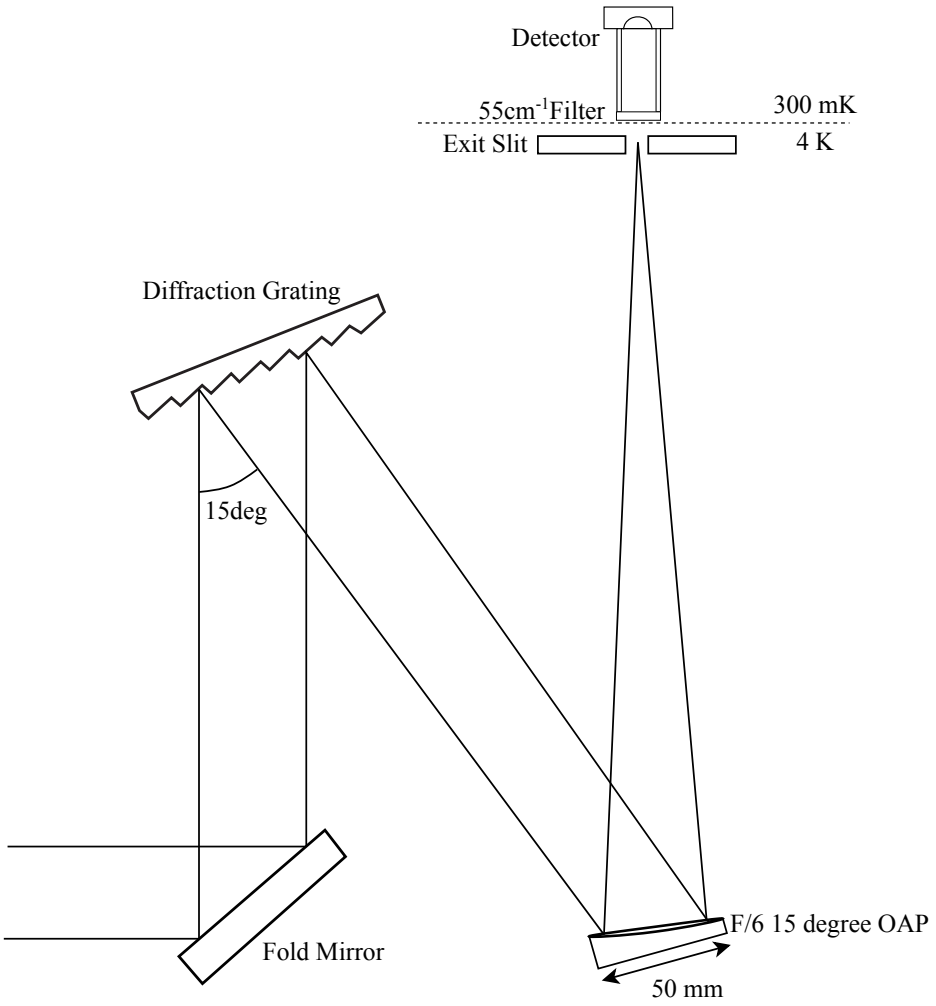

Figure 6.4: Sketch of the optical layout for the diffraction grating and detector.

radiation from the slit onto the bolometer element, and the integrating cavity serves to redirect radiation which is not immediately absorbed back to the bolometer. Both components serve to maximize the overall absorption efficiency of the detector.

The detector was re-purposed from a previous project, so the attached feedhorn (f/3) did not match the camera optics of the grating (∼f/8). However, the exit slit served as a mask, so that the wider acceptance angle of the feedhorn only viewed the 4 K edges of the slit holder. The detector horn also was fitted with a $55\,\mathrm{cm}^{-1}$ low-pass filter, which was cooled to <300 mK with the rest of the detector elements, to prevent any further stray radiation from other parts of the cryostat from reaching the detector.

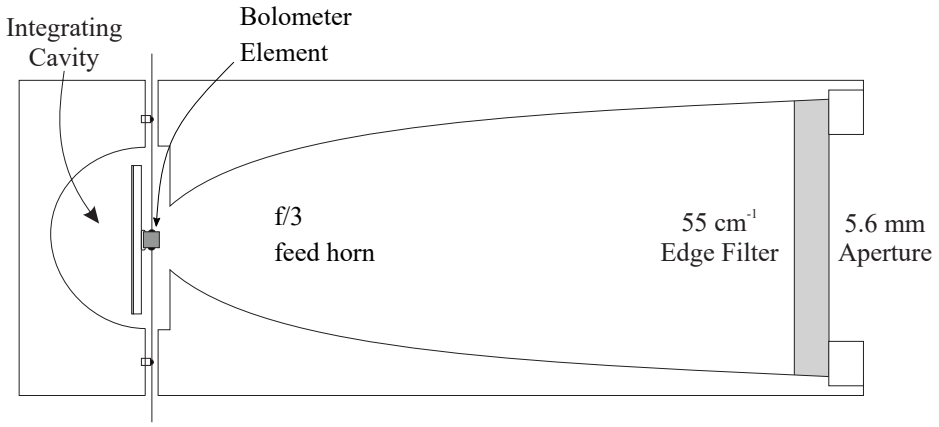

Figure 6.5: Sketch of the bolometer detector, feed horn, and filter [83].

In order to maximize the signal-to-noise ratio of the detector readout, a lock-in amplifier was utilized, which was synchronized to a mechanical chopper that was placed directly in front of the cryostat window. The frequency response of the detector determined the upper limit to the chopping frequency. From [83], the 3 dB cut-off frequency for the detector response was 52 Hz. However, since the detector operated at a lower temperature, because a fridge with a higher cooling power was used, and due to the lower incident power as a result of the post-dispersion system, the detector had a higher impedance, which when coupled to the stray capacitance of the detector further reduced the cut-off frequency. The new cut-off frequency was found to be 40(2) Hz. The optical chopping frequency was set at 40 Hz to maintain a good detector response while also avoiding $1/f$ noise from the many testing and diagnostic components.

6.1.6 System Integration

All components of the system were mounted within a 4 K cryostat. The cryostat which was used was a large scale, custom-made facility which I designed and built as part of my MSc thesis [82]. The cryostat is further described in Section 6.4. Three dimensional diagrams of the FPI and grating modules on the 4 K optical bench within the cryostat are shown in Figure 6.6.

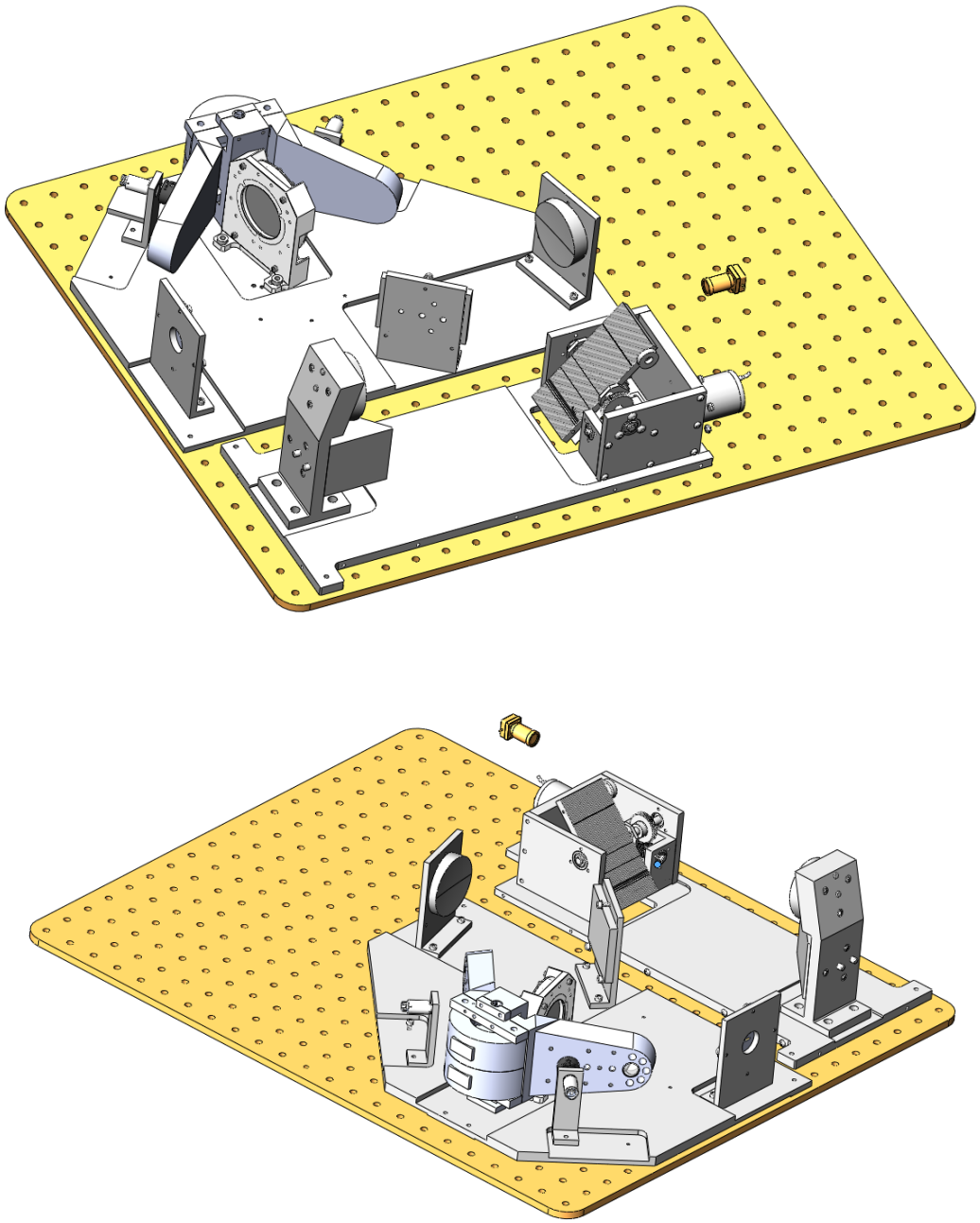

Figure 6.6: 3D model of the grating and FPI on the 4 K plate. The detector is shown, but the He10 fridge is not included for image clarity. Also missing is the exit slit and radiation shields surrounding the grating module and detector.

6.2 Pendulum Design

The dimensions of the etalon were determined by the SAFARI-like resolution and wavelength goals, and are reported in Chapter 3. The specifications for the mechanism

to change the incident angle are set by the angular scan range required to cover one interference order of the etalon. From etalon theory, the incident angular range is determined by the expression:

$$\Delta\theta_i = \sin^{-1}(\frac{\mu\lambda}{4d\sin\theta_0}) \qquad \text{[rad]} \quad (6.1)$$

where λ is the incident wavelength, μ is the refractive index of the etalon substrate, d is the etalon thickness, θ_0 is the resting incident angle, $\Delta\theta_i$ is the single-sided incident angle range. The angular ranges over the designed wavelength range for the chosen etalon with $d = 8\,\text{mm}$ and $\theta_0 = 15°$ are shown in Figure 6.7.

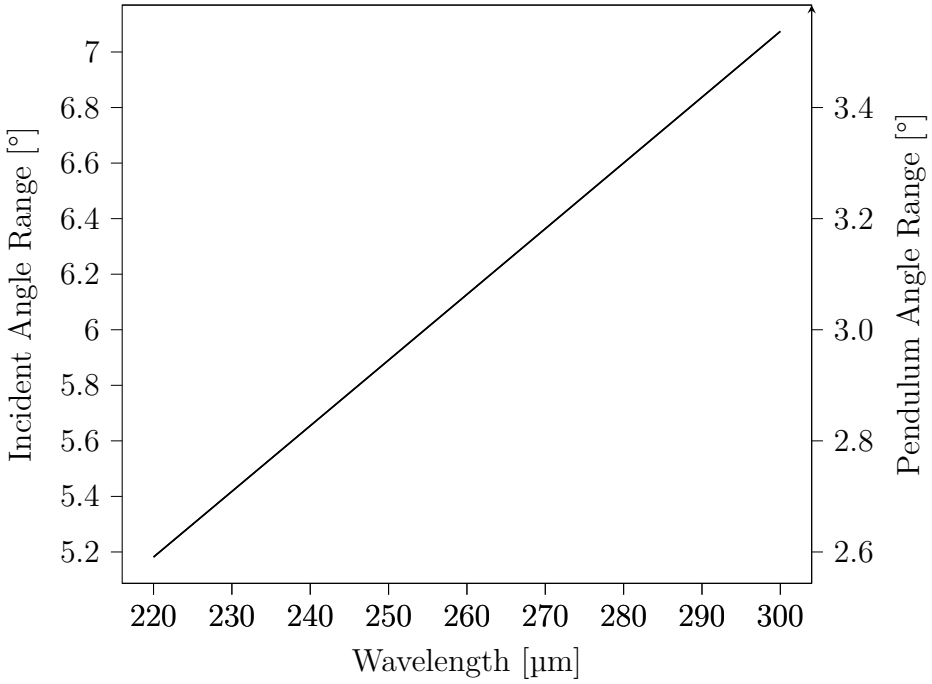

Figure 6.7: The required incident angle and pendulum angle to cover a full order for an etalon with $d = 8\,\text{mm}$, and $\theta_0 = 15°$. Note that these values show the single-ended angular ranges, and the total angular ranges are greater by a factor of 2.

For the etalon described later in Table 6.5, the maximum required scan range was $\sim 7°$ ($\pm 3.5°$), centered around an initial offset angle θ_0 of 15°. I achieved this scan range with a custom-designed and built pivoting rooftop mirror (pendulum) supported by flexure bearings and driven by RVCAs, as shown in Figure 6.8. The

scanning mechanism consisted of a pair of orthogonal mirrors which pivoted about the apex, and was machined from a monolithic block of aluminium. Two flexure bearings were used in the design to balance out radial forces on the bearings. Two voice coil actuators served to actuate the scanning arm, rotating the arm to various angles. The voice coils could also be configured to repel each other to increase stability in the center of the swing, where the restoring force of the flexures was small. The entire assembly was mounted on a post which was fastened to an aluminum base plate, which also held the etalon mount, to help maintain alignment between these components during cooling. The copper wire coils were fastened to the post, while the magnets swung with the arm. The magnets served as a counterweight in this configuration, which also conferred the advantage of having no moving wires. Position measurement of the arm was performed by a three-phase laser interferometer illuminating two corner cube retroreflectors on the back of the arm. The maximum scan range allowed by the mechanical limits of the flexures was set by bumpers on the interior of the pendulum arm to $\pm 7°$. Note that the mechanical scan range was designed to accommodate an incident angle range from $\pm 14°$ of the initial offset to allow for a thinner etalon, a longer wavelength range, or a smaller offset angle if needed.

6.2.1 Pendulum

The pendulum was manufactured to my design by B-Con Engineering [101] from a monolithic block of aluminum. A mirror finish was applied to the orthogonal faces of the inside arms by diamond-turning, with the mirrors positioned $90.00(5)°$ with respect to each other. The flexure was positioned at the apex of the mirrors, so that the distance between the parallel input and output beams did not change during scanning. The magnets from the RVCAs were attached to the moving arm, while the coil was attached to the supporting post. Mounting holes were placed on the backs of each arm for retroreflector targets which were used with a fiber-based laser

interferometer metrology system discussed later in Section 6.2.4.

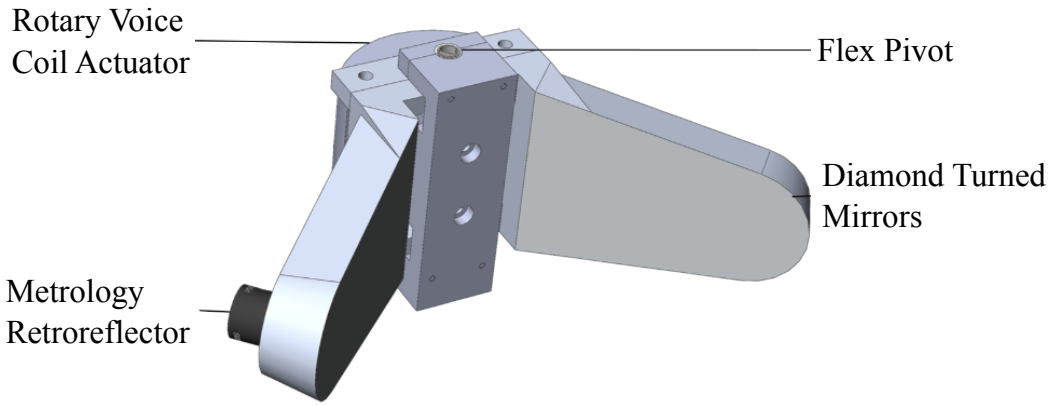

(a) The pendulum consists of a monolithic aluminum frame and is driven by rotary voice coils around a flex-pivot bearing. Metrology retroreflectors on the back of both arms provide a reference for the laser metrology.

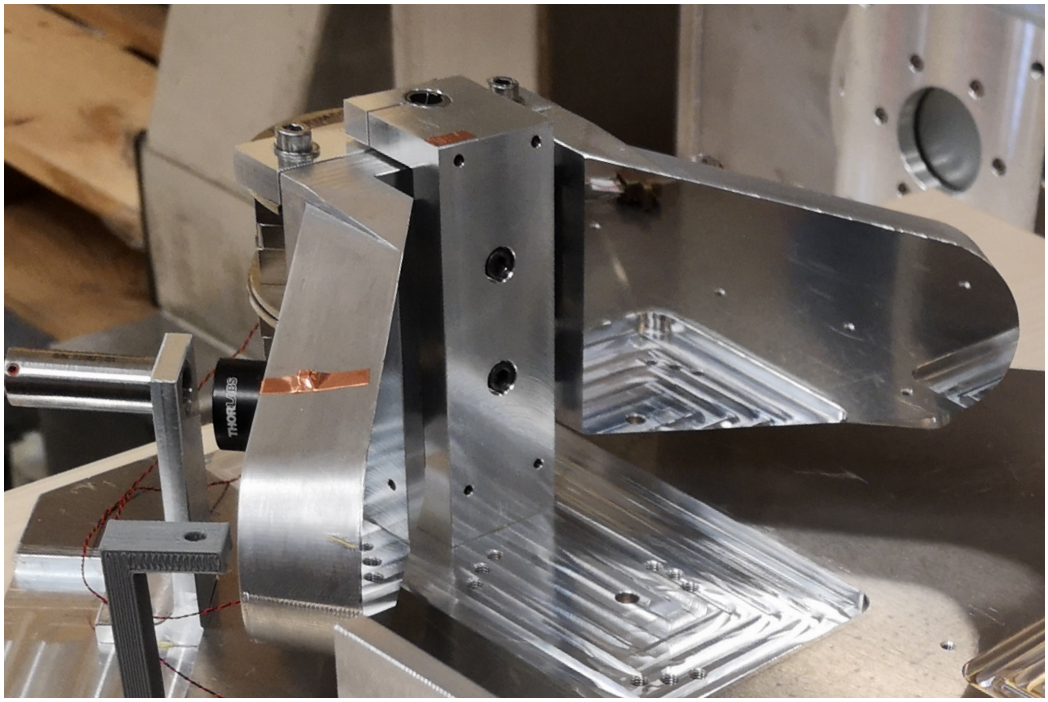

(b) The pendulum as built.

Figure 6.8: The FPI pendulum.

6.2.2 Rotary Voice Coil

The RVCAs selected were based on BEI Kimco RA29 actuators [107]. Custom RVCAs were designed to the same specifications as these, but using SmCo magnets rather than the COTS NdFeB magnets. Unlike NdFeB magnets, SmCo magnets do

not lose their field strength at cryogenic temperatures. With the magnets acting as counterweights to the pendulum, the magnets moved while the coil remained stationary, thereby reducing the stresses and wear on the electrical wires at low temperatures. The quoted specifications for the RVCAs, given in Table 6.3 were estimated by scaling the manufacturing specifications of the COTS NdFeB RVCAs by the relative residual flux density of the SmCo magnets and the NdFeB magnets. From [108], the minimum ratio (i.e. worst case) from the listed ranges of magnetic remanence for these magnetic materials was found to be 0.6(1). The system was "over designed" such that the weaker SmCo magnets would not impose a limitation on the scan range. In addition, two RVCAs were placed in parallel to allow doubling of the torque at high angles, and a varying restoring force near the midpoint of the swing, where the flexure restoring force was small.

Table 6.3: RVCA estimated specifications. The angle sensitivity and maximum current were determined using the flexure specifications from Table 6.4.

Parameter	**Value**
Scan Range	16°
Continuous Torque	$0.044(1)\,\mathrm{N\,m}$
Torque Sensitivity	$0.068(1)\,\mathrm{N\,m\,A^{-1}}$
Angle Sensitivity	$13(1)\,^\circ\,\mathrm{A^{-1}}$
Maximum Current	$0.56(1)\,\mathrm{A}$

6.2.3 Flexures

C-Flex F-20 flexures [109] with a maximum deflection of ±7.5° were chosen for the scanning pendulum. These flexures were modified to have Inconel 718 flexure blades, which retain their flexibility while operating at cryogenic temperatures [110]. Furthermore, these very flexures have space flight heritage, having been used in the Heterodyne Instrument for the Far Infrared (HIFI) focal plane chopper [111]. The flexures procured from C-Flex were, in fact, the spare flexures which were originally

manufactured for HIFI. Two flexures were incorporated into the design for stability, and to decrease the radial load (to avoid moment loading on the bearings). The flexures are also positioned at the apex of the mirrors to avoid shear of the beam as the pendulum pivots. These flexures were chosen for the scanning pendulum, because they were strong enough to support the required loads (Table 6.4), yet had a low enough spring constant to allow for the full angular travel using relatively low supplied current from the RVCAs in the above section. The specifications are given for the COTS spring steel bearings (stainless steel grade 420), and must be estimated for the Inconel 718 flexures. The spring rate was estimated by scaling the COTS specifications for the steel flexures by the ratio of the Young's modulus of Inconel 718 and SS 420. From material properties listed in [109] and [112], the ratio was found to be 1.0(1). Likewise, the load capacity was estimated by scaling the COTS specifications by the ratio of the yield strength of the two materials. From the sources above, the minimum ratio (i.e. worst case scenario) was found to be 1.5(1). As shown in Table 6.4, the loads were well below their respective limits.

Table 6.4: Estimated flexure specifications found by scaling the manufacturer specifications to the appropriate material.

Parameter	**Value**
Torsional Spring Rate	$0.31(1)\,\mathrm{N\,m\,rad^{-1}}$
Radial Load	$<90\,\mathrm{N}$
Radial Load Capacity	$1.1\,\mathrm{kN}$
Axial Load:	$\sim 20\,\mathrm{N}$
Axial Load Capacity	$4.9\,\mathrm{kN}$

6.2.4 Metrology

Position measurement of the pendulum was accomplished with a laser interferometer. While there are many ways to record position at cryogenic temperatures, laser interference remains the most accurate method over the largest range, yet also

remains the least explored method [113]. Since a similar laser interferometer position measurement system will be used on the SAFARI FTS [114], this allowed for a unique opportunity to develop and demonstrate a functioning prototype of the sensor in a low temperature, high vacuum environment, similar to the environment on the SAFARI instrument.

The laser metrology system is an incremental encoder; it does not measure absolute position but records incremental changes in position. In the absence of noise, single directional displacement is easily measured with a simple monochromatic interferometer setup, by measuring incremental phase changes between the reference and measurement laser beams. However, to determine direction in a bi-directional scan, quadrature encoding is required. With two input signals which are 90° out of phase with each other, the sign of the phase difference indicates the direction of motion.

Producing two laser signals which are 90° out of phase with respect to each other in single-mode fiber optic cables would have required using two of the four outputs of a 4x4 fiber beamsplitter. Since 50 % of the output laser power is not used in this case, two alternative methods of producing out-of-phase signals from which quadrature could be recovered were explored. The first used a three-way beam divider which gave three interference signals exactly 120° out of phase with each other; and the other method was using frequency modulation (FM) of the laser. At the time of writing, the three-phase system has been fully characterized, but the FM system was not able to perform real-time measurements, so the three-phase system was used exclusively for the results presented in this thesis.

Three Phase Metrology

Precision metrology at cryogenic temperatures (4 K) is challenging. In a recent paper, I reported on the performance of a fiber-fed, cryogenic, homodyne interferometer, which was developed for the three-phase position measurement technique [115].

In this design, a circulator guides light from a 1550 nm single mode DFB laser to a 3x3 splitter. The first output from the 3x3 splitter was terminated, the second contained an integrated reflector to return the reference beam back up the fiber, and the third output directed the measurement beam to the 4 K working surface via an optical fiber 2 m in length. The measurement beam illuminated a retroreflector target on the back of one arm of the pendulum described in Section 6.2.1. The return signals (two from the splitter and one from the circulator) were 120° out of phase with one another and were used to generate quadrature signals via the Clarke transform [116]. While this system performed well, it was clear that the performance could be significantly improved by carrying both the reference and probe outputs in a custom, armored, dual core fiber to the cryogenic workspace as shown in Figure 6.9, thereby minimizing length variations in the 2 m fiber during cool-down that may arise from vibrations. In effect, the dual core fiber provides common-mode noise rejection of the fiber fed laser signal.

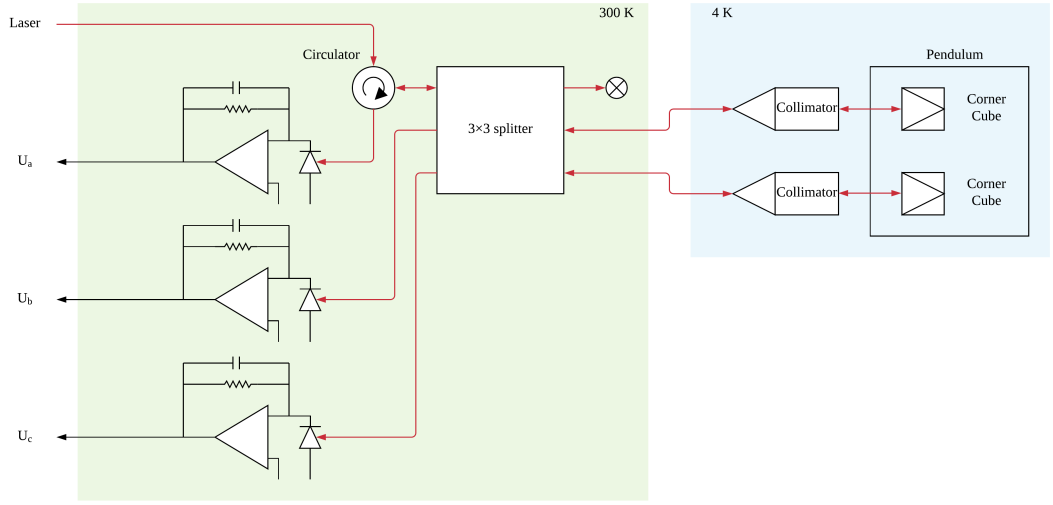

Figure 6.9: Schematic diagram of the three-phase interferometer. Red arrows indicate fiber connections. The unit, including the laser, operates under vacuum at room temperature. A custom, armoured dual core fiber carries the probe and reference beams to the 4 K workspace. The lengths of the two fibers differ by less than 0.5%.

This collimated outputs from the dual core fiber are directed to corner cube re-

flectors mounted on each of the pendulum arms (Figure 6.10). In this configuration, the resulting optical path difference between the interfering beams was four times the displacement of one pendulum arm. The signal processing steps are shown in another paper on the performance of the cryogenic laser metrology system [117], which is reproduced in Appendix D.

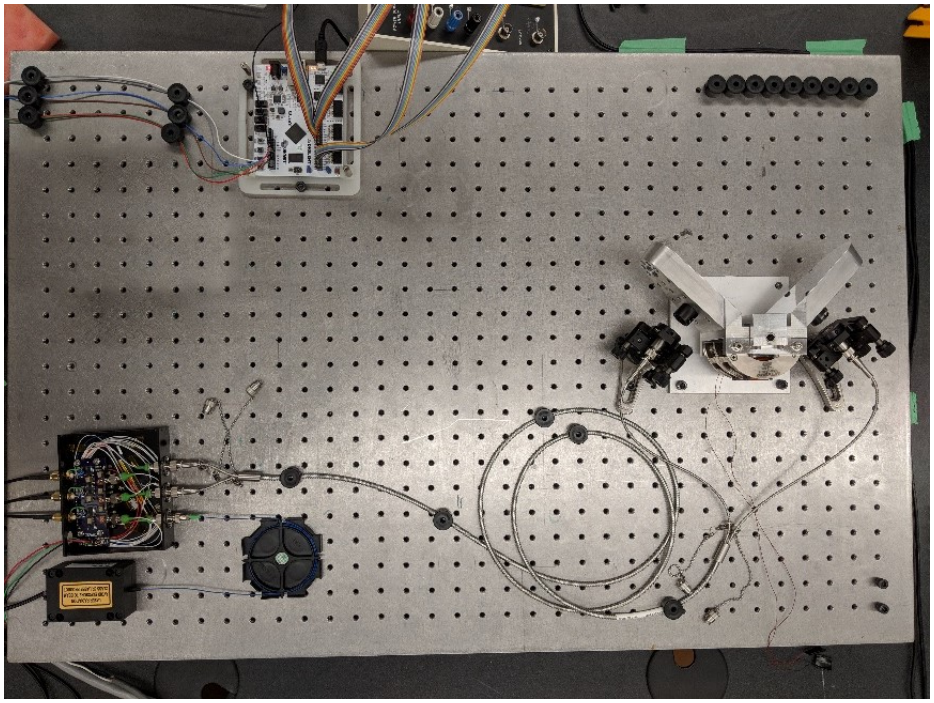

Figure 6.10: Dual core fiber metrology system. DFB laser (lower left), photonics module (immediately above laser), armored, dual core fiber connected to fiber collimators which launch beams to retroreflectors mounted on the pendulum arms.

In order to measure the position uncertainty in the metrology system, the rooftop mirror was driven at its natural resonance frequency, and optical displacement was measured at 100 kHz over a short distance near the middle of the travel range. The displacement data were fitted with a second order polynomial and the optical path uncertainty was defined as the RMS of the residual (Figure 6.11). Since the optical path difference was greater than the mechanical path by a factor of 4, the optical path uncertainty of 9.1 nm corresponded to a position uncertainty of 2.3 nm. This is an impressive result for a position measurement sensor at 4 K! Previous FIR space

missions involving a cryogenic metrology component have typically had uncertainties on the order of 1 µm.

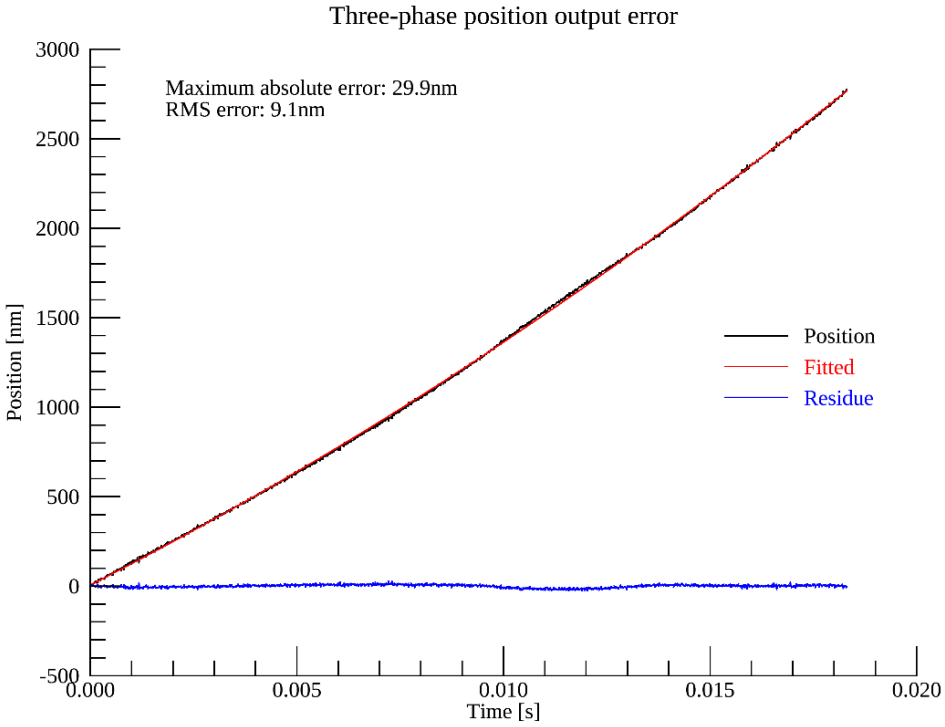

Figure 6.11: Residual error from pendulum scanning of 9.1 nm in optical path which is equivalent to a displacement uncertainty of 2.3 nm.

6.3 Etalon Development

As discussed in Chapter 3, round trip *walk-off* for a non-normal incident beam on an FP etalon can be expressed as,

$$W = 2d \tan \theta_t \qquad \text{[mm]} \quad (6.2)$$

which depends on the physical gap between the etalon plates d, and the transmitted angle θ_t. Thus, one of the ways to reduce the effects of *walk-off* is to use a thinner etalon with a high refractive index material such as silicon ($\mu = 3.4$). Since a thinner

etalon with a higher refractive index may be used to produce the same phase difference effects (Equation (3.1)), the effects of *walk-off* are diminished, as shown in Figure 6.12.

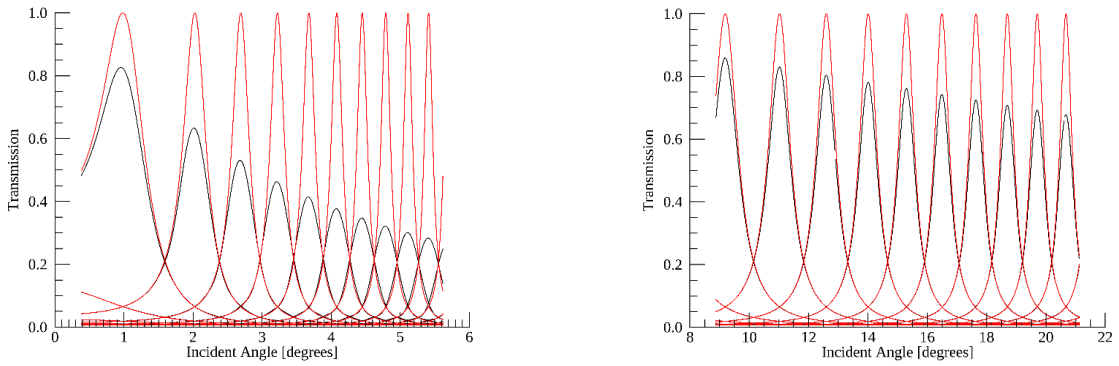

Figure 6.12: Comparison of the transmission function of an ideal FPI (red) versus an angle-scanned FPI (black). The left plot shows an airgap etalon with an offset of 3°, and the right plot shows a silicon etalon ($\mu = 3.4$) with an offset angle of 15°.

As mentioned above, the etalon substrate was a slab of high resisitivity, float zone (HRFZ) silicon in order to reduce the effects of geometric *walk-off* with the high refractive index, and minimize absorption with the high-resistivity. However, absorption in a dielectric substrate significantly reduces the peak transmitted intensity of the etalon. Furthermore, the loss tangent of silicon is not well characterized at cryogenic temperatures. HRFZ-Si samples were procured by SRON in order to measure the temperature effects on the silicon absorption properties. These measurements were included in our model to optimize the design of the angle-scanned Fabry-Pérot interferometer.

Two different methods of applying a reflective surface to the polished plane-parallel HRFZ-Si etalon substrate were initially discussed. In the first, a dielectric stacked mirror coating was manufactured using a DRIE procedure developed by SRON. Thin HRFZ-Si wafers were ground and polished to an appropriate thickness for high reflectivity at the desired wavelengths. The wafers contained an etched airgap retaining a support ring with venting holes, and were fusion bonded or epoxied to the silicon substrate to provide an airgap between the wafer and the substrate. The procedure

was repeated on both faces of the etalon substrate. A simple schematic of the device is shown in Figure 6.13a and an image of the manufactured etalon within its cryogenic mount is shown in Figure 6.13b. In this way, a H/L/H dielectric stack on both sides of the etalon was achieved to provide high reflectivity. The effective reflectivity of the etalon was modelled using the multiplication of transfer matrices for the consecutive optical interfaces, described in Chapter 3.

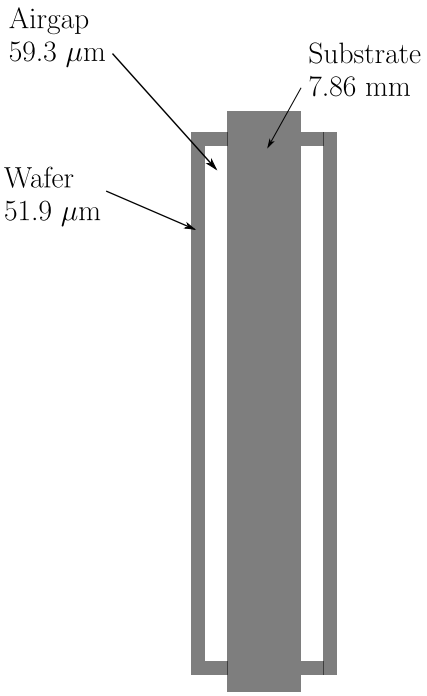

(a) Cross section of the etalon showing the wafer-airgap-substrate-airgap-wafer structure. Not to scale. The substrate has a slightly larger diameter than the wafer-airgap structure in order to be held by the cryogenic mount without damaging the delicate wafer.

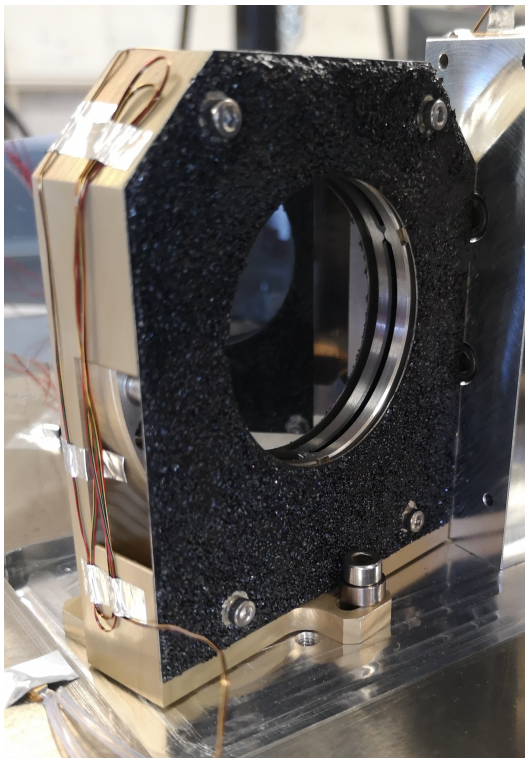

(b) An image of the completed etalon within its cryogenic mount. The edges of the mount are coated with black epoxy and carborundum pellets to absorb stray light.

Figure 6.13

The second method we explored, through a collaboration with Prof. Peter Ade at Cardiff University, was to mount reflective metal-mesh reflectors close to the etalon surfaces [69]. A small spacing between the mesh and etalon substrate was required to make use of Fresnel reflections from the etalon surface. Although a metal-mesh

silicon etalon has shown promising results in the literature [118], a complete etalon was not tested in this instrument. Although this was initially considered the lowest risk approach, the fitting of metal-mesh filters to the silicon surfaces with a high-degree of parallelism proved challenging. At the same time, because of the significant advances being made on the DRIE etalon – which was initially deemed the higher risk approach – this became the etalon of choice.

Both etalon arrangements were to be mounted in a cryogenic holder containing SPIRA spring gaskets [119], so that differential thermal contraction between the holder and the etalon did not result in deformation or damage to the etalon surfaces (Figure 6.14). The etalon holder was mounted to a fixed base plate with the potential to set an initial offset angle between 0° and 15°. The specifications of the fully silicon etalon as built, including the physical dimensions and spectral properties are shown in Table 6.5.

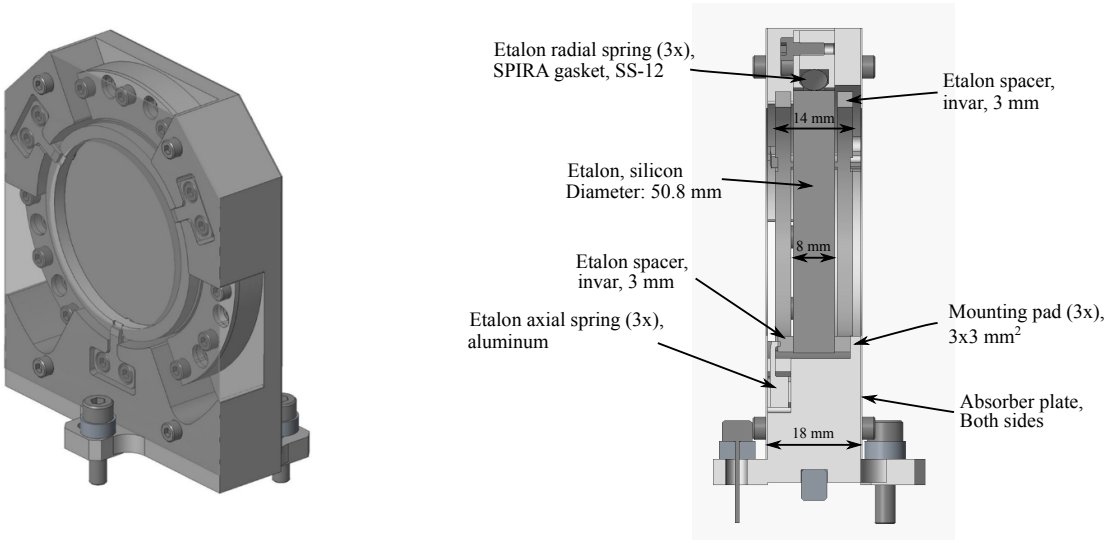

Figure 6.14: The etalon substrate is mounted in a custom-made aluminum frame for cryogenic use. The etalon is suspended within the frame using SPIRA flexible gaskets [119] so that differential thermal contraction between the mount and etalon does not damage the optics.

Table 6.5: Etalon specifications

Parameter	**Minimum**	**Nominal**	**Maximum**
Wavelength	220 µm	236 µm	300 µm
Diameter (OD)	50 mm	50.8 mm	52 mm
Clear Aperture (ID)	43 mm	45 mm	50 mm
Beam Diameter		40 mm	
Refractive Index		3.4	
Thickness	7.6 mm	8 mm	12 mm
Angle of Incidence (AoI)	0°	15°	15°
Order	180	230	247
Finesse	12.1	13.0	16.7
FSR	0.9 µm	1.0 µm	1.7 µm
Spectral Resolving Power	3000	3000	11000

6.4 Test Facility Cryostat

Cryogenic testing of the angle-scanned etalon concept required a large-scale cryogenic facility to house the etalon, accompanying filters, optical elements, mechanisms, and detector. The TFC shown in Figure 6.15 is a 4 K cryogenic facility, which is cooled by two Cryomech PT415 pulse tube coolers [120] operating in parallel. The internal 4 K volume is ∼70 L with a total cooling power of 3 W at 4 K, allowing for the testing of large optical systems in a cold environment. A Chase Research Cryogenics He-10 cooler operating within the cryostat can sustain a temperature of 225 mK for 20 hours with a heat load of 4 µW, making it suitable for operation of a wide selection of detectors [84]. The cryostat is also fitted with polypropylene windows to allow for the injection of far infrared radiation from external sources. The aforementioned thermal filters on the intermediate radiation shields further limit the radiant loading into the 4 K volume. For a full description of the cryostat design and construction, the reader is referred to my MSc thesis [82].

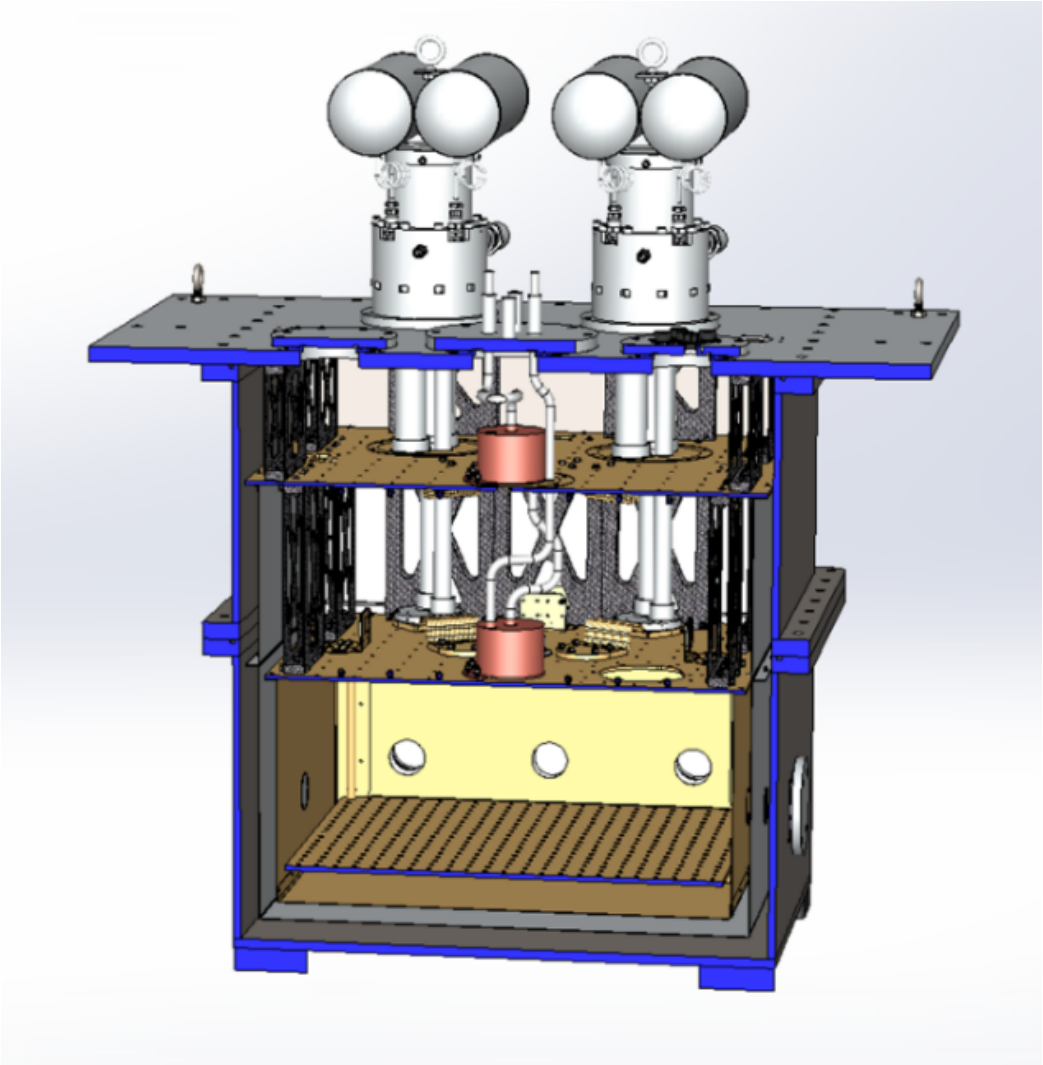

Figure 6.15: The TFC uses two Cryomech PT415 coolers to cool a 70 L volume to 4 K. The rectangular design allows for a selection of viewports, and the CFRP support plates and flexible thermal straps provide vibration isolation from the PTCs.

6.5 Control Software

The spectral acquisition process was performed by a Python 3 script which communicated with the stepper motor controller for the grating drive, arbitrary function generator controlling the pendulum position, and a data acquisition board which collected signals from the output of the lock-in amplifier, limit switches of the grating and pendulum, and position feedback from the pendulum. The scanning sequence involved stepping the grating to a known position and sweeping the pendulum through

an order of the FPI centered around the grating passband. This process was repeated for each grating position in the requested wavelength range. A full overview of the control software and operating modes of the instrument are given in Chapter 7 and Appendix C.

6.6 Conclusion

In summary, I have designed and built a cryogenic FPI/Grating spectrometer for measuring the angle-scanned etalon concept. The operation of all mechanisms of the instrument has been verified at both room temperature and 4 K. I have coupled the output to a bolometer detector to measure the resultant spectra. In the next chapter, I will discuss results from the first light measurements of the etalon, including wavelength calibration and fitting of the FPI transmission profile.

Chapter 7

Instrument Operation, Data Processing and Calibration

> I have approximate answers and possible beliefs in different degrees of certainty about different things, but I am not absolutely sure of anything, and of many things I don't know anything about but I don't have to know an answer.
>
> *The Pleasure of Finding Things Out*
> Richard P. Feynman

In this chapter, I show the first results collected from the FPI/grating instrument. Although a method for flux calibration had not yet been implemented, the spectral response of the instrument was measured, using the calibration sources from Chapter 4, and used to determine the wavelength response and instrumental line shapes. The spectral response of the instrument is the product of the spectral responses of each component. In this instrument, the components were the FPI, the grating, and the detector. From [83], the spectral response of the detector was relatively constant over the instrument wavelength range. The spectral response of the grating was approximated by a Gaussian, and could be tuned by adjusting the angle of the grating. Likewise, the spectral response of the FPI, which was given by the Airy function (Chapter 3), was tunable by adjusting the pendulum angle to change the incident angle of the beam on the etalon surface. In order to measure the combined spectral response of the instrument, a tunable, narrow-band calibration source (eg. the photomixer) was injected into the instrument. By tuning the wavelength of the

calibration source, it traced the spectral response of the instrument. This effect is visualized in Figure 7.1.

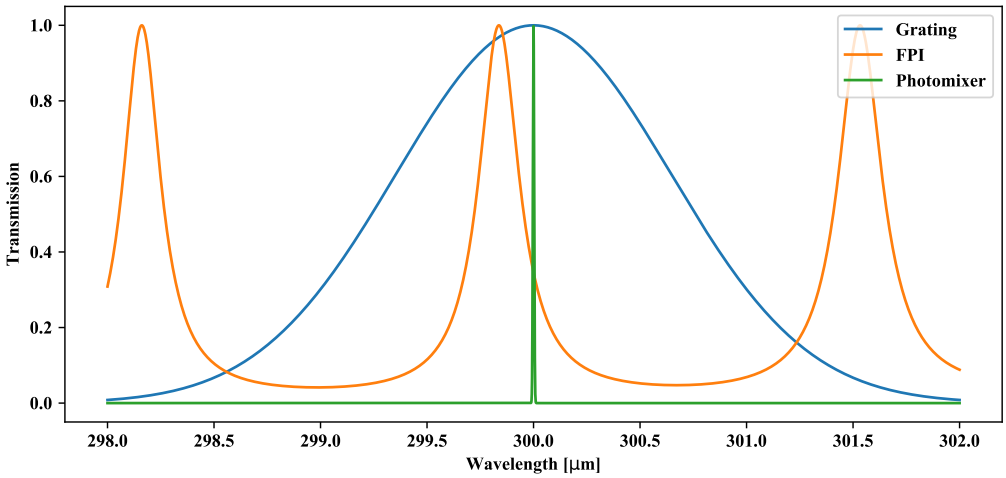

Figure 7.1: The spectral response functions for the grating, FPI, and photomixer. By tilting the grating, rotating the pendulum, or changing the laser temperatures respectively, the spectral response functions could be shifted to higher or lower wavelengths. The measured signal at the detector at any given time was the product of all spectral response functions.

The measurement of the spectral response of the instrument required the coordination of many different hardware components. In order to facilitate these measurements, an automation procedure was developed to handle the synchronization of the tuning of the grating, FPI, and photomixer. This procedure incorporated different modes of operation to account for different calibration procedures, as well as for its normal operation with a steady, broadband source. This chapter will describe these operational modes. In addition, the wavelength calibration of the grating is revisited and the wavelength calibration of the FPI is determined in order to confirm the etalon parameters. Finally, the line profiles of the grating and the FPI are measured using the photomixer and the results are compared to models which include the effects of *walk-off*. However, all measurements required the operation of the instrument at $\sim$4 K. Therefore to begin, the thermal characteristics of the instrument were observed.

7.1 Thermal Characteristics

The temperature profile of the instrument during a normal cooling cycle within the TFC, described in Chapter 6, is described here. The nominal operational temperature of the instrument was 4 K, yet there were still small <1 K temperature variations across the instrument which were due to inefficiencies in thermal coupling between components. However, the effect of these small variation on detector noise was indiscernible at these wavelengths and detector NEPs, so they were not considered a paramount issue. The devices used to measure temperature were Cernox CX-1010-SD thermometer packages [121], configured in a four-wire measurement configuration to avoid contributions of voltage drops through the cryostat wiring. The cryostat thermometer wiring consisted of high resistance American wire gauge (AWG) 39 BeCu or AWG 36 phosphor-bronze wires, which were twisted into two sets of twisted pairs to mitigate electrical pickup. A Lakeshore LS370 AC Resistance Bridge was used to record the resistance readings of each thermometer and apply previously determined calibration curves to produce temperature readings [122]. Thermometers were situated on the instrument as described in Table 7.1. The locations of the thermometers on the FPI/grating are shown in Figure 7.2

The recorded temperatures show a 0.5 K difference between the FPI base plate and the TFC 4 K plate, suggesting the base plate could have benefited from a slightly larger contact area to 4 K. The elevated temperature is likely due to heat dissipation within the voice coil actuators as well as stray radiation absorbed by the black panels around the etalon holder. The components whose temperatures were most critical to measure were the grating, etalon, pendulum and bolometer. While small temperature variations within the instrument could be expected, the design goal was to keep all components of the instrument below 6 K, to keep the peak of thermal emission out of the instrument waveband.

The etalon holder and substrate maintained a <1 K temperature difference during

Table 7.1: Thermometer locations on the FPI/Grating. Thermometer serial numbers are also given.

Channel	**Serial Number**	**Location**
1	X52844	PTC #1 45 K Stage
2	X63594	45 K Plate
3	X63720	PTC #1 4 K Stage
4	X63721	PTC #2 45 K Stage
5	X63519	PTC #2 4 K Stage
6	X62969	0.3 K bolometer Bracket
7	X63596	4 K Plate
8	X63597	Grating Stepper Motor
9	X63600	Grating
10	X63601	Grating Radiation Shield
11	X139053	FP Base Plate
12	X68576	Etalon Substrate
13	X63599	Etalon Holder
14	X139055	FP Pendulum Post
15	X139057	FP Pendulum Arm

the cool down, reaching a <0.05 K temperature difference at 4 K (Figure 7.3) showing that the thermal coupling across the SPIRA gaskets [119] and spring clamps in the etalon holder was adequate. Note that only the temperature of the perimeter of the silicon substrate was measured; it was not possible to measure the temperature of the center of the etalon.

The grating and connected components heated up significantly (∼20 K) when the stepper motor was activated (Figure 7.5). This was anticipated due to the high heat dissipation within the motor, requiring 0.4 A maximum driving current and ∼1 Ω impedance of the coil and 4 K wiring for a total heat dissipation of ∼160 mW at full power. As a comparison, the estimated total cooling power of the TFC at 4 K was ∼1.4 W. The large temperature shifts impacted the bolometer readout, so a way to reduce the heat dissipation was implemented. The solution was to keep the stepper motor inactive as often as possible. This was accomplished by only activating the stepper motor when the grating was actively moved, turning off the holding torque,

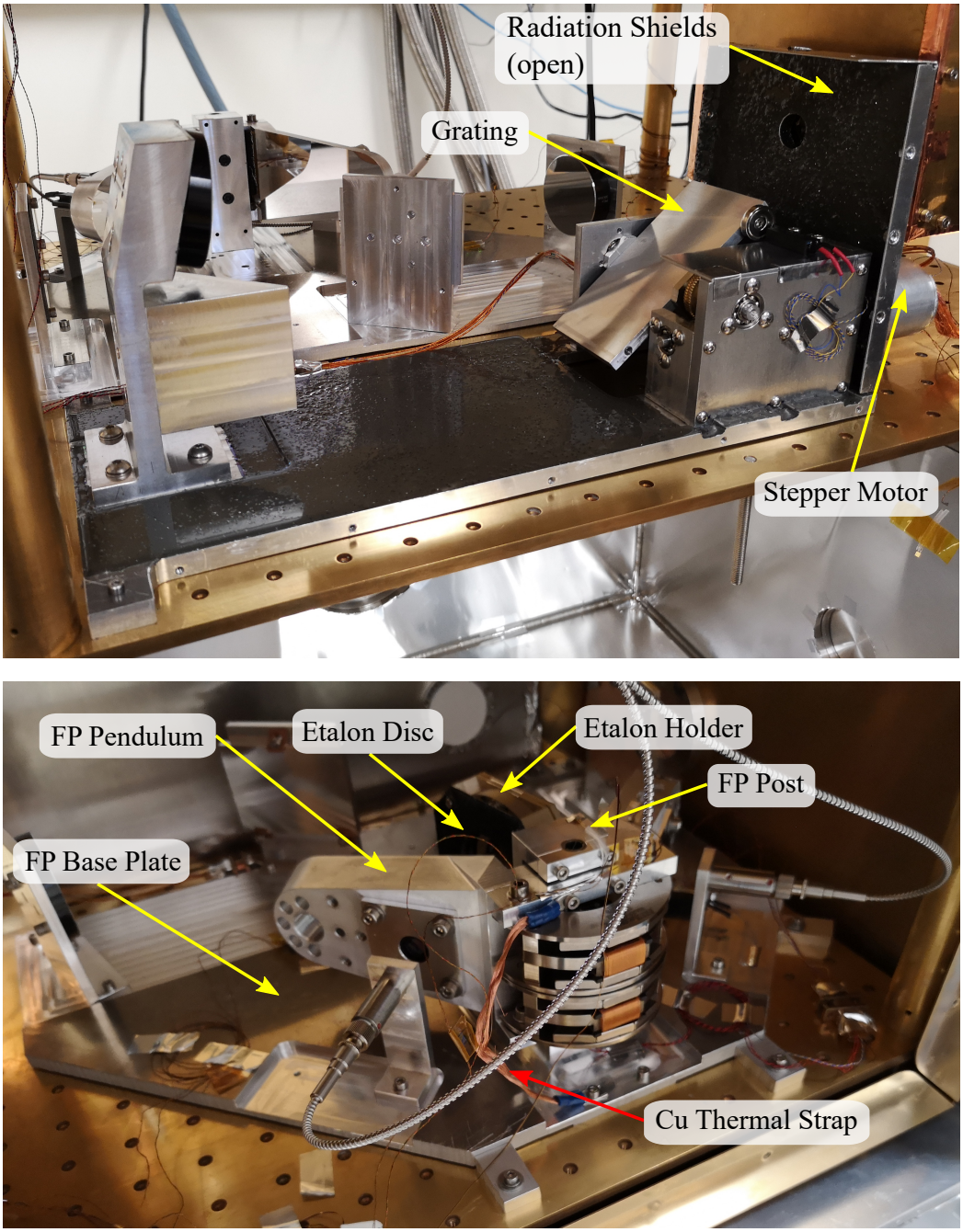

Figure 7.2: Thermometer locations on the FPI/grating (yellow arrows) and the location of a heat strap to facilitate cooling of the pendulum (red arrow).

and relying on the worm-wheel gear train to keep the grating in position between activations. The results showed that even with regular scanning operation, the temperature of the stepper motor and grating were much reduced, limiting the stepper motor temperature to 5 K during activation.

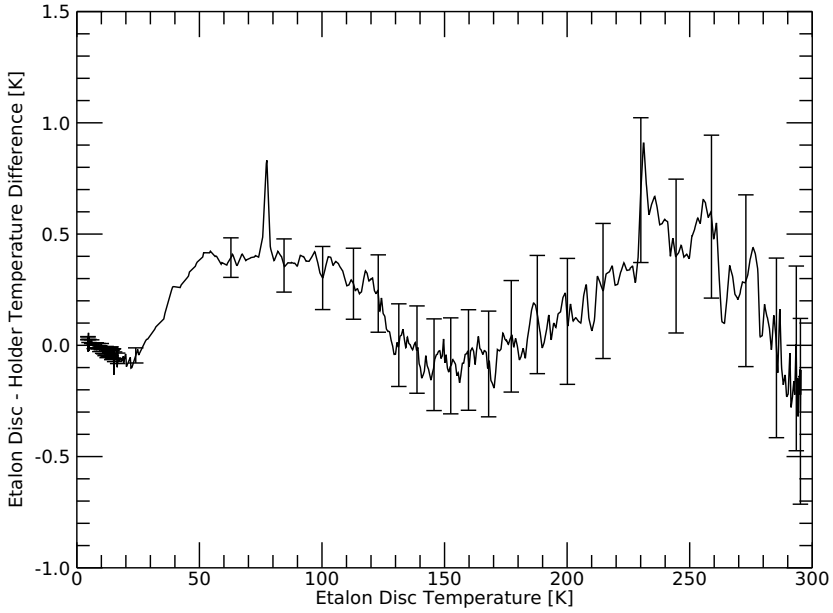

Figure 7.3: Difference in temperature between the etalon disc and the etalon holder during a cooling cycle. Uncertainties are driven by uncertainties in the calibration curves for the thermometers ∼0.1 %

During the first cooldown of the instrument, the pendulum arm temperature lagged behind the other components, requiring ∼40 hours to reach 4 K. The long cooling time was due to the low thermal conductivity of the Inconel flexures, which provided a poor thermal path for heat to escape the pendulum. To increase the cooling rate, two thin, flexible copper heat straps were added to the pendulum (Figure 7.2), which provided an additional heat path, but did not interfere with the motion of the pendulum. The decrease in cooling time is shown in Figure 7.6.

Finally, after thermal cycling of the He10 fridge, the bolometer block reached a temperature of 320 mK, while the temperature of the He10 ultracold stage reached 280 mK. This temperature differential most likely indicated a poor thermal contact between the bolometer mount or bolometer wiring and the He10 coldhead.

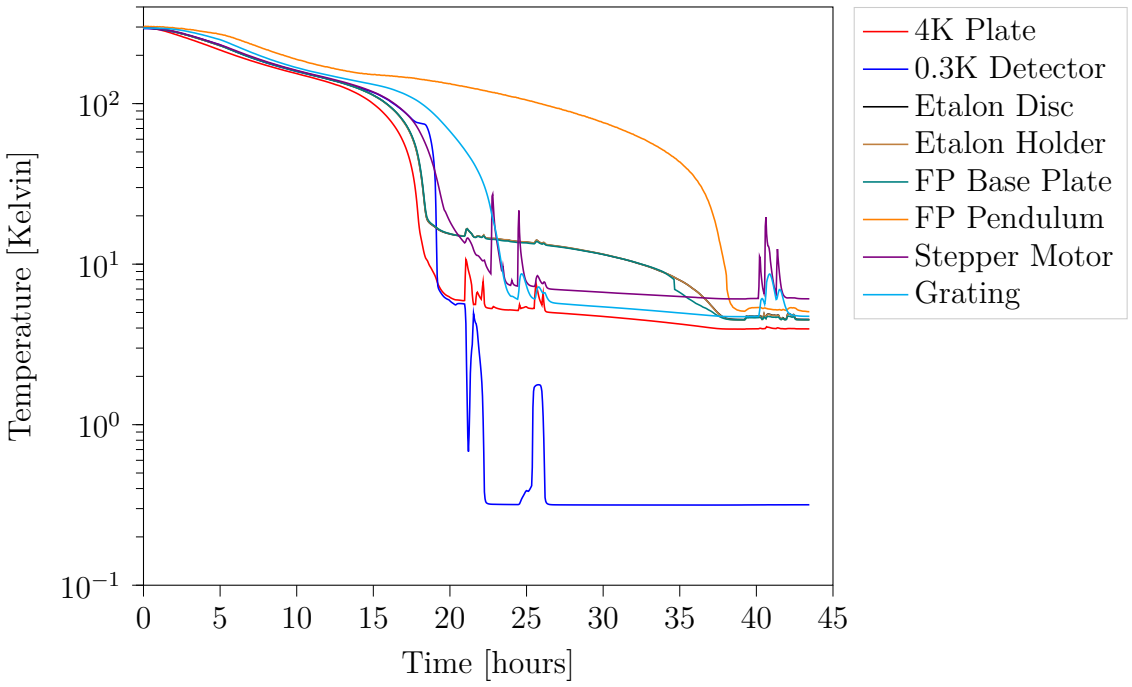

Figure 7.4: Temperatures of components of the instrument during a cooling cycle to 4 K. Temperature spikes between 20 hours to 27 hours are due to tests of individual components of the He-10 cooler. Temperature spikes once the device reaches 4 K are caused by keeping the stepper motor active for extended periods of time.

7.2 Instrument Control

Each spectral acquisition involved a complex sequence of events which selected unique resonant wavelengths, covering the wavelength range of the instrument. The goal was to create a series of small spectra which were stitched together to cover the full spectral range of the grating, at a spectral resolution determined by the FPI. The photomixer provided a tunable THz line source which could characterize the resonant wavelengths and determined the spectral response of the instrument for each setting. An optical chopper placed between the source and instrument produced a modulated signal at the bolometer which was measured with an LIA, in order to increase the signal-to-noise ratio (SNR). Scanning of the instrument required the synchronization of many different hardware components, including: actuators and limit switches for both the pendulum and grating, laser interferometer for pendulum position feedback, the lock-in amplifier and optical chopper, temperature readout for the cryostat and

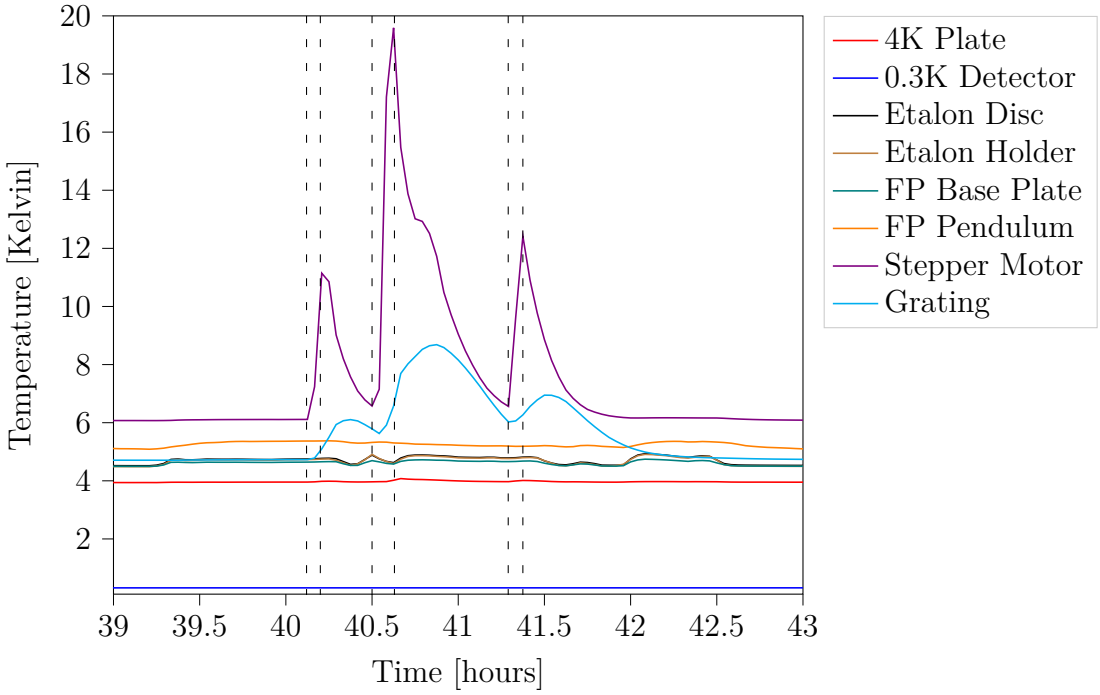

Figure 7.5: Zoomed in version of previous figure. The sharp temperature increases are due to prolonged operation of the stepper motor. The vertical lines indicate instances where the the stepper motor was activated or deactivated, which are identified by the rise or decrease in temperature of the stepper motor respectively.

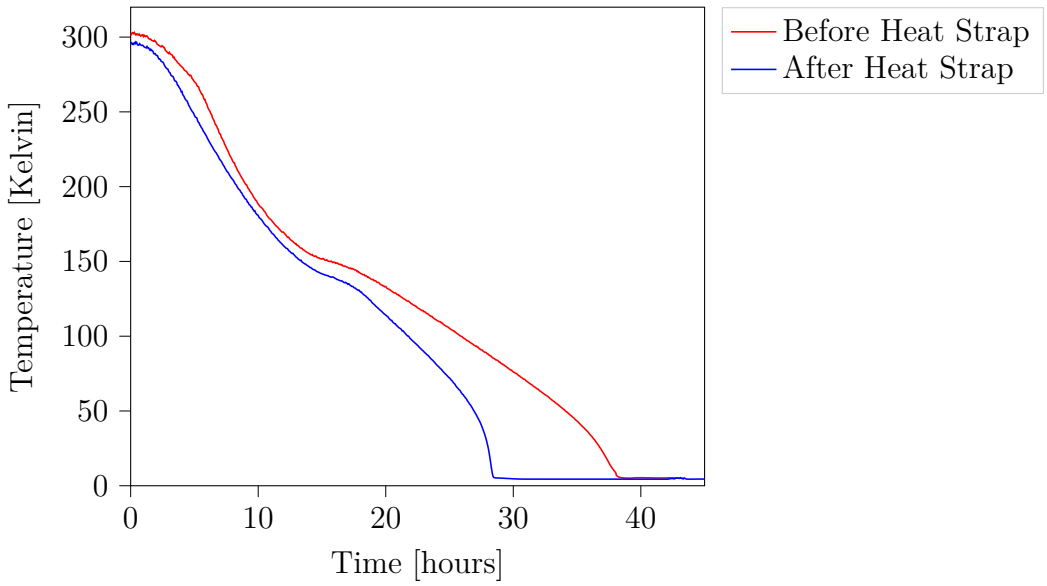

Figure 7.6: Cooling time for the pendulum with and without the added heat straps.

He-10 cooler, control of the He-10 cooler recycling, and data acquisition devices for measuring bolometer readout, position feedback, and limit switch triggers.

Additionally, for the calibration scans involving the photomixer, the added hardware included: two laser controller channels for temperature and current control of photomixer lasers, and the bias circuit for the photomixer.

While I wrote the majority of the software to control the various subsystems, at the time of writing of this thesis, not all hardware was finalized or included in the control software for the entire instrument. However, the following section will detail the current state of the scanning strategies implemented, and will identify features which will be implemented in the future. Figure 7.7 shows a complete overview of all hardware components which must interact with each other, and plans for implementing further components with the control software.

7.3 Scanning Strategies

There were three basic scanning strategies which the instrument utilized:

1. CS Pendulum Mode
2. SI Pendulum Mode
3. Grating Only Mode

Additionally, each scanning mode contained a subset of operations:

a. System Calibration Sub-Mode

b. Normal Operation Sub-Mode

At the time of writing, both the Continuous Scanning Pendulum mode and the Grating Only mode were implemented, along with the required system calibration submodes, utilizing the photomixer to determine the spectral response of the instrument.

Regardless of the scanning mode selected, each scan was initialized with a series of common functions which homed the grating, and moved it into position to start the scan. Additionally, the bolometer readout was the same for all scanning modes,

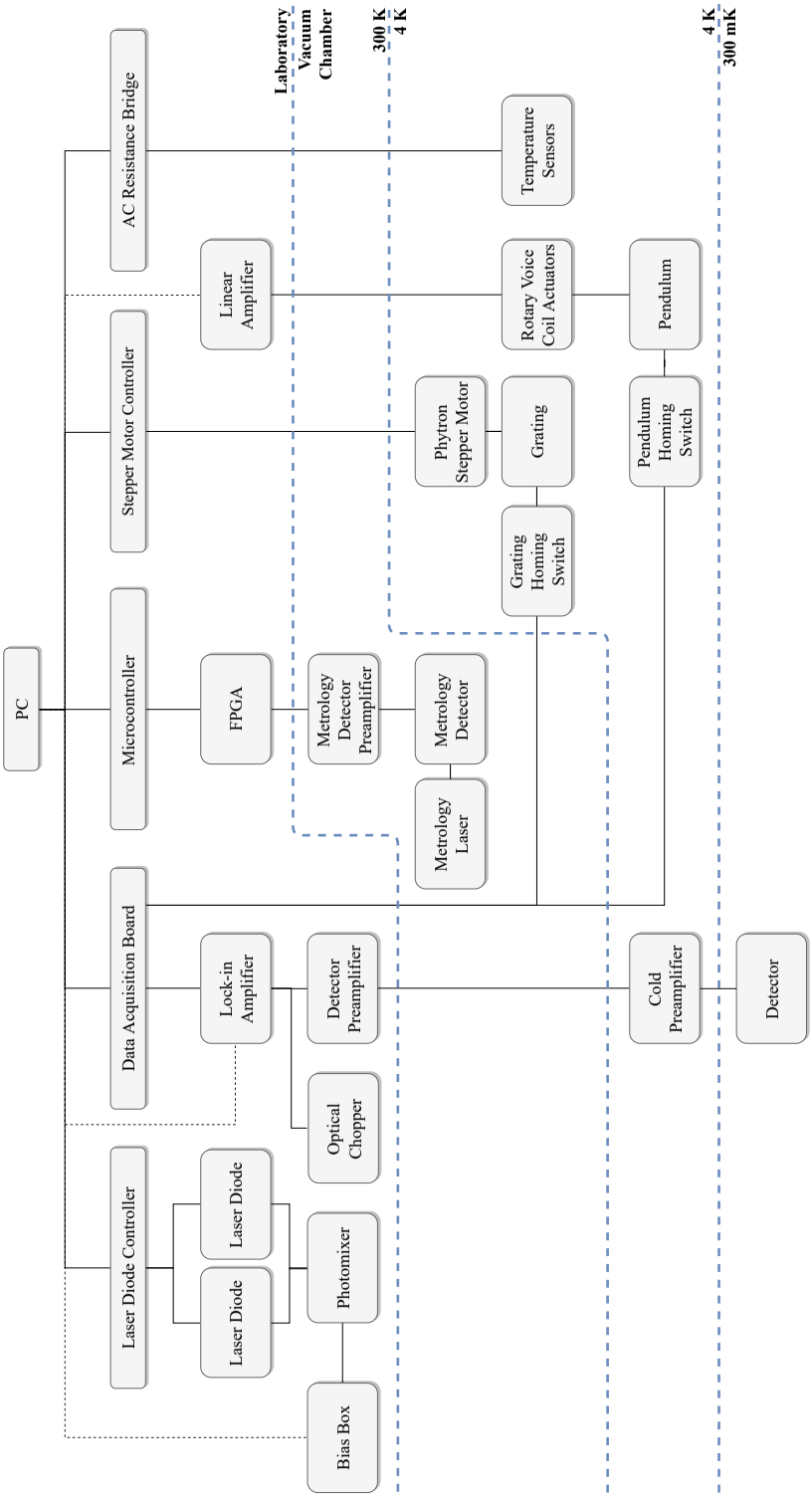

Figure 7.7: An organizational flowchart of all active components of the FPI/grating instrument. Solid lines indicate a transfer of information via electrical, optical, or mechanical signals. Dotted lines indicate connections which will be implemented in the future. Bold blue dashed lines separate different environments.

incorporating a chopper blade on the input optical beam, and an LIA, to record the output chopped signal.

7.3.1 Scan Initialization

Each scan began with a series of common functions, which included verification of temperatures, homing the positions of the grating and pendulum using the limit switches, and moving the grating to its starting position.

First, the grating and FPI components were required to be <5 K at the start of this process in order to allow cycling of the He-10 fridge. The cooling of the TFC to 4 K took ∼30 hours from room temperature. Once the He-10 fridge was cycled, the bolometer temperature was 320 mK. This process took an additional 2 hours.

Next, the grating was homed in order to give it a reference angle. For homing, a magnetic reed switch was placed on the grating housing and a permanent magnet (NdFeB) placed at the end of the grating (Figure 5.12). In the presence of a magnetic field, the ferromagnetic reeds of the switch would close, allowing current to flow. When the source of the magnetic field was removed, the spring force of the reeds would open the switch. Note that this homing procedure had to be completed once the system temperature was stable near 4 K, since the field strength of the permanent magnet changed while cooling thus the point at which the reed switch would close also changed.

The grating angle at which the switch triggered was calibrated against the photomixer and the theoretical center wavelength of the grating linespread function. The switch was set so that it remained closed over the angular range of the grating. Therefore, the procedure to home the grating was to move the grating to smaller incident angles (counter-clockwise in Figure 5.12) until the switch opened. Then the grating was reversed until the switch was closed. This last step was required because the reed switch activated and deactivated at different points. Therefore in order to use the

switch in a repeatable fashion, the grating had to approach a rising trigger edge from the same direction at approximately the same speed. The grating speed was limited to 0.6 deg/s, equivalent to 0.1 rev/s (20 step/s) on the stepper motor. The grating angle at which the switch was closed was found to be 45.20(5)° from Section 5.7.

Once the desired wavelength range was input, the grating was moved to the angle corresponding to the shortest wavelength in the range, using the expression:

$$\theta_{\min} = \sin^{-1}\left(\frac{m\lambda_{\min}}{2d\cos\phi}\right) \qquad \text{[rad]} \quad (7.1)$$

From there, the FPI portion of the instrument had two operating modes: open-loop continuous scanning, or closed-loop step-and-integrate scanning. If the FPI was not implemented, the Grating-Only scan mode would proceed.

7.3.2 LIA Detection

Regardless of the scanning mode, the differential signal from the bolometer and preamplifier was fed to an LIA, which was synchronized to the frequency of an optical chopper on the input beam. The output of the LIA and pendulum position (derived from the laser position measurement device in Section 6.2.4) were recorded simultaneously and given a time stamp. For most scans, the LIA output was averaged over 100 readings and the average and 1-sigma uncertainty were determined. The chopping frequency was set near 40 Hz, below the roll-off of the bolometer frequency response, and away from mechanical resonances in the laboratory.

7.3.3 CS Mode

In open-loop mode, the pendulum was swung through its angular scan range at a slow rate (10 mHz sinusoid). During the pendulum scan, the metrology fringe count was recorded at the same rate as the bolometer readout. The speed of the pendulum was limited by the frequency of the optical chopper and the time constant of the

LIA. Once the pendulum has swept through the full range the desired number of times (typically 5 complete oscillations), the grating was stepped by one resolution element and the process was repeated. This continued until the maximum range of the grating was reached. This operational mode was used mainly to allow some measurements while a step and integrate mode was developed. The CS process and required inputs/outputs are shown in Figure C.1 in Appendix C.

7.3.4 SI Mode

In closed-loop control, the pendulum was moved to select angles and held for the duration of the scan. This required constant position feedback to a motion controller in order to hold the pendulum at a particular angle and integrate the bolometer readout for a set period of time. The angles were selected to cover the wavelength range of a single grating resolution element in at least 15 steps which were equal in wavelength. This tended to increase the duration of the scan, but decreased effects of motion on smoothing the response of the FP, due to the steady nature of the input signal. Currently, the instability of the closed-loop control precludes step-and-integrate scanning. The low frequency mechanical resonances and lack of damping of the pendulum have prevented the use of traditional proportional integral derivative (PID) controllers. However, with added damping utilizing eddy currents produced by an aluminum fin on the pendulum and permanent magnets on the base plate, it will be possible to use traditional PID control on the pendulum in future scans. The process and inputs/outputs for SI scanning mode are shown in Figure C.2 in Appendix C.

7.3.5 System Calibration Scans

In order to calibrate the spectral response of the instrument, the photomixer was stepped through a series of wavelength settings while tuning the grating and the pendulum through their respective ranges and recording their position. A calibration scan with the photomixer involved stepping the grating through half resolution

element positions over the wavelength range of the photomixer, and scanning the pendulum around ±5° for each grating setting. Because of the wavelength dependence of the power output of the photomixer, the current calibration products are limited to >280 µm. For each grating position, the central wavelength of the grating linespread function was estimated from models and previous scans, and 3-5 output photomixer wavelengths were selected centered around this value. As with the regular operating modes, the pendulum was scanned a set number of times (typically 5), or held at each location for a set amount of time for each photomixer setting, typically 1.5 s. Current calibration runs allow for 5 oscillations of the pendulum, corresponding to 10 complete scans for each wavelength setting if forward and reverse scans are combined. Recording both forward and reverse scans separately also allows time dependent effects to be identified and removed in data processing. The modifications made to the process flow for calibration scans as opposed to normal operation for both CS and SI modes are shown in Figure C.3 and Figure C.4 in Appendix C.

7.4 Data Processing

The data are stored in a text file format showing:

1. grating angle
2. temperature of both lasers (only for calibration scans)
3. bias current of both lasers (only for calibration scans)
4. LIA output
5. 1-sigma LIA output
6. laser metrology fringe count (except grating only scans)
7. timestamp

Data for each grating position is saved as a new file, while the different pendulum positions and photomixer laser settings are saved as line elements in these files.

Since data may be collected at a fast rate, a standardized processing script was required to visualize the output. This section describes the steps which take the raw data files and produce output spectra.

The script first locates all files associated with a particular scan. Each file is associated with a "mini-scan" which involves a single grating position. From each mini-scan, the grating angle is extracted and the center wavelength λ_c of the grating profile is calculated using Equation (5.12):

$$\lambda_c = \frac{2d \sin\theta \cos\phi}{m}. \qquad [\mu\text{m}] \quad (7.2)$$

For calibration scans, the center wavelength was determined from the photomixer wavelength at peak transmission, which allowed calibration of the grating angle θ. This procedure is described further in Section 7.7. The width of the Gaussian approximation to the grating linespread function was determined from theory (Chapter 5) as well as from Gaussian fits to the calibration scans (Section 7.8). The peak wavelength and Gaussian width fully defined the grating profile. In a calibration scan, the number of unique photomixer settings was extracted, and the mini-scans were further subdivided accordingly, with each setting labelled a "micro-scan".

7.4.1 Fringe Count to Angle Conversion

For each mini-scan, the metrology fringe count was first converted from the raw 32-bit fixed point to a floating-point value. The count was then converted to an optical position, and then to a pendulum angle. The conversion from the recorded fixed point value to an optical path difference follows:

$$\text{OPD} = \frac{V\lambda_0}{2^N}, \qquad [\mu\text{m}] \quad (7.3)$$

where V is the fixed-point value, N is the radix (the number of bits dedicated to the fractional value), and λ_0 is the metrology laser wavelength. In this case, $N = 16$ and $\lambda_0 = 1550\,\text{nm}$.

For open loop oscillating pendulum scans, the zero count point was determined as the DC offset of the sinusoidal trace of the metrology count:

$$\text{OPD}_0 = \frac{\text{OPD}_{\text{max}} + \text{OPD}_{\text{min}}}{2}. \qquad [\mu\text{m}] \quad (7.4)$$

The zero count point was subtracted from all OPD measurements so that the resting angle of the pendulum corresponded to OPD = 0. Note that in future scans, the zero point will be defined by a limit switch, similar to the one which is used to home the grating. For the case where the retroreflector targets were on the back of either pendulum arm, the conversion from optical path difference to pendulum angle was,

$$\theta = \sin^{-1} \frac{\text{OPD}}{4D} \qquad [\text{rad}] \quad (7.5)$$

where D is the distance from the corner cube apex to pivot axis. In this case, $D = 60.0(1)\,\text{mm}$.

7.4.2 Timing Corrections

Initial scans showed a slight shift in peak location between forward and reverse scans. This was traced to an effective time offset between the recorded signal and the fringe count, which was caused by the delay in averaging over many output values from the LIA. The time offset in LIA recordings and metrology count was found to be 45 ms, which was corrected for by interpolating the pendulum angles on a shifted time grid. The precise time offset value was found by minimizing the difference between averaged forward and reverse scans.

7.4.3 Calibration Products

In photomixer calibration scans, the output wavelength of the device was determined from bias current and temperature for each of the photomixer lasers. The output wavelength was determined from a linear fit to the laser wavelength with temperature and a quadratic fit to the laser wavelength with bias current, found using the EXFO WA-1500 Wavemeter, with fit parameters reported in Chapter 4. The output wavelength was the difference between those of the two input lasers, given in Figure 4.5 and Figure 4.6.

7.4.4 Data Products

Finally, the micro-scans were optionally averaged together (both forward and reverse scans), and the signal (in volts) and the pendulum angle (in degrees) were saved. The next processing stage combined all scans into a complete spectra. However, this required further calibration products for the grating line profile width, and thickness, refractive index, and initial offset angle of the etalon to determine the wavelength accuracy and response.

7.5 First Light

The "first light" measurements were recorded on November 28, 2018 after the delivery of the custom fabricated HRFZ silicon etalon to the University of Lethbridge. Part of the SRON team (Dr. Willem Jellema and Carolien Feenstra) who were responsible for the fabrication of the etalon visited for these tests. The first measurements, shown in Figure 7.8, revealed a smooth line profile, measured as a function of pendulum angle, with asymmetries that matched the modelled angle-scanning transmission profiles from Chapter 3. While first light results were remarkable, showing transmission profiles close to those predicted, detailed analysis revealed line centres differed from those predicted. Additionally, the forward and reverse scans showed differing

peak locations due to the timing issues described previously. The largest discrepancy between predicted and actual wavelength response was traced to the temperature dependence of the etalon dimensions and the refractive index of silicon. Once the temperature-dependence was added, these data matched theory to a high degree. The number of free parameters in the etalon showed some initial degeneracy in the solution, where modifications to the initial offset angle, thickness, and refractive index of the etalon could produce, to first order, identical results. Further investigation was required to remove this degeneracy, by scanning over a broader range of wavelengths. However, the first results indicated there was good alignment of the instrument, and no obvious re-entrant spectra or stray-light reflections which degraded the detected signal.

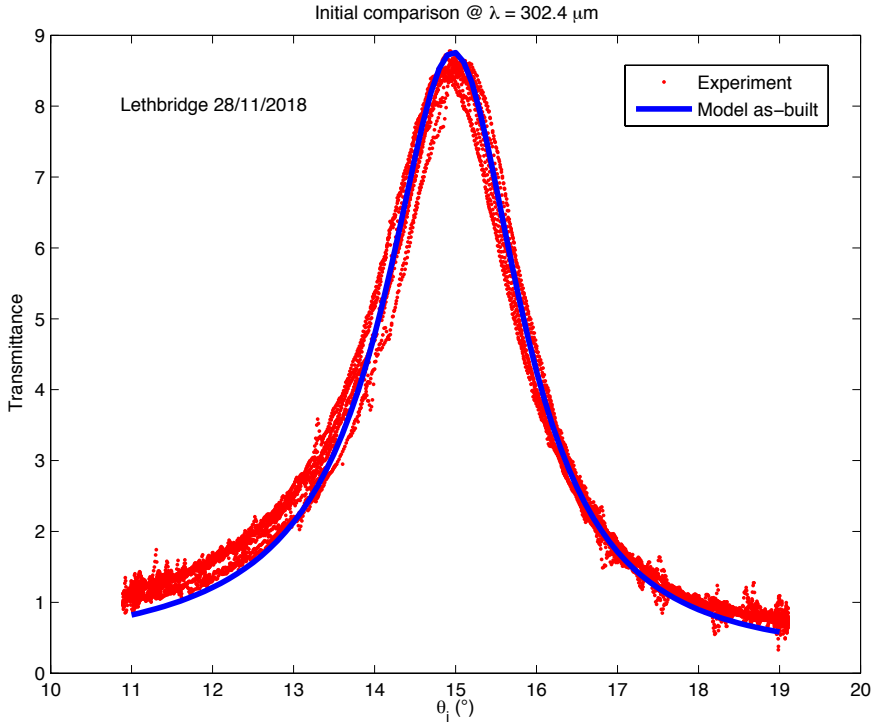

Figure 7.8: First light result obtained on Nov. 28, 2018. The red points show raw data overplotted from several scans; the blue curve shows the preliminary transmission model.

The first results produced by the instrument initiated a series of press releases within the University of Lethbridge, as well as SRON [123].

7.6 End-to-End Verification

The spectral calibration of the FPI and the variation of ILS with wavelength is described here. The calibration methodology was based on the spectral response of the instrument when the narrow, unresolved line source from the photomixer was injected. Some attempts were made to perform absolute flux calibration, but in order to do so properly, the instrument would have required a mechanism to remove and insert the etalon while the system is cold and without changing alignment. Since this was not feasible in the current experimental setup, the goal of the test campaign was to measure the effective finesse of the instrument, to determine the suitability of dielectric stack reflectors for a high finesse FPI, and to measure the effects of *walk-off* on the line profile of the device. This required accurate verification of the wavelength calibration of the instrument, as well as the produced line profile.

7.7 Wavelength Calibration

Wavelength calibration involved injecting a narrow-band source of a known center wavelength into the instrument. The peak in the recorded output was compared to the theoretical wavelength response of the instrument, and any discrepancies were identified.

7.7.1 Grating Wavelength Calibration

With the pendulum in place, and the etalon removed, so that the instrument operated in "Grating Only Mode," the grating calibration was revisited to ensure it remained consistent with previously measured values recorded in Chapter 5. The calibration procedure involved scanning the pendulum around 3-5 settings around

the estimated center wavelength for each grating position. A Gaussian profile was fit to the output LIA signal as a function of wavelength in order to find the center of the grating wavelength response (Figure 7.9). From the wavelength of the Gaussian peak, the source-calibrated grating angle was calculated using the grating equation (Equation (5.12)). From the calibrated angle, a least squares fitting routine was used to determine the value of $d\cos\phi$ and the grating angle θ at which the limit switch was triggered. A comparison of the new fitted parameters to those from the standalone grating calibration is shown in Table 7.2. In both cases, the wavelength range for calibration was 280 µm to 310 µm. Using the new calibrated parameters, Figure 7.10 shows the agreement between the data and theory.

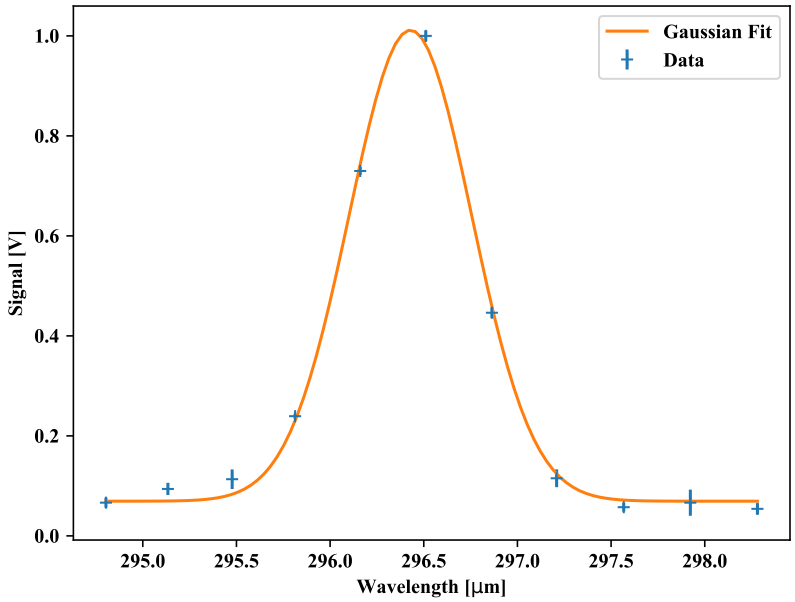

Figure 7.9: Example of a Gaussian fit to the grating profile.

7.7.2 Fabry-Perot Wavelength Calibration

With the etalon in place, the wavelength calibration of the FPI was performed using CS calibration mode (Figure C.3). For each "micro-scan", the wavelength of peak transmission as determined by the etalon model was compared to the injected

Table 7.2: Comparison of the calibrated grating parameters from the standalone grating calibration and the grating-only scanning mode. The parameters A, B, and C are coefficients in a second order polynomial fit $\lambda = A\theta^2 + B\theta + C$

Parameter	**Standalone Grating**	**Grating-Only Mode**
$d\cos\phi$	179.61(7) µm	177.31(9) µm
θ_0	45.20(4)°	45.20(5)°
A	−127(5)	−202(7)
B	448(9)	596(15)
C	−19(4)	−96(7)

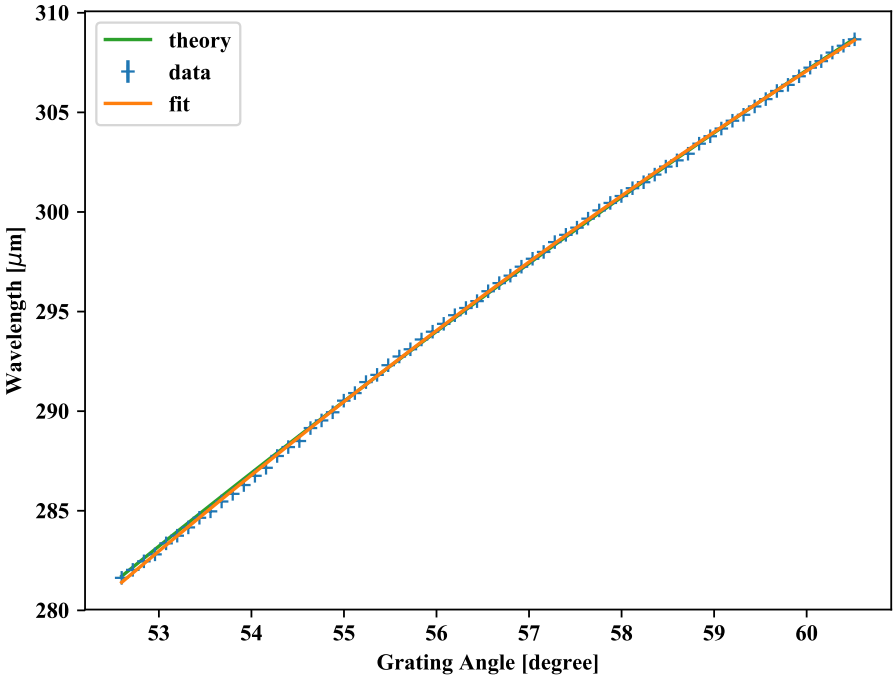

Figure 7.10: The wavelength of peak grating response variation with grating angle θ. The "theory" curve shows the result of a least squares fit to determine the combined parameter $d\cos\theta$ (given in the text). The "fit" curve shows the results of a second order polynomial fit.

wavelength. The modelled wavelength was determined using the multilayer model described in Chapter 3. Iteration of the model parameters to match the model to the known injected wavelength allowed for characterization of the uncertain parameters of the device. The parameters of the device are labelled in Table 7.3. Each parameter

that was explicitly measured is fixed within the model, while those not explicitly measured or determined from literature were variable.

Table 7.3: Variable parameters in the wavelength calibration of the FPI.

Parameter	**Variable**
Substrate Thickness	NO
Airgap Thickness	NO
Wafer Thickness	NO
Silicon Refractive Index	YES
Initial Angle of Incidence	YES

The thickness parameters of each substructure of the etalon were fixed with respect to the model parameters, since their values were well defined by a coordinate measurement machine (CMM) with $<0.1\,\mu m$ uncertainty at SRON during the manufacturing process.

Additionally, the thermal contraction of silicon has been well characterized at cryogenic temperatures [124]. Using the recorded temperatures of the thermometers attached to the edges of the silicon substrate, the new thickness parameters at the operating temperatures were applied.

The two parameters allowed to vary (refractive index and initial angle of incidence) allowed matching of the peak locations between the model and the data. The variation of each of these parameters caused different variations in the model. Since the data was recorded as signal as a function of incident angle, a change in the initial angle of incidence resulted in a static shift in the peak center locations for each scan, independent of the angle at which the peak occurs. Alternatively, a change in the refractive index of the substrate caused a variable shift in the peak center compared to the model depending on where in the angular range of the pendulum the peak is located.

The refractive index of silicon is well known for near infrared wavelengths as a function of temperature [125]. Additionally, there are some publications which report

low temperature, far infrared refractive indices [126]. However, the precise dependence of refractive index on temperature $\frac{d\mu}{dT}$ is not well characterized at FIR wavelengths. Additionally, since high resistivity silicon is a poor thermal conductor, the temperature near the center of the etalon is not well known, even with a thermometer on the edge of the substrate. Since the peak location has a strong dependence on refractive index of the etalon substrate, the refractive index was treated as a free parameter.

In addition to the uncertainties involved in the refractive index, the initial incident angle was not well known in the first scans, due to the absence of a limit switch to tell absolute angle, and a slight drift in the metrology output over long time periods due to noise on the three-phase detector readouts. Instead, angle was recorded with respect to the DC offset of the sinusoidal angle recorded for each individual mini-scan. In this way, there was no guarantee this initial offset angle remained the same for each mini-scan. In future measurements, a limit switch will be added to remove this possible drift

The calibration scheme that was adopted used the averaged forward and reverse scans and an estimated initial offset of $15(1)^\circ$ as determined by the design offset and mechanical tolerances. For each input wavelength, a number of selected refractive indices were applied to the multilayer model to predict the output. The angle at which the peak in the model occurred was found and the difference in initial offset angle was calculated. The selected refractive index was that which minimized the variance in offset angles for all mini-scans, regardless of the angle at which the peak occurred (Figure 7.11). Using this method, the optimum refractive index and initial angle of incidence are shown in Table 7.4. Applying the average values, each scan required small changes to the initial angle of incidence for the peak locations between the data and theory to match.

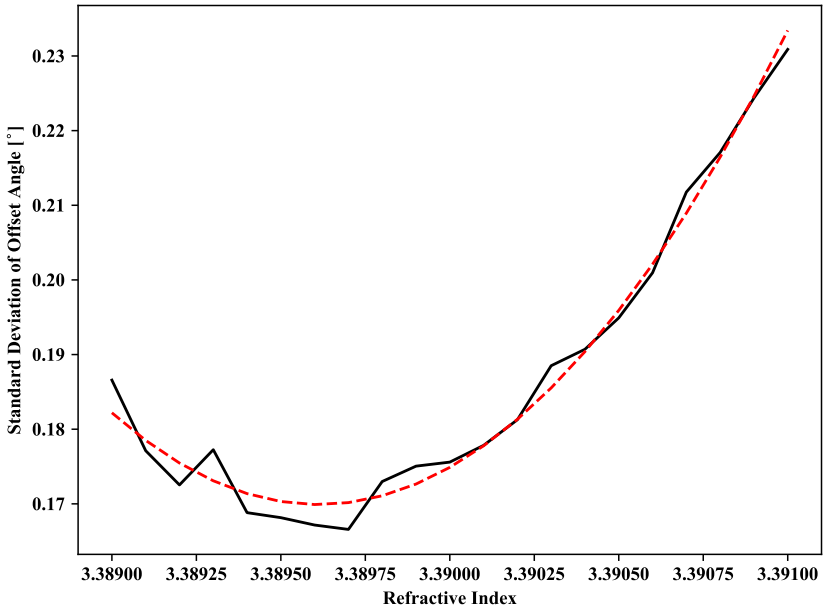

Figure 7.11: Results of the calibration scheme which minimized the variance in the offset angles. A second order polynomial fit is overlaid, which was used to find the refractive index which minimized the variance.

Table 7.4: Parameters from the wavelength calibration of the etalon.

Parameter	**Value**
Substrate Thickness	7.8600(1) mm
Airgap Thickness	59.3(1) µm
Wafer Thickness	51.9(1) µm
Refractive Index	3.3896(1)
Initial AoI	15.0(2)°

7.8 Line Profile

7.8.1 Grating Line Profile

Using the grating-only mode, the grating line profile was found by determining the width of the Gaussian fit to each mini-scan as a function of injected wavelength. The fits are presented in Figure 7.12 and compared to the theoretical fits as determined by the image size on the exit slit, given in Chapter 5. The extent of the scatter in the results is due to a small number of points across the grating linespread function from which the Gaussian fit was derived (see Figure 7.9). During the line profile

measurements, the tuning of the laser currents to adjust the output frequency was not yet implemented, due to the change in output power associated with this technique. Therefore, the frequency tuning was limited to the temperature adjustment of the lasers, which was limited to steps of 0.01 °C. More precise temperature control will result in better Gaussian fits.

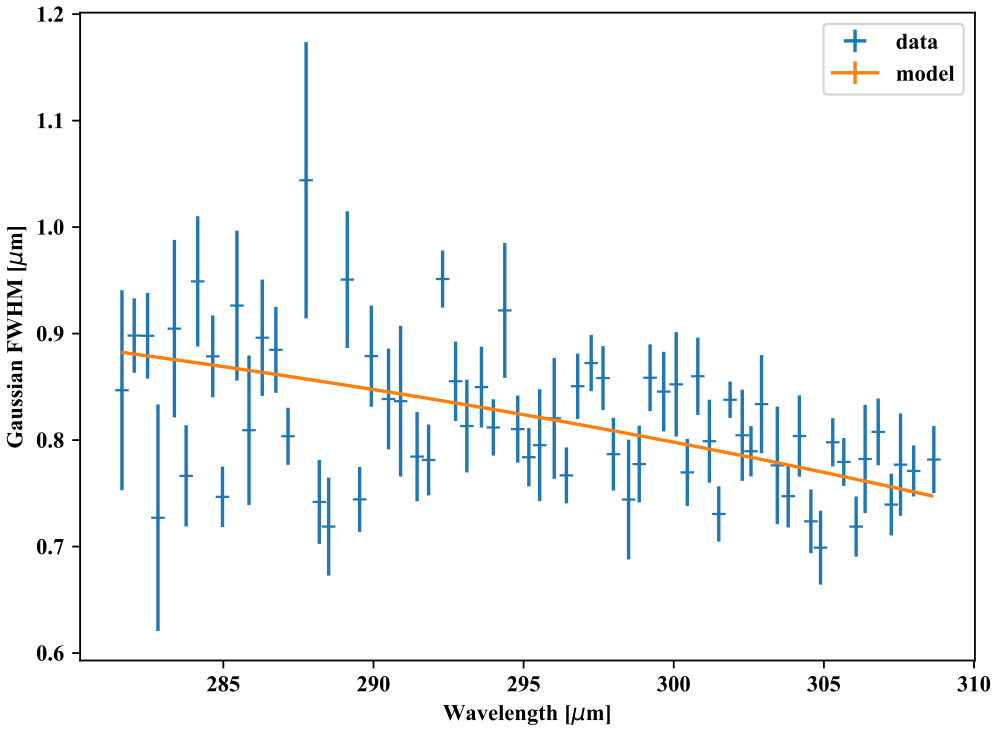

Figure 7.12: Resolving element of the grating as defined by the FWHM of the Gaussian fit to the linespread function. The results are compared to the modelled value which is determined by the optical spot size on the grating exit slit. Discrepancy between data and theory is likely the result of temperature or bias current fluctuations in the photomixer lasers, as discussed in Chapter 5.

7.8.2 Fabry-Perot Line Profile

The instrument line profile of the FPI is the shape of the transmission profile when the input is a single monochromatic source. Assuming the photomixer output is sufficiently narrow to be classified as monochromatic, the line profile for each calibration micro-scan was compared to the etalon model using the fitted parameters

from wavelength calibration. A good agreement with the multilayer model described in Section 3.2.1 would indicate effects from etalon defects and *walk-off* were small. A wider line profile would indicate a smaller finesse, indicating a significant contribution from other finesse components rather than reflectivity finesse (Chapter 3).

Both the multilayer model and a hybrid model which included *walk-off* (both models are described in Section 3.4) were compared to the calibration scans. The first model considers the etalon as a single multilayer structure and ignores the effects of *walk-off*. The model uses the parameters listed in Table 7.4.

The second model is a hybrid model of the geometric *walk-off* using the classical FP functions and the multilayer model. The multilayer model is used to estimate the bulk reflectivity and transmissivity coefficients for the dielectric mirror stacks on either side of the substrate. These coefficients are tabulated as a function of wavelength and polarization, since the reflectivity was determined by resonances in the high-low-high refractive index stack. Only the TE polarization state was used, since the output of the photomixer was linearly polarized in this orientation with respect to the etalon. The TE polarization state was selected since this oriented the E-field perpendicular to the grating grooves, which was the polarization for which the grating was most efficient (Chapter 5). The coefficients for the input and output sides of the etalons were determined independently, since at the first interface, the beam travels from a vacuum into the silicon substrate, but for the second interface the beam travels from within the substrate to the vacuum. Using the coefficients for each side of the substrate, a geometric series was built up from ray reflections within the etalon, between the inner boundaries of the substrate. This model accounts for *walk-off* within the etalon substrate by scaling each term of the geometric series by the fractional area overlap, but not within the dielectric stacked coating. However, since the thickness of the coating is $<1\,\%$ of the substrate thickness, *walk-off* within the stacked coating was negligible.

The steps involved in the line profile calibration were as follows:

1. Apply refractive index and initial AoI values from wavelength calibration
2. Fit multilayer model to data, applying small corrections to initial AoI, peak transmission, and background noise levels
3. Apply hybrid *walk-off* model using corrected parameters.

Figure 7.13 and Figure 7.14 show the FPI line profiles for four scans within the 280 µm to 320 µm range where the high photomixer output power provided good signal-to-noise. The agreement between the measured data and the etalon models is remarkable! The models relied on the input parameters determined from the wavelength calibration, which were the refractive index of the silicon etalon and the initial angle of incidence. For each individual scan, small corrections to the angle of incidence and background detector signal were applied based on the line profile fit to the multilayer etalon model. It is currently unclear if these small corrections to the initial angle of incidence are the result of drifting of the three-phase metrology signal due to noise on the photodetector readout, or due to a difference between the predicted and actual photomixer output wavelength, due to slight temperature variations. These figures are the culmination of the entire thesis, bringing together the operation of all the developed hardware, including the photomixer as a calibration source, the FPI etalon and pendulum, along with its drive and metrology, the grating and its stepper motor driver, and the TFC, detector and He-10 fridge. The control software for each component was synchronized with the tuning of the photomixer laser temperatures, the detector readout – which also required a lock-in amplifier and optical chopper to achieve high signal-to-noise – and the pendulum metrology quadrature conversion to produce the data in these plots.

There are two models which are overlaid over the data in Figure 7.13 and Figure 7.14. The first is the multilayer model, which uses the dielectric stack theory

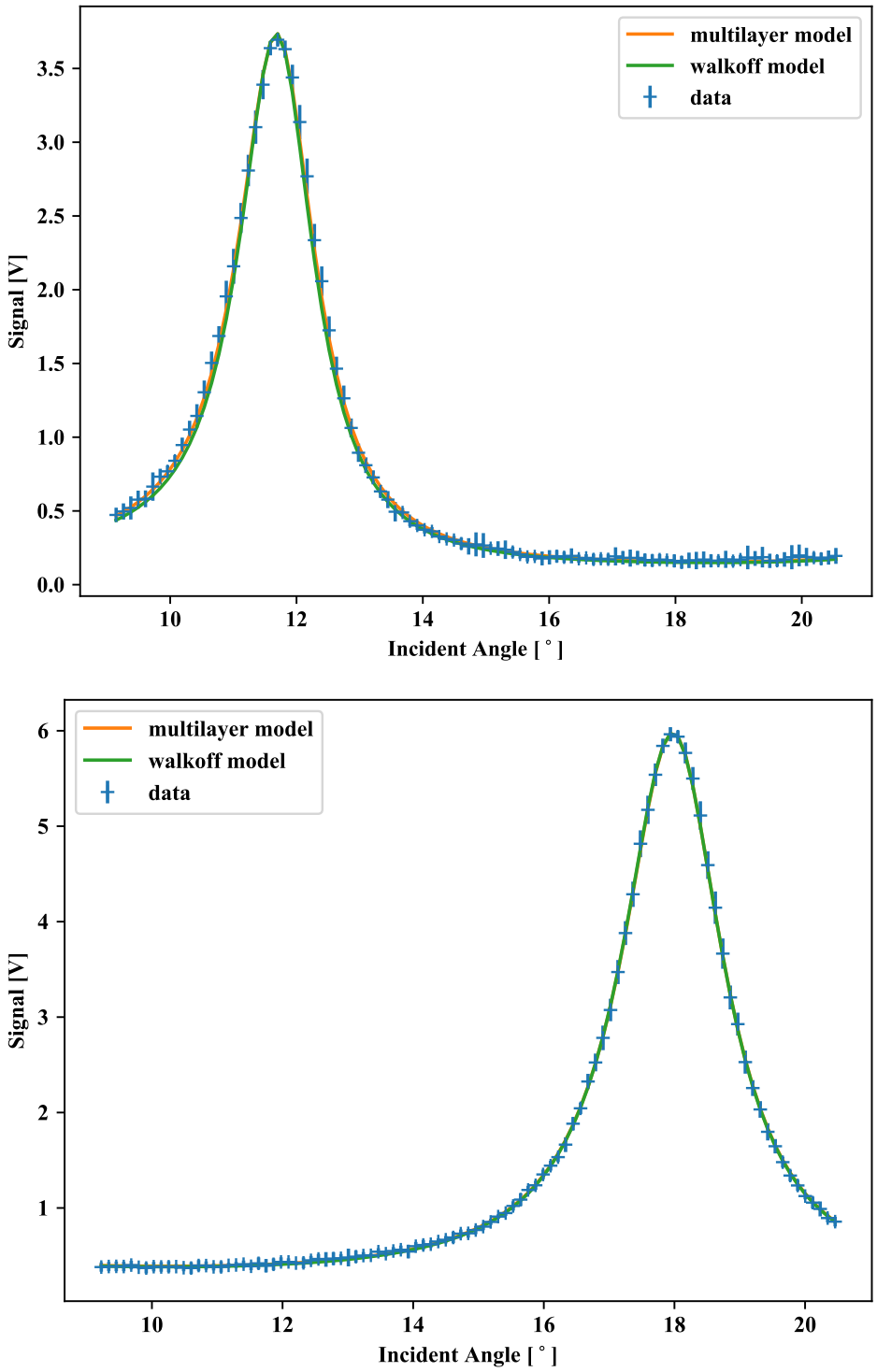

Figure 7.13: Comparisons between photomixer calibration data and modelled transmission profiles for both the multilayer model and the *walk-off* model. In the top figure, the photomixer output was 284.26(1) µm and in the bottom figure it was 301.21(1) µm.

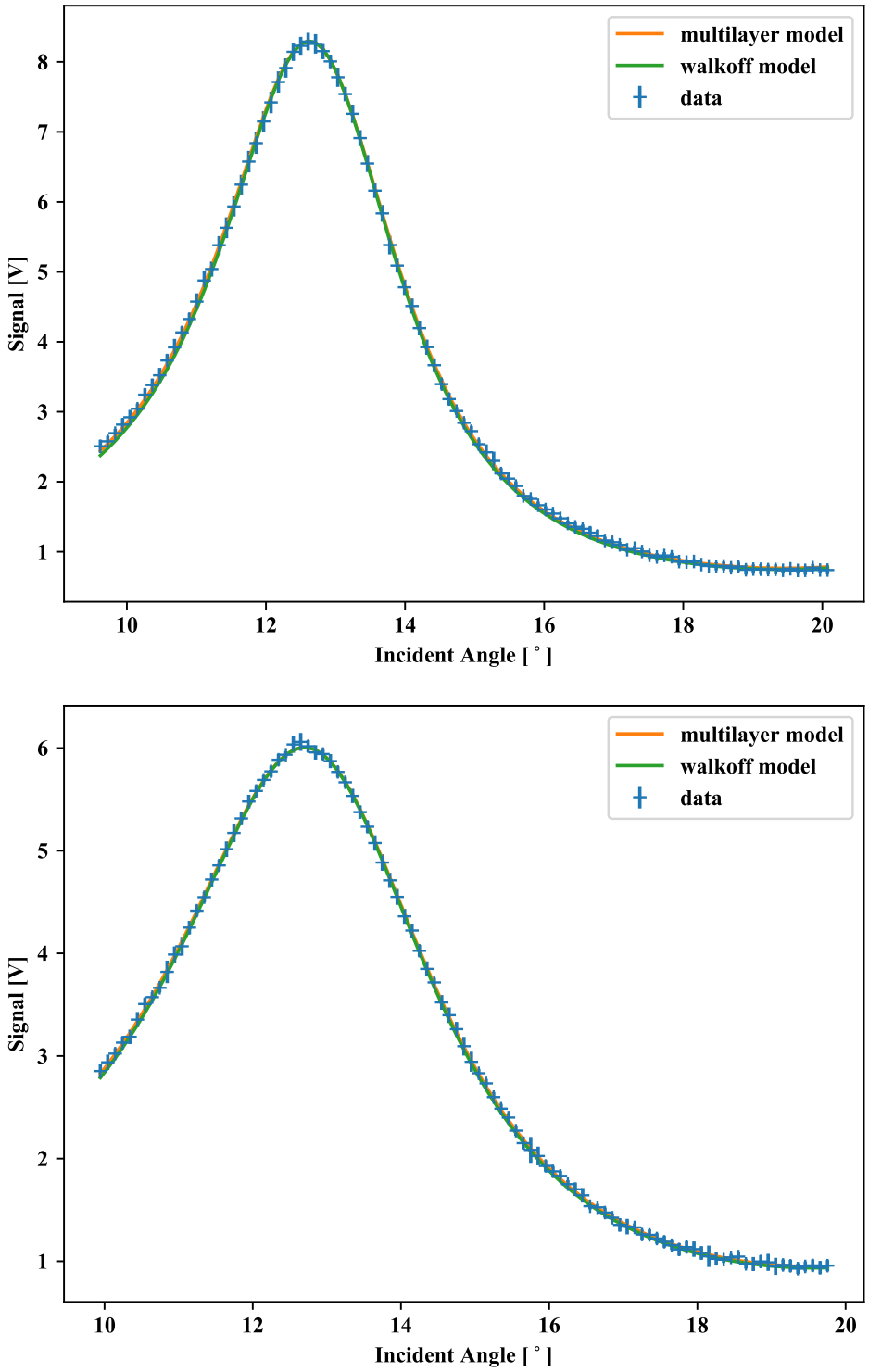

Figure 7.14: Comparisons between calibration data and modelled transmission profiles for both the multilayer model and the *walk-off* model. In the top figure, the photomixer output was 307.03(1) µm and in the bottom figure it was 314.25(1) µm.

discussed in Section 3.2.1 to predict the transmission of the etalon as a function of incident angle. The second is the *walk-off* model, which uses the dielectric stack theory to predict the complex reflectivity and transmissivity coefficients for the front and back surface of the etalon independently. The transmitted E-field is determined from the sum of multiple transmitted beams, with the changing fractional area overlap from *walk-off* applied to each transmitted beam (Section 3.2.3), which is then converted to measured intensity. The agreement of the two models with each other and with the measured data shows that for an etalon with a high refractive index, the effects of *walk-off* are manageable at these wavelengths, incident angles, and resolving powers. This is a key outcome which ultimately shows that an angle-scanned FPI, which has historically been avoided due to the detrimental effects of *walk-off*, is a viable instrument architecture for a high-resolution FIR spectrometer. Additionally, the agreement with the etalon model, which assumes the only finesse parameter is that given by the reflectivity, shows that the etalon is of high quality, and that the experimental DRIE fabrication method developed by SRON is robust and results in a stable, predictable device. The results show that we can design further angle-scanned etalons with confidence that their performance can be adequately predicted. The final step in the spectral calibration procedure was to extract the resolving power, and ensure the etalon met the design requirements.

7.9 Resolving Power

The ultimate parameter in the spectral calibration of the FPI/grating was the measured resolving power of each module. The target resolving power for the grating was $R \sim 300$ and the target for the FPI was $R \sim 3000$ in the design of each. The grating line profile with respect to incident wavelength was previously determined by scanning the photomixer output (Section 7.8). Therefore the resolving power was determined by taking the ratio of the wavelength for the peak of the Gaussian fit

to the FWHM of the Gaussian fit. Figure 7.15 shows the resolving power for each grating position, and the modelled resolving power. Since the resolving power is dependent on the wavelength stability and power stability of the photomixer, which is not measured simultaneously with the detector signal, the large spread in data points is likely a result of variations in temperature or bias current of the photomixer lasers.

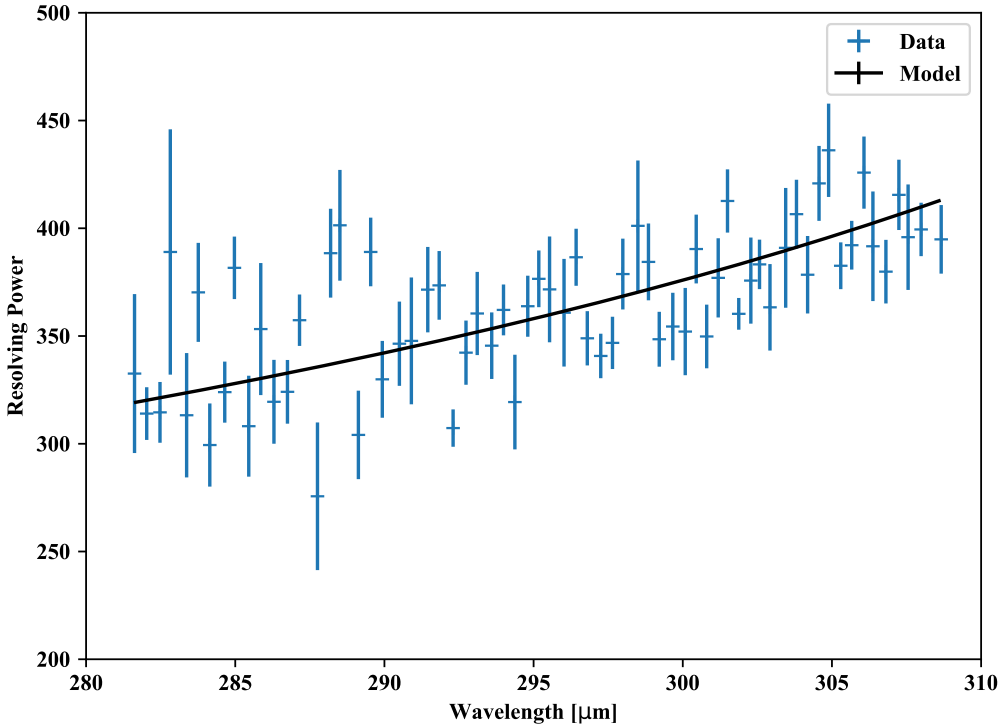

Figure 7.15: Resolving power of the grating measured in "Grating Only" mode.

For recording the resolving power of the FPI, the line profiles were measured in terms of incident beam angle, but the wavelength resolution of the photomixer was not sufficiently small to profile the instrumental lineshape in terms of wavelength. Therefore, for each scan of the pendulum, the fitted parameters were used in the multilayer dielectric model to predict the peak transmission for each pendulum angle. The resulting function was interpolated over the measured pendulum angles to convert incident beam angle to a resonant wavelength. The FWHM in terms of wavelength

was then found by identifying the half maximum points on either side of the peak. The FPI resolving power was calculated by taking the ratio of the photomixer wavelength to the FWHM. The resulting resolving power is shown in Figure 7.16 for all measured photomixer wavelengths overlaid on the modelled resolving power for the full design waveband of the FPI. The modelled resolving power was determined by measuring peak widths in terms of wavelength for discrete incident beam angles. Since the incident angle range was between 10° to 20°, the modelled resolving power is shown for each end of the range. As with the resolving power of the grating, the data shows a relatively large spread, which is surprising considering the agreement with the model in Figure 7.13 and Figure 7.14. However, as with the grating resolving power measurements, slight variations in the temperatures or bias currents of the photomixer lasers, which were not measured simultaneously with the recorded data, are the likely cause of the spread in resolving power.

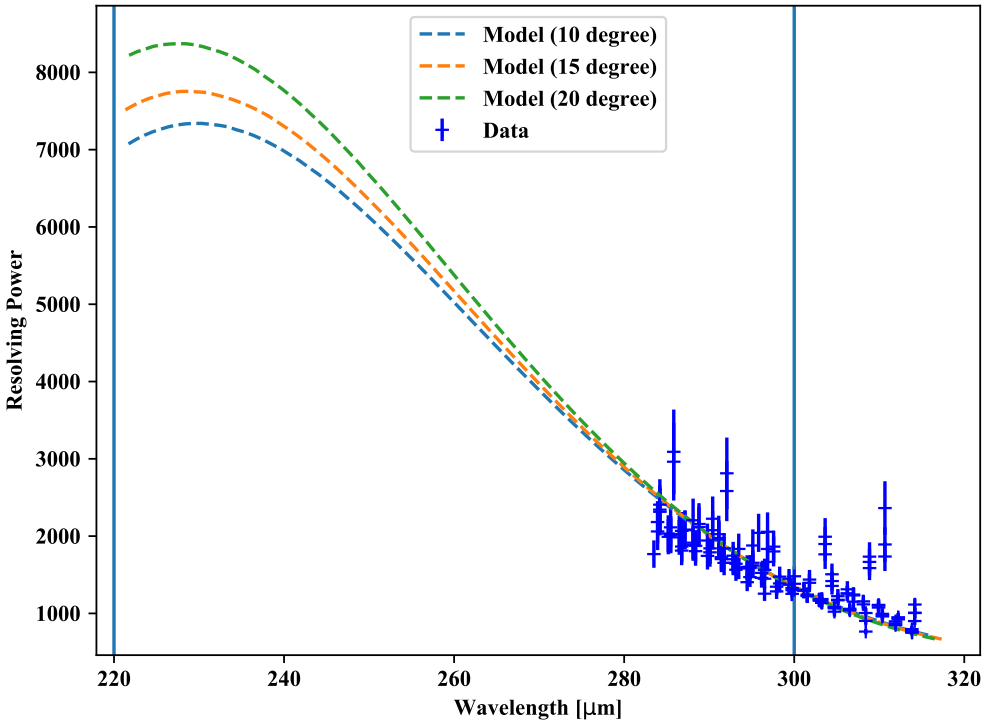

Figure 7.16: Resolving power of the FPI measured in "Continuous Scan" mode. Vertical bars show the design wavelength range of the etalon.

7.10 Conclusions

The results presented in this chapter outline the process for gathering data and calibrating the output of the FPI. The wavelength of peak transmission was determined as a function of grating angle and pendulum angle in order to characterize the physical parameters of the grating and etalon. From the determined parameters, the line profile was modelled and compared to measurements of the spectral response of the instrument. As shown, there is solid agreement between the device models and the produced data. These first results show that with a high refractive index substrate, the effects of *walk-off* were minimal, and show the first implementation of a cryogenic, angle-scanned FPI etalon as a high-resolution spectroscopic instrument.

Chapter 8

Future Work

> Home is behind, the world ahead,
> and there are many paths to tread
> through shadows to the edge of night,
> until the stars are all alight.
>
> *Bilbo Baggins in The Fellowship of the Ring*
> J.R.R. Tolkien

In this thesis, I have shown that a fully silicon etalon with dielectric stack reflectors, manufactured through DRIE, that is scanned by changing the incident beam angle is a viable high-resolution interferometer concept for a cryogenic far-infrared (FIR) spectrometer. I have shown that a resolving power of $R > 3000$ is readily obtainable at FIR wavelengths with a dual-layer dielectric stack on either face of the etalon, and that this principle may be expanded further to increase the reflectivity finesse. Also, the lineshape of the FPI matches what is predicted, with very little contribution from the effects of *walk-off* for incident angles ranging from 10° to 20°.

In addition to the design and construction of the angle-scanned FPI, in order to validate its performance I have designed and manufactured a cryogenic grating monochromator with a resolving power of $R \sim 300$. I have also developed a fiber-based laser interferometer which can be used to provide position measurement at cryogenic temperatures with nanometer level precision, and I have modified a THz photomixer, so that the output frequency is increased by a factor of two, to provide a tunable calibration source up to 1.2 THz. However, even with all the achievements in areas of cryogenic and FIR instrumentation presented in this thesis, a full system

characterization of the FPI has not yet been completed. In this chapter, I will describe the additional steps that should be considered in the next phase of this project. Since the instrument is composed of discrete components: the sources, FPI, grating, and detector, I will describe the lessons learned from developing each component, and the suggestions for further improvements.

8.1 Sources

The original calibration sources were the photomixer, an HCl gas cell, and telluric absorption lines. Of these sources, only the photomixer was developed and used for calibration. While results with the photomixer show excellent agreement with theory for the long wavelength end of the FPI, the λ^4 dependence of the output THz power resulted in a small signal-to-noise ratio below $\sim$260 µm. Additionally, the ILX LDS-3900 used to control the laser bias current and temperature had a temperature resolution of 0.1 °C, which limited the allowable wavelengths. More precise temperature selection would allow for better characterization of the instrument line profiles for both the grating and FPI. To this end, two laser diode temperature controllers were purchased from ThorLabs (TED200C), each with a temperature resolution of 0.01 °C. While these were not yet implemented at the time of writing of this thesis, the more precise wavelength selection enabled by the new temperature controllers will allow for better calibration of the instrument line profiles.

Regarding the use of rotational lines of molecular gasses measured in absorption, a hot blackbody source is required to provide a background continuum on which to measure the absorption features. Due to the spectral dispersion of the incident radiation, the radiant power in a single spectral band of the FPI was too low for the detector to measure accurately. More power can be provided by using a hotter blackbody source. However, due to the high absorption of the polypropylene cryostat windows to visible radiation, further filtering should be added in order to ensure the

cryostat windows are not damaged.

The rotational lines which will be measured in absorption could also be measured in emission against a low temperature background. A conceivable method of measuring in emission involves placing a gas cell with the gas to be measured within the cryostat. A closed-loop temperature control system could be used to elevate the temperature of the gas cell above ∼160 K to ensure HCl is in the gas phase. Additionally, regulation of the temperature of the gas cell can be used to vary the amount of molecules in the gas phase, thereby giving a variable line strength. This will require further developments to ensure the detector is sufficiently sensitive to measure these emission lines.

8.2 Grating

Overall, the grating monochromator worked as intended, providing a sufficient method for order-sorting the FPI output spectra. However, there are a few design aspects which could be improved on in future instruments. First, the framework for the grating was manufactured from aluminum plates which were fastened together. While this allowed for ease of manufacturing, it introduced challenges with the alignment of the worm-wheel gear train, both for the full rotation of the grating at room temperature and for maintaining the alignment of the gears during cooling to 4 K. In the future, a framework which is monolithic, so that misalignment between bolted joints is not an issue, would be preferred. Second, the initial requirement for a 1 mm exit slit for the grating proved to be optically inefficient due to the diffraction limited image sizes of the instrument. Future developments of the grating should take better care to ensure the grating optical efficiency is high, by using larger optics, or using a grating with a higher spectral dispersion.

8.3 Detector

The detector performance was sufficient for the characterization of the instrument line shapes for the FPI. However, there are areas in which the performance may be improved for both the detector response and the He-10 fridge to cool the detector to 300 mK. For the operation of the He-10 fridge, the initial software which enabled the cooling relied on a time-dependent sequence to ensure the condensation of the ^{3}He contained within the cooler. However, as the unit operated under different loading conditions, the hold time of the unit changed. In some cases, the time-dependent control software had to be modified on a case-by-case basis to enable the cooler to reach its base temperatures. In the future, a temperature-dependent control system should be implemented, to allow varying power to be applied to the internal heaters so that they remain at a set-point temperature. This will enable more efficient cycling of the cooler, and ensure maximum cooling time is consistently achieved.

For the detector itself, the improvements lie in the susceptibility of the wiring to microphonics. It is a common issue in pulse-tube cooled crysotats such as the TFC that vibrations caused by the pulsing of helium gas within the coolers cause small vibrations within the cryostat [127]. The low-current wiring which carries the detector signal to the preamplifier is particularly susceptible to these vibrations. Ensuring the detector wiring is fastened tightly to the mechanical supports of the TFC will lower the noise floor. Additionally, characterization of the responsivity of the detector will enable absolute flux calibration of the FPI. This requires a confocal system to allow the detector to view an internal or external calibration source.

8.4 Fabry-Pérot Interferometer

8.4.1 Lessons Learned

For the etalon itself, the absorption of silicon is not well characterized at these wavelengths and temperatures. To make the angle-scanned silicon FPI a viable in-

strument for FIR astronomy, where the incident radiation from observed sources is low, the loss tangent must be measured for the corresponding wavelengths and temperatures. Although the effects of absorption in silicon were not seen in this work, the characterization of loss tangent becomes increasingly important for systems with higher resolving power. Concepts for measuring this parameter will be discussed in Section 8.4.2.

Accurate positioning and measurement is difficult at cryogenic temperatures. While the three-phase metrology system showed an impressive nanometer level of precision, it was susceptible to $1/f$ noise when the pendulum was moving at low velocities, and for step-and-integrate positioning of the pendulum arm. As a result, the pendulum position drifted over large numbers of scans, such that the angle offset had to be calibrated for each set of "micro-scans" in the calibration measurements (see Chapter 7). With a position measurement system which was stable for a broad range of velocities, the pendulum positioning would have been much more robust.

The pendulum itself also requires modifications to enable step-and-integrate scanning. While the RVCA and flex-pivot design allows for the pivoting of the pendulum with very little heat dissipation at 4 K, it also created a highly-oscillatory system with a low resonance frequency ($\sim$1.9 Hz). Such systems are difficult to control with conventional PID systems, often only showing a stable response within a very restricted parameter space. Additionally, the velocity limits imposed by the maximum fringe counting rates of the laser metrology system produced more constraints on the step-and-integrate control system. To produce a system which is easily controllable, a method of damping could be implemented to both widen the possible parameter space, and decrease the maximum velocity of the pendulum.

8.4.2 Suggested Improvements

Loss Tangent of Silicon

To characterize the dielectric loss within the etalon, an apparatus must be constructed so that the etalon may be inserted or removed from the optical beam. This can be attained either by moving the etalon itself, or by using flip mirror to bypass the entire pendulum/etalon assembly. The current plan is to replace the plane mirror which follows the collimator to reflect light towards the pendulum with a larger plane mirror that can be rotated to instead reflect light directly towards the grating. A schematic of this plan is shown in Figure 8.1.

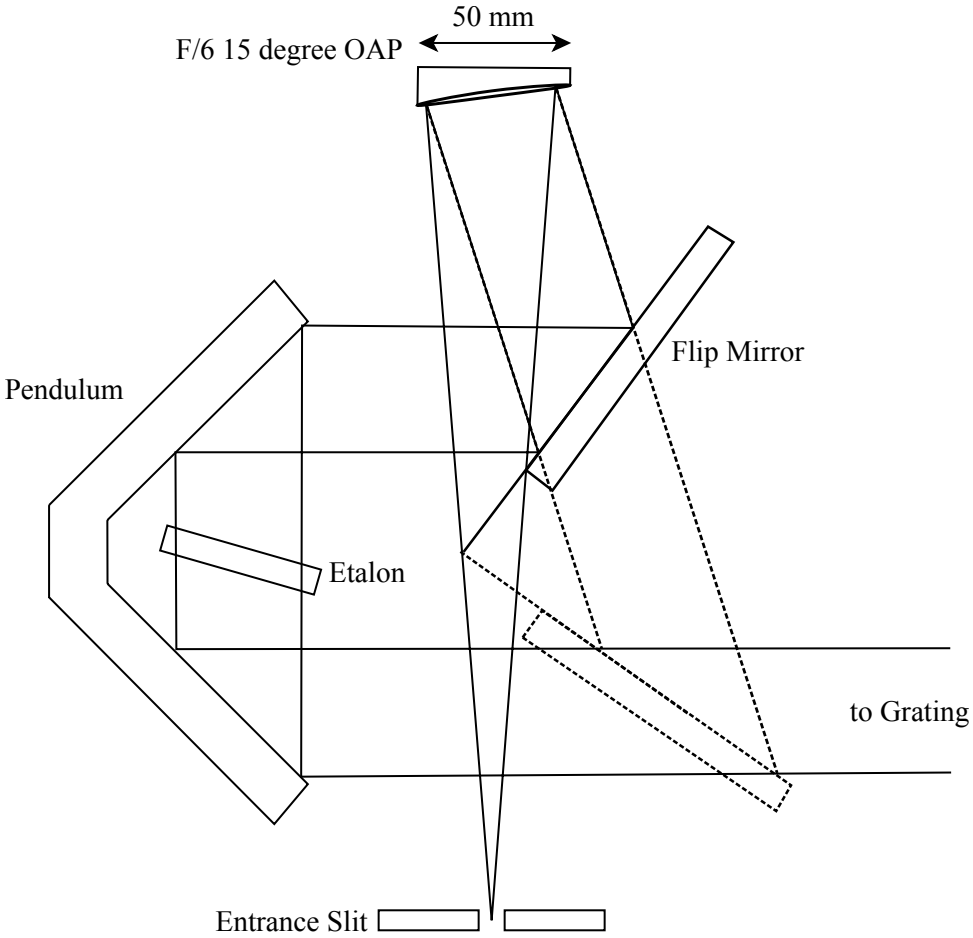

Figure 8.1: A schematic of the FPI optics with plans for a flip mirror which can either be set so that the beam passes through the etalon (solid lines), or so that the beam bypasses the etalon and pendulum (dashed lines).

Frequency Modulated Metrology

Rather than the dual-fiber, three phase metrology system to measure the displacement of the pendulum arms, a single fiber system can be used which relies on modulation of the laser frequency. By modulating between two frequencies at a stable modulation frequency, quadrature can be decoded from the detected signal. The development of such a system is already underway, and MSc student Adam Christiansen at the AIG has shown promising results of its performance at 4 K [128].

Using the frequency-modulated metrology, only a single retroreflector target was required at 4 K. Therefore, the target was moved from the end of the pendulum arm to beneath the RVCAs to shift the center of mass closer to the pivot axis, as well as to decrease the shear of the laser beam during the angular motion of the pendulum (Figure 8.2).

Damping for PID Control

Frequency modulation imposed a lower maximum velocity restriction on the pendulum arm as compared to the three phase metrology. In order to ensure the pendulum arm did not exceed this velocity, as well as to provide stability for step-and-integrate control, a passive damping element was added. The system uses permanent SmCo magnets and an aluminum or copper fin attached to the pendulum arm. Motion of the pendulum induces Eddy currents in the fin, which reduces the pendulum velocity. High purity copper or aluminum has a low electrical resistivity at 4 K, so damping will improve as the system is cooled, and heat dissipation in the fin will not affect the pendulum temperature significantly. The pendulum with the added damping components and new retroreflector position is shown in Figure 8.2.

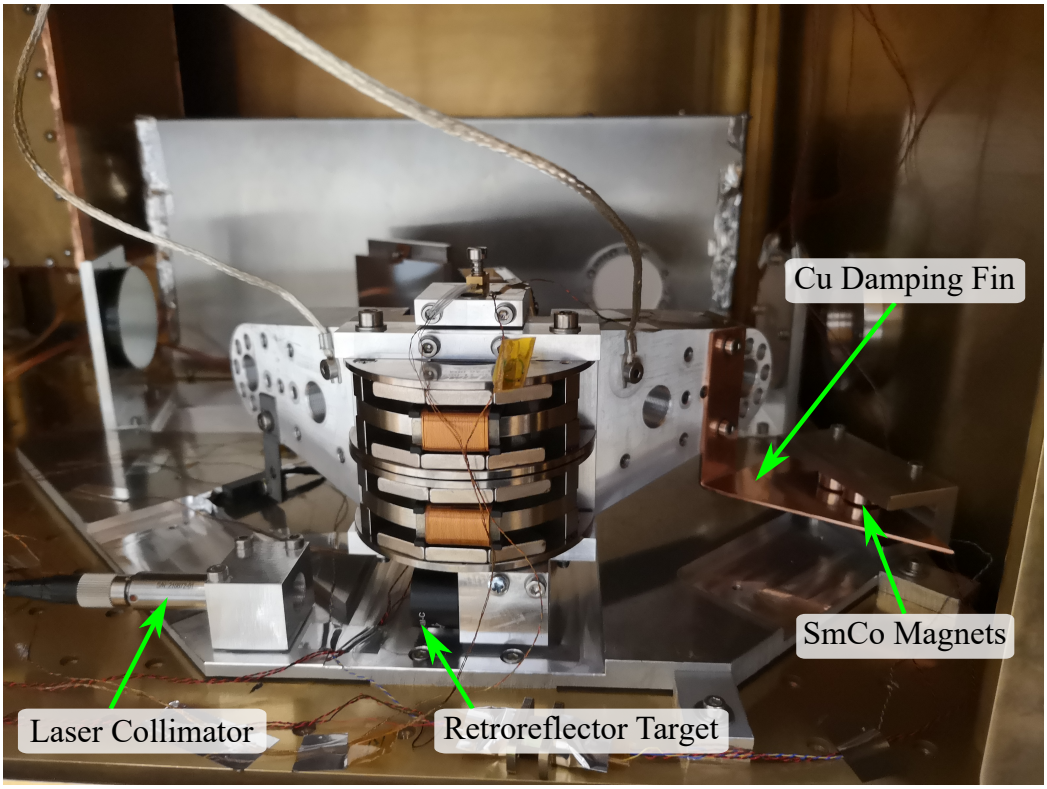

Figure 8.2: Back view of the pendulum assembly. The retroreflector target was moved from the back of the pendulum arm to beneath the RVCAs. The permanent magnets and fin for added damping are shown in the right of the picture. In later tests, the copper fin damping proved too strong at 4 K, so it was replaced with an aluminum fin.

8.5 Conclusion

The campaign to develop a cryogenic, angle-scanning FPI was successful, resulting in the first ever cryogenic high-resolution angle-scanned FPI to date. The performance of the instrument was validated, and matched predictive models with remarkable agreement, although only a small set of wavelengths within the design range was measured. Elements of the position measurement of both the grating and the pendulum could be improved in order to allow verification of the FPI performance over the full design range. The proposed improvements were addressed and plans were developed for the next phase of this project. However, actuation and measurement of devices at cryogenic temperatures is difficult, and these improvements will be implemented in the future. The addition of these components will allow for accurate measurements

of the cryogenic properties of the silicon etalon, as well as absolute flux calibration of a complete FPI/grating instrument. The improvements to the instrument described in this thesis are left as potential projects for future graduate students at the AIG.

References

[1] B. P. Abbott et al. “Observation of Gravitational Waves from a Binary Black Hole Merger”. In: *Physical Review Letters* 116 (2016), p. 061102. DOI: 10.1103/PhysRevLett.116.061102.

[2] A. Aab et al. “Observation of a large-scale anisotropy in the arrival directions of cosmic rays above 8 × 10 18 eV”. In: *Science* 357.6357 (2017), pp. 1266–1270. DOI: 10.1126/science.aan4338.

[3] Michael G. Hauser and Eli Dwek. “The Cosmic Infrared Background: Measurements and Implications”. In: *Annual Review of Astronomy and Astrophysics* 39.1 (2001), pp. 249–307. DOI: 10.1146/annurev.astro.39.1.249.

[4] P.H. Siegel. “Terahertz technology”. In: *IEEE Transactions on Microwave Theory and Techniques* 50.3 (2002), pp. 910–928. DOI: 10.1109/22.989974.

[5] Robert L Brown, Wolfgang Wild, and Charles Cunningham. “ALMA – the Atacama large millimeter array”. In: *Advances in Space Research* 34.3 (2004), pp. 555–559. DOI: 10.1016/j.asr.2003.03.028.

[6] E.E. Becklin. “Stratospheric Observatory for Infrared Astronomy (SOFIA)”. In: *Advances in Space Research* 36.6 (2005), pp. 1087–1090. DOI: 10.1016/j.asr.2005.06.027.

[7] Duncan Farrah et al. “Review: far-infrared instrumentation and technological development for the next decade”. In: *Journal of Astronomical Telescopes, Instruments, and Systems* 5.2 (2019), p. 1. DOI: 10.1117/1.JATIS.5.2.020901.

[8] Maxine Grace Trimboli. "Development of a near-field terahertz microscope for breast cancer diagnostics". Master's thesis. Lethbridge, Alta.: University of Lethbridge, Dept. of Physics and Astronomy, 2015, p. 157.

[9] Dieter Lutz. "Far-Infrared Surveys of Galaxy Evolution". In: *Annual Review of Astronomy and Astrophysics* 52.1 (2014), pp. 373–414. DOI: 10.1146/annurev-astro-081913-035953.

[10] E Hubble. "A relation between distance and radial velocity among extra-galactic nebulae". In: *Proceedings of the National Academy of Sciences* 15.3 (1929), pp. 168–173. DOI: 10.1073/pnas.15.3.168.

[11] Naseem Rangwala et al. "Observations of Arp 220 using Herschel-spire: An unprecedented view of the molecular gas in an extreme star formation environment". In: *Astrophysical Journal* 743.1 (2011), p. 94. DOI: 10.1088/0004-637X/743/1/94.

[12] F. F.S. van der Tak et al. "Probing the Baryon Cycle of Galaxies with SPICA Mid- and Far-Infrared Observations". In: *Publications of the Astronomical Society of Australia* 35 (2018). DOI: 10.1017/pasa.2017.67.

[13] Christopher K. Walker. *Terahertz Astronomy*. Taylor & Francis, 2015.

[14] J. H. Jeans. "The Stability of a Spherical Nebula". In: *Philosophical Transactions of the Royal Society A: Mathematical, Physical and Engineering Sciences* 199.312-320 (1902), pp. 1–53. DOI: 10.1098/rsta.1902.0012.

[15] J.E. Dyson and D.A. Williams. *The Physics of the Interstellar Medium, Second Edition*. Series in Astronomy and Astrophysics. CRC Press, 1997.

[16] M. Ansdell et al. "ALMA survey of lupus protoplanetary disks. I. dust and gas masses". In: *The Astrophysical Journal* 828.1 (2016), p. 46. DOI: 10.3847/0004-637X/828/1/46.

[17] Jonathan P Williams and Lucas A Cieza. "Protoplanetary Disks and Their Evolution". In: *Annual Review of Astronomy and Astrophysics* 49.1 (2011), pp. 67–117. DOI: 10.1146/annurev-astro-081710-102548.

[18] Javier Goicoechea et al. *Assessment Study Report SPICA Revealing the origins of planets and galaxies*. Tech. rep. European Space Agency, 2009.

[19] Ewine F. van Dishoeck and Geoffrey A. Blake. "Chemical evolution of star forming regions". In: *Annual Review of Astronomy and Astrophysics* 36.1 (1998), pp. 317–368. DOI: 10.1146/annurev.astro.36.1.317.

[20] B. Gundlach and J. Blum. "The stickiness of micrometer-sized water-ice particles". In: *The Astrophysical Journal* 798.1 (2014), p. 34. DOI: 10.1088/0004-637X/798/1/34.

[21] Mark J. Devlin et al. "Over half of the far-infrared background light comes from galaxies at z $\geq$ 1.2". In: *Nature* 458.7239 (2009), pp. 737–739. DOI: 10.1038/nature07918.

[22] E. Egami et al. "Probing the high-redshift universe with SPICA: Toward the epoch of reionisation and beyond". In: *Publications of the Astronomical Society of Australia* 35 (2018), e048. DOI: 10.1017/pasa.2018.41.

[23] Jarrett L. Johnson, Vecchia Claudio Dalla, and Sadegh Khochfar. "The First Billion Years project: the impact of stellar radiation on the co-evolution of Populations II and III". In: *Monthly Notices of the Royal Astronomical Society* 428.3 (2013), pp. 1857–1872. DOI: 10.1093/mnras/sts011.

[24] Isabelle Cherchneff and Eli Dwek. "The chemistry of population III supernova ejecta. II. The nucleation of molecular clusters as a diagnostic for dust in the early universe". In: *The Astrophysical Journal* 713.1 (2010), pp. 1–24. DOI: 10.1088/0004-637X/713/1/1.

[25] L. Spinoglio et al. “Galaxy evolution studies with the SPace IR telescope for cosmology and astrophysics (SPICA): The power of IR spectroscopy”. In: *Publications of the Astronomical Society of Australia* 34 (2017). DOI: 10.1017/pasa.2017.48.

[26] Laura Ferrarese and David Merritt. “A Fundamental Relation between Supermassive Black Holes and Their Host Galaxies”. In: *The Astrophysical Journal* 539.1 (2000), pp. L9–L12. DOI: 10.1086/312838.

[27] Karl Gebhardt et al. “A Relationship between Nuclear Black Hole Mass and Galaxy Velocity Dispersion”. In: *The Astrophysical Journal* 539.1 (2000), pp. L13–L16. DOI: 10.1086/312840.

[28] E. González-Alfonso et al. “Feedback and Feeding in the Context of Galaxy Evolution with SPICA: Direct Characterisation of Molecular Outflows and Inflows”. In: *Publications of the Astronomical Society of Australia* (2017). DOI: 10.1017/pasa.2017.46.

[29] E. T. Young et al. “Early science with SOFIA, the stratospheric observatory for infrared astronomy”. In: *Astrophysical Journal Letters* 749.2 (2012), p. L17. DOI: 10.1088/2041-8205/749/2/L17.

[30] M.F. Kessler. “The Infrared Space Observatory (ISO) mission”. In: *Advances in Space Research* 30.9 (2002), pp. 1957–1965. DOI: 10.1016/S0273-1177(02)00557-4.

[31] M.W. Werner. “The spitzer space telescope mission”. In: *Advances in Space Research* 36.6 (2005), pp. 1048–1049. DOI: 10.1016/j.asr.2005.04.012.

[32] Hiroshi Murakami et al. “The Infrared Astronomical Mission AKARI”. In: *Publications of the Astronomical Society of Japan* 59.sp2 (2007), S369–S376. DOI: 10.1093/pasj/59.sp2.S369.

[33] G. L. Pilbratt et al. “Herschel Space Observatory - An ESA facility for far-infrared and submillimetre astronomy”. In: *Astronomy & Astrophysics* 518 (2010), p. L1. DOI: 10.1051/0004-6361/201014759.

[34] Tracy Webb et al. *A Roadmap for Canadian Submillimetre Astronomy*. Tech. rep. Canadian Space Agency, 2013.

[35] Michael D. Audley et al. “The SAFARI detector system”. In: *Millimeter, Submillimeter, and Far-Infrared Detectors and Instrumentation for Astronomy IX*. Ed. by Jonas Zmuidzinas and Jian-Rong Gao. Vol. 10708. 0. SPIE, 2018, p. 18. DOI: 10.1117/12.2313361.

[36] Takao Nakagawa, Hideo Matsuhara, and Yasuhiro Kawakatsu. “The next-generation infrared space telescope SPICA”. In: *Space Telescopes and Instrumentation 2012: Optical, Infrared, and Millimeter Wave*. Ed. by Mark C. Clampin et al. Vol. 8442. 2012, 84420O. DOI: 10.1117/12.927243.

[37] Bruce Swinyard and Takao Nakagawa. “The space infrared telescope for cosmology and astrophysics: SPICA A joint mission between JAXA and ESA”. In: *Experimental Astronomy* 23.1 (2009), pp. 193–219. DOI: 10.1007/s10686-008-9090-0.

[38] Peter R. Roelfsema et al. “SPICA - a large cryogenic infrared space telescope Unveiling the obscured Universe”. In: *Publications of the Astronomical Society of Australia* 35 (2018), e030. DOI: 10.1017/pasa.2018.15.

[39] G Neugebauer et al. “The Infrared Astronomical Satellite (IRAS) mission”. In: *The Astrophysical Journal* 278 (1984), p. L1. DOI: 10.1086/184209.

[40] Matt Griffin et al. “The Herschel Space Observatory”. In: *2008 33rd International Conference on Infrared, Millimeter and Terahertz Waves*. IEEE, 2008, p. 1. DOI: 10.1109/ICIMW.2008.4665517.

[41] Charles Matt Bradford et al. “The Origins Survey Spectrometer (OSS): a far-IR discovery machine for the Origins Space Telescope”. In: *Space Telescopes and Instrumentation 2018: Optical, Infrared, and Millimeter Wave*. Ed. by Howard A. MacEwen et al. SPIE, 2018, p. 43. DOI: 10.1117/12.2314049.

[42] Mark Clampin. “The James Webb Space Telescope (JWST)”. In: *Advances in Space Research* 41.12 (2008), pp. 1983–1991. DOI: 10.1016/j.asr.2008.01.010.

[43] Ian Smail, R. J. Ivison, and A. W. Blain. “A Deep Submillimeter Survey of Lensing Clusters: A New Window on Galaxy Formation and Evolution”. In: *The Astrophysical Journal* 490.1 (1997), pp. L5–L8. DOI: 10.1086/311017.

[44] Luis Martin-Moreno. “Mind the gap”. In: *Nature Photonics* 3.3 (2009), pp. 131–132. DOI: 10.1038/nphoton.2009.16.

[45] Keisuke Shinozaki et al. “Mechanical cooler system for the next-generation infrared space telescope SPICA”. In: *Space Telescopes and Instrumentation 2016: Optical, Infrared, and Millimeter Wave*. Ed. by Howard A. MacEwen et al. Vol. 9904. International Society for Optics and Photonics, 2016, 99043W. DOI: 10.1117/12.2232602.

[46] J.A. Fernández-Ontiveros et al. “Tracing the Evolution of Dust Obscured Star Formation and Accretion Back to the Reionisation Epoch with SPICA”. In: *Publications of the Astronomical Society of Australia* 34 (2017). DOI: 10.1017/pasa.2017.49.

[47] H. Kaneda et al. “Unbiased Large Spectroscopic Surveys of Galaxies Selected by SPICA Using Dust Bands”. In: *Publications of the Astronomical Society of Australia* 34 (2017). DOI: 10.1017/pasa.2017.56.

[48] P. Santini et al. "SPICA and the Chemical Evolution of Galaxies: The Rise of Metals and Dust". In: *Publications of the Astronomical Society of Australia* 34 (2017). DOI: 10.1017/pasa.2017.43.

[49] E. Sturm et al. "Herschel -PACS spectroscopy of IR-bright galaxies at high redshift". In: *Astronomy and Astrophysics* 518 (2010), p. L36. DOI: 10.1051/0004-6361/201014560.

[50] B. Magnelli et al. "The deepest Herschel -PACS far-infrared survey: number counts and infrared luminosity functions from combined PEP/GOODS-H observations". In: *Astronomy & Astrophysics* 553 (2013), A132. DOI: 10.1051/0004-6361/201321371.

[51] C. Gruppioni et al. "The Herschel PEP/HerMES luminosity function – I. Probing the evolution of PACS selected Galaxies to z = 4". In: *Monthly Notices of the Royal Astronomical Society* 432.1 (2013), pp. 23–52. DOI: 10.1093/mnras/stt308.

[52] S. J. Oliver et al. "The Herschel Multi-tiered Extragalactic Survey: HerMES". In: *Monthly Notices of the Royal Astronomical Society* 424.3 (2012), pp. 1614–1635. DOI: 10.1111/j.1365-2966.2012.20912.x.

[53] Piero Madau and Mark Dickinson. "Cosmic Star-Formation History". In: *Annual Review of Astronomy and Astrophysics* 52.1 (2014), pp. 415–486. DOI: 10.1146/annurev-astro-081811-125615.

[54] Michael Rowan-Robinson et al. "The star formation rate density from z = 1 to 6". In: *Monthly Notices of the Royal Astronomical Society* 461.1 (2016), pp. 1100–1111. DOI: 10.1093/mnras/stw1169.

[55] Philippe André. "Interstellar filaments and star formation". In: *Comptes Rendus Geoscience* 349.5 (2017), pp. 187–197. DOI: 10.1016/j.crte.2017.07.002.

[56] Shota Notsu et al. "Candidate Water Vapor Lines to Locate the H_2O Snowline through High-Dispersion Spectroscopic Observations I. The Case of a T Tauri Star". In: *The Astrophysical Journal* 827.2 (2016), p. 113. DOI: 10.3847/0004-637X/827/2/113.

[57] M. J. Griffin et al. "The Herschel -SPIRE instrument and its in-flight performance". In: *Astronomy and Astrophysics* 518 (2010), p. L3. DOI: 10.1051/0004-6361/201014519.

[58] D. H. Martin and E. Puplett. "Polarised interferometric spectrometry for the millimetre and submillimetre spectrum". In: *Infrared Physics* 10.2 (1970), pp. 105–109. DOI: 10.1016/0020-0891(70)90006-0.

[59] M Vaughan. *The Fabry-Perot interferometer: history, theory, practice and applications*. CRC Press, 1989, p. 583.

[60] Paul W. Kruse. *Uncooled Thermal Imaging Arrays, Systems, and Applications*. SPIE, 2009, p. 89. DOI: 10.1117/3.415351.

[61] Christopher A Palmer and Erwin G Loewen. *Diffraction grating handbook*. 6th. Newport Corporation New York, 2005.

[62] A. A. Michelson. "The relative motion of the Earth and of the luminiferous ether". In: *American Journal of Science* s3-22.128 (1881), pp. 120–129. DOI: 10.2475/ajs.s3-22.128.120.

[63] Sumner P. Davis, Mark C. Abrams, and James W. Brault. *Fourier Transform Spectrometry*. Academic Press, 2001, p. 262.

[64] George Biddell Airy. *Mathematical Tracts On Physical Astronomy*. Cambridge: Cambridge University Press, 1826.

[65] A. Perot and Charles Fabry. "On the Application of Interference Phenomena to the Solution of Various Problems of Spectroscopy and Metrology". In: *The Astrophysical Journal* 9 (1899), p. 87. DOI: 10.1086/140557.

[66] Emil Wolf and Max Born. *Principles of Optics: Electromagnetic Theory of Propagation, Interference and Diffraction of Light*. 7th. Cambridge University Press, 1997, p. 808.

[67] E Hecht. *Optics*. 4th. Addison-Wesley, 2002.

[68] Lord Rayleigh F.R.S. "Xxxi. Investigations in Optics, with Special Reference to the Spectroscope". In: *The London, Edinburgh, and Dublin Philosophical Magazine and Journal of Science* 8.49 (1879), pp. 261–274. DOI: 10.1080/14786447908639684.

[69] Peter A. R. Ade et al. "A review of metal mesh filters". In: *Millimeter and Submillimeter Detectors and Instrumentation for Astronomy III*. Ed. by Jonas Zmuidzinas et al. Vol. 6275. 2006, 62750U. DOI: 10.1117/12.673162.

[70] R. Ulrich. "Far-infrared properties of metallic mesh and its complementary structure". In: *Infrared Physics* 7.1 (1967), pp. 37–55. DOI: 10.1016/0020-0891(67)90028-0.

[71] D. W. Porterfield et al. "Resonant metal-mesh bandpass filters for the far infrared". In: *Applied Optics* 33.25 (1994), p. 6046. DOI: 10.1364/AO.33.006046.

[72] A. Poglitsch et al. "The MPE/UCB far-infrared imaging Fabry-Perot interferometer (FIFI)". In: *International Journal of Infrared and Millimeter Waves* 12.8 (1991), pp. 859–884. DOI: 10.1007/BF01009647.

[73] D. A. Naylor and I. Furniss. "A method of determining the flatness of metal mesh elements of a far infrared Fabry-Perot interferometer". In: *Infrared Physics* 29.1 (1989), pp. 159–162. DOI: 10.1016/0020-0891(89)90019-5.

[74] P. D. Atherton et al. "Tunable Fabry-Perot Filters". In: *Optical Engineering* 20.6 (1981), p. 206806. DOI: 10.1117/12.7972819.

[75] J. M. Green. "The 'walk-off' effect in Fabry-Perot etalons-limitations to 'single-shot' linewidth measurements at longer wavelengths". en. In: *Journal of Physics E: Scientific Instruments* 13.12 (1980), pp. 1302–1304. DOI: 10.1088/0022-3735/13/12/018.

[76] R. J. Emery et al. "The Long Wavelength Spectrometer (LWS) for ISO". In: *The Long Wavelength Spectrometer (LWS) for ISO*. Ed. by John W. Lear et al. Vol. 589. 1. SPIE, 1986, p. 194. DOI: 10.1117/12.951933.

[77] Daniel J. Schroeder. *Astronomical Optics*. Academic Press, 2000.

[78] G R Davis et al. "Design and performance of cryogenic, scanning Fabry–Perot interferometers for the Long-Wavelength Spectrometer on the Infrared Space Observatory". In: *Applied optics* 34.1 (1995), pp. 92–107.

[79] Willem Jellema, David A Naylor, and Peter Roelfsema. "Post-dispersed FTS Spectroscopy on SPICA-Safari". In: *Light, Energy and the Environment*. Washington, D.C.: OSA, 2016, FM2D.6. DOI: 10.1364/FTS.2016.FM2D.6.

[80] Liang Fang et al. "Tunable Fabry–Perot filter and grating hybrid modulator to improve dispersive spectrometer resolution". In: *Applied Physics B: Lasers and Optics* 122.5 (2016), p. 145. DOI: 10.1007/s00340-016-6416-x.

[81] Gibion Makiwa. "Performance characterization of a millimeter-wave photomixer". Master's thesis. University of Lethbridge, 2011.

[82] Ian Veenendaal. "A Cryogenic Test Facility". Master's thesis. University of Lethbridge, 2016.

[83] Bradley Gustav Gom. "A cryogenic detector for submillimetre astronomy". Master's thesis. University of Lethbridge, Faculty of Arts and Science, 1999.

[84] *CHASE RESEARCH CRYOGENICS Ltd.* URL: http://www.chasecryogenics.com/.

[85] Leverson F. Costa et al. "TeraHertz Laser Generation by Optically Pumped Polar Molecules". In: *Optical Terahertz Science and Technology*. Washington, D.C.: OSA, 2007, p. MD3. DOI: 10.1364/OTST.2007.MD3.

[86] T.W. Crowe et al. "Opening the terahertz window with integrated diode circuits". In: *IEEE Journal of Solid-State Circuits* 40.10 (2005), pp. 2104–2110. DOI: 10.1109/JSSC.2005.854599.

[87] E. Pliński. "Terahertz photomixer". In: *Bulletin of the Polish Academy of Sciences: Technical Sciences* 58.4 (2010), pp. 463–470. DOI: 10.2478/v10175-010-0044-0.

[88] *Active Components Signal Laser*. FURUKAWA ELECTRIC CO., LTD. 2011. URL: https://www.furukawa.co.jp/fitel/english/active/signal.htm.

[89] E. R. Brown, F. W. Smith, and K. A. McIntosh. "Coherent millimeter-wave generation by heterodyne conversion in low-temperature-grown GaAs photoconductors". In: *Journal of Applied Physics* 73.3 (1993), pp. 1480–1484. DOI: 10.1063/1.353222.

[90] T P Pearsall and M Papuchon. "The Ga 0.47 In 0.53 As homojunction photodiode—A new avalanche photodetector in the near infrared between 1.0 and 1.6 μm". In: *Applied Physics Letters* 33.7 (1978), pp. 640–642. DOI: 10.1063/1.90447.

[91] Rüdiger Paschotta. *Encyclopedia of Laser Physics and Technology - an Open Access Resource of In-Depth Information, Free Articles, Nonlinear and Fiber Optics*. URL: http://www.rp-photonics.com/encyclopedia.html (visited on 04/14/2019).

[92] *Toptica Photonics*. 2014. URL: http://www.toptica.com/ (visited on 06/28/2018).

[93] M. Bass. *Handbook of Optics, Volume I: Geometrical and Physical Optics, Polarized Light, Components and Instruments*. 2nd ed. McGraw-Hill, 2001, p. 1628.

[94] I.S. Gregory et al. "Optimization of photomixers and antennas for continuous-wave terahertz emission". In: *IEEE Journal of Quantum Electronics* 41.5 (2005), pp. 717–728. DOI: 10.1109/JQE.2005.844471.

[95] Robert A Pease. "AN-1515 A Comprehensive Study of the Howland Current Pump". In: *Texas Instruments* April (2013), pp. 1–17. DOI: 10.1212/WNL.55.12.1921.

[96] Jonathan Tennyson. *Astronomical Spectroscopy*. WORLD SCIENTIFIC, 2011. DOI: 10.1142/7574.

[97] *Blue Sky Spectroscopy Inc. BTRAM v3*. URL: https://blueskyspectroscopy.com/ (visited on 12/19/2017).

[98] Cécile Gry et al. *THE ISO HANDBOOK LWS-The Long Wavelength Spectrometer*. Tech. rep. European Space Agency, 2003.

[99] J.M. Lerner and A. Thevenon. *Optics of Spectroscopy - A Tutorial*. 2013. URL: http://www.horiba.com/us/en/scientific/products/optics-tutorial/ (visited on 06/05/2018).

[100] *Phytron GmbH*. URL: https://www.phytron.eu/ (visited on 06/27/2018).

[101] *B-Con Engineering*. URL: http://www.bconeng.com/ (visited on 06/25/2018).

[102] Budynas and Nisbett. *Shingley's Mechanical Engineering Design, Eighth Edition*. McGraw-Hill, 2006, pp. 209–246.

[103] *Epotek Technology Inc.* URL: https://www.epotek.com/site/ (visited on 05/08/2019).

[104] *PhidgetStepper Bipolar HC-1067*. URL: https://www.phidgets.com/?tier=3&catid=23&pcid=20&prodid=1029 (visited on 05/08/2019).

[105] *Measurement Computing USB-1808 Series High-Speed, High-Precision, Simultaneous USB Devices*. URL: https://www.mccdaq.com/data-acquisition-and-control/simultaneous-daq/USB-1808-Series.aspx (visited on 05/08/2019).

[106] *PLX ACT-25B Electronic Autocollimator and Alignment Telescope*. URL: https://www.plxinc.com/products/act-25b-electronic-autocollimator (visited on 05/08/2019).

[107] *BEI Kimco*. URL: http://www.beikimco.com/ (visited on 06/25/2018).

[108] Juha. Pyrhönen, Tapani Jokinen, and Valeria. Hrabovcová. *Design of rotating electrical machines*. Wiley, 2008, p. 512.

[109] *C-Flex Bearing Co., Inc.* URL: https://c-flex.com/ (visited on 05/13/2019).

[110] J. W. Ekin. *Experimental techniques for low-temperature measurements : cryostat design, material properties, and superconductor critical-current testing*. OUP Oxford, 2006, p. 673.

[111] R. Huisman et al. "Cryogenic mechatronic design of the HIFI Focal Plane Chopper". In: *Mechatronics* 21.8 (2011), pp. 1259–1271. DOI: 10.1016/j.mechatronics.2011.03.004.

[112] *Goodfellow Inconel 718 Material Information*. URL: http://www.goodfellow.com/E/Inconel-alloy-718-Heat-Resisting-Alloy-Alloy.html (visited on 06/24/2019).

[113] Andrew J. Fleming. "A review of nanometer resolution position sensors: Operation and performance". In: *Sensors and Actuators, A: Physical* 190 (2013), pp. 106–126. DOI: 10.1016/j.sna.2012.10.016.

[114] David Naylor et al. "The SPICA SAFARI Fourier Transform Spectrometer". In: *Light, Energy and the Environment 2018 (E2, FTS, HISE, SOLAR, SSL)*. Washington, D.C.: OSA, 2018, FW3B.1. DOI: 10.1364/FTS.2018.FW3B.1.

[115] Ian Veenendaal et al. “A novel design for a cryogenic, angle-scanned, Fabry-Pérot interferometer”. In: *Advances in Optical and Mechanical Technologies for Telescopes and Instrumentation III*. Vol. 10706. International Society for Optics and Photonics. 2018, p. 107061C.

[116] W. C. Duesterhoeft, Max W. Schulz, and Edith Clarke. “Determination of Instantaneous Currents and Voltages by Means of Alpha, Beta, and Zero Components”. In: *Transactions of the American Institute of Electrical Engineers* 70.2 (1951), pp. 1248–1255. DOI: 10.1109/T-AIEE.1951.5060554.

[117] Ian Veenendaal et al. “A fibre-fed laser interferometer for optical metrology at cryogenic temperatures”. In: *Photonic Instrumentation Engineering V*. Ed. by Yakov G. Soskind. Vol. 10539. SPIE, 2018, p. 30. DOI: 10.1117/12.2287466.

[118] J J Bock et al. “Silicon-gap Fabry-Perot filter for far-infrared wavelengths”. In: *Applied Optics* 34.19 (1995), pp. 3651–3657. DOI: 10.1364/AO.34.003651.

[119] *Spira Manufacturing Corporation*. URL: http://www.spira-emi.com/ (visited on 06/27/2018).

[120] *Cryomech*. URL: http://www.cryomech.com.

[121] *Cernox — Overview — Lake Shore Cryotronics, Inc.* URL: https://www.lakeshore.com/products/cryogenic-temperature-sensors/cernox/models/pages/overview.aspx (visited on 04/15/2019).

[122] *Model 370 — Overview — Lake Shore Cryotronics, Inc.* URL: https://www.lakeshore.com/products/AC-Resistance-Bridges/Model-370/Pages/Overview.aspx (visited on 04/15/2019).

[123] Caroline Zentner. *U of L’s space imaging group scores success on two fronts — University of Lethbridge*. University of Lethbridge. 2018. URL: http://www.uleth.ca/unews/article/u-l%7B%5Ctextquoteright%7Ds-space-imaging-group-scores-success-two-fronts (visited on 05/21/2019).

[124] Thomas Middelmann et al. “Thermal expansion coefficient of single-crystal silicon from 7 K to 293 K”. In: *Physical Review B* 92.17 (2015), p. 174113. DOI: 10.1103/PhysRevB.92.174113.

[125] Bradley J Frey, Douglas B Leviton, and Timothy J Madison. “Temperature-dependent refractive index of silicon and germanium”. In: *Optomechanical technologies for Astronomy*. Vol. 6273. International Society for Optics and Photonics. 2006, 62732J.

[126] Ernest V. Loewenstein, Donald R. Smith, and Robert L. Morgan. “Optical Constants of Far Infrared Materials 2: Crystalline Solids”. In: *Applied Optics* 12.2 (1973), p. 398. DOI: 10.1364/AO.12.000398.

[127] S. Caparrelli et al. “Vibration-free cryostat for low-noise applications of a pulse tube cryocooler”. In: *Review of Scientific Instruments* 77.9 (2006), p. 095102. DOI: 10.1063/1.2349609.

[128] Adam J. Christiansen et al. “A frequency-modulated laser interferometer for nanometer-scale position sensing at cryogenic temperatures”. In: *Photonic Instrumentation Engineering VI*. Ed. by Yakov G. Soskind. Vol. 10925. SPIE, 2019, p. 40. DOI: 10.1117/12.2508900.

Appendix A

SPICA Instruments

SPICA Far-IR Spectrometer: SAFARI

The SAFARI spectrometer is primarily optimised for a moderate resolution of $R \sim 300$ instantaneously over the 34 µm to 230 µm range, to fullfil its main science driver of performing studies of galactic evolution. A secondary science driver is the requirement to study line profiles at higher wavelength resolution. For this purpose, an additional high resolution mode utilising a Martin-Puplett interferometer is included. With the grating-based design, the SAFARI/SPEC sensitivity of the $R \sim 300$ mode will be about $5 \times 10^{-20}\,\mathrm{W\,m^{-2}}$ (5σ, 1hr) for a Transition Edge Sensor (TES) NEP of $2 \times 10^{-19}\,\mathrm{W}/\sqrt{\mathrm{Hz}}$. The design allows for further improvements in TES performance, these will directly lead to better overall instrument sensitivity. The SAFARI fact sheet (Figure A.1) shows the full specifications for the SAFARI instrument.

SPICA Mid-infrared Instrument: SMI

The SMI mid-IR spectrometer/camera covers the wavelength range from 12 µm to 36 µm with three separate channels: the low-resolution channel (LR), with $R = 50 - 120$ for the 17 µm to 36 µm range, the mid-resolution channel (MRS), with $R = 1300 - 2300$ for 18 µm to 36 µm, and the high-resolution channel (HR), with $R = 28000$ for the 12 µm to 18 µm range. The SMI is composed of two main optics chains, one for LR and one for the MR/HR combination, each with their appropriate fore optics and rear optics. There are no moving parts except a shutter in the LR chain and a beam steering mirror in the MR/HR chains. The SMI fact sheet (Figure A.2) shows the full specifications for the SMI.

SPICA Far-IR Polarimeter: B-BOP

The prime science driver for the far-IR imaging component of SPICA is the polarimetric mapping of Galactic filamentary structures, which requires a high dynamic range both in spatial scales and flux density. For high mapping efficiency a large instantaneous field of view for all wavelength bands is required. In addition, the instrument requires polarizing detectors offering high sensitivity, yet also a high dynamic range. The wavelength bands are defined by the need to observe filaments on both sides of their peak emission, suggesting bands centered around 100 µm, 200 µm, and 350 µm. The required performance parameters of the instrument are summarized in the B-BOP fact sheet (Figure A.3).

SPICA/SAFARI Fact Sheet

SAFARI Overview

- Four band ***grating spectrometer***
- Continuous spectroscopic capability from 34-230 μm

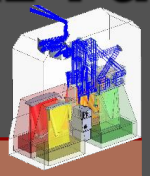

Parameter		Waveband SW	MW	LW	LLW
Band centre / μm		45	72	115	185
Wavelength range / μm		34-56	54-89	87-143	140-230
Band centre beam FWHM		4.5″	7.2″	12″	19″
Point source spectroscopy (5σ-1hr)					
LR	**Limiting flux** / x10^{-20} Wm^{-2}	7.2	6.6	6.6	8.2
	Limiting flux density / mJy	0.31	0.45	0.72	1.44
HR	**Limiting flux** / x10^{-20} Wm^{-2}	13	13	13	15
	Limiting flux density / mJy	18	17	17	19
Mapping spectroscopy* (5σ-1hr)					
LR	**Limiting flux** / x10^{-20} Wm^{-2}	84	49	30	23
	Limiting flux density / mJy	3.6	3.3	3.3	4.1
HR	**Limiting flux** / x10^{-20} Wm^{-2}	189	113	73	51
	Limiting flux density / mJy	253	151	97	67
Photometric mapping* (5σ-1hr)					
Limiting flux density / μJy		209	192	194	239
Confusion limit (5σ)		15 μJy	200 μJy	2 mJy	10 mJy

Sensitivities based on detector NEP 2×10^{-19} W/√Hz
* Mapping performance is for a reference area of 1 arcmin^2

SPICA Mission

- ESA/JAXA collaboration
- Telescope effective area 4.6 m^2
- Primary mirror temperature 8K
- Goal mission lifetime – 5 years

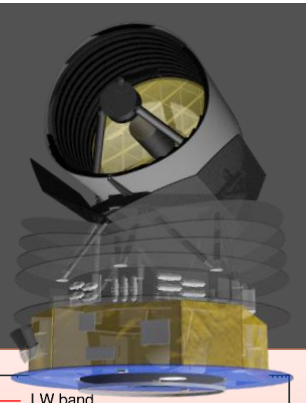

System performance v.s. target flux density, relative to the background limited case

- The sensitivity decrease is due to the increased photon noise from the target source
- Data given up to the instrument saturation limits for each band (31, 51 and 87 Jy for the SW, MW and LW bands respectively.

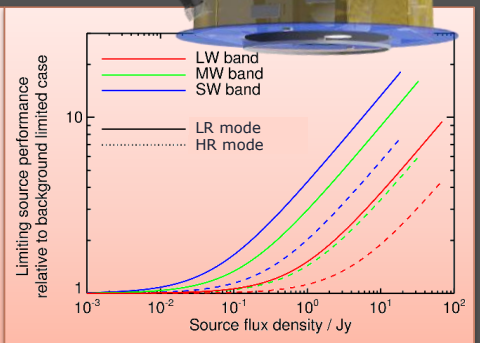

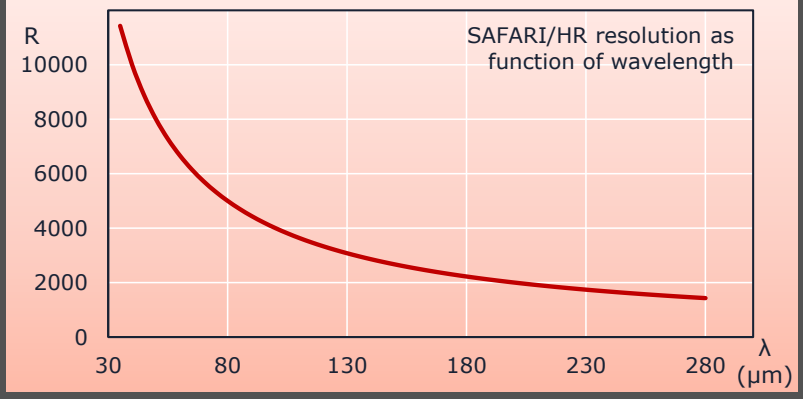

SRON SAFARI

SAFARI GS Factsheet V1.0 – 30th September 2016

Figure A.1: SAFARI Fact Sheet

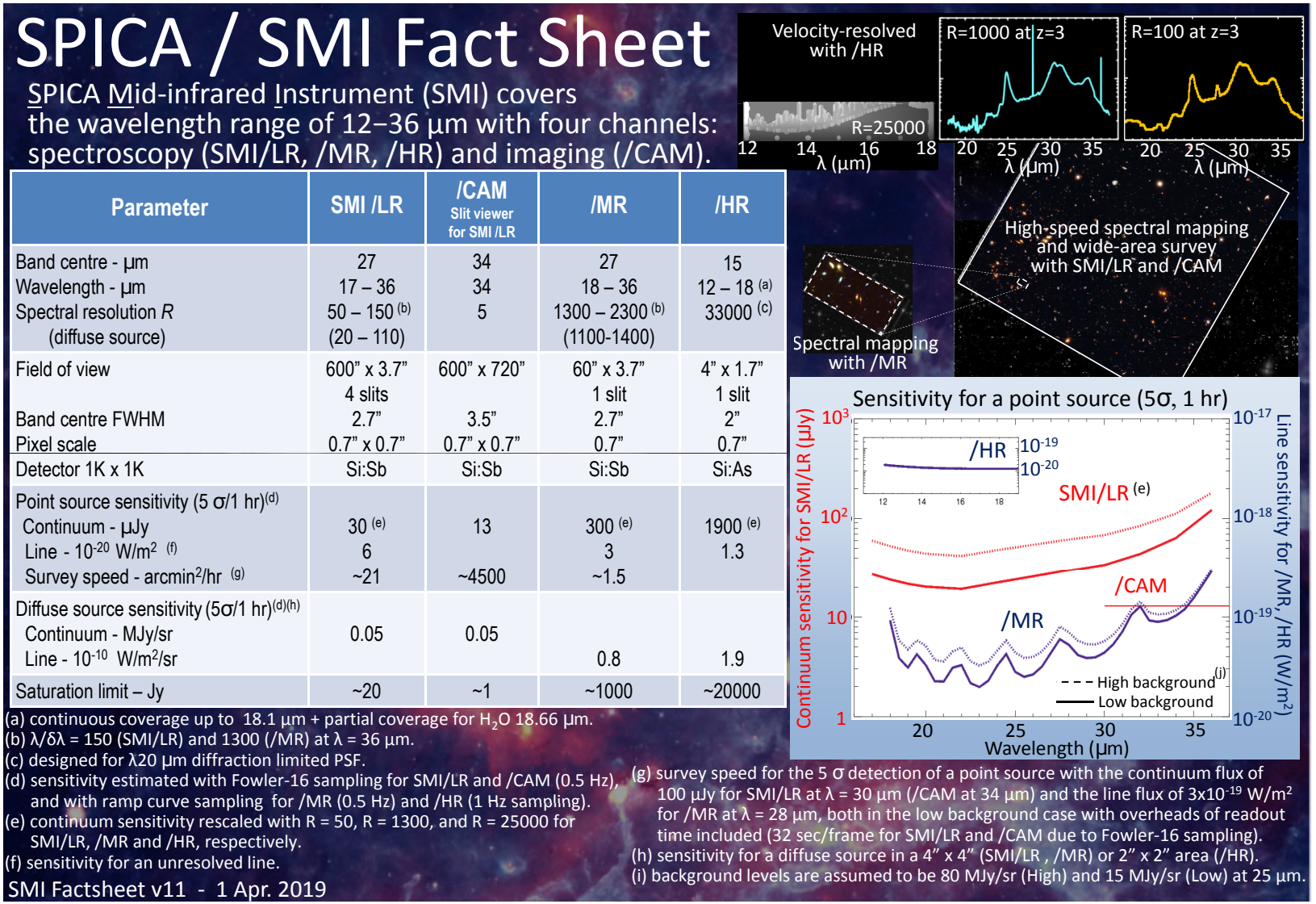

Parameter	SMI /LR	/CAM Slit viewer for SMI /LR	/MR	/HR
Band centre - μm	27	34	27	15
Wavelength - μm	17 – 36	34	18 – 36	12 – 18 (a)
Spectral resolution *R* (diffuse source)	50 – 150 (b) (20 – 110)	5	1300 – 2300 (b) (1100-1400)	33000 (c)
Field of view	600" x 3.7" 4 slits	600" x 720"	60" x 3.7" 1 slit	4" x 1.7" 1 slit
Band centre FWHM	2.7"	3.5"	2.7"	2"
Pixel scale	0.7" x 0.7"	0.7" x 0.7"	0.7"	0.7"
Detector 1K x 1K	Si:Sb	Si:Sb	Si:Sb	Si:As
Point source sensitivity (5 σ/1 hr)(d)				
Continuum - μJy	30 (e)	13	300 (e)	1900 (e)
Line - 10^{-20} W/m² (f)	6		3	1.3
Survey speed - arcmin²/hr (g)	~21	~4500	~1.5	
Diffuse source sensitivity (5σ/1 hr)(d)(h)				
Continuum - MJy/sr	0.05	0.05		
Line - 10^{-10} W/m²/sr			0.8	1.9
Saturation limit – Jy	~20	~1	~1000	~20000

Figure A.2: SMI Fact Sheet

SPICA / SAFARI_Pol Fact Sheet

A polarimetric camera with
3 simultaneous bands 100, 200 & 350 µm
on the same FOV : 2,6' x 2,6' @ 0,6 f#λ sampling

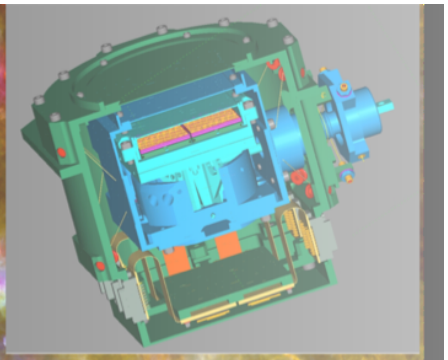

	100µm	200µm	350µm
Band edges	75—125µm	150—250µm	280—420µm
# of pixels	32 x 32 (x 2)	16 x 16 (x 2)	8 x 8 (x 2)
Pixel size	5" x 5"	10" x 10"	20" x 20"
Band centre beam FWHM	9"	18"	32"
PS sensitivity 5σ/1h/FOV (unpolarised)	21µJy	42µJy	85µJy
PS sensitivity in Stokes (Q,U) 5σ/1h/FOV (polarised)	30µJy	60µJy	120µJy
PS sensitivity 5σ/10h/1deg² (unpolarised)	0.16 mJy	0.32 mJy	0.65 mJy
PS sensitivity in Stokes (Q,U) 5σ/10h/1deg² (polarised)	0.23 mJy	0.46 mJy	0.92 mJy
Surface brightness sensitivity 5σ/10h/1deg² (unpolarised)	0.09 MJy/sr	0.045 MJy/sr	0.025 MJy/sr
Sensitivity to map Stokes parameters (Q,U) at 5% level 5σ/10h/1deg²	2.5 MJy/sr	1.25 MJy/sr	0.7 MJy/sr

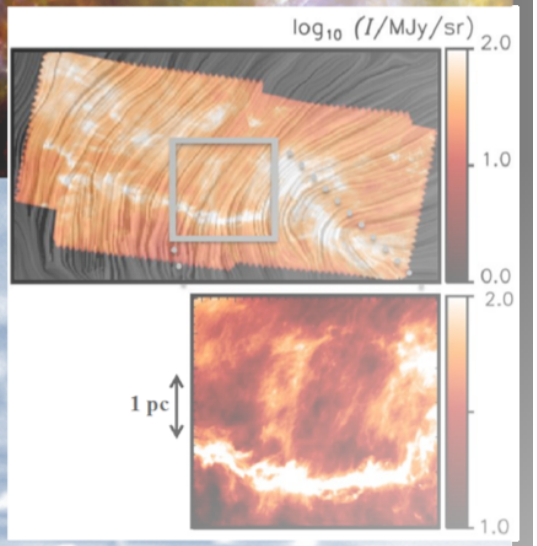

Figure A.3: POL (B-BOP) Fact Sheet

Appendix B

Photodiode IV Characteristics

For a photodiode, the generated current is the sum of the diode dark current I_D and the photocurrent I_P:

$$I = I_D + I_P. \qquad \text{[A]} \quad \text{(B.1)}$$

The dark current is the current generated when no light is incident on the device and can be expressed by the Shockley diode equation, which describes the current of a p-n junction as a function of bias voltage:

$$I_D = I_s\Big(e^{\frac{eV}{kT}} - 1\Big). \qquad \text{[A]} \quad \text{(B.2)}$$

I_s is the reverse saturation current, T is the temperature of the diode, V is the bias voltage, which is 0 for photovoltaic mode, and $-V$ for photoconductive mode, e and k are fundamental constants.

The generated photocurrent is a function of the number of absorbed photons per second N_p and the quantum efficiency Q of the photodiode. The rate of absorbed photons can be expressed as the ratio of the absorbed power P and the average energy per photon:

$$N_p = \frac{P}{h\nu} \qquad \text{(B.3)}$$

where h is the Planck constant, and ν is the average photon frequency. The generated current is the product of the number of absorbed photons per second, the quantum efficiency, and the electrical charge of a single charge carrier e:

$$I_P = \frac{QeP}{h\nu}. \qquad \text{(B.4)}$$

Figure B.1 shows a typical VI curve for a photodiode with $I_s = 10\,\mu\text{m}$, $T = 295\,\text{K}$, $Q = 0.8$, and $\nu = 194\,\text{THz}$.

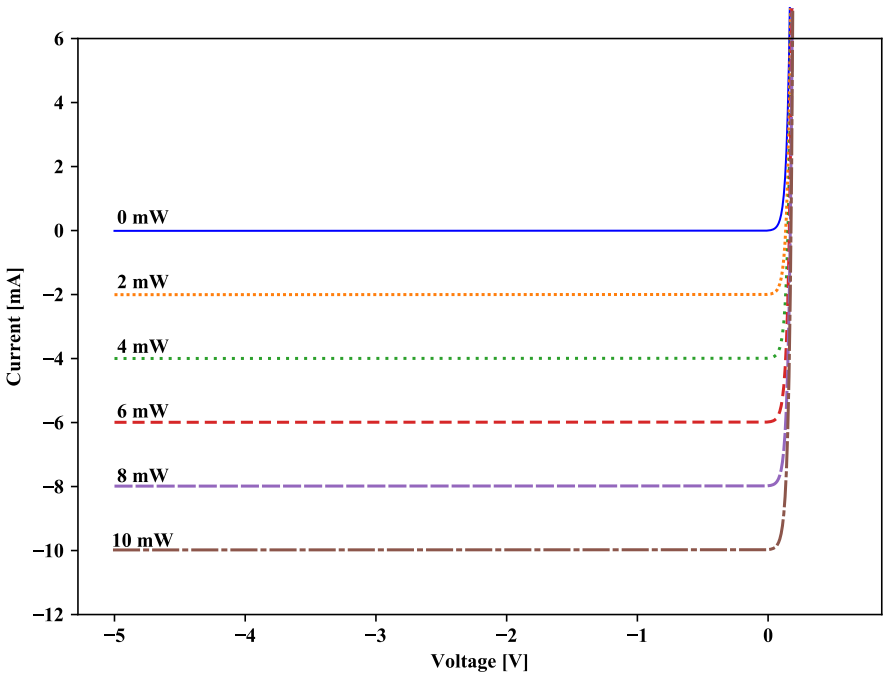

Figure B.1: Typical VI characteristics of a photodiode. Each curve represents a different incident power.

Appendix C

FPI/Grating Operating Modes

Flowcharts which describe the steps for the various operating modes of the FPI/Grating are presented here. The data processing steps which convert the raw data output into physical parameters are presented.

C.1 Operating Modes

The instrument modes of operation are described in Chapter 7. There are three main operating modes:

1. Continuous Scanning Pendulum (CS) Mode
2. Step-and-Integrate Pendulum (SI) Mode
3. Grating Only Mode

Additionally, each scanning mode contains a subset of operations:

a. System Calibration Sub-Mode

b. Normal Operation Sub-Mode

C.2 Data Processing

The processing steps which convert the raw instrument output to physical parameters are described here. For further details on each step, see Chapter 7. The calibration modes utilizing the photomixer require additional steps to determine the photomixer output frequency from the laser parameters.

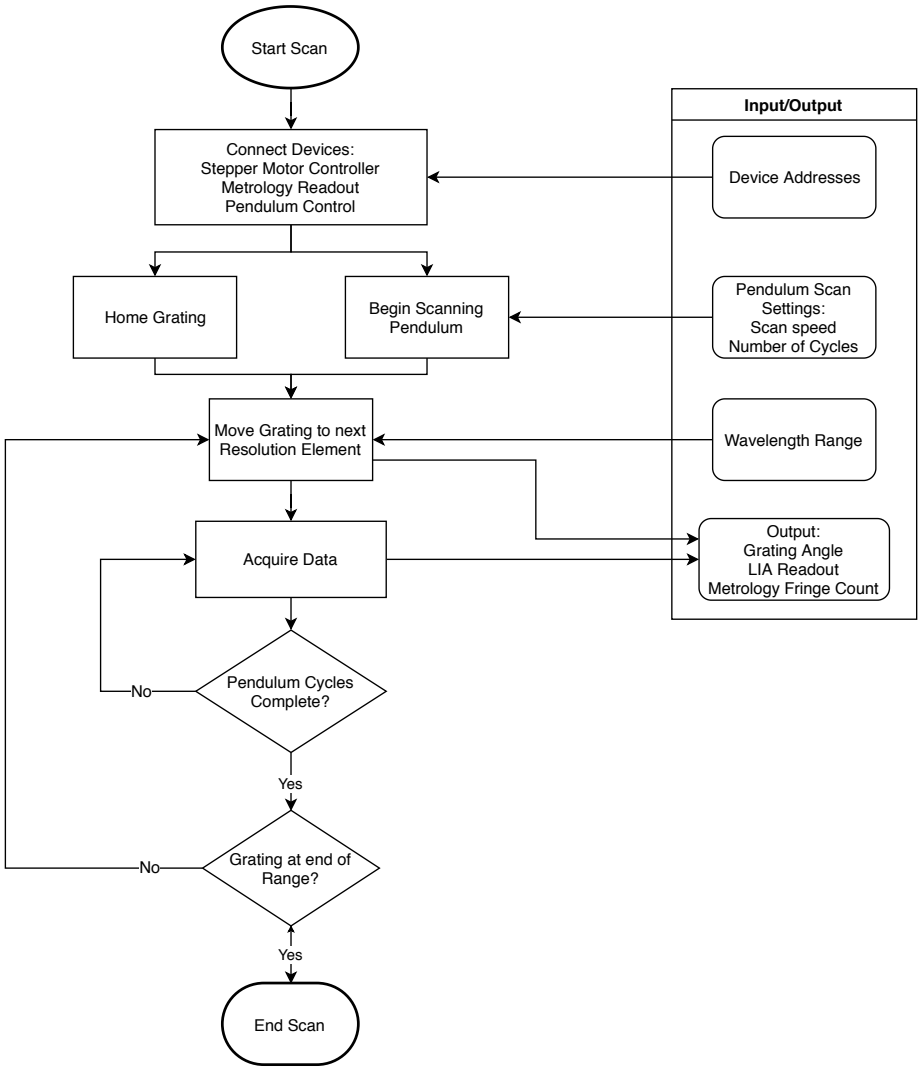

Figure C.1: Flow chart of FPI operation during Continuous Pendulum Scanning mode.

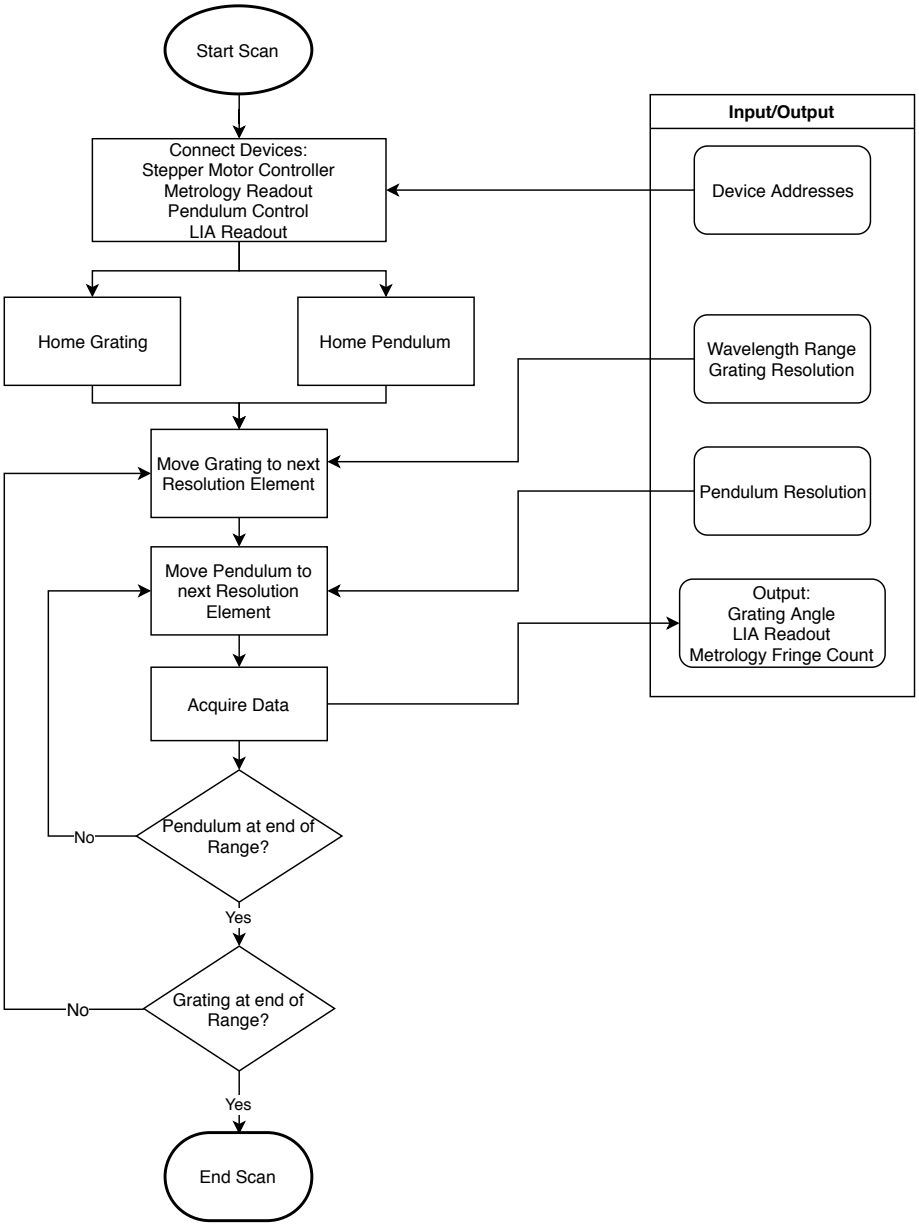

Figure C.2: Flow chart of FPI operation during Step-and-Integrate mode.

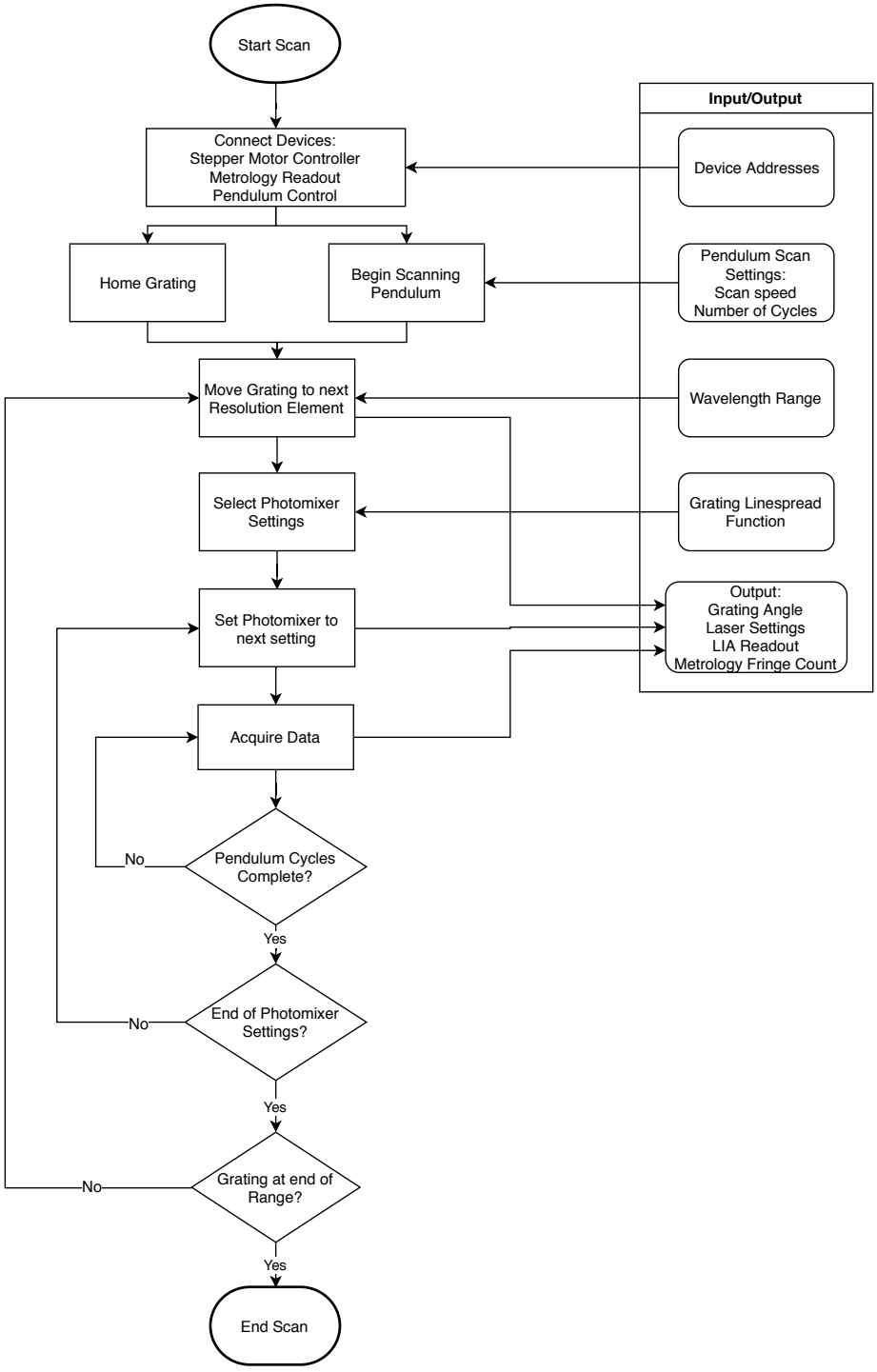

Figure C.3: Flow chart of FPI operation during a calibration scan with the photomixer using the instrument in CS mode.

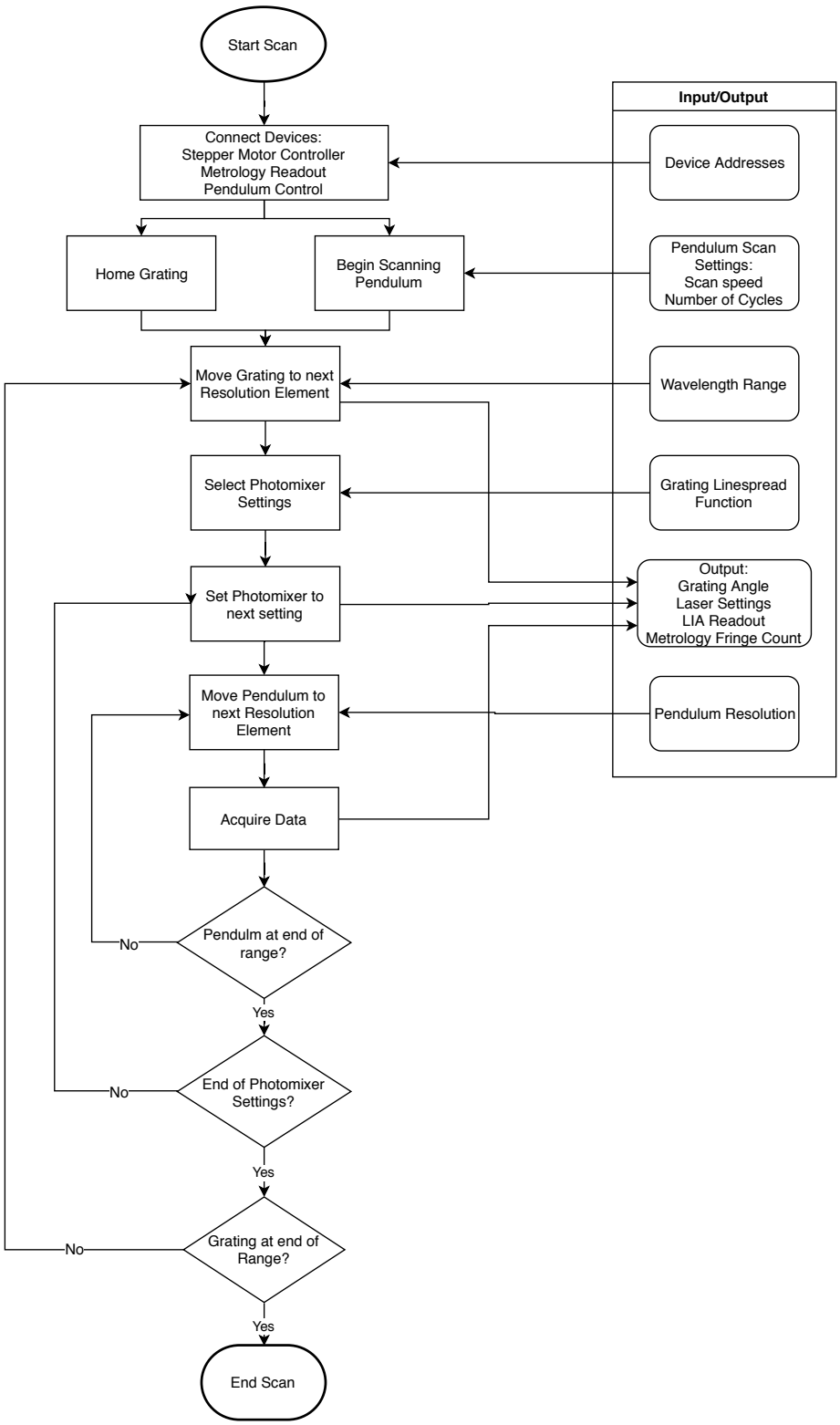

Figure C.4: Flow chart of FPI operation during a calibration scan with the photomixer using the instrument in SI mode.

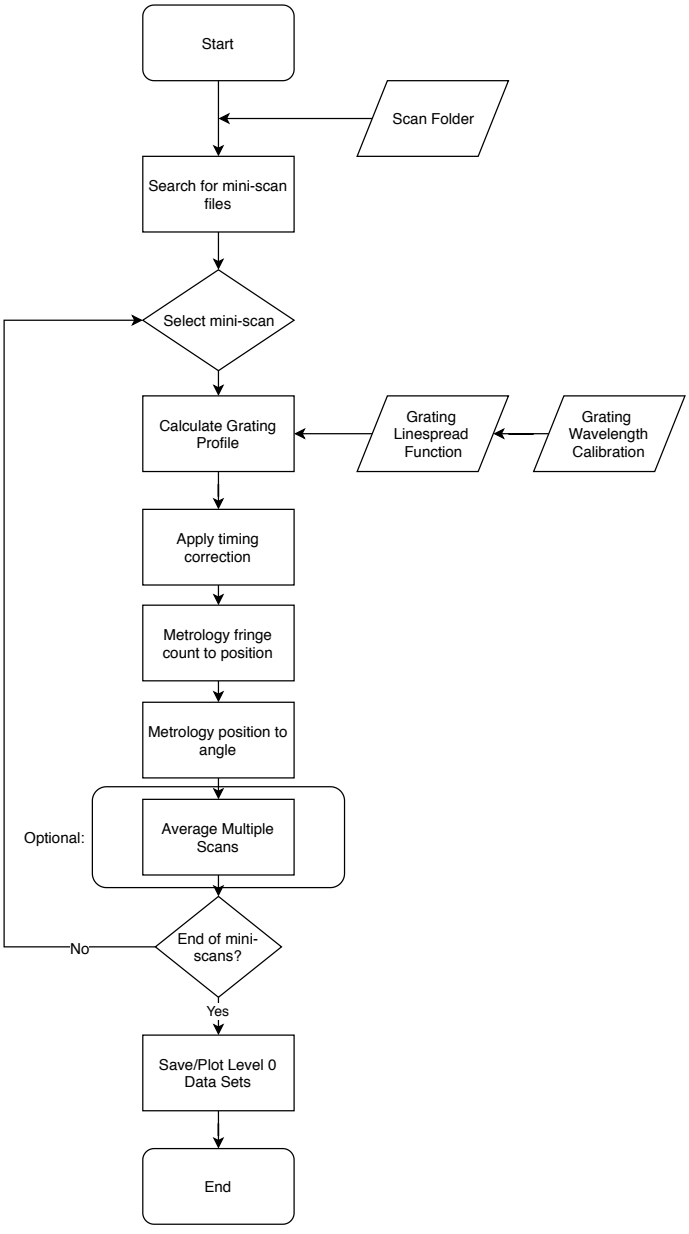

Figure C.5: Flowchart of data processing steps for a normal operation scan.

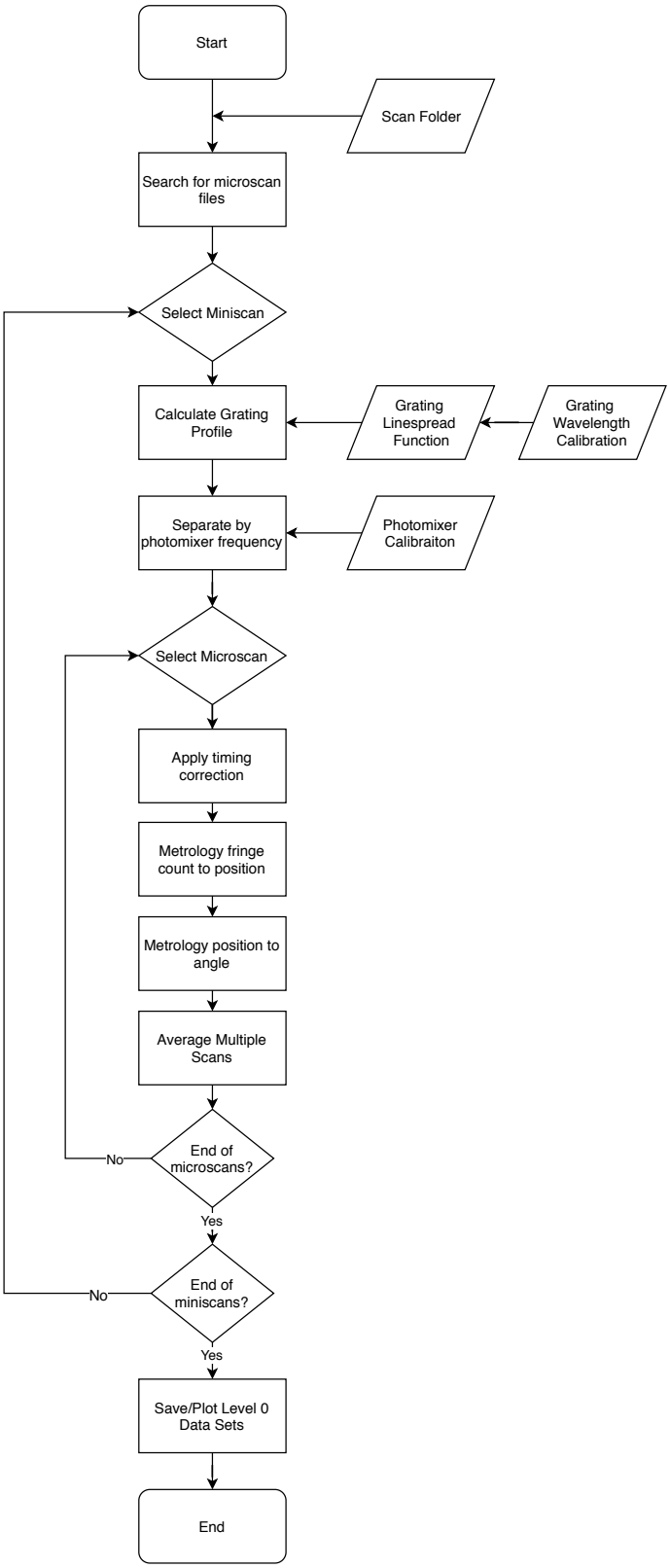

Figure C.6: Flowchart of data processing steps for a calibration scan.

Appendix D

Three Phase Metrology

A fiber-fed laser interferometer for optical metrology at cryogenic temperatures

David Naylor, Ian Veenendaal, Brad Gom, Adam Christiansen
Department of Physics and Astronomy, University of Lethbridge, Alberta, Canada

ABSTRACT

Nature is such that observations at far-infrared wavelengths are optimal for exploring both the nearby and distant Universe. The minute amount of energy carried by far-infrared photons, however, requires extremely sensitive instrumentation for their detection. Moreover, the instrumentation itself must be cooled to <4 K to avoid an unwanted photon noise component from self-emission, and often requires precision metrology at these temperatures. A variety of cryogenic metrology techniques have been used successfully on previous space astronomy missions, each having its own limitations. In this paper we present a fiber-based laser metrology system, designed for optical position metrology at cryogenic temperatures.

Keywords: Metrology, laser, cryogenic, interferometer

1 INTRODUCTION

Observations at far-infrared wavelengths are optimal for exploring both galaxy formation in the farthest reaches of the Universe and star formation within the Milky Way. Early missions such as IRAS[1], ISO[2], Spitzer[3] and AKARI[4] paved the way for the highly successful Herschel Space Observatory[5], whose larger aperture telescope (3.5 m) led to significant advances in both angular resolution and sensitivity. The sensitivity of Herschel, however, was limited by emission from its passively cooled and thus relatively warm telescope (~85 K). Future missions will use telescopes cooled to temperatures of ~6 K, to eliminate the photon noise component from self-emission, in order to reach the background limit imposed by zodiacal emission. Several missions are currently under consideration: ESA and JAXA have joined forces to develop the SPICA[6] mission, which features a telescope of similar size to that of Herschel, but one actively cooled to ~6 K; NASA is studying the Origins Space Telescope[7], which features a larger (9.1 m) aperture telescope cooled to 4K; the Far Infrared Interferometer (FIRI)[8] concept proposes to use a series of cryogenically cooled telescopes to combine stellar interferometry with Fourier transform spectroscopy to provide an unprecedented capability for high spatial resolution with extremely sensitive spectroscopy between 25 and 300 μm. In all cases, the instrument suite exploits the technique of Fourier transform spectroscopy[9] (FTS). With their high throughput, broad spectral coverage and variable resolution, coupled with their well-defined instrumental line shape and intrinsic wavelength and intensity calibration, Fourier spectrometers have a long history in astronomical research[10]. Furthermore, imaging spectroscopy is relatively easily implemented by the use of an array detector, providing a spectrum at each spatial coordinate viewed by a pixel in the array.

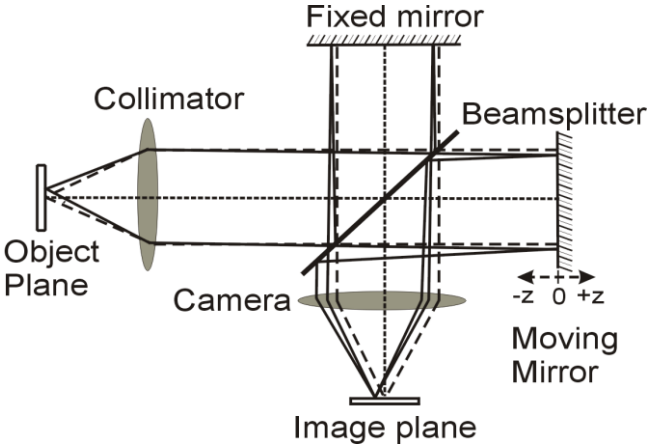

Figure 1. Schematic of the simplest form of Fourier transform spectrometer, the Michelson interferometer.

In the simplest type of Fourier spectrometer, shown in Figure 1, the collimated beam from the telescope is divided into two beams of equal intensity by a beamsplitter. After reflection from a fixed and a moving mirror, the beams recombine at the beamsplitter and are brought to a focus on the detector. The signal recorded by the detector as a function of the optical path difference (OPD), z, between the recombining beams is known as the interferogram. The interferogram represents the autocorrelation of the electric field, $E(\sigma)$, of the incident radiation and, in the ideal case, is given by the cosine Fourier transform of the spectrum, $B(\sigma)$, where σ is the frequency expressed in wavenumbers (cm^{-1}).

$$I(z) = \int_{-\infty}^{\infty} B(\sigma)\cos(2\pi z\sigma)d\sigma$$

where $B(\sigma)$ is proportional to $|E(\sigma)|^2$.

In principle, the spectrum is recovered by computing the cosine transformation of the interferogram. In practice, phase errors that arise from optical, electronical or sampling effects[9] produce asymmetric interferograms which require the use of the complex Fourier transform:

$$B(\sigma) = \int_{-\infty}^{\infty} I(z)e^{-i\,2\pi\sigma z}\,dz$$

While the design of a Fourier spectrometer is relatively straightforward, involving only two interfering beams, obtaining the spectrum requires sophisticated mathematical analysis. Regardless of their design (Michelson[11], Martin-Puplett[12], Mach-Zehnder[13]), all Fourier spectrometers possess two input ports and two output ports. In the case of a Michelson interferometer, the input and output ports are superimposed. Two consequences result: the first is that 50% of the incident radiation is returned to the source, the second is that radiation emitted by the detector assembly itself can be modulated by the interferometer and return to the detector where it is subsequently detected. While this effect is of little consequence in the optical and near-infrared, since typical instrument operating temperatures produce no emission at these wavelengths, this is not the case in the far-infrared. For these reasons, far-infrared, space borne, astronomical Fourier spectrometers must operate at cryogenic temperatures (~4 K) and employ designs that separate the two input and two output ports.

1.1 Metrology requirement

The accuracy with which the OPD within an interferometer must be known is illustrated in Figure 2 which shows a simulated interferogram from the short wavelength band of the Fourier spectrometer proposed for the SAFARI instrument on SPICA[6].

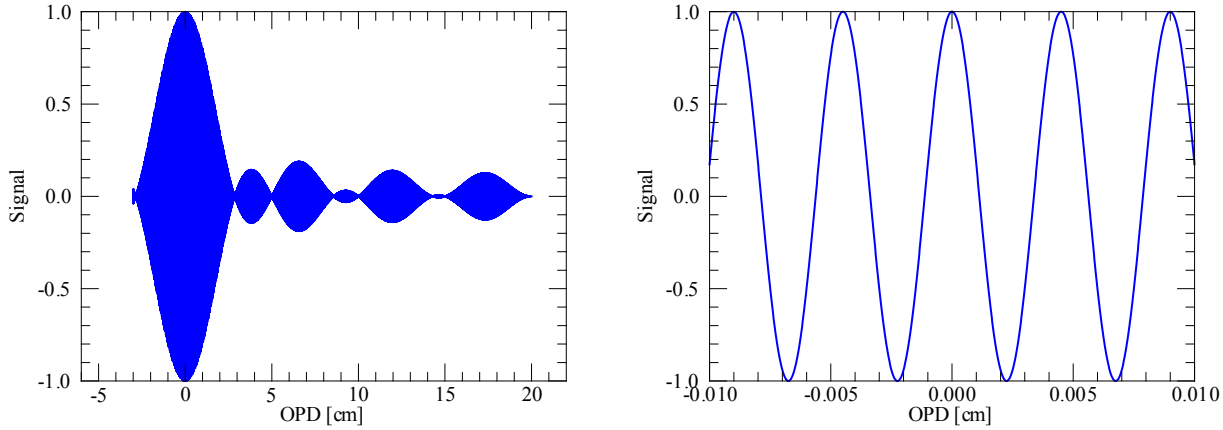

Figure 2. Simulated interferogram of the short wavelength band, centred on 45 μm, of the SAFARI FTS viewing a source with an unresolved spectral line at the centre of the bandpass having a line-to-continuum ratio of 1 (left) and a zoomed in section around the position of zero optical path difference (right).

If one assumes that the dynamic range of the interferogram is digitized by a 14-bit ADC, uncertainty at the level of the least significant bit corresponds to a maximum uncertainty in position of ~1 nm. In other words, metrology uncertainties greater than ~1 nm will exceed the uncertainty introduced by the least significant bit digitizing the interferogram signal.

Another way of expressing the maximum allowable metrology error is in terms of the residual phase error one can tolerate in the analysis after *phase correction*[9]. The rule-of-thumb is that the residual phase error should be no more than ± 1°. For the shortest wavelength of the SAFARI instrument, 34 μm, this results in allowable uncertainties of ~60 nm rms OPD, equivalent to 15 nm rms in linear displacement in the basic Mach-Zehnder[13] design.

Meeting this metrology requirement through optical design and the control of the linear stage is relatively straightforward in the laboratory environment and at room temperature, but becomes significantly more challenging in a cryogenic space environment. In a recent review, Fleming[14] compares the performance of different nanometer resolution metrology techniques, which are summarized in Table 1.

Table 1. Summary of position sensor characteristics[15].

Sensor Type	Range	Resolution [nm]	BW [kHz]	Accuracy
Resistance	$10 - 500$ μm	23	$1 - 10$	1% FSR
Capacitive	10 μm – 10 mm	2.4	100	0.1% FSR
Eddy Current	100 μm – 80 mm	1	40	0.1% FSR
LVDT	$0.5 - 500$ mm	5	1	0.25% FSR
Optical Encoder	1 m	6	> 100	5 ppm
Interferometer	> 1 m	0.5	> 100	1 ppm

Several of the techniques shown in Table 1 have been employed at cryogenic temperatures in the previous far-infrared space astronomy missions mentioned above, including: capacitance micrometry (ISO[2, 15]), inductive sensing (Spitzer[3], Herschel[5]) and optical encoding (AKARI[4, 16], Herschel[5, 17]). To date, however, no mission has adopted a laser based interferometer. The principal advantage of a laser based metrology system is that the range over which it can be used is determined by the coherence length of the laser and can easily exceed 10 km. The challenge lies in designing a system that can work under vacuum and at cryogenic temperatures. In this paper we present the preliminary performance of a fiber-based laser metrology system designed for optical position metrology at cryogenic temperatures.

2 LASER METROLOGY DESIGN

There are several interferometer designs that can provide a quadrature phase signal: polarization encoding, wavelength modulation or, by some means, establishing a fixed OPD equal to a quarter of a wavelength between the probe and reference beams in a two beam interferometer. While in principle the latter design offers a simple solution, the challenge lies in maintaining the precise difference in OPD at cryogenic temperatures.

Our design is based on the 3-phase homodyne interferometer shown schematically in Figure 3. A circulator guides light from a 1550 nm single mode DFB laser[18] to a 3x3 splitter. The 3x3 splitter is manufactured using the fused biconical taper process in which three fibers are twisted together and drawn while heat is applied. Due to this geometry, cross talk of the evanescent field around each fiber occurs. In the ideal case, the intensity of light injected into any input is equally distributed over the three exiting fibers and, as a consequence of conservation of energy, the phases of the three exiting fibers differ by 120°, producing a 3-phase system. The first output from the splitter is terminated, the second output has an integrated reflector, and the third output directs the probe beam to the 4 K working surface via an optical fiber 2 m in length. Figure 4 shows the location and temperature of the interferometer components in the test cryostat.

The probe beam is launched via a custom, fixed focus collimator of focal length 18.75 mm, made from Kovar to minimize differential contraction with the aspherical lens. A 10 mm diameter corner cube reflector prism placed on the back of one of the arms of a scanning wishbone assembly returns the beam to the collimator and subsequently to the splitter. The net result is a two beam interferometer which produces three interference signals 120° out of phase with one another. The optical signals are detected by three InGaAs photodiodes. Custom designed electronics using ultra-low noise operational amplifiers provides gain and offset circuitry to account for gain changes as the fiber cools (a factor of 0.92) and differences between the three optical return channels, notably the circulator return (a factor of 0.87). Apart from the collimator, all optical components are commercial off the shelf.

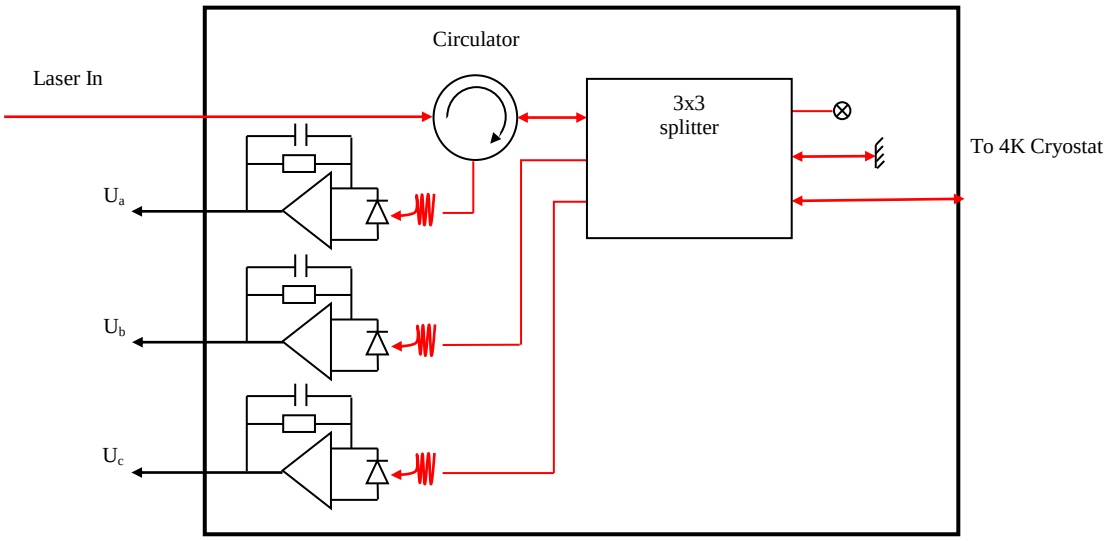

Figure 3. Schematic diagram of the 3-phase interferometer. Red arrows indicate fiber connections. The unit, including the laser, operates under vacuum at room temperature. A fiber carries the probe signal to the 4 K workspace.

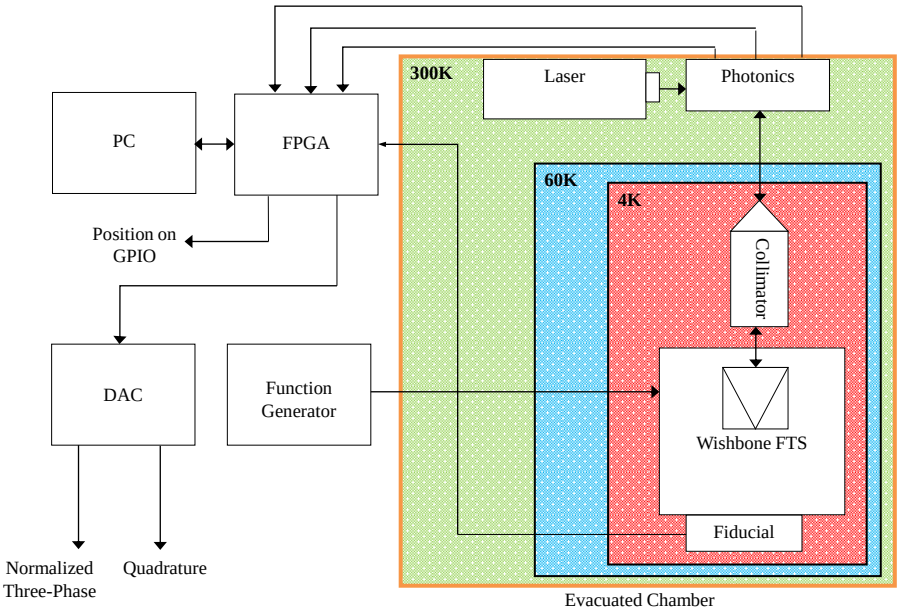

Figure 4. Schematic showing the location and temperature of components of the 3-phase interferometer.

3 DIGITAL PROCESSING

The raw 3-phase signals (U_a, U_b, U_c) generated by photonics (Figure 3) are first normalized before being converted to quadrature using the Clarke transform[19]. The digital processing takes place within a Xilinx XC7A35T Artix-7 Series FPGA on a Digilent Arty Development board[20]. The FPGA has a built-in 12-bit 1 MS/s analog-to-digital converter (ADC) and an external Digilent Pmod DA4 12-bit octal digital-to-analog converter (DAC) is used to output analog signals[21]. The FPGA was programmed in Xilinx Vivado 2017.1[22] using SystemVerilog and autogenerated Xilinx IP cores for arithmetic, ADC configuration, and clock management. The kernel of the system performs communication with a PC over USB serial, keeps track of internal status and control registers, and forwards register values to other parts of the FPGA. The FPGA is fully controllable from a PC using a datagram-based serial communication scheme in which the PC is the master and the FPGA is the slave. The PC issues reads and writes to the FPGA at run time allowing parameters of the system to be changed as required and controls the calibration and homing sequences.

Figure 5 shows a block diagram of the 3-phase to quadrature implementation in the FPGA. A function generator is used to drive the wishbone scanning mechanism. As the wishbone scans, the OPD between the probe and reference beams changes, producing interference signals separated by 120° in phase at each of the three outputs signals (U_a, U_b, and U_c). A fiducial signal, currently provided by an optical switch, provides a reference point from which displacement is measured. The 3-phases from the interferometer and the fiducial reference from the wishbone mechanism are input to the FPGA. The FPGA outputs values for the corrected 3-phase and quadrature signals on the DAC, and position values through its GPIO pins. The FPGA can communicate with a PC using a full-duplex serial interface over USB.

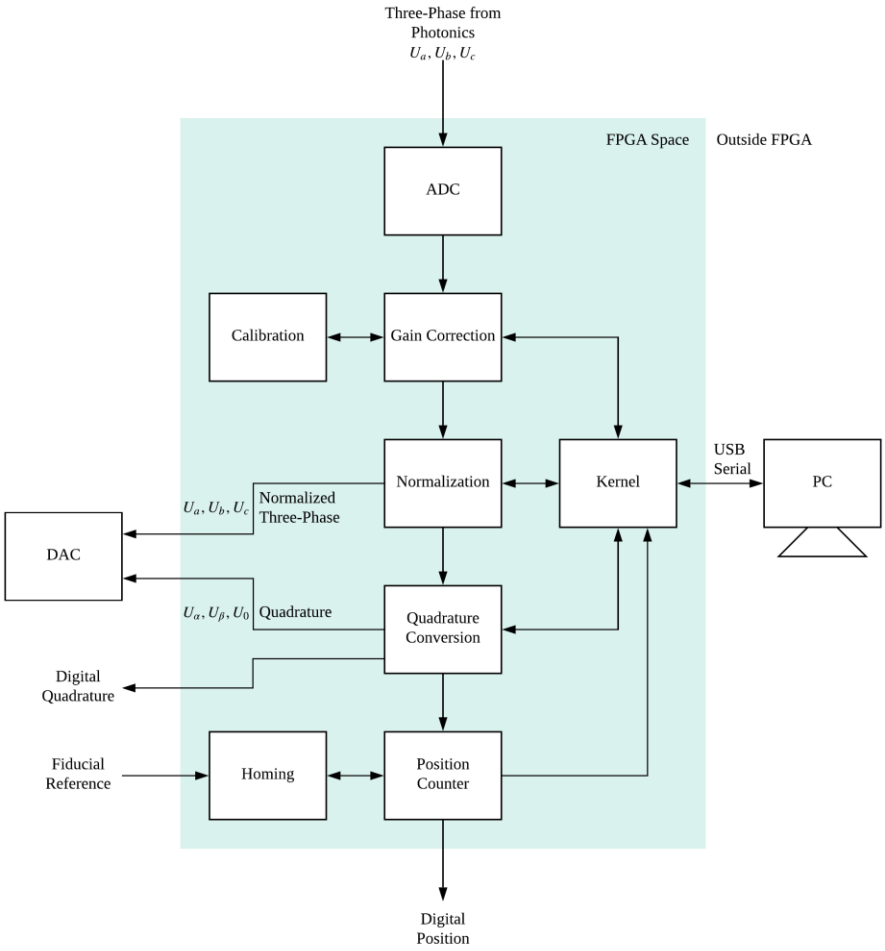

Figure 5. Schematic showing the implementation of the Clarke transform in the FPGA.

The raw 3-phase signals (U_a, U_b, U_c) are sampled by the ADC. Each 3-phase signal is calibrated independently. The goal of calibration is to remove any gain and offset specific to a given channel by projecting the signal to a bounded interval of $[-1, 1]$. With the wishbone mechanism scanning, the global extrema $E_{x,min}$ and $E_{x,max}$, for signal phase, U_x, are determined. These are used to produce gain, G_x, and offset, O_x, correction factors:

$$G_x = \frac{E_{x,.max} - E_{x,min}}{2}$$

$$O_x = \frac{E_{x,.max} + E_{x,min}}{2}$$

Calibration is initiated and terminated by a PC controlling the FPGA over USB. During gain and offset correction (Figure 6) each measured signal phase U_x is corrected in real time as a streaming operation. The corrected signal is:

$$U'_x = \frac{U_x - O_x}{G_x}$$

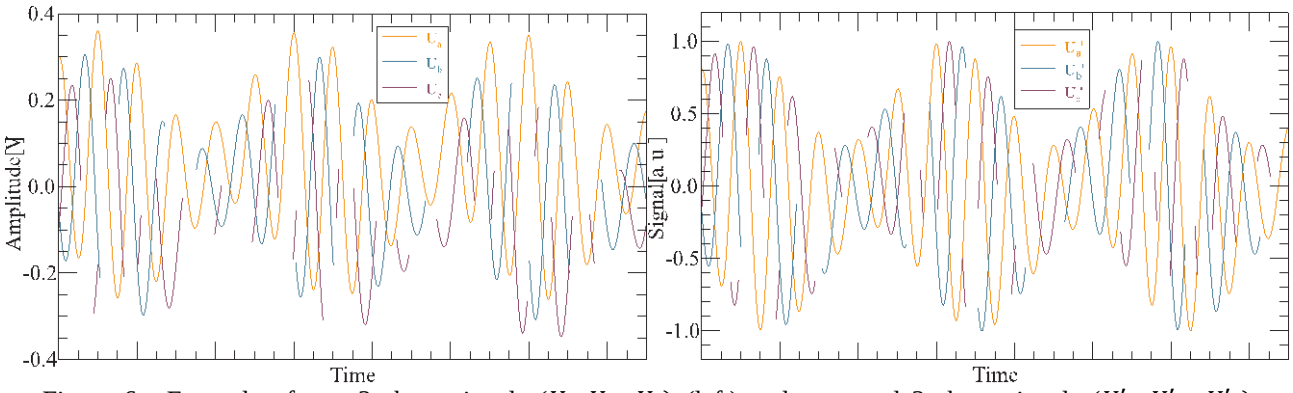

Figure 6. Example of raw 3-phase signals (U_a, U_b, U_c) (left) and corrected 3-phase signals (U'_a, U'_b, U'_c) (right).

In the final step, the corrected 3-phase signals are normalized. Under the assumption that at any given time the gains and offsets on the calibrated 3-phase signals are equal and that the 3-phase signals are separated in phase by exactly 120°, the corrected phase can be expressed as:

$$\begin{bmatrix} U'_a \\ U'_b \\ U'_c \end{bmatrix} = \begin{bmatrix} U_{m(t)} \cos(\omega t) + V(t) \\ U_{m(t)} \cos\left(\omega t + \frac{2\pi}{3}\right) + V(t) \\ U_{m(t)} \cos\left(\omega t - \frac{2\pi}{3}\right) + V(t) \end{bmatrix}$$

where $U_m(t)$ is the gain and $V(t)$ is the offset at time, t. Two properties can be exploited. First, the trigonometric identity:

$$\cos(\omega t) + \cos\left(\omega t + \frac{2\pi}{3}\right) + \cos\left(\omega t - \frac{2\pi}{3}\right) = 0$$

from which $V(t)$ scan be expressed as:

$$V(t) = \frac{U'_a + U'_b + U'_c}{3}.$$

Secondly, $U_m(t)$ can be computed using the constant power property of 3-phase:

$$U_m(t) = \sqrt{\frac{2}{3}\left[\left(U'_a - V(t)\right)^2 + \left(U'_b - V(t)\right)^2 + \left(U'_c - V(t)\right)^2\right]}$$

Finally, the normalized signals can be expressed as pure sinusoids:

$$U_x'' = \frac{U_x' - V(t)}{U_m(t)}; \qquad \begin{bmatrix} U_a'' \\ U_b'' \\ U_c'' \end{bmatrix} = \begin{bmatrix} \cos(\omega t) \\ \cos\left(\omega t + \frac{2\pi}{3}\right) \\ \cos\left(\omega t - \frac{2\pi}{3}\right) \end{bmatrix}.$$

Figure 7 shows the application of the 3-phase normalization process described above.

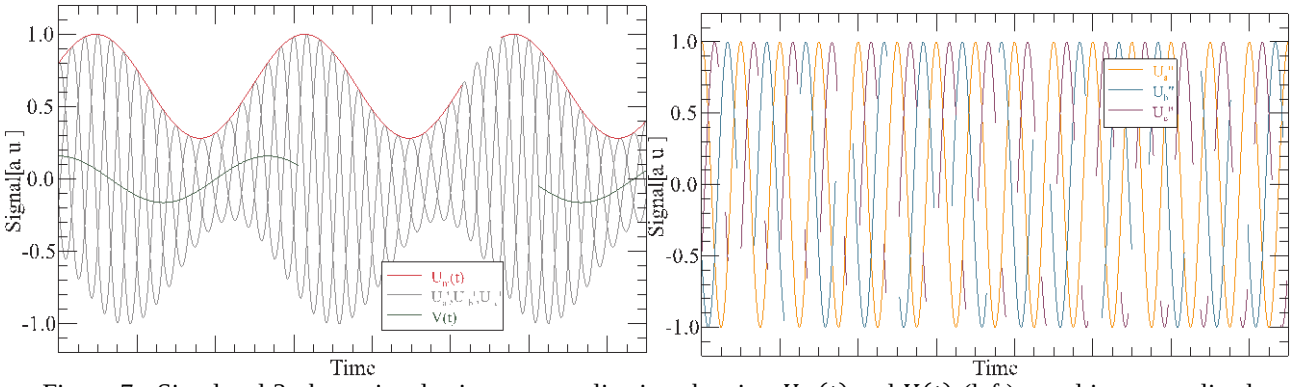

Figure 7. Simulated 3-phase signal prior to normalization showing $U_m(t)$ and $V(t)$ (left); resulting normalized 3-phase signals (right).

Application of the Clarke transform[19] converts the normalized 3-phase signals, U_a'', U_b'', U_c'', to quadrature by multiplication with the transformation matrix, $T_{\alpha\beta 0}$,

$$T_{\alpha\beta 0} = \begin{bmatrix} \frac{2}{3} & -\frac{1}{3} & -\frac{1}{3} \\ 0 & \frac{\sqrt{3}}{3} & -\frac{\sqrt{3}}{3} \\ \frac{1}{3} & \frac{1}{3} & \frac{1}{3} \end{bmatrix}$$

yielding the quadrature signals U_α, U_β, and U_0:

$$\begin{bmatrix} U_\alpha \\ U_\beta \\ U_0 \end{bmatrix} = T_{\alpha\beta 0} \begin{bmatrix} U_a'' \\ U_b'' \\ U_c'' \end{bmatrix} = \begin{bmatrix} \cos(\omega t) \\ \sin(\omega t) \\ 0 \end{bmatrix}$$

which are seen to consist of a sine, a cosine and signal that is 0 under ideal conditions. Since all 3x3 splitters have phase relationships that differ slightly from 120°, a small non-zero value for U_0 is expected. In practice, the value of U_0 provides a useful diagnostic for errors in the computed quadrature. Figure 8 shows the derived quadrature signal from the data in Figure 7. By using the spatial reference provided by the fiducial marker, the absolute position of the wishbone arm can be calculated from the current value of the arctangent of the quadrature while tracking its discontinuities. An example is shown in Figure 8.

The FPGA provides analog output for both the normalized 3-phase and quadrature signals and position in digital format as a 32-bit fixed-point number with the radix at 8. For a laser wavelength of 1550 nm, the least significant bit corresponds to an OPD of 6 nm, meeting the metrology requirement set by phase correction.

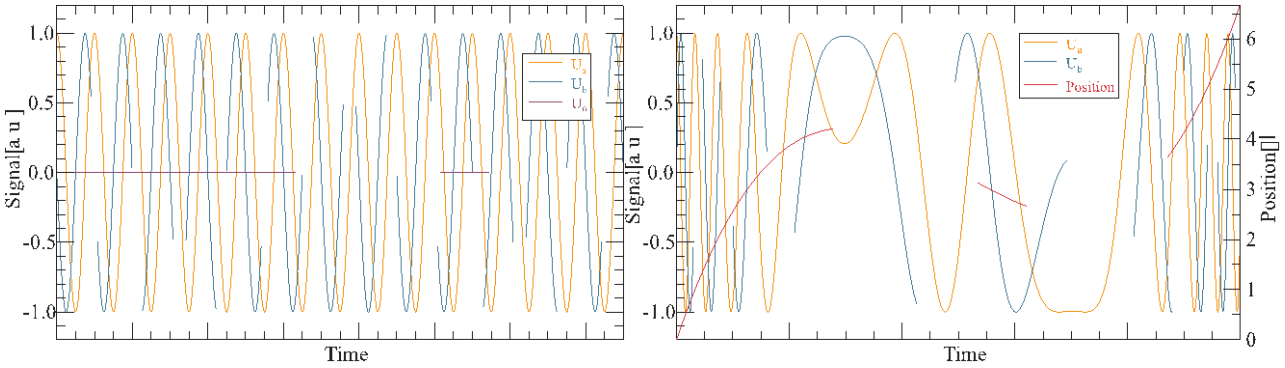

Figure 8. Quadrature signal derived from Clarke transform of data in Figure 7 (left); example of retrieving displacement from a simulated quadrature signal (right).

4 RESULTS

Video 1 shows the experimental layout of the fiber-fed laser interferometer in the laboratory. The 1.55 μm laser (lower right) feeds light into the fiber interferometer module (Figure 3; black box on antistatic pad). The output beam (yellow fiber) is coupled to the collimator, which launches and receives the beam from the retroreflector (black), itself mounted to the end of the scanning wishbone arm (middle right). The FPGA (white circuit board) ingests the raw 3-phase analog signals (U_a, U_b, U_c) shown on the right oscilloscope, and computes the normalized 3-phase signals (U_a'', U_b'', U_c'') following the procedure outlined in section 3; these are shown on the left oscilloscope.

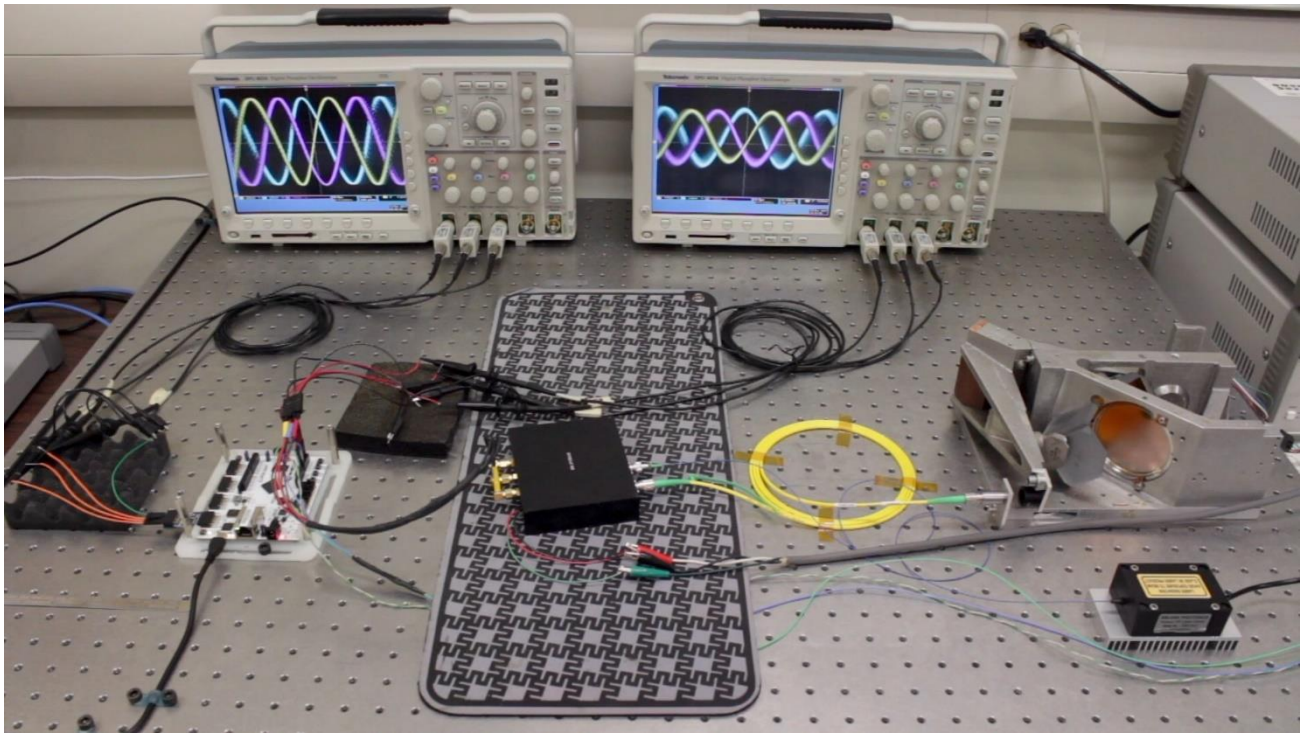

Video 1. Fiber-fed laser interferometer setup. See text for details. http://dx.doi.org/doi.number.goes.here

After bench testing, the system was installed in our cryogenic test facility[23]. As discussed in Section 2, the laser and fiber interferometer module are mounted in the cryostat, under vacuum, but at room temperature. A 2 m optical fiber carries the probe signal to the 4 K working volume as shown in Figure 9. The wishbone assembly is thermally

clamped to the gold plated copper breadboard. The copper braid seen at the middle top improves the thermal conductance from the wishbone arms to the chassis of the interferometer; without this feature the arms cool down very slowly due to the low thermal conductivity of the thin Inconel flexures. The interferometer mechanism reached a base temperature of 3.8 K and metrology fringes were observed throughout the cooldown.

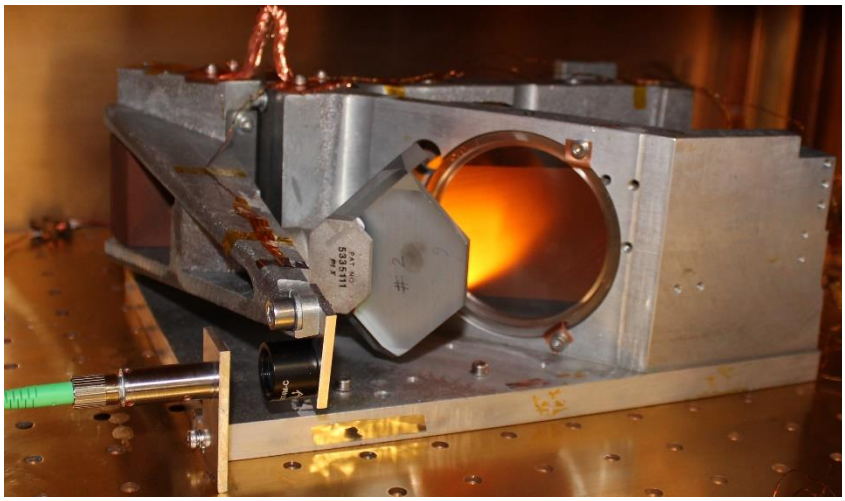

Figure 9. Fiber-fed laser interferometer installed in cryogenic test facility.

Video 2 shows the raw 3-phase analog signals (U_a, U_b, U_c) on the right oscilloscope and the computed quadrature signals U_α, U_β, and U_0, on the left oscilloscope, obtained with the interferometer operating at cryogenic temperatures.

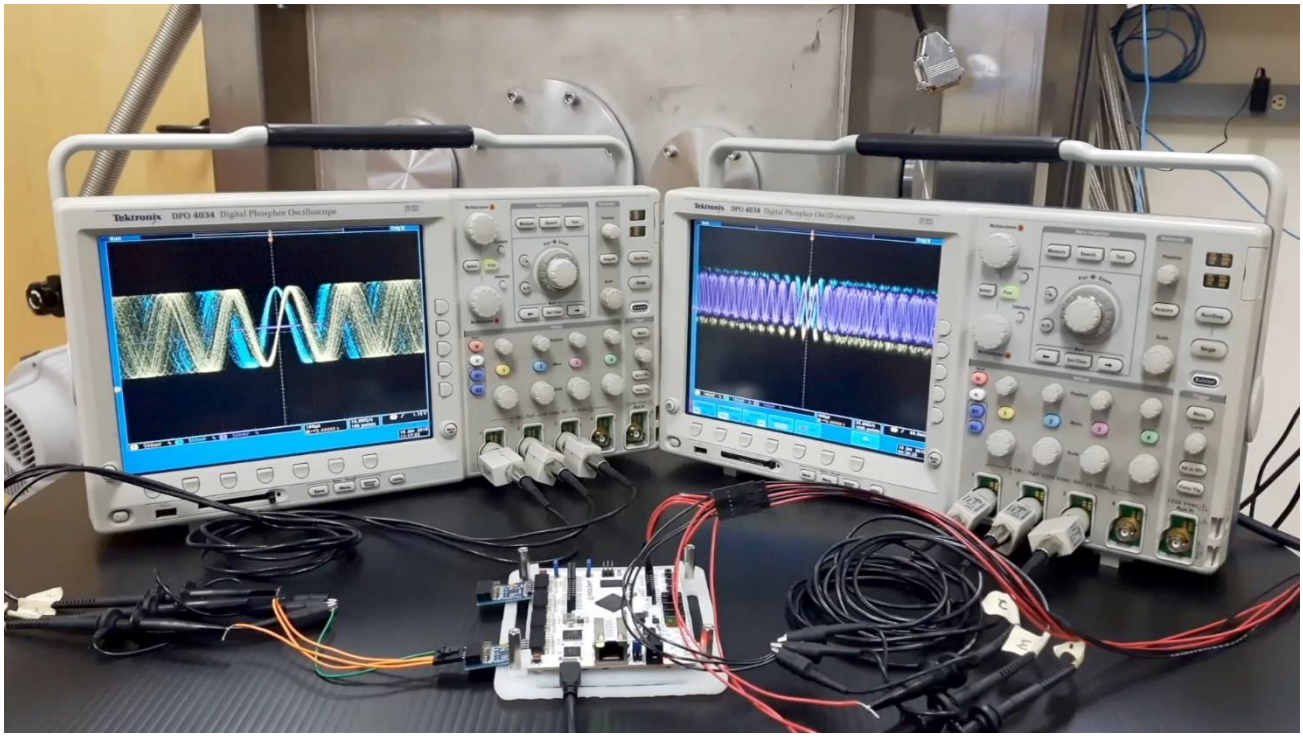

Video 2. Metrology fringes obtained from the fiber-fed laser interferometer operating at 3.8 K.
http://dx.doi.org/doi.number.goes.here

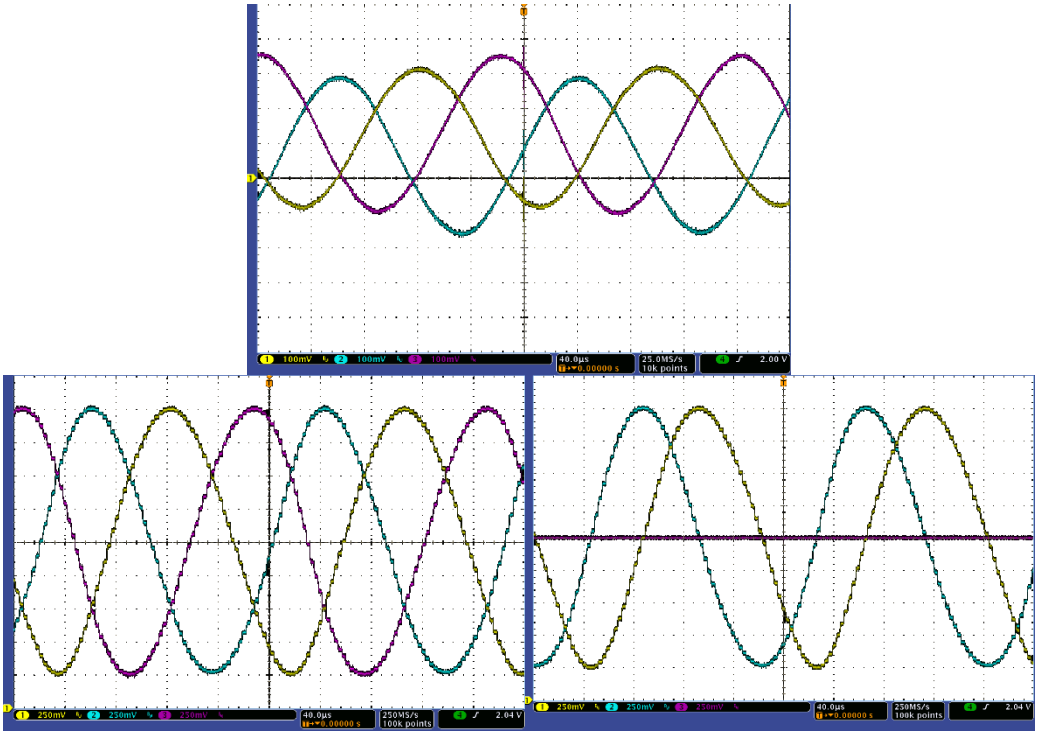

Figure 10. Example of raw 3-phase signals (top) and analog corrected 3-phase and quadrature signals computed by the FPGA (bottom left and right, respectively).

Figure 10 shows an example of the raw 3-phase signal and the corresponding corrected 3-phase and quadrature signals generated by the FPGA. The raw data has been processed independently using the measured phases, which typically differ by ~1° from their notional ±120° separation. The result is a metrology uncertainty of 6.02 nm rms. This number is in very good agreement with the resolution of the radix format adopted for digital output, where the least significant bit corresponds to 6.05 nm and the error introduced by the assumption that the phase differences are exactly 120°.

Figure 11 illustrates the rms metrology error (contours) that arises under the assumption that the phases are precisely 120° apart when they are not. For reference, the red circle indicates the error for the 3x3 splitter used in these measurements.

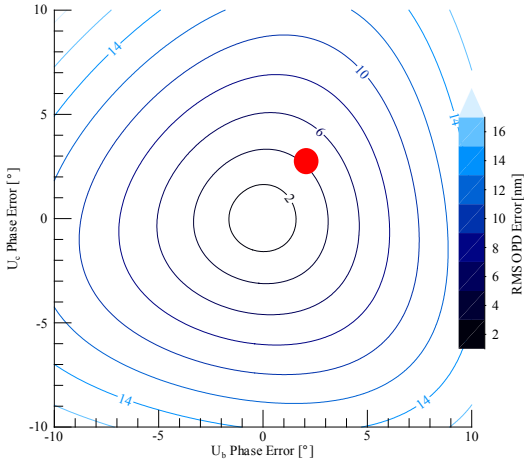

Figure 11. RMS OPD error arising from the departure of the phase of U_b and U_c from the nominal 120° from the reference signal, U_a.

5 CONCLUSION AND FUTURE WORK

We have developed and successfully tested a 3-phase homodyne fiber-fed laser interferometer for optical metrology at cryogenic temperatures. The majority of the components used in the design are commercially available off the shelf. Preliminary results under realistic space conditions of high vacuum, low temperature (3.8 K) and vibration levels equivalent to those experienced by the SPIRE instrument on the Herschel Space Observatory show metrology uncertainties of 6 nm rms. This result is in good agreement with the limit imposed by the current data format, and by the small differences between the actual and assumed phases of ±120° with respect to the reference signal.

Future work will include: increasing the resolution of the digital representation, accounting for the actual measured phases, exploring the pros/cons of using floating point arithmetic and running a second fiber in parallel with the probe fiber to account for common mode variations during the cool down.

Notwithstanding these improvements, the current system has shown that it beats the rule-of-thumb requirement for metrology precision for the Fourier transform spectrometer proposed for the SPICA SAFARI instrument by a factor of 10.

6 ACKNOWLEDGEMENTS

The authors thank Rebecca Sirota for building and validating the low noise electronics, Trevor Fulton for simulating the SAFARI interferograms, and acknowledge valuable discussions with, and technical support from Rob Lennox and Adam Collins of Eblana Photonics. This research is supported by: Alberta Innovates, Canada Foundation for Innovation, Canadian Microelectronics Corporation, Canadian Space Agency, EU FP7- FISICA, and NSERC.

7 REFERENCES

[1] G. Neugebauer et al., The infrared astronomical satellite (IRAS) mission. The Astrophysical Journal, 278:L1–L6, 1984.
[2] M. Kessler et al., The infrared space observatory (ISO) mission. Astronomy and Astrophysics, 315:L27–L31, 1996.
[3] M. Werner et al., The Spitzer space telescope mission. The Astrophysical Journal Supplement Series, 154:1, 2004.
[4] H. Murakami et al., The Infrared Astronomical Mission AKARI, Publications of the Astronomical Society of Japan, 59, S369, 2007.
[5] G. Pilbratt et al., Herschel space observatory-an ESA facility for far-infrared and submillimetre astronomy. Astronomy & Astrophysics, 518:L1, 2010.
[6] P. Roelfsema et al., SPICA - a large cryogenic infrared space telescope: Unveiling the obscured Universe Publications of the Astronomical Society of Australia, submitted 2017.
[7] M. Meixner et al., Origins Space Telescope: Science Case and Design Reference Mission for Concept 1, American Astronomical Society, AAS Meeting #231, id.#355.11, 2018.
[8] F. Helmich and R. Ivison, FIRI - a Far-Infrared Interferometer, submitted to ESA as part of Cosmic Vision 2015-2025 http://arxiv.org/abs/0707.1822, 2007.
[9] S. Davis, M. Abrams & J. Brault, Fourier transform spectrometry. Academic Press, 2001.
[10] P. Connes, Annu Rev Astron Astr. 8, 209, 1970.
[11] A. Michelson and E. Morley, On the Relative Motion of the Earth and the Luminiferous Ether, American Journal of Science. 34 (203): 333, 1887.
[12] D. Martin & E. Puplett, Infrared Physics. 10, 105, 1970.
[13] P. Ade, P. Hamilton & D. Naylor, in Fourier Transform Spectroscopy: New Methods and Applications, Optical Society of America, 1999.
[14] A. Fleming, A review of nanometer resolution position sensors: Operation and performance, Sensors and Actuators A: Physical 190, 106, 2013.
[15] G. Davis, et al., Design and performance of cryogenic, scanning Fabry–Perot interferometers for the Long-Wavelength Spectrometer on the Infrared Space Observatory, Applied optics, 34, 92, 1995.
[16] K. Mitsunobu, et al. Performance of an imaging Fourier transform spectrometer with photoconductive detector arrays: An application for the AKARI far-infrared instrument. Publications of the Astronomical Society of Japan 60, S389, 2008.

[17] M. Griffin, et al., The Herschel-SPIRE instrument and its in flight performance, Astronomy and Astrophysics, 518, L3, 2010.
[18] http://www.eblanaphotonics.com/ ; DX series.
[19] E. Clarke, Circuit Analysis of a.c. Power Systems, Wiley, New York, Volume I, 1943.
[20] https://www.xilinx.com/products/boards-and-kits/arty.html
[21] http://www.analog.com/media/en/technical-documentation/data-sheets/AD5628_5648_5668.pdf
[22] https://www.xilinx.com/products/design-tools/vivado.html.
[23] I. Veenendaal, et al. Performance of a cryogenic test facility for 4 K interferometer delay line investigations, Proceedings of the SPIE, Volume 9904, id. 99045E 12 pp., 2016.